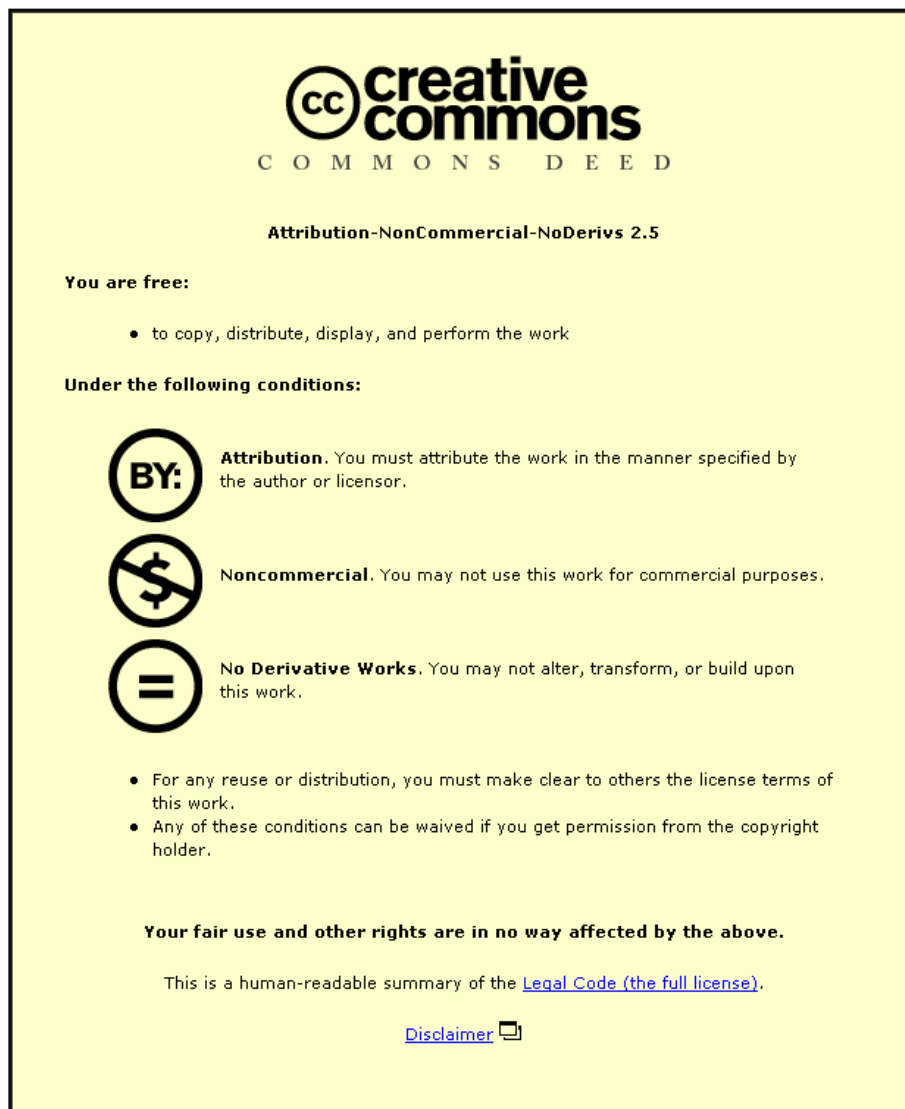


This item was submitted to Loughborough University as a PhD thesis by the author and is made available in the Institutional Repository (<https://dspace.lboro.ac.uk/>) under the following Creative Commons Licence conditions.



For the full text of this licence, please go to:
<http://creativecommons.org/licenses/by-nc-nd/2.5/>

BLDSC no:- DX 177672

LOUGHBOROUGH
UNIVERSITY OF TECHNOLOGY
LIBRARY

AUTHOR/FILING TITLE

MOORE, A.J.

ACCESSION/COPY NO.

040073899

VOL. NO.

CLASS MARK

Please note that fines are charged on ALL
overdue items.

3

08 JAN 2001

997

8

FOR REFERENCE ONLY

0400738996



BLDSC no:- DX177672

~~30 JUN 1995~~

~~29 NOV 1994~~

~~29 NOV 1994~~

~~23 FEB 1995~~

~~30 JUN 1995~~

~~28 JUN 1996~~

~~28 JUN 1996~~

~~28 JUN 1996~~

~~27 JUN 1997~~

27 JUN 1997

26 JUN 1998

25 JUN 1999

14 JAN 2000

- 6 OCT 2000

0400738996



BADWINGTON PRESS
18 THE BRIDGE CROFT
LEICESTER LE1 3LD
ENGLAND
TEL: 0533 602917



STRAIN ANALYSIS USING ESPI
APPLIED TO FRACTURE MECHANICS

by

Andrew J. Moore
B.Sc.(Hons)

A Doctoral Thesis submitted in partial
fulfilment of the requirements for the
award of Doctor of Philosophy of the
Loughborough University of Technology

September 1992

© by A.J. Moore, 1992

Loughborough University of Technology Library	
Date	SEP 93
Class	
Acc. No.	04073899

49921546

"There's been a lot of speculation that cracks are starting to appear. That's probably the case, but I would hate to try to define how big the cracks are, how critical the cracks are ... what the result will be."

General Norman Schwarzkopf

February 1991

ABSTRACT

Electronic speckle pattern interferometry (ESPI) has become an established technique for surface deformation studies. However, difficulties remain in the practical use of ESPI, primarily because results require skilled and time-consuming interpretation. The work reported here has enabled automated acquisition and processing of ESPI displacement data. Further processing has enabled the components of surface strain and stress to be determined automatically. Such measurements are of great importance for experimental fracture mechanics studies, a quantitative approach to measuring the severity of defects in a loaded structure. Having established the importance of experimental optical methods in fracture mechanics, and the particular advantages of ESPI, a study has been undertaken to determine whether ESPI can be used for quantitative fracture mechanics measurements.

Automated analysis for in-plane displacement measurements with ESPI was achieved by the phase-stepping technique. Numerical differentiation of the displacement data allowed surface strain to be evaluated. The accuracy of such measurements was investigated, particularly with regard to speckle noise inherent in the data. Speckle noise limits the accuracy of all measurements, and a practical threshold for displacement and strain of $\pm 0.03\mu\text{m}$ and $\pm 6\mu\text{strain}$ was found. From these considerations, two new phase-stepping algorithms have been proposed for ESPI. The first offers improved accuracy by the way it eliminates speckle noise; the second has allowed phase-stepping of ESPI addition fringes for the first time.

In the past ESPI has been restricted to uniaxial measurements. A new interferometer design enabled displacement to be measured along two axes simultaneously: extension to three-dimensional sensitivity is discussed. Automated displacement and strain measurements, recorded with the dual-sensitivity interferometer, are presented for a cantilever loaded at its free end.

Building on the success of these results, quantitative fracture mechanics studies were undertaken with ESPI for the first time: previously ESPI had been used only to detect the position of defects. Experimental results are presented for two specimens. Firstly displacement and strain measurements were made from a centre-notched plate loaded in uniaxial tension. These were compared with a stress function solution and a finite element model. Secondly, the commonly used fracture mechanics parameters of opening-mode stress-intensity factor (K_I) and J-integral (J) were evaluated for three compact tension specimens of various crack lengths. It was demonstrated that ESPI may be successfully used to measure K_I with a signal-to-noise ratio of 36dB over the measurement range of $0.7\text{MN/m}^{3/2}$. Measurements fall within 10% of theoretical values. The uncertainty in a single J measurement was found to be $\pm 33\%$ for the 5N/m measurement range, although this may be reduced by averaging several measurements.

The performance of ESPI is compared with alternative optical techniques, in particular moire interferometry which was used to verify all measurements from the compact tension specimens. The potential for further improving the technique and possible areas of application are discussed. It is concluded that ESPI offers particular advantages for some types of study, and that it compliments the existing range of optical techniques.

ACKNOWLEDGEMENTS

This work was carried out in the Department of Mechanical Engineering at Loughborough University of Technology between October 1988 and September 1992, and was supervised by Dr John Tyrer, whose encouragement and advice have been much appreciated. The Director of Research was Professor Ray Vitols. Funding was provided by the Science and Engineering Research Council.

I would like to thank past and present members of the Optics Group for support and assistance on many occasions, in particular Fernando Mendoza Santoyo, David Kerr, Terry West and Mike Shellabear. Thanks also to the other members of staff and postgraduate researchers in the Department of Mechanical Engineering who have made my time at Loughborough University most enjoyable. Thanks are also due to the technical staff in the Department for their contributions, especially Vic Roulstone and Steve Penney for manufacturing and maintaining equipment, Ken Topley and Vince Scothern for photographic work, Peter LeGood and Janet Redman for line drawings and Janet Smith for typing the manuscript.

Figure 3.2 was reproduced by kind permission of Mike Shellabear and Fernando Mendoza Santoyo. Moire interferometry results in Chapter 5 were recorded with the assistance of John Brownell of Rolls Royce plc.

CONTENTS

<u>ABSTRACT</u>	iii
<u>ACKNOWLEDGEMENTS</u>	v
<u>CONTENTS</u>	vi
<u>1. INTRODUCTION</u>	1
1.1 BACKGROUND TO RESEARCH	1
1.2 FRACTURE MECHANICS	2
1.3 ELECTRONIC SPECKLE PATTERN INTERFEROMETRY	3
1.4 PROJECT AIMS	5
<u>2. LITERATURE REVIEW</u>	6
2.1 FRACTURE MECHANICS	6
2.1.1 Energy Release Rate and Stress-Intensity Factor	7
2.1.2 Crack-Opening Displacement	12
2.1.3 J-Integral	13
2.1.4 Extension of Basic Parameters	16
2.2 OPTICAL METHODS IN FRACTURE MECHANICS	18
2.2.1 Photoelasticity	20
2.2.2 Optical Interferometry	22
2.2.3 Holographic Interferometry	25
2.2.4 Speckle Techniques	27
2.3 ESPI	29
2.3.1 Principles of ESPI	30
2.3.2 Out-of-plane ESPI	31
2.3.3 In-plane ESPI	32
2.3.4 ESPI Applications	35

3.	<u>AUTOMATED DISPLACEMENT AND STRAIN EVALUATION</u>	38
3.1	AUTOMATED FRINGE PATTERN ANALYSIS	38
	3.1.1 Fringe Tracking	40
	3.1.2 Heterodyne and Phase-Stepping Interferometry	42
	3.1.3 Alternative Phase Measuring Techniques	49
	3.1.4 Selection of Phase-Stepping for In-Plane ESPI	50
3.2	IN-PLANE PHASE-STEPPED ESPI	51
	3.2.1 Temporal Phase-Stepping Speckle Correlation (TPSSC)	52
	3.2.2 Digital Phase-Stepping Speckle Interferometry (DiPSSI)	57
	3.2.3 Analytic Solutions	61
	3.2.4 Accuracy of Phase Measurement	68
	3.2.5 Experimental Investigation of Accuracy of Phase Measurement	76
3.3	SURFACE STRAIN MEASUREMENT	85
	3.3.1 Methodology	86
	3.3.2 Accuracy of Strain Measurement	92
3.4	CLOSURE	94
4.	<u>SIMULTANEOUS MEASUREMENT OF PERPENDICULAR IN-PLANE DISPLACEMENT COMPONENTS</u>	97
4.1	INTRODUCTION	97
4.2	DEMONSTRATION OF TECHNIQUE	102
	4.2.1 Investigation of Surface Preparation	102
	4.2.2 Experimental Demonstration	106
4.3	COMBINATION WITH PHASE-STEPPING	110
	4.3.1 Experimental System	110
	4.3.2 Accuracy of Displacement and Strain Measurement	115
	4.3.3 Experimental Demonstration	118
4.4	CLOSURE	126
5.	<u>FRACTURE MECHANICS APPLICATIONS</u>	130
5.1	CENTRE-NOTCHED PLATE	130
5.2	COMPACT TENSION SPECIMEN	143
	5.2.1 ESPI measurements	143
	5.2.2 Moire Interferometry Measurements	150
	5.2.3 K_I -Evaluation from Displacement Measurements	157
	5.2.4 Crack-Opening Displacement Evaluation	166

5.2.5 J-Integral Evaluation	168
5.2.6 ESPI and Moire Interferometry Results	169
5.3 CLOSURE	178
<u>6. DISCUSSION</u>	182
6.1 EXPERIMENTAL RESULTS	182
6.1.1 Chapter 3	182
6.1.2 Chapter 4	187
6.1.3 Chapter 5	190
6.2 FURTHER WORK	195
6.2.1 Potential Applications	195
6.2.2 ESPI Technique	197
<u>7. CONCLUSIONS</u>	199
<u>APPENDICES</u>	202
<u>A. STRESS FUNCTION THEORY</u>	203
A.1 TWO-DIMENSIONAL STRESS FUNCTION	203
A.2 CANTILEVER LOADED AT FREE END	205
A.3 CENTRE-NOTCHED PLATE IN UNIAXIAL TENSION	206
<u>B. INTERPRETATION OF ESPI FRINGE DATA</u>	213
B.1 SPECKLE PATTERN INTERFEROMETRY	213
B.2 GENERALISED FRINGE FUNCTION	214
<u>C. IMAGE PROCESSING HARDWARE AND SOFTWARE</u>	217
C.1 HARDWARE	217
C.2 SOFTWARE	218

<u>D.</u>	<u>LIST OF SYMBOLS</u>	225
<u>E.</u>	<u>PUBLICATIONS</u>	227
	<u>REFERENCES</u>	229

1. INTRODUCTION

This thesis describes research undertaken into the application of electronic speckle pattern interferometry (ESPI) to fracture mechanics studies. Section 1.1 describes the background to the research programme. An overview of the philosophy behind fracture mechanics is given in Section 1.2, including the role of experimental techniques in its development and verification. A specific experimental technique that has not previously been applied to quantitative fracture studies, namely ESPI, is introduced in Section 1.3. From the discussion in these sections, the project aims are drawn in Section 1.4. This chapter therefore serves as a broad introduction to the thesis. It is also a glossary of the terms most commonly used throughout the thesis: the section where further information can be found is given. The remainder of the thesis is divided as follows. Chapter 2 reviews previous relevant work from the literature, covering other optical techniques applied to fracture studies. Chapters 3 and 4 document work undertaken on the ESPI technique to enable automated, quantitative fracture mechanics analysis. Chapter 3 describes the automation of displacement measurement with ESPI, and the subsequent extraction of surface strain from the displacement data. Chapter 4 considers a new design of ESPI interferometer enabling the required measurements to be made more easily. These techniques are applied to two fracture mechanics studies in Chapter 5. The results obtained in Chapters 3, 4 and 5 are discussed in Chapter 6 with regard to the aims stated in Chapter 1. Suggestions for further work and potential applications are also discussed in Chapter 6. Conclusions are drawn in Chapter 7. Specific aspects of ESPI and fracture mechanics theory are given in the Appendices.

1.1 BACKGROUND TO RESEARCH

This work forms part of the ongoing research at the Department of Mechanical

Engineering at Loughborough University of Technology into optical methods in engineering metrology. The technique of electronic speckle pattern interferometry (ESPI) had been invented and developed as part of the research programme at Loughborough. The principles of ESPI are discussed in Sections 1.3 and 2.3. It had been demonstrated that ESPI could measure orthogonal in-plane and out-of-plane components of surface displacement, Section 1.3. Work had started on the automated extraction of displacement data from ESPI measurements. This was generally qualitative in nature and had considered out-of-plane ESPI only (e.g. automatic determination of out-of-plane resonant vibration modes and their display as wire-mesh plots). In-plane ESPI studies involved tedious manual interpretation of the results. With this background, work started under Science and Engineering Research Council grant 88306946, "The application of optical methods in fracture mechanics". The primary objective was to determine if ESPI could be used for fracture mechanics studies, with the implicit assumption that a preliminary study of in-plane ESPI would be required.

1.2 FRACTURE MECHANICS

Fracture mechanics theory was first proposed in the 1950s to explain brittle (rapid) fracture in engineering structures. Having noted that the stress level at a crack tip is raised far above the stress in the net section, it was proposed that the severity of the crack could be related to the geometry of the structure by the stress-intensity factor, K . The crack would propagate when K reached a critical value, K_c , that under certain conditions could be regarded as a material property. These conditions included plane strain and plastic yielding limited to a small region at the crack tip. These terms are discussed in Section 2.1.1. The basic premise of fracture mechanics is that a measurement of K_c made in the laboratory may be applied to predict fracture in the real structure, giving a quantitative assessment of the severity of defects. However, the conditions required for valid K_c are not often experienced in practice: brittle-fracture does not generally take place in thin sections or when preceded by yielding. Hence the theory was

extended, and different parameters describing conditions at the crack tip were proposed. Of relevance to this thesis are the crack-opening displacement (the relative displacement of opposite faces at the crack tip) and the J-integral (a measure of the non-linear elastic work to fracture), Sections 2.1.2 and 2.1.3. Again it was proposed that the crack would extend, although not necessarily catastrophically this time, when these parameters reached a critical value. The critical value is measured experimentally, and may be considered a material property under certain conditions. These conditions for crack-opening displacement and J-integral are discussed in Sections 2.1.2 and 2.1.3 respectively.

Quantitative fracture analysis therefore requires two values to be compared: the actual value of the characterising parameter at the crack tip at a given load, and a critical value at which the crack will extend. The critical value is determined in a closely controlled test. A method to determine the actual value at a given load is then required. Some of the most common methods are discussed in Section 2.2, where it is shown that experimental measurements are often needed to measure the characterising parameters for complex three-dimensional structures. Generally the procedure is to make an experimental measurement of displacement, strain or stress at the crack tip, for the application of a known load. From these measurements, an estimation of the characterising parameter is made. Therefore experimental methods play an important role in fracture mechanics studies. In particular, optical methods are an attractive measurement method because they are non-contacting. As the subject of this thesis, the emphasis of Section 2.2 is on optical methods. Displacement measurements made with ESPI could possibly be applied in this manner, particularly in situations where ESPI shows advantages with respect to other optical methods. The ESPI method is introduced in the following section.

1.3 ELECTRONIC SPECKLE PATTERN INTERFEROMETRY

The operation of ESPI relies on interference between coherent wavefronts. It is

one of a family of coherent light techniques that includes holographic and speckle interferometry. When two mutually coherent wavefronts are combined, an interference pattern is formed that characterises the phase relationship between them. The resulting interference pattern will change if the phase relationship between the two beams changes. If this phase change is introduced by the displacement of a reflecting or scattering surface, details of the displacement will be contained in the interference pattern. Interferometry may be used to measure surface displacement if the displacement information can be extracted from the interference pattern. The method of fringe formation for ESPI is described in Section 2.3.1. A brief summary follows.

For ESPI, a TV camera is placed in the coherent interferometer. At least one beam of the interferometer is scattered from the surface under test. Two interference patterns (called interferograms) are recorded, between which the surface being studied is deformed. The phase change introduced in the scattered wavefront is extracted by correlating these two interferograms. This correlation is typically performed by an electronic subtraction. The result of the correlation is in the form of fringes (dark and bright correlation bands) superimposed on the test surface. These fringes map loci of constant phase difference between the interfering wavefronts. This phase difference is related to the surface deformation during the measurement period, and enables accurate measurements of surface displacement to be made. Typically the incremental surface deformation represented between adjacent fringes is $\approx 0.3\mu\text{m}$. The interferometer is sensitive to displacements in a single direction, termed the sensitivity vector. The sensitivity vector is determined by the optical configuration of the interferometer. Typical interferometer configurations are discussed in Section 2.3. Conveniently, three mutually orthogonal sensitivity vectors can be chosen: out-of-plane and two orthogonal in-plane measurements with respect to the test surface. Two and three dimensional measurements may then be made by straightforward vector addition of the orthogonal measurements. The ability to measure orthogonal displacement components is an attractive feature of ESPI, and greatly simplifies the measurement procedure. This is one of the possible advantages of applying ESPI

to fracture mechanics problems. Other possible advantages are discussed in Section 2.3.4. Section 2.3.4 also discusses reports in the literature of fracture mechanics studies using ESPI. It is shown that these studies have generally been qualitative in nature.

1.4 PROJECT AIMS

From the foregoing discussion, the following aims for the research programme may be drawn:

1. Fracture studies with ESPI will produce correlation fringes denoting displacement at the crack tip. A quantitative study of these displacements is required, and thus automated evaluation is desirable. Also the evaluation of surface strain and stress would make ESPI a more useful experimental mechanics technique, and are required for the calculation of some fracture parameters. Again, automated analysis is desirable.
2. Determine if ESPI may be used in quantitative fracture mechanics studies. From the experience gained, determine the merits of ESPI with respect to other optical techniques.

2. LITERATURE REVIEW

A critical review of previous work relevant to the present study is presented in this chapter. The review is divided into three sections. Firstly some basic fracture mechanics concepts are introduced in Section 2.1. This section is kept brief, since it is not the aim of this thesis to propose new fracture mechanics theory, nor can the suitability of a given fracture criterion be discussed without knowledge of a specific application. The discussion highlights the importance of experimental methods in developing fracture mechanics theory and in its implementation in practice. Section 2.2 describes experimental techniques, and in particular optical methods, which have been applied in the study of fracture. The measurements made with these techniques can be compared with the results presented in this thesis in order to judge the relative merits of ESPI in fracture analysis. Finally, Section 2.3 reviews the ESPI technique, and the research and development that have refined it to its present status.

2.1 FRACTURE MECHANICS

The aim of fracture mechanics is to enable engineers to design against fracture in a quantitative manner. The general concept is to relate mechanical features of a laboratory test specimen, such as the stress level and geometry, to a parameter that is a measure of the material's resistance to fracture. Once a critical value that is supposed to be a material property is exceeded, the crack extends. Knowledge obtained in this way is applied to avoid fracture in engineering structures. Whether the failure predicted is rapid and leads to catastrophic failure, or the crack extends and then arrests, depends entirely on the service conditions and specimen geometry.

The first theories of fracture mechanics were proposed in the mid-1950s, and were

generally concerned with the static, residual strength of specimens prior to rapid fracture. Plastic deformation was assumed to be restricted to a small region at the crack tip: the fracture was considered brittle and the theory became known as linear elastic fracture mechanics (lefm). Section 2.1.1 describes the most commonly used fracture criterion in lefm, namely the stress-intensity factor. Interest quickly spread to fracture conditions preceded by plastic deformation (but not the general yield condition). Fracture parameters such as the crack-opening displacement, Section 2.1.2, and J-integral, Section 2.1.3, were proposed, and form the basis of what is known as elastic-plastic fracture mechanics (epfm). Under static loading conditions, in the linear elastic regime, these three parameters are related to one another. As fracture mechanics has burgeoned into the vast field of study that it is today, a modified version of these three parameters has been proposed to characterise failure under very different conditions than those for which they were originally considered. For example, modified forms of the stress-intensity factor have been used to predict fatigue crack growth, stress corrosion cracking and dynamic fracture. Parameters of this type are briefly described in Section 2.1.4, and represent far less well understood fracture criteria than, for example, the stress-intensity factor under plane strain conditions. They represent current attempts to apply fracture mechanics theory to useful engineering situations. They are described, because ultimately ESPI could find applications in these areas. However, it is the purpose of this thesis to determine if ESPI can be successfully applied to fracture mechanics studies. To obtain this "proof of principle" the analysis is restricted to the simplest case, namely static, lefm. This section therefore concentrates on the stress-intensity factor, crack-opening displacement and J-integral, and their relationship in the linear elastic regime. The texts by Knott¹, Rolfe and Barsom² and Broek³ have provided a valuable background for this review.

2.1.1 Energy Release Rate and Stress-Intensity Factor

Early concepts of the ultimate tensile strength of a body focused on the stress

required to fracture the crystal lattice across a plane. By equating the energy that must be supplied to separate the atoms to infinity with the energy required to create two new surfaces this theoretical tensile strength is approximately $E/10$ for many materials¹, where E is Young's modulus. Griffith⁴ noted that in practice the tensile strength is two orders of magnitude lower than this, and proposed that the macroscopically homogeneous test sample might contain small defects that concentrate the stress sufficiently for the ideal fracture strength to be attained in localised regions of the sample. He suggested that a crack would extend spontaneously under the applied stress only if the total energy of the body decreased as the crack length increased. Strain energy, W , released by the crack extension would be absorbed in creating the new surfaces, U . The evaluation of U is very complicated in the presence of plastic deformation, and Griffith restricted his consideration to brittle materials i.e. those that behave elastically prior to crack propagation. Work done by the forces applied to the system, B , is also difficult to evaluate except under certain loading conditions (e.g. fixed-load or fixed-grip loading). Considering the *reduction* in potential energy, P , of the system:

$$P = W - U + B \quad (2.1)$$

Griffith⁵ evaluated a plane stress fracture stress, σ_F , given by:

$$\sigma_F = \sqrt{\frac{2 E \gamma_{ST}}{\pi a}} \quad (2.2)$$

where γ_{ST} is the surface tension of the material at the fracture temperature, and a is the crack length. Griffith tested this theory on glass rods containing defects of various lengths, and found that a constant value of $(\sigma_F \sqrt{a})$ was obtained at fracture. Although the value was approximately three times that predicted by equation (2.2), a functional relationship between failure stress and crack length was a significant discovery.

When testing the onset of unstable fracture in steels, Orowan⁶ rewrote Griffith's relationship to accommodate limited plastic deformation in a thin layer adjacent

to the crack wall. Again, for plane stress conditions:

$$\sigma_F = \sqrt{\frac{E(2\gamma_{ST} + \gamma_P)}{\pi a}} \quad (2.3)$$

where γ_P was the energy per unit area expended in plastic work, and is approximately three orders of magnitude larger than γ_{ST} . Felbeck and Orowan⁷ found a constant value for $(\sigma_F\sqrt{a})$ at fracture for steel specimens with various initial crack lengths, but the value of γ_P required to satisfy equation (2.3) was approximately five times larger than might be expected from X-ray analysis of the crack surface. Rather than trying to evaluate γ_P , Irwin and Kies⁸ proposed that its experimentally determined value could be used as a measure of the material's resistance to fracture, provided that plastic deformation at instability was much smaller in extent than the crack length or sheet width. Irwin and Kies assumed the contribution of external forces to be negligible for fast fracture and heavy grips i.e. $B=0$. Considering the rate of change of potential energy with increasing crack length, the criteria for the onset of instability became $dW/da \geq dU/da$. They demonstrated that the strain energy release rate dW/da is partially dependent on the specimen dimensions, enabling the balance point for instability $dW/da \geq dU/da$ to be calculated as a function of the crack length and the applied stress. The value of dU/da was presumed to be a material property that could be determined by a suitable test. Irwin and Kies⁹ proposed the compliance method to evaluate dW/da . The compliance method is described in Section 5.2.6. The value obtained is dependent on the type of loading used, since in practice work done by the external forces is not zero. This emphasises the difficulty in applying the energy balance approach to the body as a whole, and explains why later analysis concentrated on characterising fracture with crack tip parameters.

In a subsequent paper, Irwin¹⁰ considered the stress distribution ahead of a stationary crack for various specimen geometries, and found that:

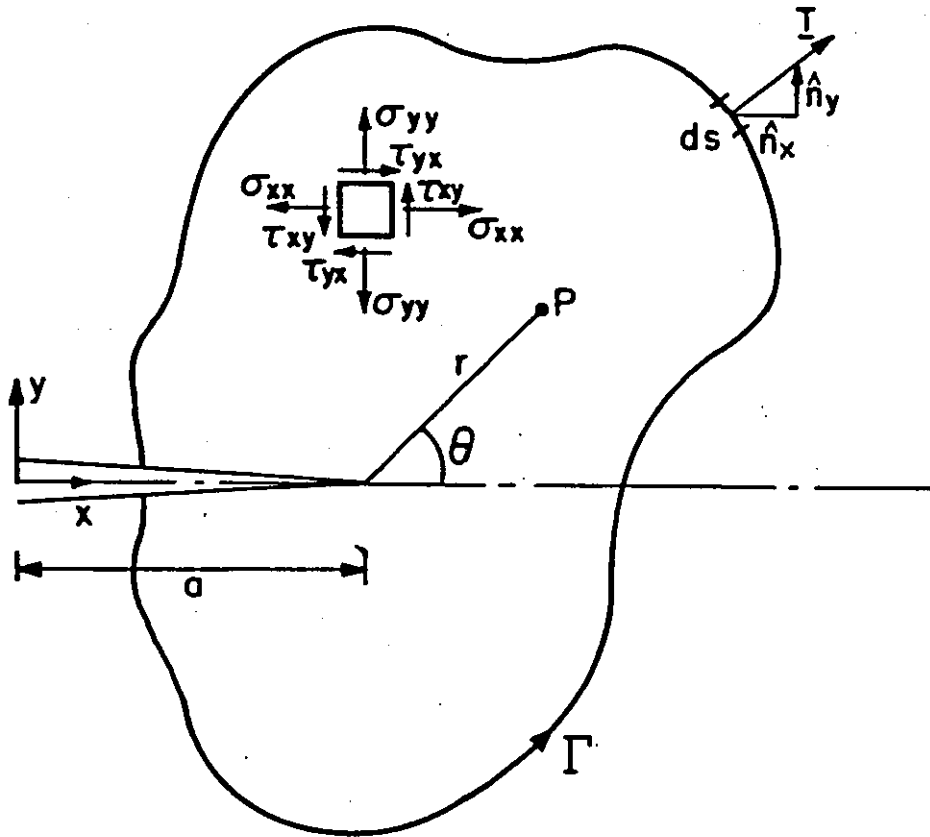


Figure 2.1 Crack tip geometry

$$\sigma_{xx} = \frac{K_I}{\sqrt{2\pi r}} \cos \frac{\theta}{2} \left(1 - \sin \frac{\theta}{2} \cos \frac{3\theta}{2} \right)$$

$$\sigma_{yy} = \frac{K_I}{\sqrt{2\pi r}} \cos \frac{\theta}{2} \left(1 + \sin \frac{\theta}{2} \cos \frac{3\theta}{2} \right) \quad (2.4)$$

$$\tau_{xy} = \frac{K_I}{\sqrt{2\pi r}} \cos \frac{\theta}{2} \sin \frac{\theta}{2} \cos \frac{3\theta}{2}$$

where (r, θ) is a polar coordinate system with origin at the crack tip, Figure 2.1. σ_{xx} and σ_{yy} are the components of normal stress, and τ_{xy} is the shear stress with respect to the xy coordinate system shown. This solution is discussed in Appendix A. The stress distribution is unique at the crack tip and independent of the loading conditions and specimen geometry. The loading and geometry influence the stress distribution through the parameter, K , the stress-intensity factor. Irwin

considered opening-mode, or mode I, fracture since brittle fracture is generally associated with crack motion perpendicular to the direction of greatest tension. The same principles have been found to apply to mode II (shear) and mode III (anti-plane) fracture¹⁻³, but are not discussed in this thesis. By the principle of virtual work, Irwin¹¹ demonstrated that the strain energy release rate, dW/da , was equivalent to a crack extension force, G , and that for plane stress:

$$G = \frac{K^2}{E} \quad (2.5)$$

Thus, if the onset of unstable fracture can be predicted by the attainment of a critical strain energy release rate dW/da , it can also be predicted by the attainment of a critical stress distribution at the crack tip, characterised by K_{Ic} . The equivalence of the energy and stress-intensity factor approaches to fracture is the basis of linear elastic fracture mechanics. In general, the stress-intensity factor may be written in the form¹⁻³:

$$K_I = Y \sigma \sqrt{\pi a} \quad (2.6)$$

where σ is a characterising stress. Y is a calibration function which defines K_I for the specific body under test, known as the geometrical shape factor. It is usually defined as a function of (a/W) , where a is a characterising crack length and W is a characterising dimension. Methods of calculating K_I are discussed in Section 2.2.

A considerable amount of experimental work was quickly undertaken to evaluate K_{Ic} for various materials¹². The value of K_{Ic} is strongly dependent on the plate thickness and can only be regarded as a material property once a certain thickness has been exceeded. The variation in value is attributed to increased plastic constraint along the crack front as the plate thickness is increased¹². K_{Ic} also varies with temperature, the rate at which the specimen is loaded, and notch acuteness. Therefore conditions under which K_{Ic} can be determined are carefully defined¹³. However, in-service conditions frequently differ from those required by the standard: thin sections and failure preceded by plastic deformation are not uncommon. Consequently the concepts of lefm have been extended for more

general application.

2.1.2 Crack-Opening Displacement

Whilst considering the effects of the plastic zone and plastic flow prior to rapid fracture, Wells¹⁴ observed that the crack faces at the tip may move apart without an increase in the crack length. The crack-opening displacement or crack tip-opening displacement, δ , is a measure of the relative movement of the two crack faces. Wells proposed that fracture might occur when the crack-opening displacement reached a critical value δ_c . Burdekin and Stone¹⁵ derived a theoretical value of δ based on Dugdale's strip yield model for the plastic zone radius. Assuming the plastic zone to be of small extent (i.e. linear elastic fracture mechanics) they calculated that for the infinite plate with centre crack:

$$\delta = \epsilon_{ys} \left(\frac{K_I}{M\sigma_{ys}} \right)^2 \quad (2.7)$$

where σ_{ys} is the material yield stress, and ϵ_{ys} is the elastic strain to the yield point. M is a measure of the plastic constraint present at the crack tip, and may take values between one (plane stress) and approximately three (plane strain). Substituting equation (2.5) into equation (2.7) gives:

$$\delta = \frac{G}{M\sigma_{ys}} \quad (2.8)$$

The relationship between crack-opening displacement and strain energy release rate gave theoretical footing to the concept of δ_c under linear elastic conditions. Experimental work by Burdekin and Stone¹⁵ confirmed these relationships for materials of low work-hardening capacity for strains less than $0.5\epsilon_{ys}$. Tests on mild steel, which demonstrates work-hardening, at strains greater than $0.5\epsilon_{ys}$, deviated considerably from the theory. However, evidence of a critical crack-opening displacement in the presence of plasticity was found, but as with all models of

elastic-plastic fracture currently devised, the relevance of δ_c could not be proven.

The standard procedure¹⁶ to measure δ_c is very similar to that derived for K_{Ic} although the specimen thickness should be the same as that used in service. Knott¹ found evidence that the value of δ_c at crack initiation is a material property independent of specimen geometry, above a certain specimen thickness, at a given loading rate, notch acuteness and temperature. If the material tested is of sufficient thickness for plane strain conditions to exist at the crack tip, the result is quoted in terms of K_{Ic} . Under these circumstances δ_c denotes the condition for instability and catastrophic failure occurs. However, for thinner sections, δ_c does not predict total instability. The standard¹⁶ makes provision for the measurement of the crack-opening displacement required to initialise slow, stable crack growth, δ_b , or the value at the maximum force plateau, δ_u . In these situations, δ_c is an unrealistically conservative criterion for design against fracture, but it is not clear which value of δ should be used instead. A design curve² is therefore frequently used relating the non-dimensionalised crack-opening displacement ($\delta/2\pi\epsilon_{ys}a$), to the nominal applied strain, (ϵ/ϵ_{ys}). A safety factor is included to ensure that the available test data falls on the safe side of the curve. This highlights the empirical nature of the δ_c concept in the elastic-plastic regime. However, the relation under linear elastic conditions is clearly defined.

2.1.3 J-Integral

In order to describe failure in non-linear elastic materials, Rice and Rosengren¹⁷ returned to the energy balance approach of Griffith, Section 2.1.1. The difficulties encountered in evaluating the terms of equation (2.1) for the body as a whole were avoided by considering a region around the crack tip only, Figure 2.1. Rice expressed the rate of strain energy release, dW/da , and the (negative) work done by the applied force on the region, dB/da , in terms of a line integral on any curve, Γ , surrounding the notch tip. The line integral, J , is equivalent to the potential energy release rate, and is defined by:

$$J = \int_{\Gamma} \left(W dy - T \frac{\partial u}{\partial x} ds \right) \quad (2.9)$$

The integral is evaluated in an anti-clockwise direction, starting from the lower crack surface and ending on the upper surface. T is the traction vector on Γ according to an outward unit vector n normal to the curve. u is the displacement vector and s the arc length along Γ . From Section 2.1.1, the strain energy release rate, G , can be considered as the potential energy release rate for crack extension under constant load. Thus for linear elastic conditions, J is equivalent to G , and by equations (2.5) and (2.8):

$$J = \frac{K^2}{E} \quad (\text{Plane stress}) \quad (2.10)$$

$$J = M \sigma_{ys} \delta \quad (2.11)$$

Rice and Rosengren¹⁷ demonstrated that J is constant for a notch with traction free surfaces for any path Γ . Thus in the presence of small scale yielding, a Γ -contour passing through elastic material encompassing the plastic zone can be used. Even when considerable yielding occurs in the vicinity of the crack tip, behaviour at the crack tip can be inferred from elastic regions well away from the tip. This extends the concept of linear elastic fracture mechanics into the elastic-plastic regime.

Following the derivation of J on energetic grounds, Hutchinson¹⁸ interpreted J as a crack tip characterising parameter under non-linear elastic conditions. In analogy with the interpretation of G in linear elastic fracture mechanics, the stress distribution close to the crack tip is expressed in terms of a single parameter. However, unlike the linear elastic case in which a given value of K uniquely defines the stress condition at the crack tip, the stress state defined by J depends on the material. The exact relation depends on the form of the stress-strain law assumed for the material: Hutchinson considered both a piece-wise-linear stress-strain relation, and the Ramberg-Osgood stress-strain relation for strain-hardening

metals. For the latter:

$$\frac{\epsilon}{\epsilon_{ys}} = \frac{\sigma}{\sigma_{ys}} + \alpha \left(\frac{\sigma}{\sigma_{ys}} \right)^n \quad (2.12)$$

where α is a constant and n is the strain-hardening coefficient. Hutchinson derived the stress singularity in this instance to be:

$$\sigma_{ij}(r, \theta) = \left(\frac{JE}{\alpha \sigma_{ys}^2 I_n r} \right)^{1/n+1} \sigma_{ij}(\theta) \quad (2.13)$$

where I_n is a numerical constant dependent on the stress-strain relation. σ_{ij} is short-hand notation to denote the components of stress. Hutchinson tabulated values for I_n , and evaluated $\sigma_{ij}(\theta)$ to determine the plastic zone boundary under various conditions. For the linear elastic case ($n=1$) the lefm solution that σ_{ij} is proportional to $1/\sqrt{r}$ is obtained, equation (2.4). The more general case in which σ_{ij} is proportional to $1/r^{1/n+1}$ is known as the HRR singularity (after Hutchinson, Rice and Rosengren).

Most materials demonstrate incremental plasticity rather than non-linear elasticity, meaning that the final deformation is dependent on the loading history. J is therefore only valid under monotonic loading to the onset of crack advance, at which point some unloading of regions of the material will occur. Furthermore, energy absorbed during plastic deformation is no longer available to propagate the crack, and the strict energy balance is lost. Despite these restrictions, Landes and Begley¹⁹ found evidence that a value of J_{Ic} could be determined and used as an engineering estimate of fracture toughness near crack initiation. The subscript implies plane strain conditions at the crack tip. A minimum specimen thickness is required in the standard test to measure J_{Ic} to ensure plane strain²⁰, but is less than the thickness required for a valid K_{Ic} test. Consequently J_{Ic} is useful in quality control where smaller specimen sizes can be tolerated, and as a ductile fracture criterion for those materials that lack sufficient thickness or brittleness for K_{Ic} .

2.1.4 Extension of Basic Parameters

The stress-intensity factor was discussed in Section 2.1.1 as the primary parameter characterising fracture in the linear elastic regime. Although K_{Ic} must be determined experimentally, there is a strong theoretical basis to the method. This theoretical basis breaks down in the elastic-plastic regime; the premise of quantitative fracture analysis remains, but the foundation is empirical rather than theoretical. Crack-opening displacement and the J-integral form the mainstream of elastic-plastic fracture mechanics, and were described in Sections 2.1.2 and 2.1.3. As stated earlier, for the purposes of this thesis, the well defined relationships between K , δ and J in the linear elastic regime will be used to verify the use of ESPI in quantitative fracture mechanics studies. However, from a fracture mechanics viewpoint, it is the application of experimental techniques such as ESPI in less well understood situations that is of current interest. A few such situations are briefly discussed in this section. The selection is by no means exhaustive, but serves to demonstrate two points: firstly that the parameters K and J may be modified to describe situations very different from those for which they were originally defined, and secondly to indicate situations in which ESPI may ultimately find applications.

From Section 2.1.1, plane strain conditions are required for the K_{Ic} concept to be valid. Brittle fracture under these conditions is characterised by a plane fracture surface. For plane stress conditions the fracture mechanism is wholly ductile, although failure is "brittle" in an engineering sense because the crack propagates rapidly. Maximum shear stress occurs in the planes at 45° to the specimen thickness, and consequently the fracture surface is slanted rather than plane. K_c at crack initiation is higher than K_{Ic} because plastic yielding at the crack tip absorbs much of the energy available for fracture. For intermediate thicknesses, crack initiation is characterised by "pop-in", a sudden increase in crack extension at constant load. Pop-in is caused by the advance of a plane crack front at the specimen centre, but its advance is prevented by side ligaments (shear lips) which fail by energy-absorbing yielding. The energy balance for continued crack advance

under these conditions is complicated: K_I increases with increased crack length, but the shear lips increase in width with increased crack length and absorb more energy. In practice, the resistance to crack extension, K_{R} , is found to increase with crack growth, and an increase in stress is required to propagate the crack further²¹. For plane strain, K_{R} is constant and equals K_{Ic} the critical value for brittle failure. It has been proposed that an experimentally determined graph of K_{R} against crack extension, from a specimen of service thickness, can be used to predict if the applied K will cause rapid failure at K_c or if the crack will arrest, for a given starting crack length. Therefore, the R-curve characterises resistance to fracture of materials during incremental slow-stable crack extension. R-curve applications are becoming more widely accepted²². Another application of the stress-intensity factor is in the analysis of fatigue crack growth data. Non-linear fracture mechanics is not generally applied due to mathematical difficulties, e.g. material unloading as the fatigue crack advances. A crack is assumed to have initiated in the structure, and fracture mechanics principles are applied to fatigue crack propagation to a critical length at which rapid failure occurs. The fatigue cycle is described by $K = K_{max} - K_{min}$, where K_{max} and K_{min} are values of K_I calculated from the maximum and minimum stress during the cycle. It has been demonstrated experimentally that if K is constant, the fatigue crack growth rate is constant. For many materials, the Paris²³ equation may be applied:

$$\frac{da}{dN} = C(\Delta K)^m \quad (2.14)$$

where N is the number of fatigue cycles, C is a material constant and m an experimentally determined exponent. An excellent review of this method is given in Chapter 8 of reference 3, and discusses the extension of fracture mechanics concepts to fatigue in the presence of a corrosive medium.

Established fracture procedures have been used to study defects in metallic structures undergoing long-time creep straining. For elastic, non-linear viscous materials with creep strain-rate, the strain energy density, W , may be replaced by the rate of stress working, W' , where

$$W' = \int \sigma d\epsilon \quad (2.15)$$

The integration is performed over some well-defined historical strain accumulation period. Substituting W' for W in equation (2.9) defines a new line integral $C(t)^{24}$ i.e. a rate form of the normal J-integral. As for J , $C(t)$ is path independent for elastic or non-linear elastic materials. At large times, t , creep spreads widely, and $C(t)$ tends to C^* . This is another contour integral defined by Landes and Begley²⁵ characterising the crack tip singularity of steady state stress under creep conditions. A further modification due to Blackburn²⁶ introduced the concept J^* , in which W is calculated from the final state of strain so that the term is independent of the history by which the state of strain was attained. Hellen²⁴ demonstrated J^* to remain path independent for incremental plasticity finite element calculations, including those containing thermal and residual stress terms which cannot be incorporated in J without loss of path independence. These integrals have the general advantage of avoiding the crack tip region where experimental measurements are likely to be in error.

2.2 OPTICAL METHODS IN FRACTURE MECHANICS

Section 2.1 demonstrated that an accurate prediction of the parameter chosen to characterise crack tip conditions is required for failure to be predicted by fracture mechanics principles. Those parameters may be the stress-intensity factor in linear elastic fracture mechanics, or crack-opening displacement and J-integral in elastic-plastic fracture mechanics. For the reasons already given, this thesis is concerned with the measurement of such parameters under static, linear elastic conditions. Therefore, applications discussed in this section will be similarly restricted. Before considering some of the optical experimental methods that have been applied to measure fracture mechanics parameters, it is worthwhile to consider the limitations of theoretical and numerical techniques.

Theoretical methods concentrate almost exclusively on the stress-intensity factor, for which the theoretical basis is most clearly defined. From equation (2.6), a shape factor Y is required to determine K for a given specimen geometry. Analytic solutions for Y which satisfy all the boundary conditions exactly give an explicit expression for K , but are only available for the simplest geometries. The Westergaard solution for an infinite sheet with central crack of length $2a$ subjected to uniform stress applied perpendicular to the crack line is such an example. This solution is discussed in Appendix A, using Muskhelishvili's formulation of Airy's stress function as the sum of two complex functions. However, the modelling of realistic structures requires approximations based on more advanced mathematical techniques. Solutions for a variety of geometries are compiled in compendia²⁷, and involve mathematical techniques such as boundary collocation and integral transforms. A review of these methods, which generally consider two-dimensional problems, has been given by Cartwright and Rooke²⁸. In the absence of a suitable theoretical solution the finite element method has become an invaluable tool for the estimation of stress-intensity factors. Virtually any two-dimensional problem can be solved either by considering crack tip stress and displacement fields, from energy calculations, or the inclusion of special crack tip elements²⁸. Theoretical methods to determine K can be used to evaluate J in the linear elastic regime, equation (2.10). Furthermore the evaluation of contour integrals, equation (2.9), in the elastic-plastic regime can be independently checked by the virtual crack extension method²⁴. Finite element modelling is also available to three-dimensional analysis, and the solution of many linear elastic problems is limited only by computer capacity. However, by the nature of the technique, finite element modelling is only an approximation to the behaviour of the real structure and the accuracy of a result cannot be assumed. For this reason, it will never completely replace empirical testing, and should be considered as a complementary technique. Thus empirical techniques are required for structures where theoretical and numerical methods are not available or need to be verified.

Very many experimental techniques have been used in fracture mechanics. The scope of this review is restricted to those techniques which are most relevant to

this study. This includes techniques which share ESPI's ability to make whole field measurements without requiring surface preparation or contact. These techniques are considered in four classifications, presented in chronological order of their invention. Photoelasticity is considered first, Section 2.2.1, followed by classical interferometry (Section 2.2.2), hologram interferometry (2.2.3) and speckle photography (2.2.4). ESPI is considered separately in Section 2.3.

2.2.1 Photoelasticity

Photoelasticity relies on the property of stress-induced birefringence of certain plastics. For a two-dimensional specimen viewed along one axis of principal stress, the optical axes occur parallel to the remaining two principal planes, σ_1 and σ_2 (i.e. planes on which $\tau_{xy} = 0$). The induced birefringence is proportional to the stress and varies from point to point in the image. Thus the interference pattern produced on combining the wavefront from the optic axes may be used to measure the relative retardation of the two beams in a circular polariscope²⁹. The isochromatic fringes formed in the circular polariscope in this way are proportional to the principal stress difference, $\sigma_1 - \sigma_2$, at each point. The principal stress direction, at angle ϕ to the x-axis, is measured in a plane polariscope: the isochromatic fringe pattern is modulated by isoclinic fringes which are loci of constant principal stress direction i.e. constant ϕ . The value of ϕ can be determined from the specimen orientation in the plane polariscope. The complete state of stress is defined by σ_1 , σ_2 and ϕ . Thus isochromatic ($\sigma_1 - \sigma_2$) and isoclinic (ϕ) curves are not sufficient in themselves to provide the complete stress solution for interior points. One solution is to measure the change in specimen thickness, proportional to $\sigma_1 + \sigma_2$, with a full-field interference technique. Measurements may be made from a second transparent, but optically isotropic, model; the contours of constant thickness are termed isopachics. Holographic interferometry, Section 2.2.3, is an attractive method for recording the isopachics; the original photoelastic specimen may be used with the isochromatic, isoclinic and isopachic data all present in one recording³⁰. The combined isochromatic-isopachic pattern is

difficult to interpret, even with recording methods such as differential and reversed loading. The difficulty of isochromatic-isoclinic fringe separation has hampered automated fringe analysis: a phase-stepping method has been proposed by Patterson and Wang³¹, but has difficulty coping with isotropic points i.e. $\sigma_1 = \sigma_2$.

Photoelasticity has found many applications in fracture mechanics. Natural cracks may be introduced to specimens by placing a sharp blade normal to, and in contact with, the surface to be cracked and striking the blade. Alternatively, artificial cracks can be introduced by machining, or by removing a metal shim prior to solidification when casting the model. Many investigators have studied the maximum allowable notch tip radius for an artificial crack to model the natural crack: values as large as 1.2 mm (0.047") have been cited³². The first fracture mechanics application involved using a multi-spark light source to record four sequence photographs of transient isochromatic fringe patterns in a fracturing edge notch specimen³³. The material fringe constant was strain dependent, and the state of stress could not be determined accurately. In a discussion to this work, Irwin proposed a method to evaluate K_I from the isochromatic fringe pattern. This and other two parameter (K_I and σ , Appendix A) techniques were reviewed and compared by Etheridge and Dally³⁴. The methods generally require the maximum shear stress to be related to the isochromatic fringe order at two or three selected points (r, θ) using equations (2.4). Sanford and Dally³⁵ improved the accuracy of such measurements by using data gathered from many points: a least-squares approach was used to solve a set of over-determined simultaneous equations in K_I , K_{II} and σ (i.e. mixed mode loading). Inaccuracies due to errors in measuring r and θ were minimised.

Photoelasticity remains one of the few techniques able to measure the stress distribution in the interior of a body. Thus it is particularly useful for studying arbitrary cracks in a general three-dimensional structure. Such problems are characterised by a variation in K along the crack front. Three-dimensional photoelasticity requires the stresses to be frozen into the model by heating and annealing the specimen under load. The specimen can then be cut into slices and

analysed. A review of these methods and their application to fracture mechanics has been given by Smith³⁶. A particular disadvantage of testing a model rather than the actual specimen becomes apparent for stress-frozen photoelasticity: similitude between model and structure requires equal Poisson's ratio, ν , for the two materials. However, $\nu=0.5$ for most stress freezing polymers, rather than 0.3 for most metals. This causes a typical error of approximately $\pm 5\%$ in K evaluation in addition to experimental errors.

The birefringent coating technique can be used to make measurements from an actual structure. Gerberich³⁷ measured the plastic enclave profile in cracked thin plates of materials of varying work-hardening capacity. These results were used by Hutchinson¹⁸ in comparison with his predicted plane stress plastic zone shape, for which he found reasonable agreement. Muller and Gross³⁸ measured J with the birefringent coating method, but could not measure the rotational term $\partial v/\partial x$ directly. This is a general problem for evaluating J from measured strain fields, but is not encountered with displacement measurement techniques. Experimental and theoretical difficulties in making strain measurements around crack tips have been reported with the birefringent coating method³². These are due to the non-uniformity of strain through the birefringent coating in the region of high strain gradient at the crack tip. The coating also prevents in-plane displacement measurements to be made from the surface.

2.2.2 Optical Interferometry

Optical interferometry is a non-contacting, whole-field technique that can measure out-of-plane displacements to the order of visible wavelengths of light. The technique was first applied to fracture mechanics by Opperl and Hill³⁹ when three-dimensional effects rendered the birefringent coating technique inapplicable. An interference pattern was produced in monochromatic light between the highly polished specimen surface and an optical flat placed in contact with the surface. For two-dimensional stress states the fringes are contours of constant $(\sigma_1 + \sigma_2)$ or

$(\epsilon_1 + \epsilon_2)$ in the elastic range, or $(\epsilon_1 + \epsilon_2)$ in the plastic range i.e. isopachic fringes, where ϵ_1 and ϵ_2 are the principal strains. Oppel and Hill³⁹ used the technique as a qualitative study of permanent strain distribution in a fatigue-cracked specimen. Underwood and Kendall⁴⁰ returned to the problem of crack growth in a ductile material³⁷ and studied out-of-plane displacement in the plastic enclave. The surface was also scratched with a grating of approximate pitch 200 l/mm to enable in-plane measurements to be studied by the moire technique. Results in a 10x10mm² region were compared with finite element and etching results, as well as the HRR field.

Moire techniques are an alternative to classical interferometry in which fringe patterns are formed by the interaction of structured light patterns, rather than the interference of coherent wavefronts. The patterns can be formed either by projecting or physically applying the gratings. Advantages are that white light can be used, and the fringe sensitivity can be varied from fractions of a micron up to several millimetres by reducing the spatial frequency of the gratings. A great many variations of the moire method have been investigated, for measuring both in-plane and out-of-plane displacement components⁴¹. For coarse gratings (e.g. 40 l/mm) the moire phenomenon can be explained in terms of mechanical interference. High frequency gratings require an explanation involving optical interferometry i.e. constructive and destructive interference of coherent components of light emerging from the grating. This is generally termed moire interferometry⁴², and gratings as fine as 4000 l/mm have been used (approaching the theoretical limit of sensitivity of $\lambda/2$, where λ is the wavelength laser illumination). More typical fringe sensitivities are in the range of 1 μ m. The technique requires a phase grating to be bonded to the specimen surface. The reference (virtual) grating is formed in the overlapping region of two coherent, collimated laser beams, which illuminate the surface grating at equal and opposite angles. Moire fringes are formed by the mutual interference of the wavefronts diffracted normal to the surface.

Many applications of moire techniques to fracture mechanics have been reported,

and only the most relevant are cited here. Barker et al⁴³ modified the least-squares method of K evaluation proposed for photoelasticity³⁵ to consider displacement fields. A multi-parameter expression of the Westergaard solution enabled displacement measurements made some distance from the crack tip by moire-of-moire (i.e. incremental load) to be used to evaluate K. This technique has been used in Section 5.2.3, where it is described in more detail. Epstein et al⁴⁴ used this K evaluation procedure to measure K_I for a three-point bend specimen with moire interferometry; a review of other moire techniques in fracture mechanics (e.g. amplitude moire, shadow moire) appears in this reference. J evaluation from moire interferometric measurements has been reported⁴⁵. The required components of strain and the rotational term, $\partial v/\partial x$, were calculated manually from the displacement field by counting fringe densities over a gauge length of approximately 1.5 mm on the specimen surface. Automatic fringe analysis was restricted to fringe thinning (Section 3.1.1) and manual fringe counting was required to calculate strain⁴⁶. This process was very slow. The components of strain were calculated at 25 points (separated by approximately 3mm) on a contour surrounding the crack tip. J was calculated around the contour by interpolating between measurement points.

Asundi⁴⁷ has reported a moire interferometer for the simultaneous measurement of two orthogonal in-plane and the out-of-plane displacement components. The in-plane components were recorded on a single interferogram and were separated by spatial filtering (Sections 3.2.1 and 4.4). The out-of-plane component was recorded separately, but the image was distorted due to non-normal observation. This system was used to record the displacement distribution for a perspex compact tension specimen, although no quantitative analysis was performed. Limitations of the moire interferometry technique include the size of object that may be studied, limited by the size of grating that can be placed on to a surface and diameter of the optics used in producing the collimated interrogation beams. The surface grating also limits applications to nominally flat surfaces. However, a considerable advantage is the large correlation length: large rigid body motions can be compensated for during the test by manipulating the reference grid. Also

the low noise of moire fringes and the ability to resolve fine detail is useful for differentiation to obtain strain data.

2.2.3 Holographic Interferometry

Holography is an optical technique whereby the interfering wavefronts of two mutually coherent laser beams are recorded photographically and can be reconstructed to produce a three-dimensional image of the object. In holographic interferometry (HI) holograms of an object in different states are combined to form an interferogram with fringe patterns indicating the differences between states⁴⁸. The interferometer is sensitive to displacements along the direction which bisects the object illumination and viewing directions. For normal illumination and viewing directions, the fringes denote pure out-of-plane deformation. Typically the viewing window of the hologram is restricted to approximately 30° from the hologram normal, and thus any interferogram will always contain a substantial out-of-plane displacement component. Three recording procedures are generally used, each of which requires the solution of simultaneous equations to extract the orthogonal components of displacement:

- i) multiple views of a single hologram;
- ii) three separate holograms, with separate sensitivity vectors; or
- iii) multiple object illumination beams with a single hologram plate.

Method (iii) is most closely related to ESPI and does not require the different perspectives present in (i) and (ii) to be corrected.

Separation of the in-plane from the out-of-plane displacement components represents a serious difficulty in HI. Techniques to separate the in-plane component of displacement have been proposed. Ennos⁴⁹ recorded two double-exposure holograms inclined to the specimen surface at equal angles. By numerical subtraction of the fringe orders, determined at a number of corresponding points on the two perspective-corrected views, a resolved in-plane displacement component was extracted. An alternative solution demonstrated by

Boone⁵⁰ used dual object beam illumination (see for example speckle photography and in-plane ESPI, Sections 2.2.4 and 2.3.3) to record superimposed in-plane and out-of-plane fringes. Schluter and Nowatzky⁵¹ phase-stepped the out-of-plane component by π radians, and separated the in-plane displacement by subtracting the two phase-stepped fringe patterns (Section 4.4). Neither of these methods have been applied to fracture mechanics. However, a third method⁵² has been used for fracture studies: a Denisyuk hologram was recorded from which the out-of-plane component was readily available. The hologram was then viewed at two equal and opposite angles, from which the in-plane displacement was obtained by subtracting fringe orders from the perspective-corrected interferograms (as above). Alternatively, the double-exposed hologram could be interrogated as a speckle-correlation photograph: in-plane deformation was available either from the formation of the Young's fringes (sending an unexpanded laser beam on to one point of the image) or the use of the spatial filtering technique of Burch-Tokarski. (Both these methods are discussed in Section 2.2.4). Boone⁵³ demonstrated these techniques for two cracked bodies, but performed no quantitative analysis. Problems with the Denisyuk set up included adjusting the object/reference beam ratio, and possible emulsion swelling distorting the in-plane components of displacement. More generally, the sensitivity of HI restricts the range of displacement that can be measured with respect to, for example, moire interferometry. Also the technique is not suited to plastic deformation studies due to the change in microscopic surface form that accompanies plastic behaviour. However, HI is attractive when compared to traditional interference methods because the optical quality of components may be reduced and no background fringes are produced for a non-optically flat surface. Therefore many fracture mechanics applications have been proposed, in addition to the qualitative study by Boone.

Dudderar⁵⁴ used an out-of-plane sensitive HI to record isopachics for incrementally loaded specimens. Transmission holograms were recorded for transparent specimens. Fringes were always lost at pop-in, demonstrating the problems associated with a small correlation length. However, a new reference hologram

could be made, and the loading continued. Dudderar and Gorman⁵⁵ later extended this work to measure K_I for transparent specimens. Juptner⁵⁶ applied similar techniques, but for reflection holograms. Instead of the single transmission hologram, three interferograms with different viewing axes were recorded. Several workers have used HI's ability to measure displacements at elevated temperatures. Hsu et al⁵⁷ measured the crack-opening displacement for a compact tension specimens held at 120°C for up to 860 hours. They overcame the correlation problem by including an invar bar in the oven for hologram repositioning. Fan and Shen⁵⁸ evaluated the J integral in the presence of a thermal strain gradient and compared the results with a finite element prediction.

2.2.4 Speckle Techniques

The phenomenon of "speckle" occurs whenever coherent light is scattered diffusely, and is caused by the mutual interference of many individual scattered wavefronts. Speckle photography was first proposed by Burch and Tokarski⁵⁹. The basic technique involved photographing a specimen under laser illumination. Two exposures were recorded on the same film, the specimen being deformed between the exposures. It was demonstrated that the double exposure could be used to measure in-plane displacements of greater than a speckle diameter by illuminating the film with collimated light. The recorded image was reimaged by means of a lens in whose focal plane was placed a small circular aperture stop. Bright and dark fringes were observed through the aperture denoting surface displacement resolved in the direction of the aperture from the centre of the transforming lens⁶⁰. The technique is sensitive to displacements of several speckle diameters (tens of micrometers). An alternative method to interrogate the double-exposed film is to measure the speckle displacement at the corresponding point on the developed film. This is done by probing the film with a narrow laser beam⁶⁰. The far field diffraction pattern is similar to that from a mask containing two small apertures separated by the speckle displacement, i.e. Young's fringes. Duffy⁶¹ proposed a third method by using a double-aperture lens. A fine grating pattern

was produced in each speckle, which changed its orientation as the speckle position changed. Superimposing photographs taken before and after displacement produced a moire pattern representing contours of displacement.

For speckle photography, displacements greater than a speckle diameter are required. Leendertz⁶² proposed illuminating the surface with two beams of coherent laser light, symmetrically positioned about the surface normal. This enabled in-plane displacements of less than the speckle diameter to be measured (of the order of a few microns). A photograph of the speckle pattern was taken and the negative returned to its holder, thus acting as a mask through which the surface was viewed. When the surface moved in its own plane towards one beam and away from the other, interference effects caused changes in the brightness of each speckle. Where the speckles returned to their original intensity the speckle pattern was correlated with its recorded image and the light transmitted by the mask fell to a minimum. Elsewhere in the image the transmitted intensity increased, forming contours of constant displacement as a series of speckle correlation fringes. This is the basis of speckle interferometry, and is discussed in Section 2.3. The distinction from speckle photography is that the speckles must remain correlated in order to see the fringes. Archbold et al⁶³ demonstrated that speckle correlation fringes could be formed by a double exposure on to the same piece of film i.e. photographic speckle interferometry. It was also demonstrated that the double exposure with dual illumination could be used to measure in-plane displacements of greater than a speckle diameter by observing the spatial filtering method of Burch-Tokarski. The technique was again sensitive to displacements of several speckle diameters. Furthermore, rigid body motion was eliminated from the observed fringe pattern.

Evans and Luxmoore⁶⁴ applied the Young's fringe method to study displacements around an edge crack in araldite specimens. Only measurements in a vertical direction normal to the crack line were analysed, due to the laborious nature of processing Young's fringes manually. Measurements were made very close to the crack tip (< 2.0 mm), and despite some scatter in the results, good agreement

with Westergaard's solution was obtained. Huntley⁶⁵ reported an image processing system to automatically analyse speckle photographs. The photograph was mounted to an x-y translation stage, driven by stepper motors under microprocessor control. A stationary laser beam interrogated the photograph at each position, and the Young's fringes interpreted by a Fourier transform method. This enabled full-field u and v displacement components to be measured around a crack⁶⁶ from which K_I was evaluated by a least-squares algorithm⁴³. J was also calculated, and good agreement with equation (2.10) was found. In both studies^{64,66}, the photographic film was translated with respect to the specimen between exposures to reduce rigid body motion in the speckle photograph. The dual-illumination beam method was used by Chiang et al⁶⁷ to measure crack-opening displacement for a centre cracked specimen. Similar results have been presented for white light speckle^{68,69}. White light speckle methods allow out-of-plane deformation to be measured, which cannot be achieved with traditional speckle photography. More recently, Chiang and Hareesh⁷⁰ used a modified version of the moire speckle method of Duffy⁶¹ to record three-dimensional displacement fields. In-plane displacement was encoded in the displacement of random speckles whereas out-of-plane displacement was embedded in the distortion of projected grating lines. Experimental results were compared with the HRR displacement field, and the shape of the plane stress plastic zone compared with the HRR prediction.

2.3 ESPI

ESPI has been developed over the last twenty years from the holographic and speckle techniques described in the previous sections. Much of the early research and development took place at two centres: Loughborough University in the UK and the Norwegian Institute of Technology in Trondheim. As the technique became more widely used in research and industry, more research groups have become interested and made contributions to ESPI technology. The basic principles of ESPI are described in Section 2.3.1. The out-of-plane and in-plane

configurations used throughout this thesis are described in Sections 2.3.2 and 2.3.3 respectively. Section 2.3.4 considers some relevant applications from the literature, and recent developments in the ESPI technique.

2.3.1 Principles of ESPI

The principles of photographic speckle interferometry were discussed in Section 2.2.4. Speckle correlation was performed by using a negative of the surface in its reference (undeformed) state as a mask through which the deforming surface was viewed. Later modifications included introducing a TV camera to record the speckle pattern, and performing the correlation by electronic subtraction⁷¹. Many applications and different interferometer designs have been proposed since then. These include out-of-plane and in-plane sensitive interferometers for displacement measurement; surface contouring techniques; time-average, stroboscopic and pulsed harmonic-vibration analysis; transient vibration analysis⁷¹. It is ESPI for displacement measurement that is of primary interest here; in particular the two configurations for measuring out-of-plane and in-plane displacements used throughout this thesis.

In order to measure static surface displacements with ESPI, it is necessary to know the relationship between the fringe pattern and the surface motion. This relationship is called the fringe function and depends on the optical configuration of the interferometer. (For harmonic surface vibrations, considered briefly in Section 3.1.3, it also depends on the type of illumination e.g. continuous or pulsed. However, harmonic vibrations are not considered here). From Section 2.2.3, HI is sensitive to displacements resolved along a single direction. The direction of the resolved component is determined by the sensitivity vector which is a function of the optical geometry of the interferometer. In general, it is necessary to record three sets of data, each with a different sensitivity vector, and solve them simultaneously to determine the three-dimensional displacement. The computational errors introduced in solving the data sets depend on the spatial

separation of the sensitivity vectors, and is minimum for mutually orthogonal vectors. Similarly, ESPI is sensitive to displacements in a single direction, and therefore measures one resolved component of displacement at a time. However, using ESPI it is possible to construct interferometer configurations which have sensitivity either parallel to or perpendicular to the observation vector, and these can be combined to satisfy the ideal requirement of three mutually orthogonal sensitivity vectors. If the observation vector is made perpendicular to the observed surface, then the three measurements can correspond directly to two in-plane and one out-of-plane components. This is a distinct advantage of correlation interferometry over wavefront interferometry. Furthermore, the three measurements can be made sequentially on one camera (or simultaneously with one or more cameras and a single imaging system, Chapter 4) thus eliminating the need for different observation directions.

The fringe function for ESPI is derived in Appendix B in terms of a phase change ϕ which can be expressed as:

$$\phi = k \Gamma d_n \quad (2.16)$$

where $k = 2\pi/\lambda$ is the wave number. Γ is the fringe sensitivity factor that determines how many fringes correspond to a given surface displacement, and d_n is the component of object displacement resolved along the sensitivity vector \mathbf{n} . Γ and \mathbf{n} are determined by the optical geometry of the interferometer, and are derived for out-of-plane and in-plane sensitive interferometers in the following two sections. A notation consistent for both the out-of-plane and in-plane cases is used⁷².

2.3.2 Out-of-Plane ESPI

For out-of-plane sensitive ESPI, the object under test is illuminated and viewed along its surface normal, and the light scattered from the object is combined with a reference wavefront. A practical configuration is shown in Figure 2.2. The object

is viewed along the z axis, and any point $Q(x,y,z)$ in the object space is focused to a corresponding point $P(m,n)$ in the image plane. The object beam lies in the xz plane and is offset from the viewing axis by a small angle θ . For a general displacement d , having components u,v,w , such that $Q(x,y,z)$ moves to $Q'(x+u,y+v,z+w)$, the change in optical path length Δl of the reflected object beam is shown in Figure 2.3 and is given by:

$$\Delta l = w(1 + \cos\theta) + u\sin\theta \quad (2.17)$$

where u and w can take positive or negative values. Therefore the total phase change at the image plane is:

$$\phi = \frac{2\pi}{\lambda} (w(1 + \cos\theta) + u\sin\theta) \quad (2.18)$$

For small θ (typically $< 5^\circ$) the term in u can be ignored with respect to the term in w , and the system can be considered sensitive to w motion only. Therefore:

$$\phi = \frac{4\pi}{\lambda} w \quad (2.19)$$

Comparing equations (2.16) and (2.19) gives the fringe sensitivity factor for this configuration as $\Gamma=2$, and the sensitivity vector is a unit vector in the observation direction, $\mathbf{n}=\hat{\mathbf{z}}$.

2.3.3 In-plane ESPI

From Sections 2.2.3 and 2.2.4, a common optical arrangement for in-plane sensitivity is to illuminate the surface at equal angles to the surface normal with collimated beams, Figure 2.4. From Figure 2.3, a small general displacement d will cause path length changes of:

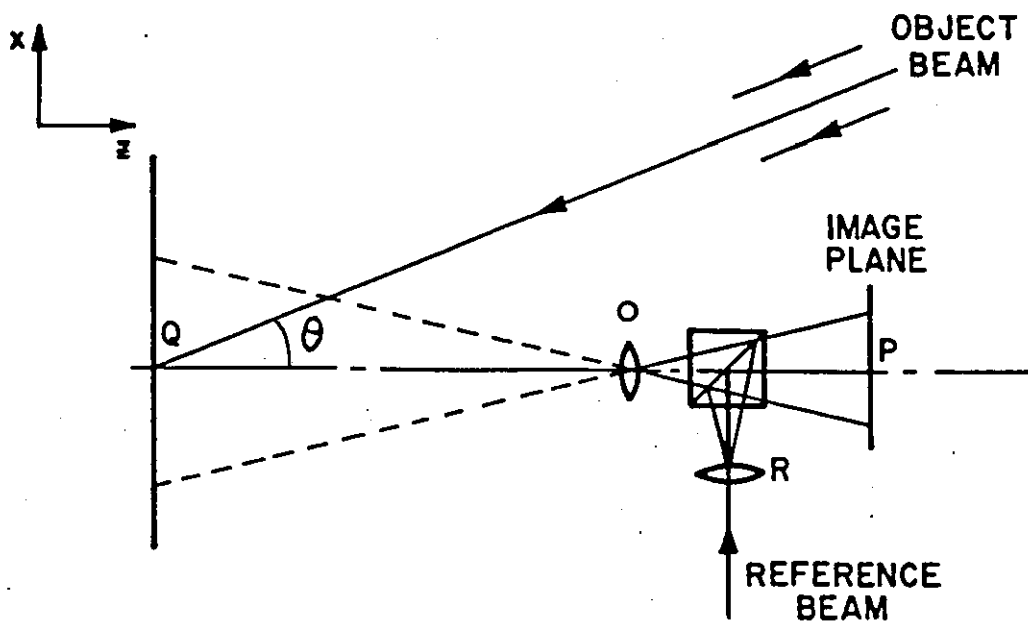


Figure 2.2 Out-of-plane interferometer

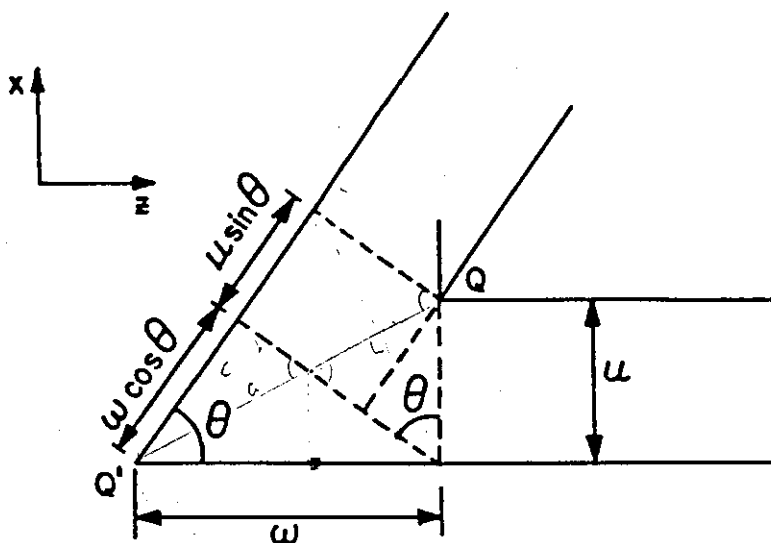


Figure 2.3 Path length change due to object displacement

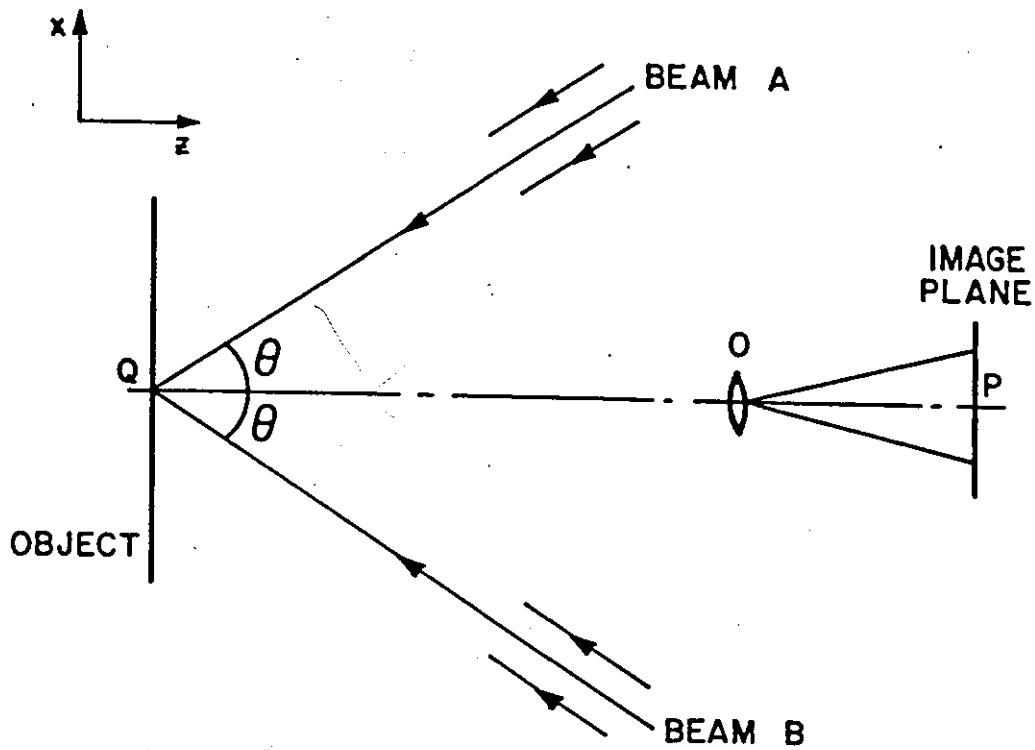


Figure 2.4 In-plane sensitive interferometer

$$\Delta l_A = w(1 + \cos\theta) + u\sin\theta$$

$$\Delta l_B = w(1 + \cos\theta) - u\sin\theta \quad (2.20)$$

This produces a total phase change at the image plane of:

$$\begin{aligned} \phi &= \frac{2\pi}{\lambda} (\Delta l_A - \Delta l_B) \\ &= \frac{4\pi}{\lambda} u\sin\theta \end{aligned} \quad (2.21)$$

Hence the fringe sensitivity factor $\Gamma=2\sin\theta$, and the sensitivity factor $\mathbf{n}=\hat{\mathbf{x}}$. For illumination beams rotated to the yz plane, a similar analysis gives $\Gamma=2\sin\theta$ and $\mathbf{n}=\hat{\mathbf{y}}$. Note that if the surface is not planar, then this configuration gives some out-of-plane sensitivity at points where the surface normal is not parallel to the z axis. The values of Γ and \mathbf{n} are only constant across the object for plane illumination

wavefronts. Spherical wavefronts will cause the sensitivity vector to rotate and give some z-sensitivity. Also the sensitivity to in-plane displacement decreases towards the edge of the field of view. If diverging beams are expanded from a remote point, these variations in the sensitivity vector are minimised. ϕ is independent of the viewing direction equation (2.21) and so the only effect of oblique viewing is to change the perspective of the image.

2.3.4 ESPI Applications

ESPI has frequently been applied to qualitative fault detection where the presence of defects may be demonstrated by an increase in the fringe density or a discontinuity in the fringe pattern⁷³. Barker and Fourney⁷⁴ reported an interesting application using photographic speckle interferometry for a transparent (but optically isotropic) compact tension specimen. Two very thin sheets of coincident coherent light travelling in opposite directions were passed through the specimen normal to the crack surface. A double exposure photograph was recorded of the scattered-light speckle pattern. By equation (2.21) this gave maximum sensitivity to in-plane displacements, although the intensity of the scattered radiation was very low. Crack-opening displacement was plotted against through-thickness position in the specimen. Herbert et al⁷⁵ reported a qualitative study of various cracking mechanisms in an epoxy powder coating. Out-of-plane fringes were recorded over a 1mm² region. The fringe visibility was low due to the presence of rigid body motion with high levels of magnification. However, some differences between fringe patterns for different cracking mechanisms could be seen. Furthermore, an estimate of the plastic zone size was made from the distance between outermost fringes, and used to determine a relative fracture energy. One final application appears in Jones and Wykes⁷⁰, page 304, where the crack-opening displacement was measured for a compact tension specimen from in-plane displacement measurements made perpendicular to the crack line. Measurements were not made sufficiently close to the crack tip to observe non-linear crack tip effects. The fringes were counted manually.

The discussion will now be broadened from fracture mechanics applications to more general advances in the ESPI technique. Strain measurement with ESPI is considered first. Winther⁷⁶ measured three-dimensional strains using ESPI in the conventional holographic configuration of three illumination vectors, with a single reference beam incident on the TV camera. (A slightly different method was proposed by Button et al⁷⁷ in which three dual object beam interferometers were used). The surface profile of the object under test (contouring) was also measured by translating the output end of one of the three optical fibres directing the illumination beams to the object, and recording a fourth interferogram. Fringe positions were marked at between 400 and 500 points. The fringe order was entered manually at these points, from which displacement, profile and strain was calculated. The process required operator intervention and did not take advantage of the full-field of measurement points. Surface contouring is necessary to relate the measured displacement at each point to the surface normal at that point. For the work presented in this thesis the surface profile was already known, and therefore no contouring was undertaken. An impressive system using the same principles as Winther was described by Vrooman and Maas⁷⁸. The system incorporated automatic fringe analysis. This work, published concurrently with the work presented in this thesis, represents the only other routine extraction of strain data from ESPI displacement fringes. Differences between the two implementations are discussed in Chapter 3.

Several ESPI systems are available commercially. These include the Vidispec (Ealing), HC4000 speckle camera (Newport), Retra TV-holography system (Conspectum) and an electro-optic holography system (Recognition Technology). All these systems use low power, continuous wave lasers and are intended primarily for out-of-plane use, although the user can construct an in-plane system with additional optics if desired. The SD800-ESPI system (Spectradata) is unique in supplying combined out-of-plane and in-plane measurement capability in one system. The system can also be supplied with a second, orthogonal in-plane sensitivity direction. "Simultaneous" out-of-plane and in-plane displacement measurement is claimed⁷⁹ although the user must actually switch sequentially

between the illumination configurations.

All the ESPI examples discussed so far have used continuous wave laser illumination. A very interesting area of recent research is ESPI with pulsed lasers. The first demonstration was due to Cookson et al⁸⁰ using a ruby laser and vidicon camera. Many difficulties were experienced synchronising the laser pulses (10 second repetition rate) with the active period of the camera. The advent of pulsed lasers with high repetition rates used in conjunction with charge coupled device (CCD) cameras has renewed interest in the technique with regard to its application in harsh environments and for dynamic studies⁸¹. When using ESPI with a pulsed laser, two modes of operation can be achieved: subtraction and addition. These modes are described in Section 3.2.3. In particular the addition mode of operation may find applications in fatigue crack growth or dynamic fracture studies.

3. AUTOMATED DISPLACEMENT AND STRAIN EVALUATION

The purpose of this chapter is to discuss the phase-stepping procedure introduced to in-plane sensitive ESPI in order to automate fringe analysis. Section 3.1 describes various fringe analysis procedures, from which the suitability of phase-stepping became apparent. The implementation of the technique is described in Section 3.2, along with factors likely to introduce errors to the measurements. An experimental determination of the accuracy of displacement measurement is described. The evaluation of surface strain from the displacement data is described in Section 3.3. The accuracy of strain measurement is also determined in Section 3.3.

3.1 AUTOMATED FRINGE PATTERN ANALYSIS

A number of optical metrology techniques produce an output in the form of fringes which represent contours along which the parameter being measured is constant. The use of fringe patterns is very powerful in extracting qualitative information, but it is generally extremely tedious and time consuming to extract quantitative data from the fringe pattern. However, quantitative data is required if the information contained in the fringe pattern is to be compared with other non-interferometric measurements. Thus when digital image processing systems became available in the mid-1970s, many researchers seized the opportunity to begin automating the analysis of fringe patterns in order to extend the effectiveness of these optical techniques as practical measuring tools. Since then, various fringe analysis procedures have been proposed. Before comparing some of the more common procedures, and their particular application to ESPI, it is useful to consider what is required from a fringe analysis system.

In its most general form, whether manual or automatic, fringe analysis involves the following stages:

- i) record a good quality fringe pattern;
- ii) determine the relative order of each fringe in the image;
- iii) calculate the measured parameter across the image, from the fringe order and the fringe function, equation (2.16).

Certain difficulties must be addressed at each stage. They exist for all optical techniques irrespective of the process of fringe generation, although the severity may vary between techniques. With reference to ESPI fringes, the difficulties associated with each stage may be summarised as follows:

Stage (i) Noise: ESPI fringes are inherently noisy: fringes of low spatial frequency are embedded in noise (speckles) of higher spatial frequency. These frequencies overlap, and make it impossible to devise a general smoothing procedure that eliminates all the speckle noise without significantly degrading the signal-to-noise ratio (SNR).
Intensity Variations: The mean intensity of the speckle pattern may vary over the specimen surface, possibly due to diffuse scattering on different surface finishes or the illumination beam profile. Therefore, image processing routines which are applied to reduce speckle noise may reduce the SNR in some regions of the image unless they adapt to the local mean intensity of the image.

Stage (ii) Ambiguity of Displacement Direction: ESPI displays the optical phase difference introduced due to surface deformation indirectly, by the formation of correlation fringes. Therefore the direction of displacement along the sensitivity axis is ambiguous, unless the likely displacement of the surface can be predicted from the target constraints.

Sub-fringe Resolution: In order to increase the sensitivity of measurement for a given optical configuration, the displacement

must be determined at points in the image that do not lie on fringe maxima or minima. An accurate procedure to interpolate between fringe centres is required, that is not rendered impractical by computational complexity.

Stage (iii) Equilibrium Surface Contour: In order to interpret the two-dimensional displacement map defined by the fringes in the image plane, the shape of the object in three-dimensional space must be known. For a general analysis, this will require the surface contour to be measured before deformation. The fringe data can then be combined with the surface profile at each pixel to give the true displacement.

As already noted, no techniques for measuring surface contours are presented in this thesis: the equilibrium surface profiles of objects tested were known previously. Thus automated procedures of fringe pattern analysis are critically assessed in the following three sub-sections based on their ability to deal with noise, intensity variations, ambiguity of displacement direction and sub-fringe resolution. A comprehensive review of these procedures was given by Reid⁸². Here, the discussion is restricted to ESPI correlation fringes. From this analysis, the preferred procedure for automated analysis of in-plane sensitive ESPI fringe patterns was selected.

3.1.1 Fringe Tracking

The positions of fringe maxima and/or minima are identified and tracked across the interferogram. The aim is to reduce the amount of data for storage and subsequent processing. Many fringe tracking algorithms have been used, but they generally fall into two categories. The first category is suitable for good quality fringes (i.e. high SNR) and rely on local grey-level information in the image. For example, Funnel⁸³ was able to trace fringe maxima from a moire interferometer

simply by selecting the largest grey-level from a restricted set of a pixel's immediate neighbours: the position associated with this grey-level was assumed to be the next point on the fringe peak. A more robust method applied to moire profilometry by Yatagai et al⁸⁴ was to mark a fringe peak if the grey-level was a local maximum in one or more directions passing through a given pixel. In the presence of noise these methods will extract many false skeletons, and the process must be interactive to allow points marked as maxima to be deleted, inserted or repositioned. ESPI fringes do not have a continuous grey-level profile. Thus when processing ESPI data in this way, Button et al⁸⁵ found that the tracked path consistently deviated from the fringe extrema, even when a smoothing filter was applied to reduce speckle noise.

The second category is less sensitive to noise in the image, and involves binarising a smoothed fringe pattern with a user defined threshold level. Fringe skeletons may be produced by edge detection⁸⁵ or thinning⁸⁶ of the binarised fringes. This is inaccurate since it is no longer the fringe extrema that are tracked. Also, when the intensity varies across the image, a threshold level which satisfactorily separates bright regions of the picture may lose all information in less bright regions. Even if the threshold value varies over the picture, difficulties arise unless the fringes are well separated. Nakadate et al⁸⁶ found that operator intervention was required to fuse disconnected regions of the same fringe order and remove fused areas of two different fringe orders. They concluded, perhaps with some exasperation, that "it seems almost impossible to extract perfectly the centre line of bright and dark [ESPI] fringes".

Having skeletonised the fringe pattern, fringe orders must be assigned. Automatic procedures have been proposed⁸⁷ but fringe orders are usually entered by the operator⁸³⁻⁸⁶ to prevent an erroneously numbered fringe propagating errors across the image. If data is required at points between the fringe extrema, polynomial curves can be fitted to the numbered fringe skeletons⁸⁸. This is computationally intensive: it took Nakadate et al⁸⁶ five hours on a PDP11/34 to fit fourth-order polynomials to out-of-plane ESPI data in order to calculate surface slope and

bending moment.

In conclusion, fringe tracking algorithms are not suitable for displacement and strain evaluation in fracture mechanics analysis. Although no modifications to the interferometer are required, considerable operator intervention is needed and the process relies on his skill in assigning fringe orders. Post-processing the displacement data to obtain surface strain is slow due to interpolating between fringe centres. However, working within these limitations, it is possible to derive useful systems for certain problems. For example, Hurden⁸⁹ produced wire mesh plots of vibration modes with an out-of-plane ESPI system. Here fringe tracking was performed manually by the operator with a light pen.

3.1.2 Heterodyne and Phase-Stepping Interferometry

The operator intervention associated with fringe tracking can be eliminated if the optical phase difference between the interfering beams is calculated directly. Few optical techniques detect phase directly and display it as an intensity distribution: Schlieren and phase contrast microscopy are two examples. Instead, the phase information is indirectly detected by the formation of interference fringes. Therefore, to detect the absolute phase value, the interference fringes must be manipulated in some way. One such technique is heterodyne interferometry, in which a frequency shift is applied to one of the interfering wavefronts. From Appendix B, the intensity at time t and point $P(m,n)$ in the image plane of a general two-beam interferometer, in which the two beams are mutually coherent and have equivalent polarisation states but different optical frequencies, is given by:

$$I(m,n,t) = I_A + I_B + 2\sqrt{I_A I_B} \cos ((\omega_A - \omega_B)t + \phi) \quad (3.1)$$

$I_A(m,n)$ and $I_B(m,n)$ are intensities due to each beam independently, $\phi(m,n)$ is the phase difference between the two beams and ω_A , ω_B are the angular frequencies. The intensity at any point in the interference pattern varies sinusoidally at the

difference, or beat, frequency ($\omega_A - \omega_B$). The phase difference between the two interfering wavefronts $\phi(m,n)$ is transformed into the phase of the beat frequency. If the beat frequency can be resolved by an optoelectronic detector, the interference phase can be measured with high accuracy independently of the intensities I_A and I_B using an electronic phase meter: the phase of the electrical output from a moveable detector is compared with that from a stationary reference detector. Both the fringe interpolation and direction of displacement problems of classical interferometry are solved, and the measured phase is unaffected by intensity variations and stationary noise.

These techniques were first proposed for classical amplitude-division interferometers, to evaluate accurately the phase and amplitude changes introduced by specular⁹⁰ or transparent⁹¹ objects placed in one arm of the interferometer. In both instances, the frequency of the reference beam was shifted by approximately 100Hz. Larger beat frequencies decrease the measurement time and increase accuracy. Thus in later applications such as dual reference beam holographic interferometry, Dandliker et al⁹² shifted the frequency electro-optically by 80kHz. By scanning the reconstructed hologram with an array of three detectors, Dandliker and Thalman⁹³ determined the difference of interference phase (proportional to surface strain) in two orthogonal directions simultaneously, rather than the interference phase itself. Despite rather slow measurement speed (approximately one second per point) the accuracy of phase measurement ($2\pi/100$) and the spatial resolution ($>10^6$ resolvable points) were extremely high.

With regard to ESPI, the technique will not work well with low bandwidth television detectors as the beat frequency is limited to less than 25Hz i.e. the camera frame rate. Heterodyne operation with ESPI could be achieved if a non-storage, instantaneous type of TV camera (image dissector) was included, as used by Crane in a Twyman-Green interferometer⁹⁰. Such an ESPI system was proposed by Macovski et al⁹⁴, in which the reference beam of an out-of-plane interferometer was offset in optical frequency. The intention was to isolate the desired interference signal from the dc background term by a suitable bandpass

filter centered on the beat frequency. However, due to the low sensitivity of the image dissector, Macovski et al resorted to the more usual subtraction of images recorded by an integrating-type camera (Vidicon) to suppress the unwanted dc term. Heterodyne operation was therefore not achieved.

Phase-stepping, or quasi-heterodyne, techniques were originally introduced so that photodiode arrays (CCDs) or TV cameras could be included in heterodyne interferometers. These techniques allow the simultaneous evaluation of optical phase at a number of pixels by the suitable manipulation of intensity values recorded at those pixels. The associated loss in spatial resolution and accuracy is offset by shorter measurement periods since the image is no longer scanned mechanically. Like heterodyning, quasi-heterodyning methods are immune to stationary noise and variations in intensity across the image. Quasi-heterodyning can be divided into three broad categories of operation. These are briefly described in the following paragraphs as they are rarely presented with consistent notation in the literature. The inter-relation between approaches is made clearer by the discussion.

Case 1: The first category, and most closely related to heterodyning, involves applying a continuous, linear shift in the phase of one arm of the interferometer. This is analogous to the shift in frequency used in heterodyning, and causes the fringe pattern to modulate. If the phase is shifted through 2π radians every T seconds, the intensity at P(m,n) may be written as:

$$I(m,n,t) = I_A + I_B + 2\sqrt{I_A I_B} \cos \left(\frac{2\pi}{T}t + \phi \right) \quad (3.2)$$

Wyant⁹⁵ used this procedure in a lateral shear heterodyne interferometer to actively correct wavefront aberrations in a telescope caused by deformations in the optics and atmospheric disturbances. He proposed an integrating technique to determine optical phase under low light levels, when detecting the zero crossings of two ac signals was prone to error due to electrical noise. To determine $\phi(m,n)$, the integrated output from each of the elements on the detectors was read out at

the end of four equal intervals covering a period, T. Thus:

$$E = \int_{-T/8}^{T/8} I dt + \int_{T/8}^{3T/8} I dt + \int_{3T/8}^{5T/8} I dt + \int_{5T/8}^{7T/8} I dt \quad (3.3)$$

where:

$$A = \int_{-T/8}^{T/8} I dt = \frac{(I_A + I_B)}{4} + 2\frac{\sqrt{I_A I_B}}{\pi} \cos \phi$$

$$B = \int_{T/8}^{3T/8} I dt = \frac{(I_A + I_B)}{4} - 2\frac{\sqrt{I_A I_B}}{\pi} \sin \phi$$

$$C = \int_{3T/8}^{5T/8} I dt = \frac{(I_A + I_B)}{4} - 2\frac{\sqrt{I_A I_B}}{\pi} \cos \phi$$

$$D = \int_{5T/8}^{7T/8} I dt = \frac{(I_A + I_B)}{4} + 2\frac{\sqrt{I_A I_B}}{\pi} \sin \phi$$

Then:

$$\phi(m,n) = \tan^{-1} \frac{D - B}{A - C} \quad (\text{Modulo } 2\pi) \quad (3.4)$$

At each point in the interference pattern, the phase can be found within some multiple of 2π . Knowing that $\phi(m,n)$ is a continuous function, phase discontinuities are easily resolved. This process is termed unwrapping, and is described in Section 3.2.1. The rms error in measured phase was quoted as $2\pi/50$. The variation of optical path with time must be strictly linear, although the effect of non-linearity can be reduced by increasing the number of integration periods. Stumpf⁹⁶, for example, proposed using eight integration periods. Accuracy is generally improved as the period T decreases, since sensitivity to environmental disturbances is

reduced. However, very fast electronics will be required if data is to be collected at all the detector elements at faster than the TV rates. Stumpf⁹⁶ demonstrated the general compromise employed: he modified the CCD camera to scan only 24 x 32 pixels at 710 Hz. Creath⁹⁷ used this phase-shifting technique with ESPI, Section 3.2.2, using a 100 x 100 diode array.

Case 2: The second approach to quasi-heterodyne interferometry has its roots in synchronous detection and is amenable to standard TV systems. To synchronously detect a signal, the signal is multiplied with sine and cosine signals of the same frequency and averaged over many periods of oscillation. An early analogue implementation to determine the phase of a wavefront transmitted by a hologram was proposed by Ichioka and Inuiya⁹⁸. They used an off-axis reference beam to disperse the self- and cross-interference terms in the spatial frequency domain, and TV recording to convert this to a temporal domain distribution. The TV signal was divided, and the two parts mixed separately with sine and cosine signals. Following band-pass filtering to isolate the cross-interference term, the arctangent of the ratio of the two signals (optical phase, modulo 2π) was displayed by a cathode ray tube as a continuous-tone brightness signal. The quasi-heterodyne technique based on this synchronous detection method was first described by Bruning et al⁹⁹. Rather than linearly shifting the reference phase with a translating mirror, the phase was moved in discrete steps. The intensity distribution in the fringe pattern is no longer a function of time, but of the path length l of the reference beam, and is given by:

$$I(m,n,l) = I_A + I_B + 2\sqrt{I_A I_B} \cos\left(\frac{2\pi l}{\lambda} + \phi\right) \quad (3.5)$$

Bruning et al recognised that $I(m,n)$ is sinusoidal in l for all (m,n) within the fringe pattern, and may be represented by a Fourier series with the dc term and first harmonics only:

$$I(m,n,l) = a_0 + a_1 \cos\left(\frac{2\pi l}{\lambda}\right) + b_1 \sin\left(\frac{2\pi l}{\lambda}\right) \quad (3.6)$$

where:

$$a_0 = I_A + I_B = \frac{1}{qp} \sum_{i=1}^{qp} I(m,n,l_k)$$

$$a_1 = 2\sqrt{I_A I_B} \cos \phi(m,n) = \frac{2}{qp} \sum_{i=1}^{qp} I(m,n,l_k) \cos \left(\frac{2\pi l_k}{\lambda} \right)$$

$$b_1 = 2\sqrt{I_A I_B} \sin \phi(m,n) = \frac{2}{qp} \sum_{i=1}^{qp} I(m,n,l_k) \sin \left(\frac{2\pi l_k}{\lambda} \right)$$

$$l_k = \frac{k\lambda}{q} \quad k = 1, 2, \dots, qp$$

The integer p denotes the number of periods (fringes) over which the interference pattern is sampled and q the quantisation of each period. Then

$$\phi(m,n) = \tan^{-1} \left(\frac{b_1}{a_1} \right) \quad (\text{Modulo } 2\pi) \quad (3.7)$$

The Fourier representation is analogous to the synchronous detection method with multiplication by sine and cosine terms at discrete points in the cycle. The carrier frequency is the reciprocal of the sampling time, which in this instance is the time required to step the phase by 2π radians. Accuracy will improve with the number of points per cycle. Bruning et al⁹⁹ used $p=4$ and $q=25$ for 100 intensity readings, which requires a minimum of four seconds to digitise and a considerable amount of computation. The rms error in measured phase was estimated as $2\pi/100$ radians. In general this technique is impractical for full-field techniques, due to the large image memory requirements; the use of this technique with ESPI has not been reported in the literature.

Case 3: The last of the three quasi-heterodyne techniques is a simpler version of the phase-stepping method of Bruning et al⁹⁹ and requires fewer images to be

recorded. Originally proposed by Carre¹⁰⁰, the phase reduction algorithm requires four measurements of the intensity at a point, each one with an additional phase shift of $\Delta\phi(m,n) = 2\alpha(m,n)$ radians. The intensity at each point $I(m,n)$ is given by:

$$I_k = I_A + I_B + 2\sqrt{I_A I_B} \cos(\phi + \Delta\phi_k) \quad (3.8)$$

where:

$$\Delta\phi_k(m,n) = (2k-5)\alpha(m,n), \quad k = 1,2,3,4$$

The optical phase and the phase-step size are given by:

$$\phi(m,n) = \tan^{-1} \sqrt{\frac{(3(I_2 - I_3) - (I_1 - I_4))(I_2 - I_3) + (I_1 - I_4)}{(I_2 + I_3) - (I_1 + I_4)^2}} \quad (3.9)$$

$$\alpha(m,n) = \tan^{-1} \sqrt{\frac{3(I_2 - I_3) - (I_1 - I_4)}{(I_2 - I_3) + (I_1 - I_4)}} \quad (3.10)$$

The equations are simplified if the size of the phase step is known at each point in the image, in which case only three measurements of the intensity are necessary. More readings can still be used if desired. Maintaining the notation of equation (3.8), but letting $\Delta\phi_k(m,n) = (k-1)\alpha(m,n)$, $k = 1,2,3$, the phase is given by:

$$\phi(m,n) = \tan^{-1} \frac{(I_3 - I_2) + (I_1 - I_3)\cos \alpha + (I_2 - I_1)\cos 2\alpha}{(I_1 - I_3)\sin \alpha + (I_2 - I_1)\sin 2\alpha} \quad (3.11)$$

Equation (3.11) enables the size of the phase-step $\alpha(m,n)$ to vary across the image plane. However, a further simplification is possible if the phase-step is assumed to be constant for all values of (m,n) . Franz et al¹⁰¹ described a Twyman-Green interferometer for hybrid optical-digital computation of two-dimensional Fourier transforms for $\alpha = \pi/2$ radians. An algorithm requiring only two interferograms with a single $\pi/2$ phase-step between them was also demonstrated. A common alternative is $\alpha = 2\pi/3$ radians^{102,103}, giving:

$$\phi(m,n) = \tan^{-1} \frac{\sqrt{3} (I_3 - I_2)}{(2I_1 - I_2 - I_3)} \quad (3.12)$$

Despite fewer images than the method due to Bruning et al⁹⁹, rms phase error is usually quoted as approximately $2\pi/100$ radians¹⁰³ for fringes of holographic quality. This technique is well suited to applications such as holographic interferometry and ESPI, where measurements have to be made at a large number of points. In addition, the small memory requirements combined with the simplicity of the algorithms for calculating the original phase difference makes the use of an inexpensive microcomputer feasible. For those applications which require the intensity data to be available in a single frame period, there exist techniques to spatially separate the phase-stepped images¹⁰⁴.

3.1.3 Alternative Phase Measuring Techniques

The advantages of calculating phase rather than tracking intensity are apparent from Section 3.1.2, but recording several images is a drawback of the phase-stepping technique. Consequently methods of calculating the interference phase from a single interferogram have been proposed. These generally fall into one of three categories, and require the interferometer to be adjusted initially to give a set of parallel fringes: the measurement parameter is then encoded as deviation in the symmetry of the carrier fringes. Incorporating carrier fringes restricts the dynamic range of the interferometer. Accuracy increases with decreasing wavelength of the carrier frequency. Typically carrier fringes with a wavelength of three or five pixels are used. Such high fringe densities are difficult to achieve with ESPI: speckle decorrelation and the fringe spacing approaching the speckle diameter combine to reduce fringe visibility significantly. However, the three techniques are briefly described below for completeness.

Takeda et al¹⁰⁵ applied a digital fast Fourier transform to an interferogram

containing carrier fringes of spatial frequency f_c , and the encoded phase to be measured $\phi(x,y)$. Spatial frequencies in one of the side lobes associated with f_c were selected and shifted to the origin. The inverse Fourier transform was calculated giving a function with complex values, from which ϕ was deduced as the arctangent (imaginary/real). The main sources of error are those associated with the use of the FFT, incorrect filtering in the Fourier space and noise in the interferogram. The speed of processing, especially for high resolution images, is limited due to the computational intensity of calculating the forward and inverse transforms. Preater of London University has applied this technique to in-plane ESPI subtraction interferograms recorded with a pulsed ruby laser for components rotating at high speed, although no details have been published at the time of writing. A faster approach proposed by Mertz¹⁰⁶ is to assume that the spatial period of the carrier fringes has a known value, in this instance three pixels per fringe. The carrier frequency f_c can then be isolated directly from the image plane with a three-sample convolution filter having complex coefficients. This is applied to each group of three adjacent pixels, and the phase calculated as the arctangent(imaginary/real). Womack¹⁰⁷ proposed multiplying the measurement fringe pattern (with tilt) by a reference pattern of nearly the same spatial frequency. This generates a low spatial frequency moire pattern, which may be separated by lowpass filtering. The process was then repeated, this time with a reference pattern in quadrature with the first. The phase can be determined from the arctangent of the ratio of the two moire patterns at each point. This last example is analogous to the (temporal) synchronous detection technique of Ichioka and Inuiya⁹⁸ and is sometimes called spatial synchronous detection.

3.1.4 Selection of Phase-Stepping for In-Plane ESPI

Section 3.1.1 demonstrated that fringe tracking is not a suitable method for automated displacement and strain method with ESPI. Considerable operator intervention would be required to correct erroneously marked maxima or minima, and fringe orders must be assigned manually. Fringe interpolation requires

polynomial fitting to the intensity data which is generally slow. Section 3.1.3 discussed methods requiring a single interferogram from which the optical phase is extracted, thus solving the direction of displacement ambiguity. Difficulties associated with using ESPI with carrier fringes were described. Furthermore, for this study, static fringe patterns were considered and so analysing a single interferogram was not strictly necessary. This leaves the quasi-heterodyne or phase-stepping techniques of Section 3.1.2. Spatial separation techniques could then be applied if dynamic studies were required subsequently. Many algorithms were discussed in Section 3.1.2, and it therefore remains to select a suitable one from these. In general, it appears to be simpler to apply discrete phase steps to the interferometer, rather than a linear phase ramp, under digital computer control. This restricts the discussion to Cases (ii) and (iii) of Section 3.1.2. As discussed in that section, accuracy increases with number of images, although the data acquisition time and memory requirements increase, and the calculation of phase becomes more complex. With the likelihood of testing several specimens at several loads and the general trend of personal computer-based fringe analysis, it was decided to gather the smallest amount of data for each test i.e. use as few images as possible. The single-step algorithm originally proposed by Franz et al¹⁰¹ and applied to ESPI by Kerr et al¹⁰⁸ only requires two images, but must be used with care. It is not immediately apparent, but the implicit assumption of the technique is that the modulation amplitude and background intensity are equal.* This cannot always be guaranteed in practice. Thus the two-step algorithm of equation (3.12) was used for the remainder of the thesis.

3.2 IN-PLANE PHASE-STEPPED ESPI

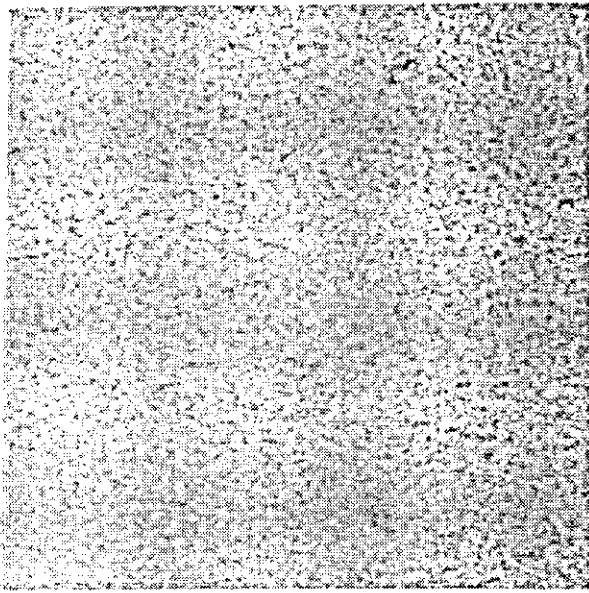
Phase-stepping methods were first applied to out-of-plane ESPI in 1985. The phase difference between the beams of a classical interferometer (hereafter simply called the phase) is a smoothly varying function of position in the detector array. However, with ESPI, the calculated phase will vary randomly due to the random phase of individual speckles. Three methods to suppress random speckle noise for

*Phase is calculated as $\text{atan}(I_1/I_2)$, where $I_1=1+\sin\phi$ and $I_2=1-\cos\phi$. The expressions for I_1 and I_2 assume that the modulation amplitude and background intensity are equal. If they are not equal an error is introduced.

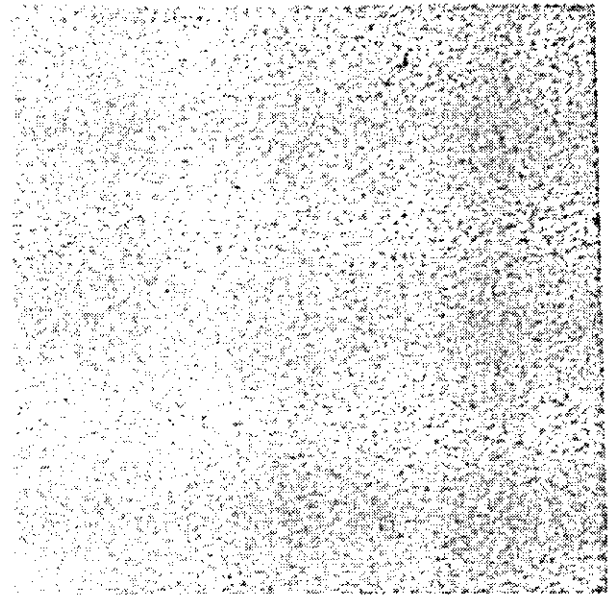
phase-stepped ESPI have been proposed in the literature; these are briefly described in Sections 3.2.1 to 3.2.3. Although each method was originally proposed for an out-of-plane interferometer, the analysis and examples consider an in-plane system. The phase-stepping and image digitisation sequence for the results presented were performed with the Optics Group Kontron image processor, hosted by a DEC MicroVax minicomputer¹⁰⁹ (Appendix C). A further complication with phase-stepped ESPI is that the random distribution of speckle intensity will cause some pixels to saturate, and others to fail to give intensity modulation above the detector noise level. This reduces the measurement accuracy and adds to the error sources more usually associated with the phase-stepping method. The likely magnitude of these errors for the experimental system are discussed in Section 3.2.4. An experimental investigation is deferred to Section 3.2.5.

3.2.1 Temporal Phase-Stepping Speckle Correlation (TPSSC)

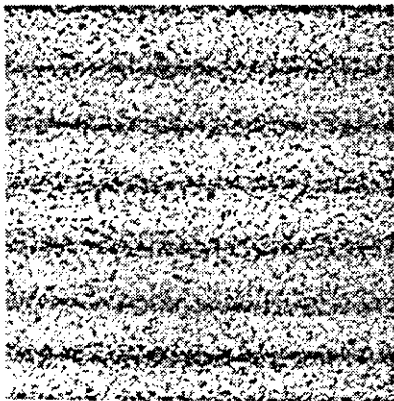
Of the phase-stepping methods applied to ESPI, TPSSC¹¹⁰ is the most closely related to the quasi-heterodyne classical interferometers of Section 3.1.2. Briefly, phase-shifted correlation fringes are recorded, and a filter applied to remove high spatial frequency speckle noise. The phase reduction algorithm can then be applied to the filtered data. This technique has been implemented at Loughborough University of Technology for out-of-plane ESPI¹⁰⁹, making use of state-of-the-art framestores to generate the correlation fringes. The technique is illustrated in Figure 3.1, with data obtained from an horizontal in-plane (x-) sensitive interferometer. The object studied was a flat 80mm x 80mm aluminium plate, painted white, and mounted to a rotation stage in the xy-plane. Following the TPSSC method as originally proposed¹¹⁰, Figure 3.1(a) shows the reference (undeformed) speckle pattern, and Figure 3.1(b) the speckle pattern when the plate was rotated by a small angle in its own plane. Figure 3.1(b) is one of three phase-stepped speckle patterns, for which the intensity may be approximated by:



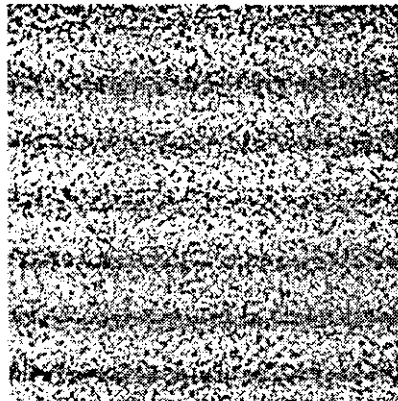
(a)



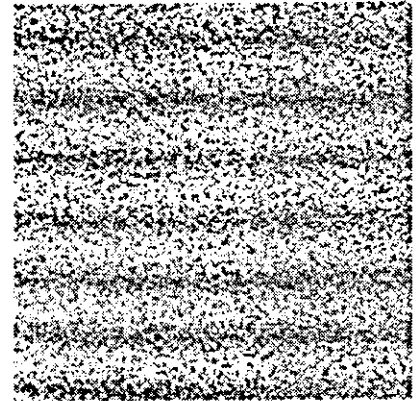
(b)



(c)

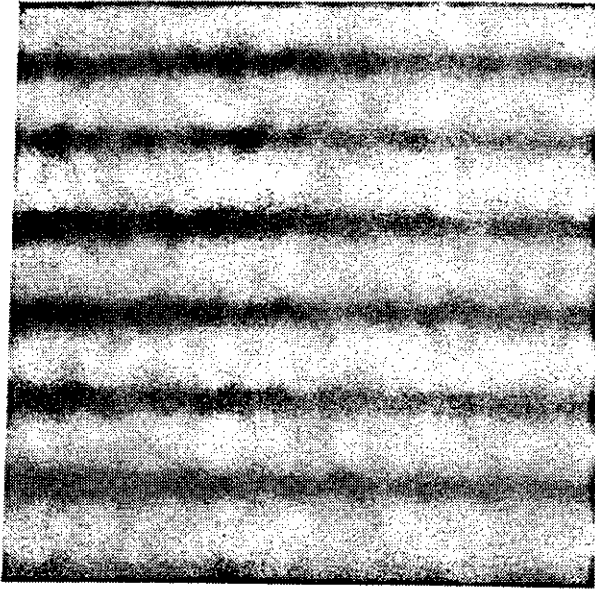


(d)

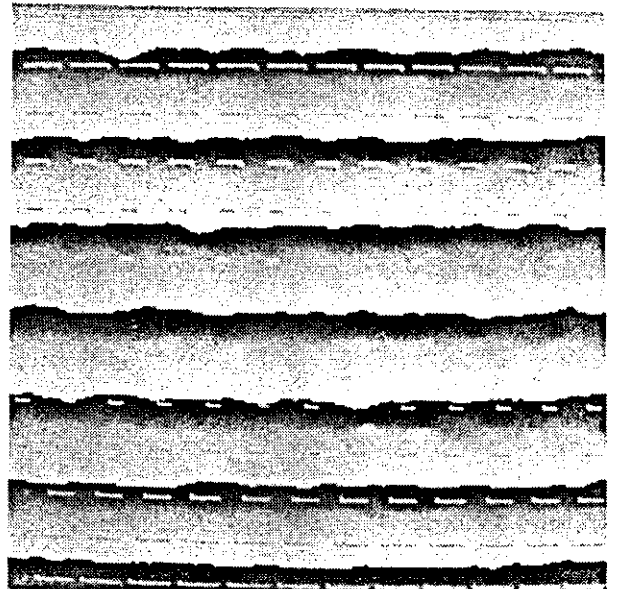


(e)

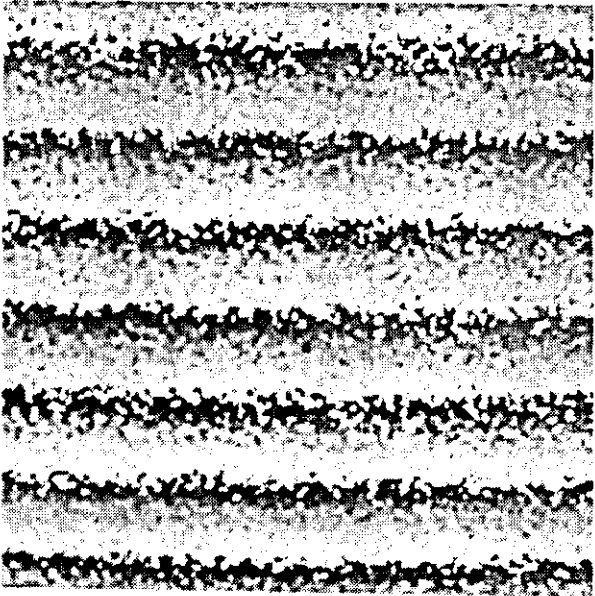
Figure 3.1 Temporal phase-stepped speckle correlation (Continued overleaf)



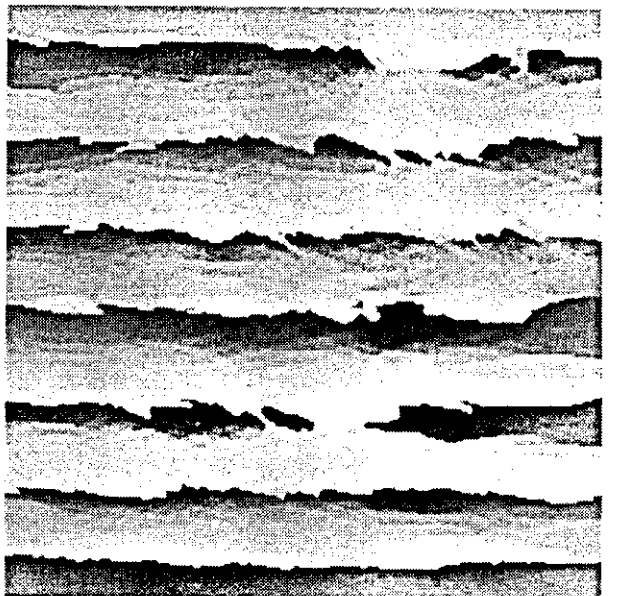
(f)



(g)



(h)



(i)

Figure 3.1 (continued) Temporal phase-stepped speckle correlation

$$I_{def,k+1}(m,n) = I_A + I_B + 2\sqrt{I_A I_B} \cos \left(\psi + \phi + \frac{2k\pi}{3} \right) \quad (3.13)$$

where $k = 0,1,2$. $\psi(m,n)$ is the composite phase angle between the two beams that incorporates the random speckle phase, and $\phi(m,n)$ is the phase difference introduced between the two beams due to the resolved component of surface displacement in the x-direction. For Figure 3.1(a), $I_{ref}=I_{def,k+1}$ with $k=0$ and $\phi(m,n)=0$. Phase-stepped correlation fringes may be generated by:

$$\begin{aligned} I_{k+1}(m,n) &= |I_{def,k+1} - I_{ref}| \\ &= 2\sqrt{I_A I_B} \left| \cos \left(\psi + \phi + \frac{2k\pi}{3} \right) - \cos (\psi) \right| \end{aligned} \quad (3.14)$$

The absolute difference is used to model the exclusive-or (subtraction) operation of the framestore (Appendix C). The result is shown in Figures 1(c)-(e) for $k=0,1,2$ respectively. The fringes move perpendicular to the tangent of the fringe curve by one-third of their width. Generally it is quicker to digitise directly the correlation fringes produced by a dedicated external framestore¹⁰⁹. The interferometer can be adjusted to optimise fringe visibility, and three rather than four images are digitised.

Assuming that $\phi(m,n)$, varies slowly with respect to $\psi(m,n)$, equation (3.14) describes two functions modulated by each other: the first at higher spatial frequency than the second. Hence by applying a suitable filter to reduce the high spatial frequency speckle noise, cosinusoidal fringes are obtained. Conceptually, this is the same as setting $\psi(m,n)=0$ i.e.

$$\begin{aligned} I_{k+1}(m,n) &= 2\sqrt{I_A I_B} \left| \cos \left(\phi + \frac{2k\pi}{3} \right) - 1 \right| \\ &= 2\sqrt{I_A I_B} \left(1 - \cos \left(\phi + \frac{2k\pi}{3} \right) \right) \end{aligned} \quad (3.15)$$

Figure 3.1(f) shows the result of applying three iterations of a 7×7 local neighbourhood average filter to Figure 3.1(c). The corresponding map of phase values calculated by equation (3.12) from the three filtered images is shown in Figure 3.1(g). Phase values in the range $-\pi$ to $+\pi$ radians are scaled to 0 to 255 grey-levels for display. Discontinuities in the grey-value occur due to the asymptotic nature of the arctangent function. To determine the displacement across the object, these discontinuities must be removed. This process is termed phase unwrapping and is discussed in the following paragraph.

To reconstruct a continuous phase map, all occurring 2π phase discontinuities must be detected and removed. However, due to the finite sampling interval and the presence of noise, phase discontinuities will always be less than 2π . Therefore, in practice, a threshold has to be specified; this was taken to be π for the work presented in this thesis. A simple unwrapping algorithm was used, based on adding an offset (in multiples of 2π) to the phase value at a given pixel if the absolute phase difference between adjacent pixels exceeded π . The offset is changed each time a 2π step is detected. Starting at the top left pixel of the image, the offset is set to zero. The first column is then scanned to determine the offsets for the first pixel of each row. Finally the offset for each row is calculated, starting with the offset in the first column. This fairly basic routine can be prone to error in the presence of noise, and more complex unwrapping algorithms have been proposed¹¹². These algorithms are generally slower than the simple routine just described, but are intended to be used by operators who are not familiar with fringe analysis. Therefore, rather than devising a robust (i.e. noise immune) routine, the simple routine was used with careful optimisation of the interferometer and judicious selection of the area of phase map to be unwrapped. When used in this way it was found to be acceptable.

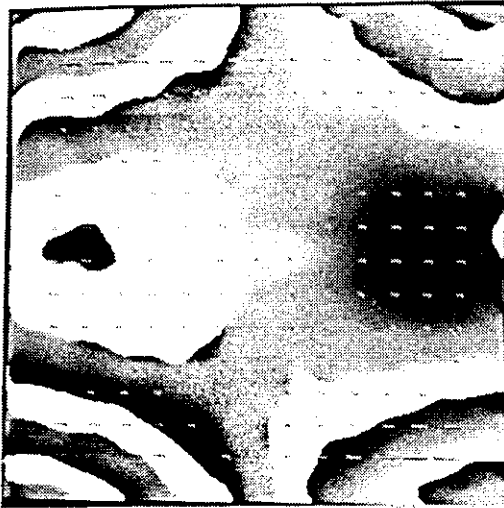
Phase data can be converted to displacement data from the fringe function, equation (2.16). Routines were written to represent the displacement at selected points with arrows superimposed on to the image whose length is proportional to the absolute value of displacement. Taking the centre of the plate as reference,

a clockwise rotation is shown in Figure 3.1(g). Displacement data from two phase maps with orthogonal sensitivities can be vectorially combined. Phase data recorded by Mendoza et al¹¹³ with a pulsed Nd:YAG laser to investigate the in-plane vibrations of a metal plate pinned at its centre is used as an example of the routines developed. Figures 3.2A and 3.2B show the phase-stepped results for plate excitation frequencies of 21.8 and 30.5kHz respectively. In each figure (a) is the u-sensitive phase map with displacement overlaid, (b) is the v-sensitive phase map, and (c) is the total in-plane displacement vector plot superimposed on a white-light image of the plate.

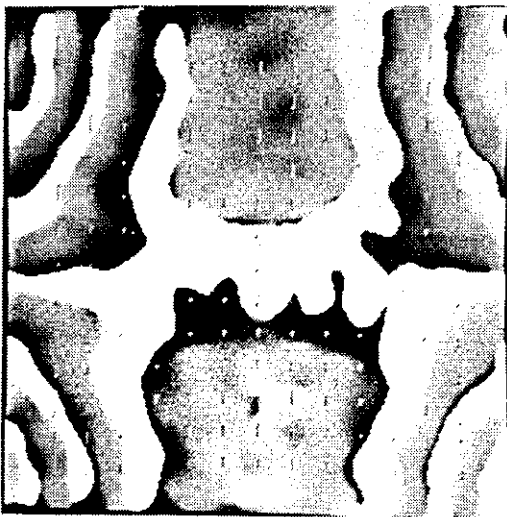
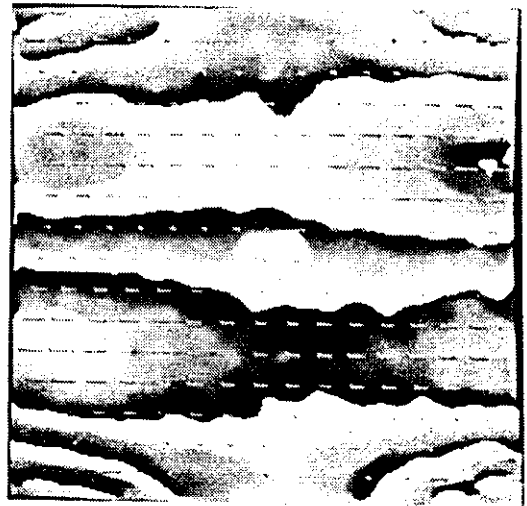
Pre-processing the correlation fringes to reduce speckle noise is a drawback to the TPSSC technique. The accuracy with which the phase is measured clearly depends on the selection of the filter. For example, Figure 3.1(h) shows the phase map when a single iteration of a 3x3 neighbourhood average filter is used. A considerable portion of the high spatial frequency noise remains in the filtered fringe pattern, resulting in a noisy phase map. The other extreme is demonstrated in Figure 3.1(i): 11 iterations of an 11x11 neighbourhood average filter were applied, reducing spatial frequencies associated with the fringe function. The SNR of the fringe pattern is degraded, and the phase information is lost. The overlap in spatial frequencies between the fringe function and speckle carrier prevent all the speckle noise being removed by any filter. This can be seen in the "mottled" nature of a phase map produced by a successful filter, Figure 3.1(g). Locally adaptive and/or directionally sensitive filters may be required if the fringe visibility varies considerably over the image. The effects of the pre-processing filter need to be understood, and this is investigated further in Section 3.2.5.

3.2.2 Digital Phase-Stepping Speckle Interferometry (DiPSSI)

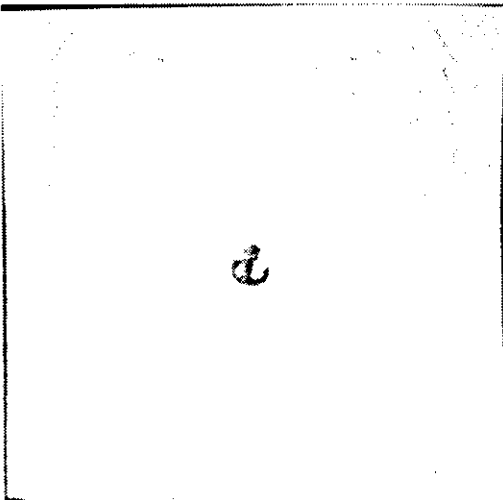
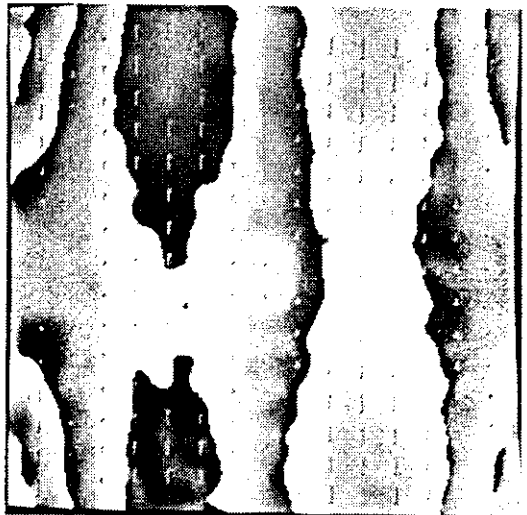
In this approach, each pixel in the television image is treated as an individual interferometer. Briefly, the phase before and after the object deformation is calculated at each pixel. Random speckle phase cancels when the difference



(a)



(b)



(c)

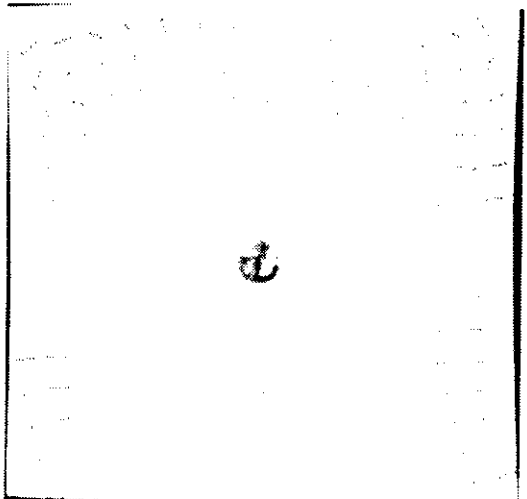


Figure 3.2A Square plate vibrating at 21.8kHz, phase-stepped analysis

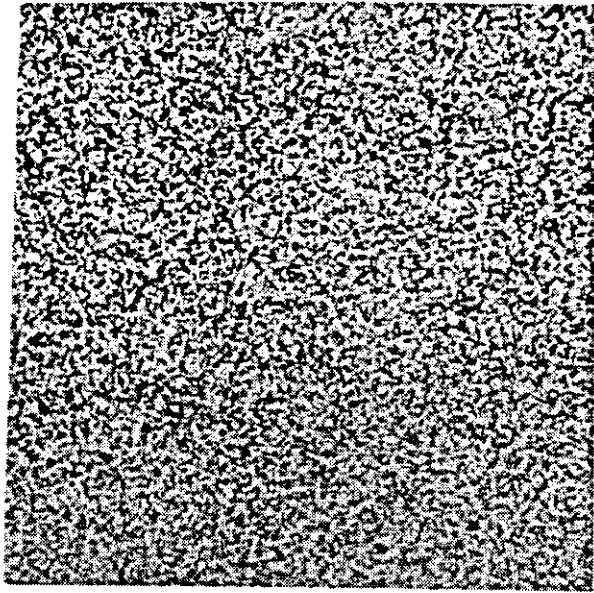
Figure 3.2B Square plate vibrating at 30.5kHz, phase-stepped analysis

between the two phase values is taken, leaving a continuous map of phase representing the deformation only^{97,114}. Intensity fringes are not formed: the process involves speckle phase correlation rather than speckle intensity correlation.

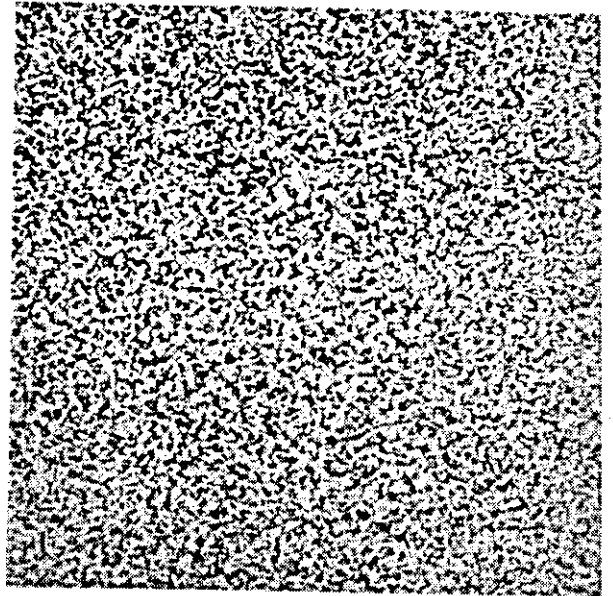
To illustrate the technique, the reference (undeformed) speckle pattern of Figure 3.1(a) is considered as one of a set of three phase-stepped images. The intensity, $I_{\text{ref},k+1}$ at each pixel will correspond to equation (3.13) with $\phi(m,n)=0$. Three deformed speckle patterns corresponding to equation (3.13) and Figure 3.1(b) are recorded as before. The phase reduction algorithm is applied to both sets of data: the reference data set yields the random speckle phase $\psi(m,n)$, Figure 3.3(a), and the deformed data set gives $\psi(m,n)+\phi(m,n)$, Figure 3.3(b). Subtracting the two phase maps removes the random speckle phase, leaving the phase difference introduced by object deformation, Figure 3.3(c). In general, the accuracy with which phase can be calculated at any pixel depends on the amplitude with which the intensity modulates, Section 3.2.4. From equation (3.12), the modulation amplitude is given by:

$$I_M(m,n) = 2\sqrt{I_A I_B} = \frac{1}{3} \sqrt{3(I_3 - I_2)^2 + (2I_1 - I_2 - I_3)^2} \quad (3.16)$$

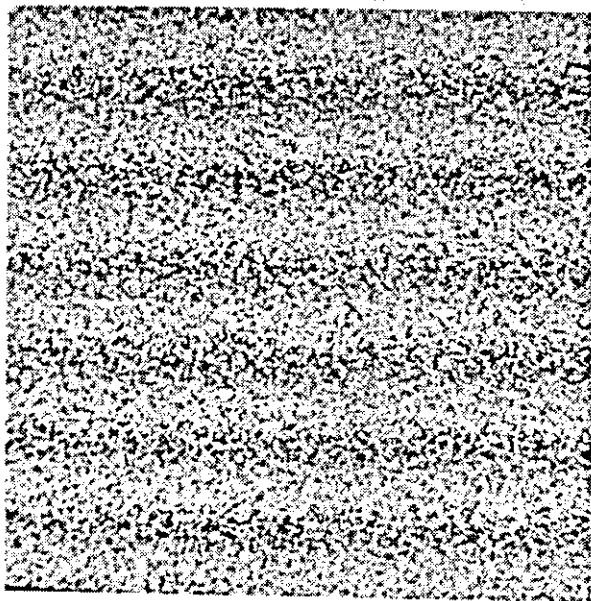
Those pixels at which $I_M \leq 4$ grey-levels from either Figures 3.3(a) or 3.3(b) are marked in Figure 3.3(d). The phase cannot be accurately determined at these pixels and they must be corrected at a later stage. The same criterion was applied when calculating the phase map of Figure 3.1(g) by the TPSSC method: due to the averaging effect of the lowpass filter, no pixels gave $I_M \leq 4$. Further inaccuracies occur in the phase calculated at a pixel if that pixel shows zero intensity or is saturated in any of the three images. Once again this effect is rarely seen in TPSSC due to the lowpass filter. Therefore the phase map produced by DiPSSI is speckled with points of unknown phase, causing simple unwrapping routines as described in Section 3.2.1 to fail. More complex routines which unwrap around marked pixels have been proposed¹¹²; marked pixels can then be replaced by an average of their non-marked neighbours. Alternatively a valid phase from



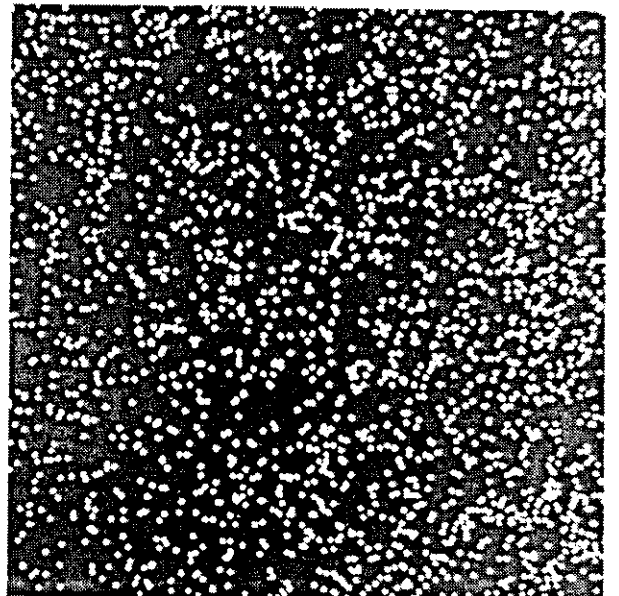
(a)



(b)



(c)



(d)

Figure 3.3 Digital phase-stepped speckle interferometry

the set of nearest pixels can be substituted for a marked pixel, and more simple unwrapping routines implemented⁹⁷.

Differences between the TPSSC and DiPSSI approaches are immediately apparent. TPSSC enables a reduction in data acquisition and processing time, and requires less image memory: three images and two mirror steps, as opposed to six images and four mirror steps with DiPSSI. However information from saturated and zero intensity pixels, and those that do not modulate correctly will be filtered back into the interferogram. Consequently the accuracy is reduced. These effects are discussed more fully in Section 3.2.4, but first a phase-stepping approach using correlation fringes but not requiring a lowpass filter is described.

3.2.3 Analytic Solutions

In the TPSSC method, correlation fringes are calculated from the intensities recorded before and after deformation by subtracting them and taking the modulus. As discussed, the random speckle noise that modulates the sinusoidal correlation fringes must be removed before the phase reduction algorithm can be applied. However, Kujawinska et al¹⁰⁴ proposed a method to extract the phase of the deformed object from the same set of data without forming correlation fringes. To illustrate the technique, it is simplest to recast the equations representing the data gathered by the TPSSC method into a simpler form:

$$\begin{aligned}
 I_1 &= I_{ref} = I_{BG} + I_M \cos(\psi) \\
 I_{k+2} &= I_{def,k+1} = I_{BG} + I_M \cos\left(\psi + \phi + \frac{2k\pi}{3}\right)
 \end{aligned}
 \tag{3.17}$$

where $k=0,1,2$ and $I_{BG}=I_A+I_B$ is the background illumination. There are four equations in four unknowns, which may be solved analytically to give:

$$\phi(m,n) = \tan^{-1} \left(\frac{-ac + b\sqrt{a^2 + b^2 - c^2}}{-bc - a\sqrt{a^2 + b^2 - c^2}} \right) \quad (3.18)$$

where:

$$a = \frac{I_3 - I_4}{\sqrt{3}}; \quad b = \frac{2I_2 - I_3 - I_4}{3}; \quad c = \frac{I_2 + I_3 + I_4}{3} - I_1$$

in which the typographical errors of reference 104 have been corrected. The quantity $\sqrt{(a^2+b^2-c^2)}$ is equivalent to $I_M \sin \psi$ and may take positive or negative values depending on the value of the random speckle phase, ψ , at any particular point. Therefore two solutions exist for the phase, ϕ , differing by the sign before the square root. Since ψ varies randomly from point to point, there is no clear criterion as to which value of ϕ should be chosen. Kujawinksa et al¹⁰⁴ resolved this by selecting the solution that maintained the smoothest function within a 3x3 local neighbourhood. This is analogous to the lowpass filtering required with the TPSSC method, in that the displacement phase is assumed to vary with low spatial frequency compared to the random speckle phase. However, the filter is applied to the phase data rather than the fringe function: the phase value that is selected has been calculated from the intensity modulation of a single pixel.

The advantages of digitising fringes rather than recording speckle patterns were discussed in Section 3.2.1; these included fewer images and less computation to extract the deformation phase. Indeed, in double-pulsed addition ESPI, only correlation fringes can be digitised. The disadvantages of lowpass filtering to suppress random speckle noise were also discussed: reduced accuracy for subtraction fringes and failure with addition fringes. (ESPI addition fringes are introduced later in this section). This raises an interesting question: does a solution exist for correlation fringes, which enables each pixel in the image to be treated as an individual interferometer? Such a solution would be applied directly to each pixel of the correlation fringe pattern without the need for a pre-processing filter. This would offer improved accuracy for subtraction fringes and

give the ability to phase-step addition fringes for the first time. Subtraction fringes are considered first, and then addition fringes.

Modifying equation (3.14) to include a phase-step of arbitrary size gives:

$$I_{k+1}(m,n) = I_M \left| \cos\left(\psi + \phi + \frac{2k\pi}{l}\right) - \cos(\psi) \right| \quad (3.19a)$$

where $k=0,1,\dots,(l-1)$. Considering terms in I_{k+1}^2 to remove the modulus, a three-step solution ($l=4$) was found. To demonstrate the technique, four images corresponding to equation (3.19a) were computer generated, Figure 3.4(a). These are analogous to the fringes of Figure 3.1(c)-3.1(e), although this time the fringes move through 1/4 of their width. ϕ varies linearly with horizontal position, n , in the image i.e. $\phi(n)=2\pi wn/256$ for a 256×256 pixel image, where $w=2$ represents the number of optical waves. $\psi(m,n)$ is randomly generated in the range $-\pi < \phi < \pi$ radians. In reality, I_A and I_B also vary from pixel to pixel, but a uniform $I_M=128$ was assumed. The terms in I_{k+1}^2 are:

$$I_1^2 = I_M^2 \cos^2(\psi) - 2I_M^2 \cos(\psi) \cos(\psi + \phi) + I_M^2 \cos^2(\psi + \phi)$$

$$I_2^2 = I_M^2 \cos^2(\psi) + 2I_M^2 \cos(\psi) \sin(\psi + \phi) + I_M^2 \sin^2(\psi + \phi)$$

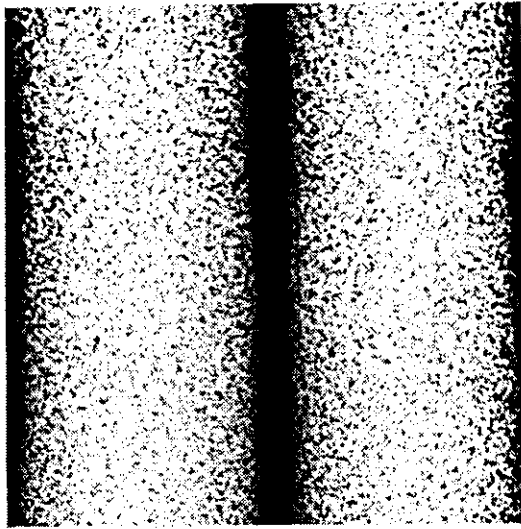
$$I_3^2 = I_M^2 \cos^2(\psi) + 2I_M^2 \cos(\psi) \cos(\psi + \phi) + I_M^2 \cos^2(\psi + \phi) \quad (3.19b)$$

$$I_4^2 = I_M^2 \cos^2(\psi) - 2I_M^2 \cos(\psi) \sin(\psi + \phi) + I_M^2 \sin^2(\psi + \phi)$$

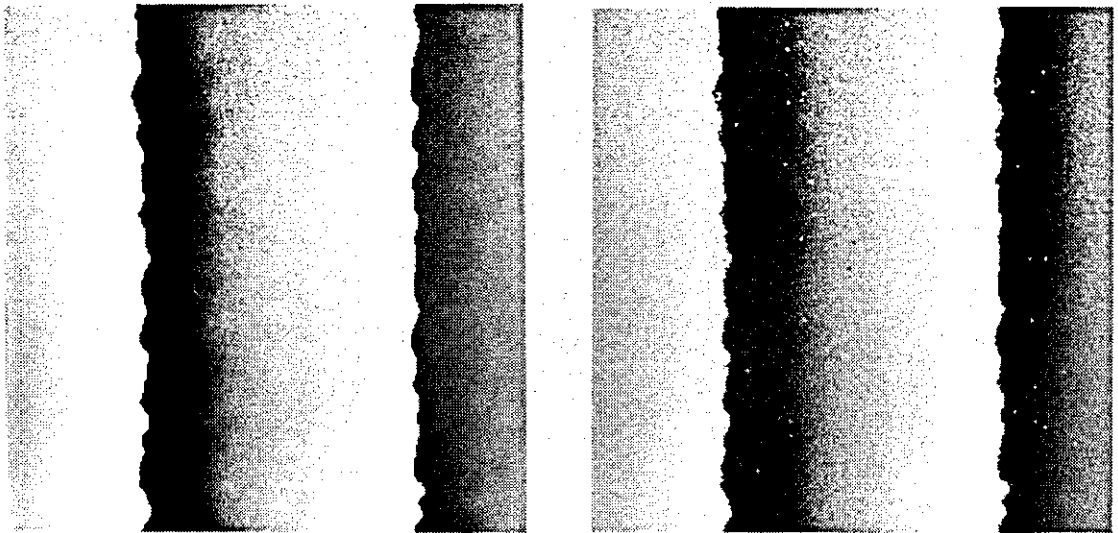
It is easiest to consider the solution in two stages. Firstly the combined random speckle and displacement phase, $\psi + \phi$, is calculated from:

$$\psi(m,n) + \phi(m,n) = \tan^{-1} \frac{I_2^2 - I_4^2}{I_3^2 - I_1^2} \quad (3.20)$$

This is a commonly used algorithm¹¹⁰ but with terms in I_{k+1}^2 rather than I_{k+1} . The random speckle phase must be subtracted at each pixel. To do this, the terms a



(a)



(b)

(c)

Figure 3.4 Analytic phase-stepping for subtraction fringes

and b are defined such that:

$$a = I_1^2 + I_2^2 + I_3^2 + I_4^2 = 2 I_M^2 (2 \cos^2 (\psi) + 1)$$

$$b = \sqrt{(I_3^2 - I_1^2)^2 + (I_2^2 - I_4^2)^2} = 4 I_M^2 \cos (\psi)$$

In the more usual form of equation (3.20) with terms in I_{k+1} rather than I_{k+1}^2 , $b=4I_M$. The random speckle phase may be calculated by solving the quadratic in $\cos(\psi)$, i.e:

$$\psi(m,n) = \cos^{-1} \frac{a + \sqrt{a^2 - 2b^2}}{2b} \quad (3.21)$$

b may take positive or negative values according to the random speckle phase, ψ , at a particular point. Combined with the square root in equation (3.21), a total of four solutions for ψ exist at each pixel. To select the correct solution, the four solutions were compared with the phase value calculated by applying equation (3.20) to the lowpass filtered images of equation (3.19a), Figure 3.4(a). This comparison phase-map is shown in Figure 3.4(b). The nearest of the four solutions to the value from the comparison phase map was selected as the correct solution, Figure 3.4(c). Note the slight error in selecting phase at the phase discontinuities: the remainder of the image shows a smooth phase profile, unlike the phase map of Figure 3.4(b) in which the phase mottling is clearly visible. If I_A and I_B had been allowed to vary randomly Figure 3.4(c) would include points at which no valid phase could be calculated.

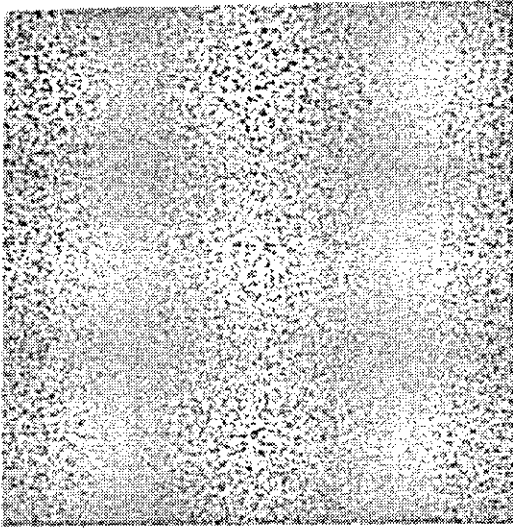
Addition fringes are obtained in real time from ESPI using a twin pulsed laser, when two pulses are fired during a single frame of a CCD camera⁸¹. From equation (3.13) addition fringe intensity may be approximated by:

$$\begin{aligned} I_{k+1} &= I_{ref} + I_{def,k+1} \\ &= 2I_{BG} + I_M \left(\cos (\psi) + \cos \left(\psi + \phi + \frac{2k\pi}{T} \right) \right) \end{aligned} \quad (3.22)$$

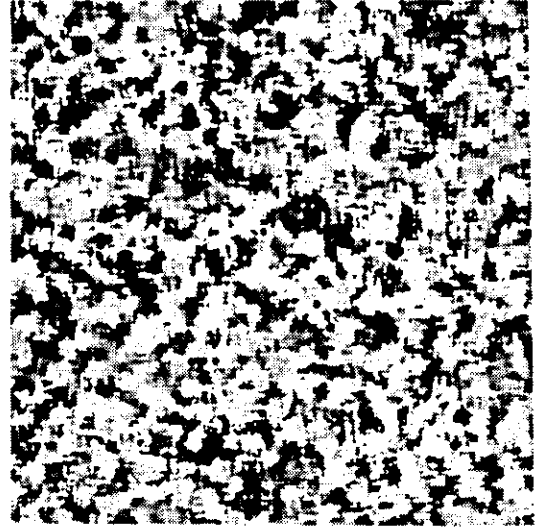
where $k=0,1,\dots,(l-1)$ and $I_{BG}=I_A+I_B$. To demonstrate the solution, the fringes of Figure 3.5(a) were computer generated. $2I_{BG}=128$ grey-levels, and $I_M=15$ grey-levels, the mean modulation amplitude of the experimental data in Sections 3.2.1 and 3.2.2. Figure 3.5(a) shows the result of applying a single iteration of a 7×7 pixel neighbourhood average filter to the three images and calculating the phase with equation (3.12): the fringe pattern is removed by the filter, and phase information is lost. This has prevented phase-stepping of addition fringes in the past. However, a two-step ($l=3$) solution for ϕ can be used. Firstly equation (3.12) is applied to the unfiltered data to calculate the random speckle phase plus the deformation phase, $\psi + \phi$. It then remains to eliminate the random speckle phase, which is achieved in a similar way to the previous section i.e:

$$\begin{aligned} \psi(m,n) &= \cos^{-1} \frac{1}{3I_M} (I_1 + I_2 + I_3 - 6I_{BG}) \\ &= \cos^{-1} \frac{I_1 + I_2 + I_3 - 6I_{BG}}{\sqrt{3(I_2 - I_3)^2 + (2I_1 - I_2 - I_3)^2}} \end{aligned} \quad (3.23)$$

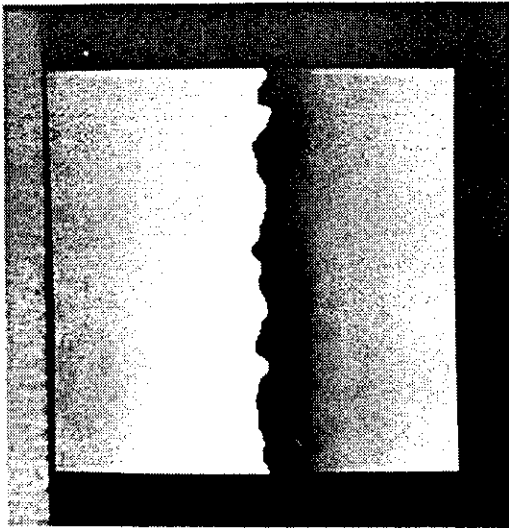
The terms $2I_{BG}$ and $I_M \cos \psi$ cannot be isolated from equation (3.22). However, an estimation of $2I_{BG}$ can be made if it is assumed that the statistical average of both cosine terms in equation (3.22) is zero. Thus for each image, the mean intensity in the $(256/w) \times (256/w)$ pixel neighbourhood of each pixel was evaluated, and substituted into equation (3.23). Two values of ψ exist due to the sign of the square root in equation (3.23). Once again the correct solution at each pixel was chosen by reference to a comparison phase map, Figure 3.5(c). The comparison phase map was calculated by applying equation (3.12) to subtraction fringes which were calculated using equation (3.19). The fringes are the same as Figure 3.4(a), but step through one-third of their width. Random speckle noise was removed with three iterations of a 7×7 pixel neighbourhood average filter. Notice that the minimum intensity for the addition fringes is shifted by π radians from the zero position for subtraction fringes. Thus a π radian offset was added to the



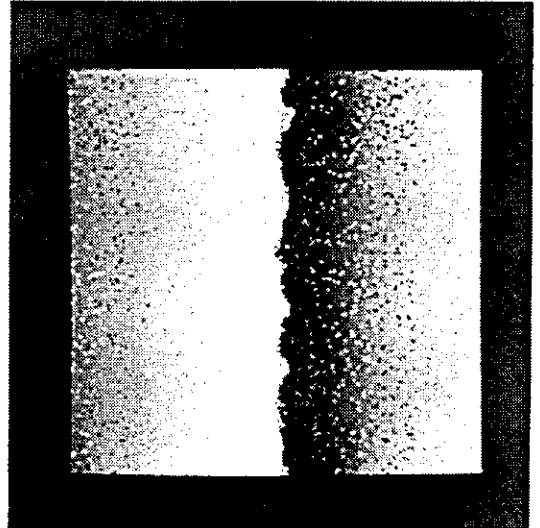
(a)



(b)



(c)



(d)

Figure 3.5 Analytic phase-stepping for addition fringes

comparison phase map calculated from subtraction fringes (compare Figures 3.4(b) and 3.5(c)). The phase selected at each pixel is displayed in Figure 3.5(d). Once again a smooth phase profile is seen, compared with the mottled effect in Figure 3.5(c). A 65x65 pixel window was used to calculate $2I_{BG}$, rather than using a $(256/w) \times (256/w)$ pixel window. This gave a reasonable approximation to $2I_{BG} = 128$ grey-levels. Noise in the calculated phase was attributed to errors in estimating $2I_{BG}$, although digitisation errors and mottling in the comparison phase map will also contribute. The area of valid phase data is reduced because of the 65x65 pixel window required to calculate $2I_{BG}$. Phase can be calculated to the image edges if the mean intensity calculated from a larger area is valid.

These algorithms have been demonstrated for experimental data (Appendix E). These demonstrations are not presented here because the two algorithms were devised too late for inclusion in the main body of work i.e. fracture mechanics applications. Thus the TPSSC method is used in the remainder of the thesis. However, both the algorithms presented will probably be the subject of future research.

3.2.4 Accuracy of Phase Measurement

Certain sources of error exist which must be minimised if accurate phase-stepped measurements are to be made. For this discussion the error sources will be divided into two categories: firstly those that are inherent to the phase-stepping process, and secondly those introduced by the speckled nature of ESPI fringes. The first category have been extensively investigated elsewhere, and so the discussion is restricted to how they can be minimised and to their likely magnitude. Errors introduced due to speckle noise with TPSSC have yet to be treated comprehensively elsewhere. Therefore these effects are discussed more fully.

Error Sources Inherent in Phase-Stepping Interferometry: The phase-stepping algorithms described in Section 3.1.2 assume the background intensity $I_{BG}(m,n)$ and the modulation intensity $I_M(m,n)$ to be constant during the data collection period. Further, equation (3.12) assumes the phase shifts to be equally spaced and well-known. Thus, the accuracy of a single phase measurement using the phase-stepping method with any optical technique is determined by the accuracy of intensity values recorded and by the accuracy of the phase shifts. Errors in intensity and phase shift can be systematic or statistical. Assuming a well optimised interferometer, in which no extraneous fringes are present on the detector and optical noise due to dust particles is minimised, the main error sources falling into each classification are:

Systematic: Miscalibrated phase step;

Non-linear phase step;

Non-linear detector;

Statistical: Electronic noise of detector;

Phase noise due to perturbations (mechanical/thermal/laser source).

The systematic errors will in general produce periodic phase errors, whilst the form of any statistical phase error will depend on the properties of the disturbance producing it. Sensitivity to each error source can vary between phase reduction algorithms. For example, Carre's¹⁰⁰ original three-step algorithm, equation (3.9), does not require a phase-step of known size and is therefore immune to miscalibration of the phase-step provided that steps of equal size are used i.e. a linear phase-step. The likely magnitude of errors in the following discussion are for the two-step algorithm of equation (3.12).

Miscalibrated phase step: If a constant calibration error is present, the phase shift may be written as $\alpha' = \alpha(1 + \epsilon)$ where α is the desired phase shift, α' is the actual phase shift, and ϵ the normalised error. Schwider et al¹¹⁵ demonstrated that an error term is introduced corresponding to the phase distortion of the object except that the spatial frequency is doubled. For the experiments reported here, a plane mirror mounted to a piezo-stack (pzt) in one arm of the interferometer was used to step the phase. The pzt was calibrated in both Michelson and Mach-Zehnder

interferometers before employing the phase-stepper calibration procedure proposed by Cheng and Wyant¹¹⁶. By this procedure, five fringe patterns with four $\pi/2$ phase-shifts between each are recorded. With correct calibration of the pzt, the first and last interferograms are identical. Cheng and Wyant estimated $2\pi/120$ uncertainty in pzt calibration by this method, corresponding to a peak-valley phase error for the two-step algorithm of approximately the same magnitude^{103,116}.

Non-linear phase step: A non-linear phase-step error may be modelled as $\alpha' = \alpha(1 + \epsilon\alpha)$ and again produces a sinusoidal error at twice the spatial frequency of the fringe pattern¹¹⁵. Unlike phase errors due to a constant calibration error, those due to non-linearities in the phase-step cannot be eliminated with the appropriate selection of phase reduction algorithm. However, Schwider et al¹¹⁵ demonstrated that the error in phase will decrease as the number of steps increases. Having calibrated the pzt as described in the previous paragraph, non-linearity effects were reduced by manually measuring the fringe movement for $2\pi/3$ phase steps. No modification to the voltage applied to the pzt was required, and the pzt was assumed linear over the voltage range.

Non-linearity of detector: A non-linear response from a detector will introduce phase errors with a frequency of four times the fringe frequency¹¹⁷. These errors can be modelled by expanding the photoelectric voltage from the detector into a power series:

$$I' = I + \epsilon_2 I^2 + \epsilon_3 I^3 + \epsilon_4 I^4 + \dots$$

where I is the incident optical irradiance and I' the detected value. When I' is substituted into the phase reduction algorithm certain orders of detection error cancel and do not affect the phase measurement. The remaining non-linearities add and contribute to a phase error. Generally the greater the number of steps, the smaller the effect of detector non-linearities. CCD cameras were used for all phase-stepped work presented in the thesis, for which a linear characteristic can be assumed. Thus it was assumed that no error was introduced from this source.

Electronic noise of detector: The error in the phase measurement due to detector noise for the two-step algorithm can be found by modifying the analysis of Wyant⁹⁵. The two-step algorithm is written in the form:

$$\phi(m,n) = \tan^{-1} \frac{N}{D} \quad (3.24)$$

where $N=\sqrt{3(I_3-I_2)}$ and $D=2I_1-I_2-I_3$. The standard deviation of the noise in both N and D equals $\sqrt{6}\sigma_I$, where σ_I is the standard deviation of the intensity noise for a single measurement. The corresponding standard deviation in the phase noise $\sigma_\phi(m,n)$ in each pixel is given by:

$$\sigma_\phi(m,n) = \left[\left(\frac{D}{N^2 + D^2} \right)^2 + \left(\frac{N}{N^2 + D^2} \right)^2 \right]^{1/2} \sqrt{6} \sigma_I \quad (3.25)$$

If equation (3.16) is rewritten as $9I_M^2(m,n)=N^2+D^2$, then equation (3.25) becomes

$$\sigma_\phi(m,n) = \sqrt{\frac{2}{3}} \frac{\sigma_I}{I_M} \quad (3.26)$$

This implies that the modulation intensity has to be maximised and the intensity noise minimised to achieve low phase noise. The intensity noise standard deviation was estimated as 1.28 grey-levels, calculated from the specified CCD detector SNR of 46dB with 8-bit quantisation. The mean modulation intensity for the phase-stepped speckle pattern of Figure 3.1(a) is 15 grey-levels, giving a lower limit on the peak-valley phase noise of $2\pi/90$ radians.

Environmental disturbances: Air turbulence in the laboratory and mechanical vibrations produce unwanted changes in the optical path difference between the arms of the interferometer. This represents a random error in the phase-step which is dependent on the laboratory conditions at the time of the measurement. The size of the phase-step was checked from the digitised images, and is therefore subject to the same environmental disturbances. The error is therefore no larger than that due to miscalibration of the pzt i.e. $2\pi/120$ radians peak-valley. The

output power of the laser was assumed constant over the measurement period, and is not a source of intensity noise.

Assuming that the errors from the previous four sections can be summed, an approximate minimum peak-valley error of $2\pi/36$ is obtained, from which the rms error for a given phase measurement would be approximately $2\pi/100$. Speckle noise clearly degrades this further; for out-of-phase ESPI phase errors of $2\pi/15$ have been estimated for TPSSC¹¹⁰ and $2\pi/30$ for DiPSSI^{97,114}. Speckle noise is discussed below.

Error Sources in Phase-Stepped Speckle Interferometry: Assessing the accuracy attainable with phase-stepped ESPI is complicated because reliable data is not available at all pixels. Indeed, even the systematic phase errors discussed in the previous section for phase-stepped classical interferometry are not strictly systematic in ESPI: due to the random speckle intensity those errors become randomly distributed in the image plane. The problem will be discussed initially in general terms for DiPSSI: each pixel is treated as an individual interferometer, which has enabled theoretical considerations of the accuracy to be made for both in-plane and out-of-plane systems. The discussion is then extended to TPSSC.

From Section 3.2.1, the phase is calculated inaccurately at pixels that saturate in any of the three images. This provides a figure in the analysis for the maximum allowable intensity at any pixel. Also, the modulation amplitude at each pixel must be larger than a specified minimum. This minimum is defined by the phase accuracy required from the measurements by equation (3.26). From these two requirements a minimum acceptable speckle intensity can be evaluated. The fraction of acceptable measurement points can then be found by integrating the speckle pattern intensity probability density function (pdf) between these two limits. This calculation was performed¹¹⁸ for an out-of-plane sensitive interferometer with a smooth reference wavefront, where it was assumed that the speckle pattern was fully resolved. The fraction of acceptable measurement pixels

was derived as a function of the useful dynamic range of the detector only, which is related to the detector SNR and the required accuracy of phase measurement. As would be expected, for a specified SNR, the fraction of acceptable points was found to decrease as the allowable phase error was decreased. The question of accuracy is further complicated by decorrelation of the speckle pattern due to rigid body motion of the test surface⁹⁷. Surface translation causes the light scattered from a given point in the object to be incident on the viewing lens at a different angle so that the displaced pattern is not identical in form to the original pattern. Errors in the phase recorded at the image plane occur. They can be reduced by applying a filter to the unwrapped phase data: for example a 30x30 smoothing filter based on a first-order polynomial line fit has been reported⁷⁸.

In TPSSC, an intensity correlation is performed to generate fringes. Therefore, decorrelation of the speckle pattern due to rigid body motion results in reduced fringe visibility¹¹⁹. This will not introduce errors into the measured phase, although the reduced SNR will reduce the accuracy of phase measurements by equation (3.26). Thus if the analysis of likely errors was to follow DiPSSI, it would be necessary to estimate the number of acceptable points by integrating the fringe function pdf. The limits of integration would be minimum intensity, derived from the accuracy of phase measurements required, and the saturation intensity. As a starting point, the grey-level histogram for the speckle pattern of Figure 3.1(a) is shown in Figure 3.6. Goodman¹²⁰ derived an approximate expression for the intensity pdf for a spatially averaged depolarised speckle pattern as:

$$p(I) = \frac{1}{\Gamma(2M)} \left(\frac{2M}{\langle I \rangle} \right)^{2M} I^{2M-1} \exp\left(\frac{-2MI}{\langle I \rangle} \right) \quad (3.27)$$

where $\langle I \rangle$ is the mean intensity, M is the number of correlation cells (speckles) influencing each pixel, and $\Gamma(\)$ is the gamma function. For a fully resolved speckle pattern $M=1$. This is generally only achieved in ESPI systems with a pinhole aperture; more usually a larger aperture is required to collect sufficient light. For the speckle pattern of Figure 3.1(a) $\langle I \rangle = 140$ grey-levels. Equation (3.27) is plotted in Figure 3.6, which indicates that $M=15$ models the experimental system.

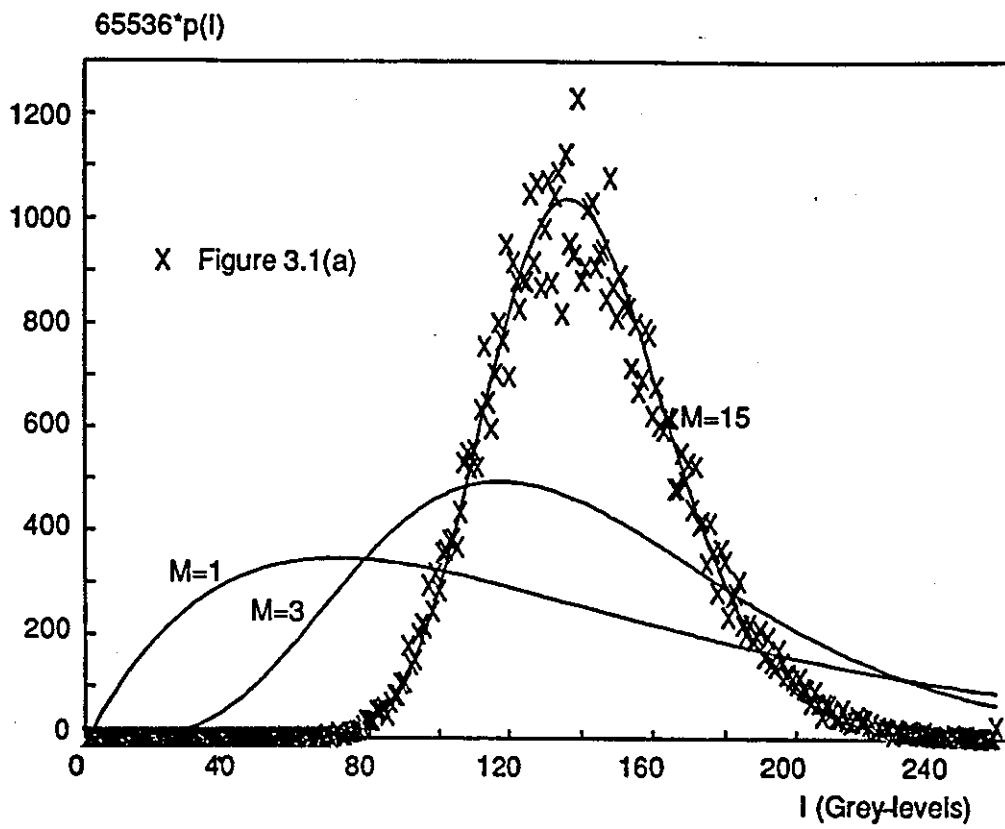


Figure 3.6 Speckle pattern intensity distribution

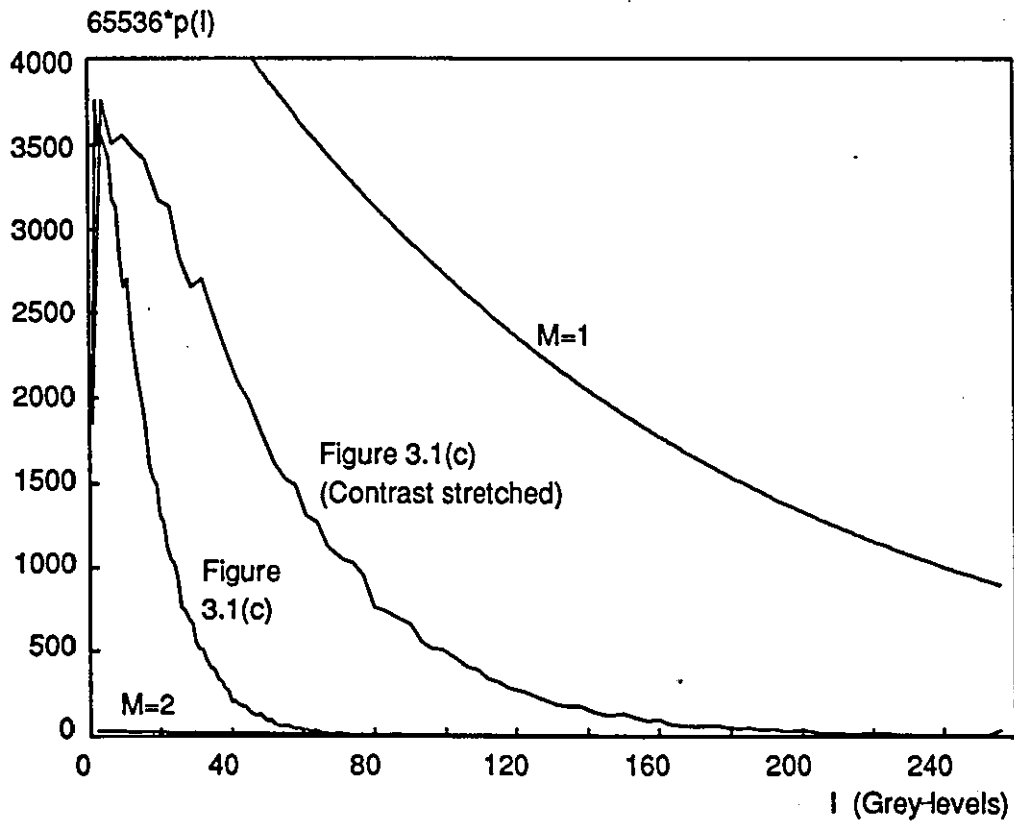


Figure 3.7 Fringe intensity distribution

Slettemoen¹²¹ calculated the pdf for ESPI fringes recorded with a speckle reference beam, in which the speckle pattern is fully resolved. In this case, the pdf for the cross-interference term is:

$$p(I) = \frac{1}{\Gamma(1/2)\sqrt{2}(\sqrt{\langle I_A \rangle \langle I_B \rangle})^{1/2}} \left| \frac{I}{\sqrt{\langle I_A \rangle \langle I_B \rangle}} \right|^{1/2} K_{1/2} \left(\frac{|I|}{\sqrt{\langle I_A \rangle \langle I_B \rangle}} \right) \quad (3.28)$$

Slettemoen assumed square law rectification to remove negative values: here equation (3.28) is doubled and $0 < I < 255$ to model full-wave rectification in the framestore. $K_{1/2}()$ is a modified Hankel function of order 1/2. $\langle I_A \rangle$ and $\langle I_B \rangle$ are the mean intensities when the two beams illuminate the surface independently. Equation (3.28) is plotted in Figure 3.7 for $\langle I_A \rangle = \langle I_B \rangle = \langle I \rangle / 2$, marked $M=1$. To establish a better fit to the experimental data, an approximate solution for the case of speckle averaging was attempted. Taking the characteristic function of equation (3.28) as derived by Slettemoen (equation 17)¹²¹ combined with the "box-car" approximation method used by Goodman¹²⁰, an approximate pdf for spatially averaged correlation fringes was calculated as:

$$p(I) = \frac{1}{\pi^{M/2} 2^{M-1}} \frac{\Gamma(1/2)}{\Gamma(M)} \left(\frac{1}{2} \frac{M}{\sqrt{\langle I_A \rangle \langle I_B \rangle}} \left| \frac{MI}{\sqrt{\langle I_A \rangle \langle I_B \rangle}} \right| \right)^{M-1/2} K_{M-1/2} \left(\frac{MI}{\sqrt{\langle I_A \rangle \langle I_B \rangle}} \right) \quad (3.29)$$

This is identical to equation (3.28) for $M=1$. Restricting M to integer values gives K of half integral order, in which case it can be expressed in terms of elementary functions. Equation (3.29) with $M=2$ is plotted in Figure 3.7, which is worse than equation (3.28). The analysis therefore falls short for want of an accurate pdf. Assuming that an adequate pdf could be found, the lowpass filter applied to reduce speckle noise would then need to be incorporated into the model. The theoretical analysis was stopped at this stage, and the experimental evaluation of accuracy of phase measurement presented in the next section was undertaken.

3.2.5 Experimental Investigation of Accuracy of Phase Measurement

In order to investigate the effects of preprocessing ESPI correlation fringes, and the resulting phase accuracy that may be expected, the horizontal in-plane sensitive interferometer of Figure 3.8 was constructed. Two 16cm diameter collimated beams were expanded from an argon-ion laser on to the object plane (xy-plane) with a 45° angle of incidence. The object studied was a flat 80mm x 80mm aluminium alloy plate, painted white, and mounted to a rotation stage. The central 60mm x 60mm region of the plate was viewed by a Phillips CCD camera, and real-time correlation fringes were produced by the framestore. Typical fringes obtained by rotating the plate in the xy-plane are shown in Figure 3.9(a). Sets of three phase-stepped interferograms were recorded for several angles of plate rotation in the range 4 to 23 seconds of arc (3 to 19 correlation fringes) in both clockwise and anticlockwise directions. A phase map could be calculated from each set of data. Each of these phase maps contained an rms error of approximately $2\pi/100$ radians, primarily due to small errors in the phase step (Section 3.2.4). Each data set was then used to investigate the effects of speckle noise reduction on the resulting phase map, with other sources of phase error reduced to their practically achievable limits. The procedure followed with each data set is described next.

Fourier filtering^{122,123} was the first smoothing technique applied to each set of phase-stepped interferograms. To do this, a digital Fast Fourier Transform (FFT) algorithm was applied to calculate the two-dimensional frequency spectrum of a digitised fringe pattern, Figure 3.9(a). The power spectrum, Figure 3.9(b) represents the absolute values of the transformed image compressed to 256 grey-levels plotted on logarithmic complex phase-frequency axes with the origin at the centre. In this instance, the central spot corresponds to the dc (zero frequency) term, with two adjacent lobes corresponding to the fringe spatial frequency and the higher spatial frequency speckle noise contained in the darker region around the outside. To reduce the speckle noise and leave the fringe function intact, a circular mask of sufficient radius to enclose the central diffraction spots of the

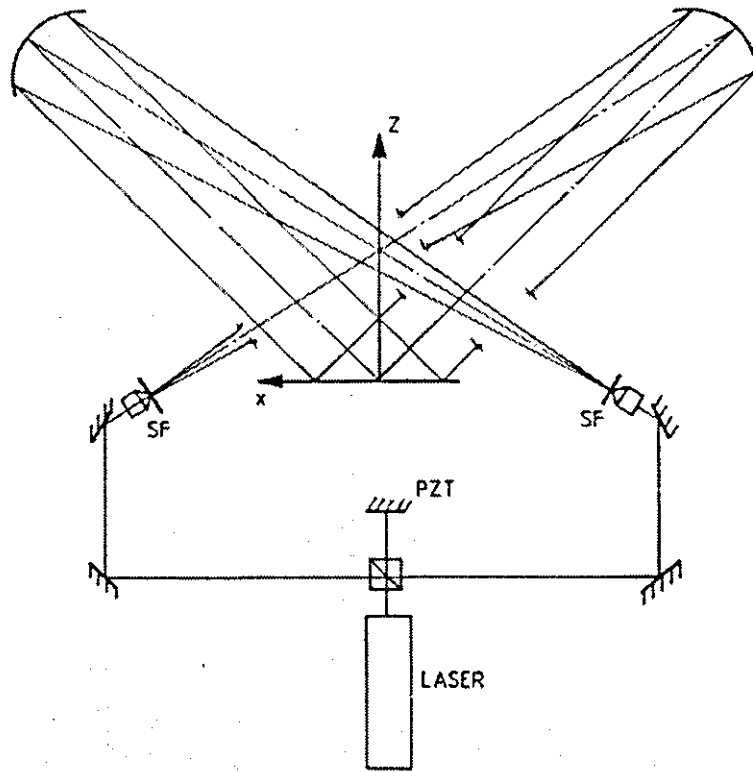


Figure 3.8 In-plane interferometer with phase-stepping mirror (PZT)

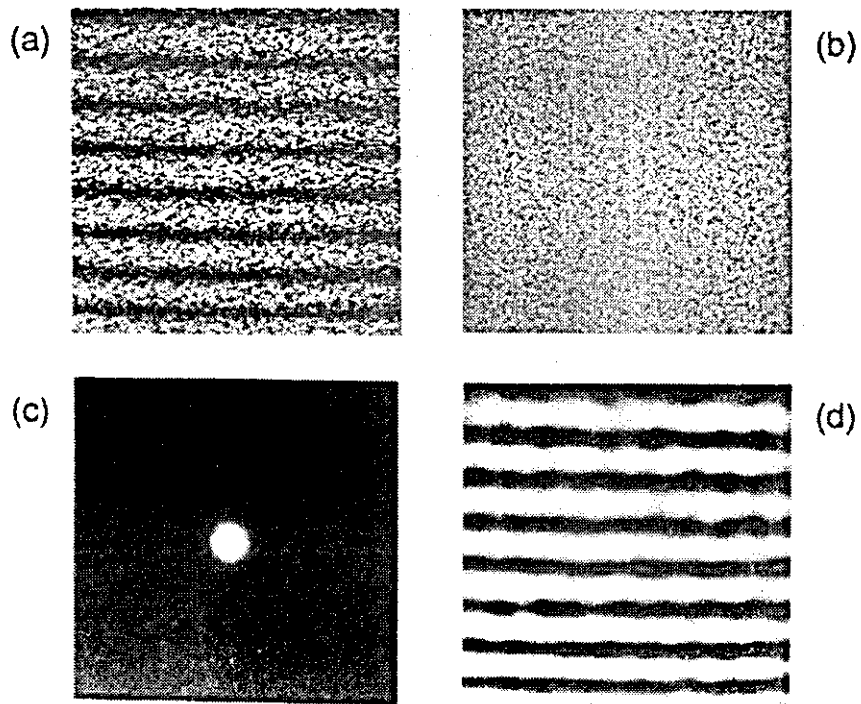
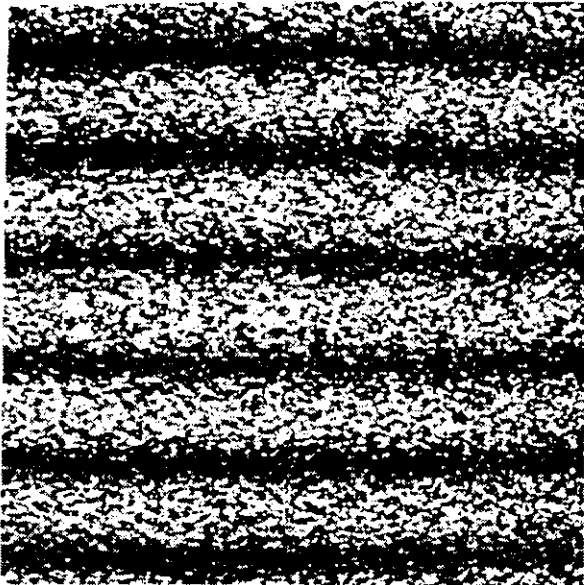


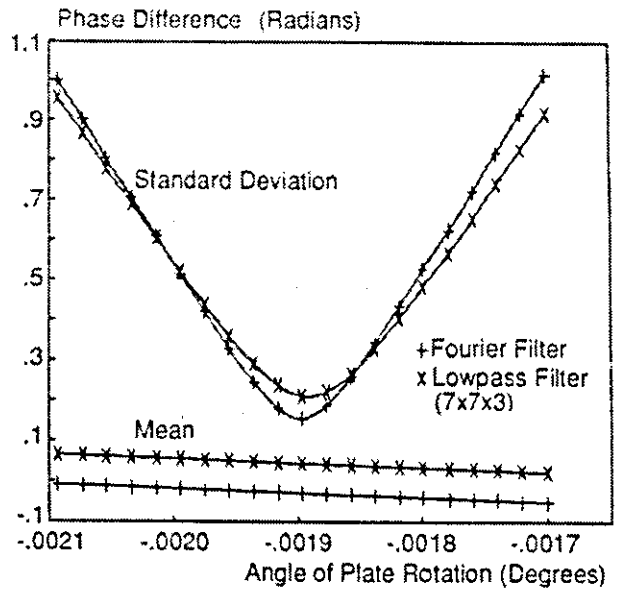
Figure 3.9 Stages in Fourier filtering

power spectrum was defined, Figure 3.9(c). This defines a frequency domain in the power spectrum that is transferred to the original transform as a weight factor for the masking procedure: grey-level 255 in the mask relates to a weight factor of 1, grey-level 0 to weight 0. The inverse FFT is then calculated to produce the filtered fringe pattern of Figure 3.9(d). Clearly the mask radius must increase with increasing fringe density i.e. increasing fringe spatial frequency. Ideally the mask should exclude the central diffraction spot since it does not contain fringe information. However, the circular mask was used because the dc component does not significantly reduce the fringe visibility for ESPI subtraction fringes, and its removal would require a hand drawn mask. Once the filter had been applied to each of the phase-stepped interferograms of a given data set the phase map was calculated.

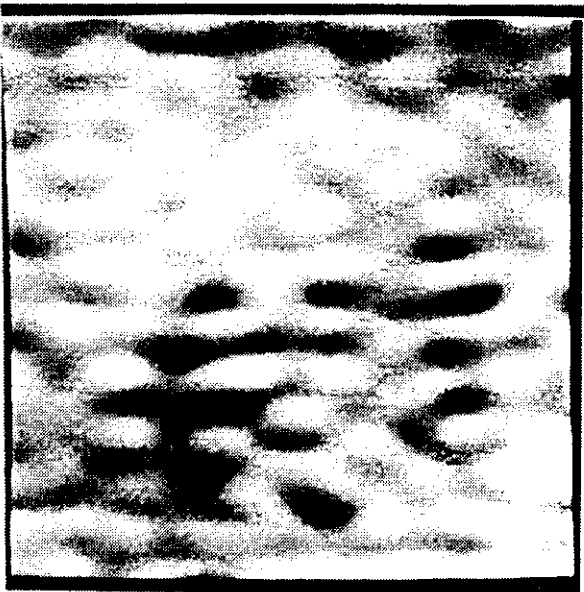
To assess the performance of the Fourier filter, the difference between the experimentally determined phase map and a theoretical wrapped phase value (calculated from the angle of plate rotation) was evaluated at each pixel. Wrapped phase values were compared to prevent dependence of this difference term on the unwrapping algorithm. Phase differences were restricted to the range $-\pi$ to $+\pi$ radians to accommodate phase discontinuities, and incorrectly modulating pixels marked by the phase reduction algorithm were given the maximum value of π radians. The magnitude of phase differences between the experimental data and theoretical model is dependent on the angle of plate rotation assumed. In order to exclude differences between data sets due to the uncertainty in the angle of plate rotation, this angle was chosen such that the standard deviation of the phase difference term was minimised. To illustrate this process, an original data set with 5.9 correlation fringes is shown in Figure 3.10(a). The corresponding variations in the standard deviation of the phase difference as the assumed angle of plate rotation is varied are shown in Figure 3.10(b). Notice that the mean phase difference varies slowly, since the centre of rotation was not exactly at the centre of the image. In each case, the angle of rotation of the plate at which the minimum value of standard deviation in phase difference occurred, when using a Fourier filter, was assumed for the subsequent analysis. Comparison with three



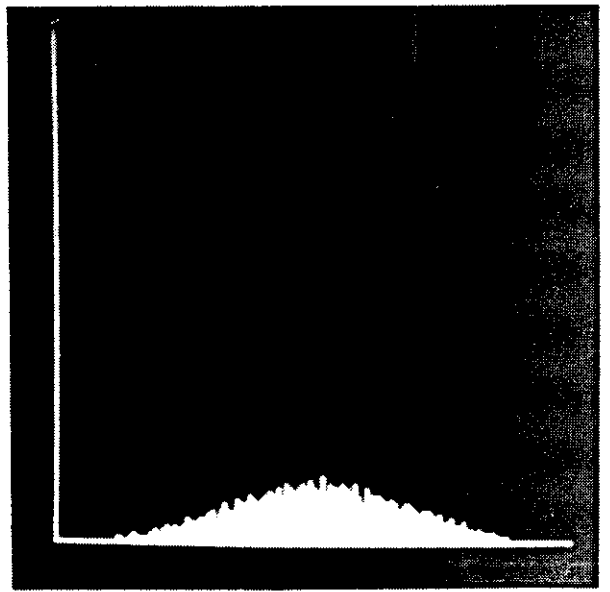
(a)



(b)



(c)



(d)

Figure 3.10 Determination of angle of plate rotation

iterations of a 7x7 pixel neighbourhood average filter demonstrates that this angle is valid for the spatial domain filters tested later in this section. The associated difference map between theoretical and experimental values for the data set is shown in Figure 3.10(c), where the maximum error (π radians) is denoted by a grey-level of 255 and the minimum error ($-\pi$ radians) by 0. A piezo calibration error is indicated by the sinusoidal structure in the difference map, at twice the correlation fringe frequency. However, modifications in the sinusoidal structure are evident due to low spatial frequency components of the original fringe pattern that are passed by the Fourier filter and ringing introduced by the ideal cut-off of the circular mask. Thus the difference map represents the combined uncertainty in measured phase due to systematic errors and remaining speckle noise in the processed correlation fringes, with sources of random error reduced to a practical minimum. Due to the Gaussian distribution of these differences, Figure 3.10(d), the error of phase measurement under experimental conditions may be expressed as $\pm 3\sigma$, where σ is the standard deviation of the error distribution.

Fourier filtering is slow due to its high computational content (e.g. the time required by the Kontron for three 256x256 images is approximately 70 seconds) and is considerably slower on many PC-based image processing packages. With dedicated hardware, PC-based FFTs can be calculated extremely quickly (e.g. the ITEX-VIPA image processing accelerator board should filter three images in approximately 22 seconds, once software bugs have been removed). Even then, the user must select a suitable mask. Therefore, situations arise where it is faster, cheaper or simply more convenient to apply spatial domain convolution filters to reduce speckle noise in the ESPI fringes. Suitable lowpass filters are standard on all general image processing packages, and three of the most common were investigated.

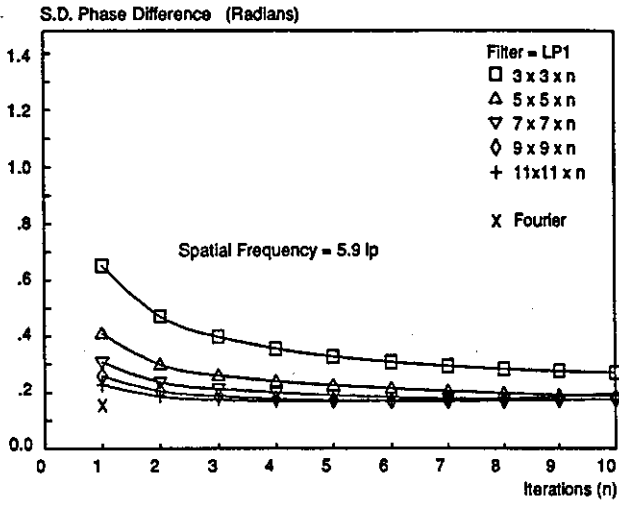
The first two investigated were standard neighbourhood average filters in which the resulting grey-level of the central pixel is the weighted sum of the grey-levels of its neighbourhood points, with the weights being the coefficients of the filter matrix (kernel). To preserve a central pixel, only odd filter matrix sizes were

considered, although this is not necessary for the Kontron implementation. Also, to maintain generality, only square filter matrices have been considered: a 25(horizontal) x 1(vertical) filter will out-perform the 5x5 filter matrix for the horizontal fringes of this test, but is not generally the case. If the one-dimensional size of the filter matrix is denoted by W, then the kernels for the two filters tested, when W=5, were:

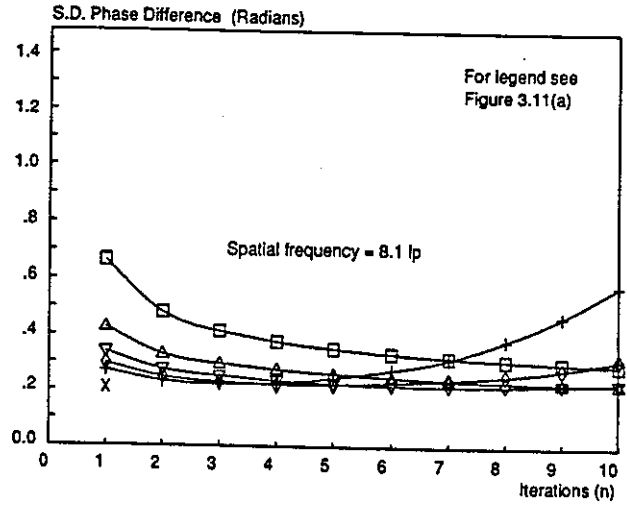
$$LP1 = \begin{pmatrix} 1 & 1 & 1 & 1 & 1 \\ 1 & 1 & 1 & 1 & 1 \\ 1 & 1 & 1 & 1 & 1 \\ 1 & 1 & 1 & 1 & 1 \\ 1 & 1 & 1 & 1 & 1 \end{pmatrix}, \quad LP2 = \begin{pmatrix} 0 & 0 & 1 & 0 & 0 \\ 0 & 1 & 1 & 1 & 0 \\ 1 & 1 & 1 & 1 & 1 \\ 0 & 1 & 1 & 1 & 0 \\ 0 & 0 & 1 & 0 & 0 \end{pmatrix}$$

The lowpass neighbourhood average filters LP1 and LP2 blur the image due to the averaging process, giving uncertainties in the spatial location of the phase fringe discontinuities. These uncertainties are revealed at intermediate phase values as the grey-level "mottling" discussed in Section 3.2.1. The third spatial domain filter investigated was a median filter, in which the resulting grey-level of the central pixel is the median grey-level of those in the filter matrix. This operates as a lowpass filter without blurring the image. Square filter matrices were again defined, whose one-dimensional size must be odd to obtain a central value.

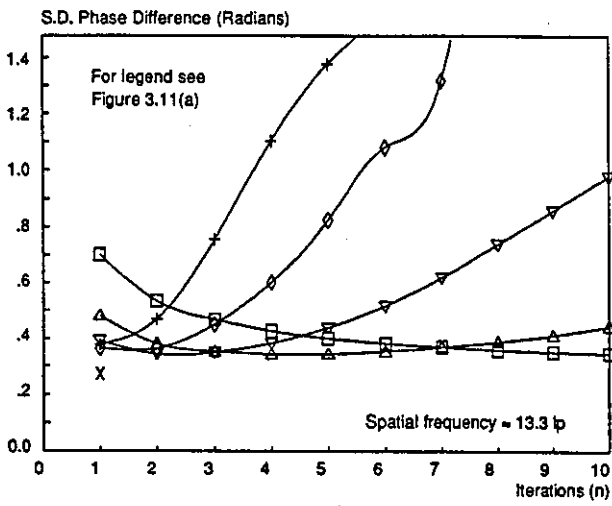
Figure 3.11(a)-(d) shows the result of applying the digital neighbourhood average filter, LP1, for a range of fringe densities. The fringe density is quoted as the number of fringes in the vertical direction. This is equivalent to the number of line pairs (lp) i.e. a spatial frequency. Therefore, Figure 3.11(a), at a spatial frequency of 5.9 lp, corresponds to Figure 3.10. Again, the difference between the experimentally determined phase map and a theoretical wrapped phase value calculated from the angle of rotation of the plate was calculated at each pixel. For reference, the result for the Fourier filter with circular mask is marked in each case. If a filter of one-dimensional size W is applied n times, the effective size of the matrix increases to $(W-1)n + 1$, and the cut-off frequency is reduced. For subsequent analysis the following relationship was assumed:



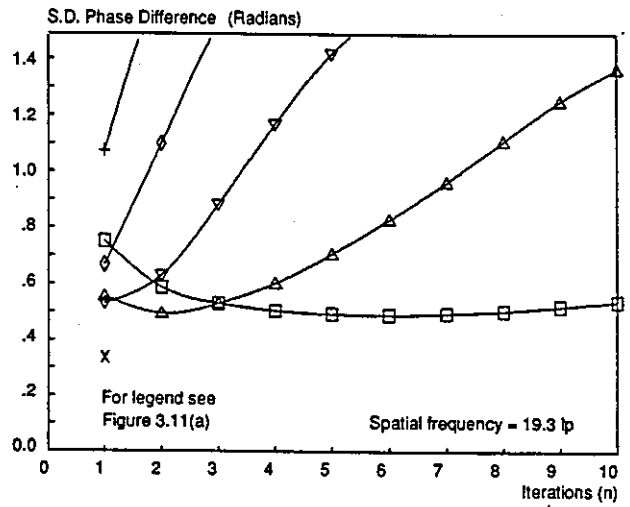
(a)



(b)



(c)



(d)

Figure 3.11 Standard deviation of phase difference against number of iterations of filter LP1

$$\text{Cut-off frequency} = \frac{256}{((W-1)n + 1)} \quad (\text{Line pairs}) \quad (3.30)$$

Therefore at low spatial frequencies, Figure 3.11(a), increasing the number of iterations of the filter reduces the cut-off frequency and hence reduces speckle noise more effectively. However, at higher fringe frequencies, Figure 3.11(b)-(d), this cut-off frequency overlaps that of the correlation fringes resulting in reduced fringe visibility. Consequently the phase error increases once the cut-off frequency is reduced below that of the fringe function. The optimum number of iterations for a given filter at a given spatial frequency occurs when the standard deviation of the phase difference has its lowest value. These values have been collated in Table 3.1. Also shown in the table are the maximum number of iterations of a filter of a given size that can be applied before the cut-off frequency as calculated from equation (3.30) is equal to, or less than, the fringe spatial frequency. Reasonable agreement between the theoretical and experimental columns indicates that Figure 3.11(a)-(d) have the correct form. The standard deviation of phase difference can then be used to quote the accuracy of phase measurement with some confidence.

The full range of spatial frequencies tested is indicated in Figure 3.12, where 20 lp represents the approximate limit for automatic analysis by the TPSSC technique for the system. Unwrapping errors frequently occurred at fringe densities higher than this, due to excessive reduction of the SNR in the filtered image; operator intervention is then required to locate and correct sources of error. From Figure 3.12, the general trend is for errors in the measured phase to increase as the fringe spatial frequency increases. This is because the overlap in spatial frequencies between the fringe function and the speckle noise increases, and more speckle noise remains in the filtered fringes. For the Fourier filter, and assuming that at least two correlation fringes are present, an rms phase error of $2\pi/42$ radians is obtained. Therefore phase values can be quoted with a minimum uncertainty of $\pm 2\pi/14$ or $\pm 0.03\mu\text{m}$. The rms error increases at approximately $2\pi/570$ radians/lp. Measurements for the 7×7 neighbourhood average filter LP1 are

Spatial Frqcy (lp)	Iterations, n, of LP1									
	Experimental (- = ≥ 10)					Theory (- = > 10)				
	3x3	5x5	7x7	9x9	11x11	3x3	5x5	7x7	9x9	11x11
3.5	-	-	-	-	-	-	-	-	8	7
5.9	-	-	-	6	5	-	-	7	5	4
8.1	-	-	7	4	3	-	7	5	3	3
8.3	-	9	6	3	2	-	7	4	3	2
13.3	-	4	2	2	1	9	4	3	2	1
13.9	-	4	2	1	1	8	4	2	2	1
15.5	9	3	2	1	1	7	3	2	1	1
19.3	6	2	1	1	1	6	3	2	1	1

Table 3.1 Optimal number of iterations of LP1 against fringe spatial frequency

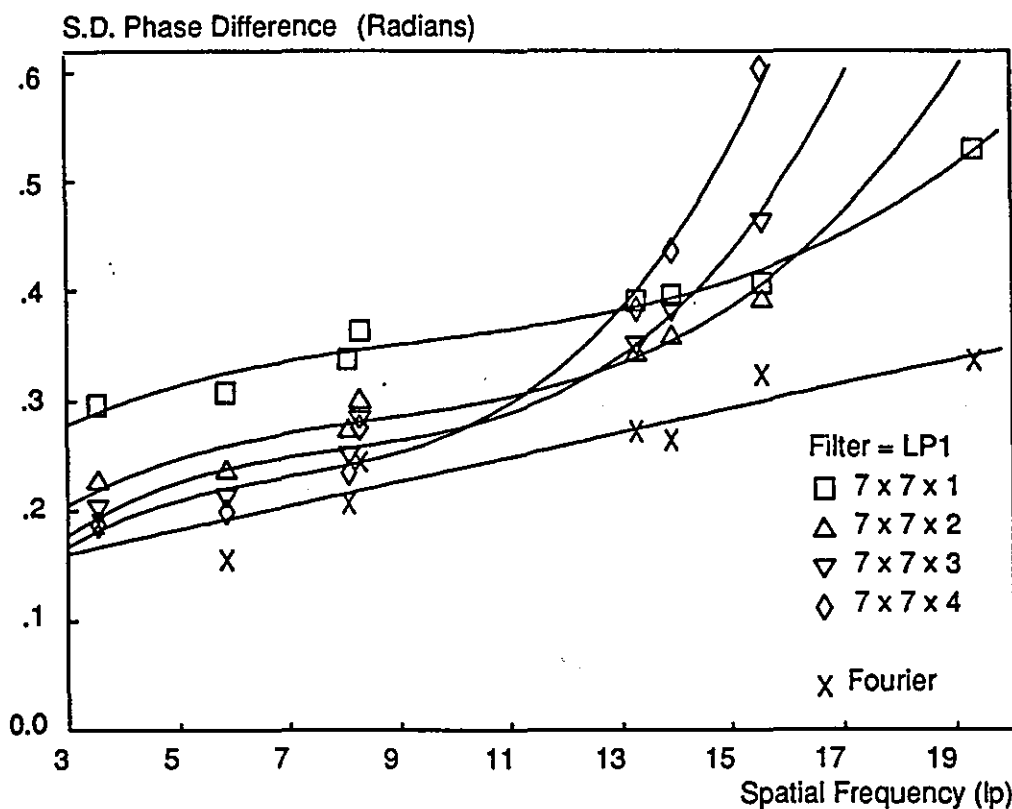


Figure 3.12 Standard deviation of phase difference against fringe spatial frequency

included on the same graph. At low spatial frequencies, a well chosen spatial domain filter can match the performance of the appropriate Fourier filter. Clearly the cut-off frequency of the neighbourhood average filter remains constant, and as the spatial frequency increases the performance deteriorates. Even with the selection of a more suitable mask for LP1, Figures 3.10(c) and 3.10(d) indicate that a Fourier filter most effectively reduces speckle noise at higher spatial frequencies. The superior performance of the Fourier filter is explained by its global rather than local operation. LP1 was found to be the most successful spatial domain filter, giving lower phase noise for the same number of iterations at most spatial frequencies. Therefore results for LP2 and the median filter have not been presented. One interesting point is that a large number of iterations of the median filter at higher spatial frequencies does not rapidly increase the phase error, as found for LP1: statistical properties of the filter prevent degradation of the SNR below a certain level, at which point the phase difference remains constant with increasing iterations. However, more than simply comparing filters, this analysis has enabled an estimation of the noise present in the in-plane TPSSC phase data to be made.

3.3 SURFACE STRAIN MEASUREMENT

When load is applied to a solid object, three-dimensional displacement occurs throughout its volume. For opaque objects, an optical method such as ESPI can only give information about displacements at the surface. The surface strain, or in-plane strain components, can be determined if the three-dimensional displacement vector and surface normal are known at each measurement point. Results in this thesis are presented for plane objects loaded in the xy plane. Therefore out-of-plane motion is small with respect to the in-plane motion. Also the plane objects were viewed along the surface normal, z axis. Therefore in-plane interferometers can be arranged with sensitivity vectors parallel to the x and y axes. The normal in-plane strain components parallel to the x and y axes, ϵ_{xx} and ϵ_{yy} , and the shear strain, γ_{xy} , are given by¹²⁴:

$$\epsilon_{xx} = \frac{\partial u}{\partial x} ; \quad \epsilon_{yy} = \frac{\partial v}{\partial y} ; \quad \gamma_{xy} = \frac{\partial u}{\partial y} + \frac{\partial v}{\partial x} \quad (3.31)$$

The calculation of strain requires the first spatial derivatives with respect to the x and y axes of the local in-plane displacement to be determined. This can be carried out by a least-squares polynomial fit to the displacement data. The method used is described in Section 3.3.1. An experimental investigation of accuracy is described in Section 3.3.2.

3.3.1 Methodology

To determine the first spatial derivative of displacement, a linear least-squares fit of a plane surface to the phase values in the neighbourhood of each pixel was used. This gives the derivatives with respect to x and y simultaneously. The procedure requires each pixel to be considered the centre of a p x p pixel square, where p is an odd integer. If $\phi(m,n)$ is the measured phase at each pixel, and $\phi_i(m,n)$ the value given by the fitted plane surface, then a linear least-squares fit is given by minimising the expression:

$$S = \sum_{i=1}^{p^2} (\phi - \phi_i)^2 \quad (3.32)$$

where the summation is performed over the p x p pixel neighbourhood. Substituting in the expression for a plane yields the following expression to be minimised:

$$S = \sum_{i=1}^{p^2} (a_1 x_i + a_2 y_i + a_0 - \phi_i)^2 \quad (3.33)$$

The gradients parallel to the x and y axes are a_1 and a_2 respectively, and a_0 is the offset at the centre of the pixel neighbourhood. Equation (3.33) is minimised by solving simultaneously the three equations given by:

$$\frac{\partial S}{\partial a_0} = 0 ; \quad \frac{\partial S}{\partial a_1} = 0 ; \quad \frac{\partial S}{\partial a_2} = 0 \quad (3.34)$$

This gives:

$$\sum_{i=1}^{p^2} \phi_i = p^2 a_0 + a_1 \sum_{i=1}^{p^2} x_i + a_2 \sum_{i=1}^{p^2} y_i$$

$$\sum_{i=1}^{p^2} x_i \phi_i = a_0 \sum_{i=1}^{p^2} x_i + a_1 \sum_{i=1}^{p^2} x_i^2 + a_2 \sum_{i=1}^{p^2} x_i y_i \quad (3.35)$$

$$\sum_{i=1}^{p^2} y_i \phi_i = a_0 \sum_{i=1}^{p^2} y_i + a_1 \sum_{i=1}^{p^2} x_i y_i + a_2 \sum_{i=1}^{p^2} y_i^2$$

Assuming each pixel to lie at the centre of a local (m,n) coordinate system, then $\Sigma x_i = \Sigma y_i = \Sigma x_i y_i = 0$. This simplifies the calculation and makes it faster to implement, but valid phase values must be present at all points in the $p \times p$ pixel neighbourhood. Equations (3.35) then reduce to:

$$\sum_{i=1}^{p^2} \phi_i = p^2 a_0$$

$$\sum_{i=1}^{p^2} x_i \phi_i = a_1 \sum_{i=1}^{p^2} x_i^2 \quad (3.36)$$

$$\sum_{i=1}^{p^2} y_i \phi_i = a_2 \sum_{i=1}^{p^2} y_i^2$$

The values a_1 and a_2 are estimates of the first derivative of phase with respect to the x and y coordinate axes at each location (m,n), expressed in radians/pixel. Multiplication by a calibration factor relating radians to displacement (the fringe function) and the length of the object given by one pixel gives the surface strain.

Routines were written on the MicroVax to implement equations (3.36) for unwrapped phase data. These routines are described in Appendix C; a brief outline follows. Strain is calculated at each point in a window specified by the user. Pixels positioned at the window edge will not be surrounded by a $p \times p$ pixel neighbourhood of valid phase values and equations (3.36) cannot be applied. Consequently the window size is reduced by $(p-1)/2$ pixels at all edges. In the initial implementations, a least-squares fit of phase data to a line was performed, rather than to a plane. Greater rejection of noise present in the phase data is achieved with the plane fit because more data points are sampled, Section 3.3.2. The least-squares fit of a plane, rather than a line was suggested by Vrooman and Maas⁷⁸. Vrooman and Maas also note that calculating a_0 may be used to smooth the phase data. They use this method to reduce decorrelation phase errors in all their reported experimental work, and subsequently calculate strain from the smoothed data. This technique could be applied to TPSSC to remove phase mottling, but does not represent the fundamental accuracy of TPSSC. Therefore it was not employed. An example of phase smoothing by equation (3.36) is shown in Section 5.2.2.

Differentiating the unwrapped phase data amplifies any noise present, because it acts as a filter whose gain is proportional to spatial frequency. It was seen in Section 3.2.5 that the greatest source of noise in ESPI phase data is due to speckle, and that the pre-processing filter in TPSSC is most important in reducing this noise. Also, the influence of random speckle noise can be decreased by increasing the size of the $p \times p$ pixel neighbourhood for the plane fit. For example, Brownell¹²⁵ demonstrated that errors in calculated strain due to eight-bit quantisation of computer generated cosine fringes could be reduced to less than 1% when more than five pixels were used in a least-squares line fit. It would seem likely that more than five pixels will be required to reduce speckle noise to acceptable levels. However, because no study of in-plane strain measurement with TPSSC had been undertaken, data was not available on the relationship between the number of pixels in the least-squares fit and the pre-processing filter, and the resulting accuracy in measured strain. Therefore the experimental study of Section

3.3.2 was undertaken. Before starting this section, some general observations about strain measurement from displacement data, and with ESPI in particular, are made.

Strain was calculated by fitting a first order (plane) surface to the unwrapped phase data. Displacement profiles of order two or more will be subject to a systematic error. Increasing the number of pixels in the surface fit reduces speckle noise but increases systematic errors for displacement profiles of order two or more. Therefore the neighbourhood of pixels chosen for strain calculations should be as small as possible, but sufficiently large to reduce random speckle noise to an acceptable level. The size of this systematic error may be estimated for a given displacement profile when the number of pixels used in the least-squares line fit has been chosen, for example Section 5.2.6. These systematic errors could be reduced by fitting a surface of higher order to the displacement data, but would considerably increase the computation time.

The limit for regular success with the simple unwrapping algorithm was found to be approximately 20 correlation fringes, Section 3.2.5. With a 60mm object viewed, this corresponds to a dynamic range of approximately 120μ strains. This dynamic range increases in proportion to the magnification for techniques such as moire interferometry which have a long correlation length: the same number of fringes may be recorded, but the gauge length (the length on the specimen surface over which the strain is calculated) is reduced in proportion to the magnification. The theoretical limit is determined by the resolution limit of the imaging system. The range of strain measurements with ESPI also increases with increased magnification, but at a rate slower than in proportion to the magnification. When the object moves in its plane, the speckle pattern in the image plane moves in the opposite direction in proportion to the magnification, M , of the viewing system. Jones and Wykes (equation (F.20))⁷¹ calculated that the speckle pattern becomes decorrelated for a general object displacement, d , of:

$$d = \frac{(NA)\lambda}{M} \quad (3.37)$$

where NA is the numerical aperture i.e. the ratio between the viewing lens focal length and aperture. Equation (3.37) shows that the maximum displacement that can be measured decreases with increasing magnification. By the same argument, the rigid body translation required to decorrelate the speckle pattern also decreases, which explains why fringes at high magnification have poor visibility. Consequently, dynamic range does not increase in proportion to M. The exact relationship will depend on the rigid body motion suffered by the test object.

The accuracy of measurements in techniques which produce high quality fringes may be increased by averaging over several fringes i.e. a gauge length of N fringes improves accuracy by a factor of N. Much lower fringe frequencies are generally obtained with ESPI, and a gauge length of several fringes would therefore cover a large proportion of the image. At low fringe spatial frequencies it is likely that not even one complete fringe would be included. Thus the basic gauge length must be chosen to reduce speckle noise to an acceptable level irrespective of the maximum fringe spatial frequency present in the image. An approximate gauge length may be calculated as follows. For a fringe pattern with three correlation fringes, the phase noise is approximately $\pm 2\pi/14$ radians. Taking a gauge length of 25 pixels ($=25 \times 60\text{mm}/256$) gives an uncertainty in measured strain of $\pm 8.8\mu\text{strains}$. (The experimental figure obtained from a plane fit is $\pm 6.5\mu\text{strains}$, Section 3.3.2). The accuracy of measured strain is also affected by the optical magnification, although this effect is not discussed until later: in Section 4.3.2 it is demonstrated that the accuracy of measured strain is independent of magnification over the limited magnification range used in this thesis; a mechanism for this behaviour is discussed in Section 6.1.

Finally for this section, the effects of rigid body motion on the measured strain distribution will be discussed. In general testing, rigid body motion consists of translation and rotation of the loaded test surface, and is difficult to eliminate experimentally. Rigid body translation introduces a constant, but not necessarily integer, fringe shift over the specimen. Thus zero-displacement points may not be denoted by fringe minima. A static point may be known from the specimen

constraints, or an arbitrary point may be chosen. If unwrapped phase values are referenced to this point, it automatically becomes a point on the zero order fringe. Thus rigid body translation may be ignored, provided that it is not so large as to decorrelate the speckle pattern and that a suitable point for phase-unwrapping can be chosen. Rigid body rotations introduce a constant gradient fringe field, dependent on the angle of rotation, and a fractional fringe shift that depends on the centre of rotation. By the preceding discussion, a fractional fringe shift may be ignored, and so the centre of rotation can be assumed to lie in the field of view. Assuming polar coordinates (r, θ) with origin at this centre of rotation, the displacement due to a clockwise rotation through a small angle α is given by:

$$\begin{aligned} u &= r(\cos\alpha - 1)\cos\theta - \sin\alpha \sin\theta \approx -r\sin\alpha \sin\theta \\ v &= r(\cos\alpha - 1)\sin\theta + \sin\alpha \cos\theta \approx r\sin\alpha \cos\theta \end{aligned} \quad (3.38)$$

Thus rigid body motion appears as a horizontal fringe pattern for u measurements, Figure 3.10(a), and a vertical fringe pattern for v measurements. These displacements add to those due to surface strain alone, and distort the fringe pattern. An example of this is seen in Figure 5.2(c) and the accompanying discussion. In general, the strain distribution calculated from the measured displacement will therefore include a contribution from the rigid body translation. These contributions are given by:

$$\begin{aligned} \epsilon_{xx} &= \frac{\partial u}{\partial x} = \cos\theta \frac{\partial u}{\partial r} - \frac{\sin\theta}{r} \frac{\partial u}{\partial \theta} = 0 \\ \epsilon_{yy} &= \frac{\partial v}{\partial y} = \sin\theta \frac{\partial v}{\partial r} + \frac{\cos\theta}{r} \frac{\partial v}{\partial \theta} = 0 \\ \gamma_{xy} &= \frac{\partial u}{\partial y} + \frac{\partial v}{\partial x} = \sin\theta \frac{\partial u}{\partial r} + \frac{\cos\theta}{r} \frac{\partial u}{\partial \theta} + \cos\theta \frac{\partial v}{\partial r} - \frac{\sin\theta}{r} \frac{\partial v}{\partial \theta} \\ &= -\sin\alpha + \sin\alpha = 0 \end{aligned} \quad (3.39)$$

Thus the rigid body motion does not affect the normal or shear strain distribution,

but is measured as a "pseudo-strain" in the two components of shear strain.

3.3.2 Accuracy of Strain Measurement

To assess the accuracy of strain measurement, the data sets from Section 3.2.5 (Accuracy of Displacement Measurement) were used once again. These were recorded with a horizontal in-plane sensitive interferometer for various angles of rotation of a metal plate. $\partial u/\partial y$ was evaluated for each of the data sets. Ideally this value should be constant for all points in the image, and equal to $-\sin\alpha$ from equation (3.39). The difference between the measured and theoretical values at each pixel represents the uncertainty in strain measurement due to speckle noise. The difference value also includes systematic errors reduced to their practically achievable limits for the system tested. These differences are linearly related to the phase differences, which were shown in Figure 3.10(d) to be distributed with a Gaussian profile. Thus the strain error will also be distributed with a Gaussian profile, and the error of strain measurement may be expressed as $\pm 3\sigma$, where σ is the standard distribution of the error distribution. To exclude uncertainties in measuring the angle of plate rotation, the angle determined experimentally for each data set in Section 3.2.5 was used.

Results for the Fourier filter are shown in Figure 3.13 for a sample data set. Increased noise rejection with number of pixels included in the least-squares fit can be seen. This test was originally performed for a least-squares *line* fit to the unwrapped phase data, and is denoted by the solid line. The later implementation, with a least-squares *plane* fit to the data is indicated by the dotted line: the x-axis corresponds to the side length of the square neighbourhood. Greater noise rejection is achieved. The typical trend for spatial domain convolution filters is also shown in Figure 3.13, in this instance for a 7×7 neighbourhood average filter. Initially the difference term is reduced with more iterations ($n=1,2$) of the filter, as speckle noise is more effectively suppressed. As n is increased further, the SNR of the fringes is reduced and the difference term increases ($n=3,4$). The variation

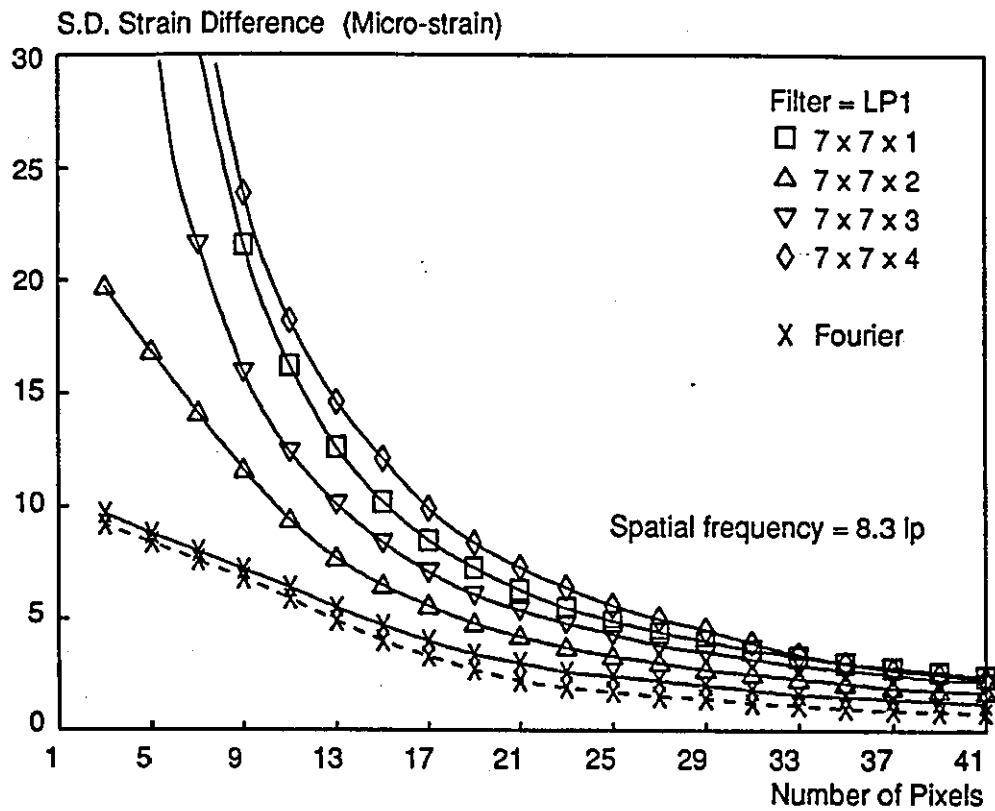


Figure 3.13 Standard deviation of strain difference against number of pixels in least-squares fit

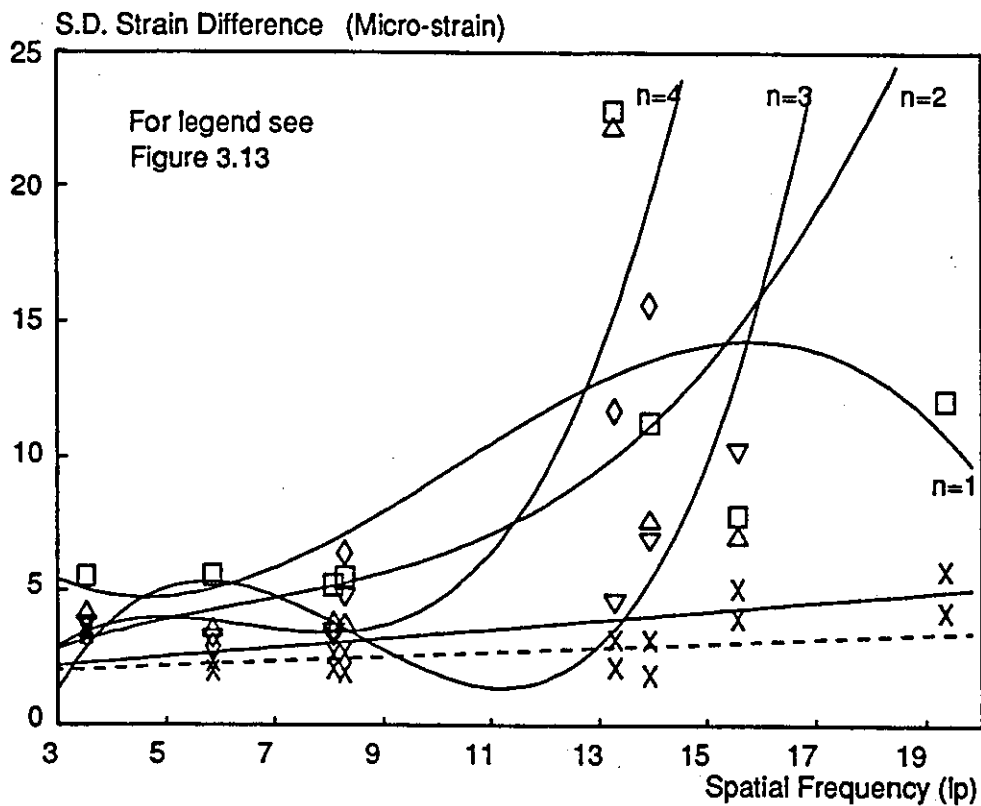


Figure 3.14 Standard deviation of strain difference against fringe spatial frequency

in strain difference against spatial frequency is shown in Figure 3.14 for these four spatial domain filters. Twenty five pixels were used in the least-squares fit. The general trend is for an increase in strain difference as the spatial frequency increases, rising rapidly once the cut-off frequency of the filter is smaller than the fringe spatial frequency. The 7x7x1 and 7x7x2 filters exhibit peaks at a spatial frequency of approximately 13 lp, inconsistent with the gradually increasing strain difference. The probable cause is a failure in the unwrapping routine for this data set with these two filters. The Fourier filtered results show the same general increase in error with spatial frequency. No rapid rise occurs at higher spatial frequencies in this instance, because the cut-off frequency of the Fourier filter is matched to the individual data sets. At higher frequencies the Fourier filter gave superior results to LP1, LP2 and the median filter. Once again, LP1 was found to be the most successful spatial domain filter. Results are presented in Figure 3.14 for the Fourier filter with least-squares line (solid line) and plane (dotted line) fits. For the latter case, and assuming a minimum of two correlation fringes, the minimum rms error is $1.9\mu\text{strains}$, which may be quoted as $\pm 5.7\mu\text{strains}$. The rms error rises at the rate of approximately $0.08\mu\text{strains/lp}$. Shear strain values require the combination of two strain measurements, and will therefore be subject to an error increased by the factor $\sqrt{2}$.

3.4 CLOSURE

Methods to automate displacement and strain analysis by extracting the optical phase difference encoded in in-plane ESPI correlation fringes have been discussed, and the TPSSC method was implemented. The primary drawback of this solution is the need to pre-process the fringes to reduce high spatial frequency speckle noise. Contributions from saturated and incorrectly modulating pixels are filtered back into the image. Furthermore, fringe SNR may be significantly reduced by the filter in some regions if the fringe visibility is not uniform across the image. However, the ability to work with correlation fringes produced by an external framestore, the reduction in the number of images required, and

reduction in the time required for data acquisition and phase calculation compared to DiPSSI make the technique attractive. Two new algorithms were devised for ESPI correlation fringes. Both eliminate the need for a preprocessing filter to be applied to the intensity fringes. Both require a correct solution to be chosen from the values calculated at each pixel: for subtraction this is one of four values, and for addition one of two values. The algorithm for subtraction was demonstrated on fringes computer generated with full-wave rectification to remove negative values. The algorithm will also work when negative values from subtraction have been removed by squaring. The solution offers improved accuracy compared to TPSSC, and should yield results of the same order of accuracy as DiPSSI. The addition fringe phase-stepping algorithm has enabled phase extraction from addition fringes for the first time. In this case, there is no exact solution to determine the background intensity, and a locally measured value was substituted into the solution. For both techniques, the correct phase value was chosen from a comparison phase map that was calculated by the usual TPSSC method. This selection procedure cannot be used for addition fringes recorded with the twin-pulsed system, and is not ideal for subtraction fringes. Alternative procedures need to be investigated, but the comparison phase map technique was acceptable to demonstrate the methods.

Errors in displacement and strain measurements were quantified for the TPSSC implementation. The measurements included systematic errors reduced to their practically achievable limits for the experimental system, and random noise due to speckle frequencies remaining in the phase data. The figures thus obtained were taken together to represent typical experimental displacement and strain errors for the system. The disadvantage of experimental error assessment is that it is specific to the system used. It also requires certain factors to remain constant in subsequent tests: for example the fringe visibility and speckle contrast for the data sets were 0.5 and 0.9 respectively. Fringe visibility was calculated by $(I_{\max} - I_{\min}) / (I_{\max} + I_{\min})$ where I_{\max} and I_{\min} are the mean grey-level along correlation fringe maxima and minima respectively. Speckle contrast was defined by Goodman¹²⁰ as the standard deviation of speckle intensity divided by the mean intensity, and is

a measure of the fringe SNR. Errors in calculated phase and strain increase with decreasing fringe SNR. Consequently substantial deviation in the fringe visibility would require the analysis to be repeated.

Fourier filtering was found to be the most successful filter for suppressing speckle noise in the phase and strain data. Minimum errors of $\pm 2\pi/14$ radians and $\pm 6\mu\text{strains}$ respectively were determined. These values increase as the fringe spatial frequency increases i.e. increasing overlap with the frequencies associated with speckle noise. Nakadate et al¹¹⁰ estimated a phase error of $2\pi/15$ radians for out-of-plane ESPI measurements by the TPSSC method, which possibly justifies applying the experimental values determined in this chapter to other in-plane systems. Currently, no corresponding error figure is available for in-plane phase and strain measurement with TPSSC. Typically the errors in phase measurement with DiPSSI are quoted as $2\pi/30$ radians. Vrooman and Maas⁷⁸ quote a repeatability in strain measurement with DiPSSI of $0.3\mu\text{strains rms}$. Strain is calculated from phase data smoothed by calculating a_0 from equation (3.36) over a 30×30 pixel window. Without this smoothing, a reasonable estimate of strain error is possibly $\pm 3\mu\text{strains}$, although this cannot be confirmed from the literature.

Examples of in-plane phase-stepped ESPI were given in Figures 3.1 and 3.2. No examples of strain measurements were given, although the methodology was described. The first strain measurement results appear in the next chapter, Figure 4.15.

4. SIMULTANEOUS MEASUREMENT OF PERPENDICULAR IN-PLANE DISPLACEMENT COMPONENTS

Two in-plane ESPI illumination geometries are required to measure the two-dimensional displacement and strain maps for a plane object viewed along its surface normal. For static loading conditions it is acceptable to record these two interferograms sequentially. However, for time-dependent strain fields, both illumination geometries must be used simultaneously so that identical strain conditions exist for both. A new interferometer devised to measure two in-plane interferograms at the same time is described in this chapter. The method of operation is described in Section 4.1, and an experimental verification given in Section 4.2. Section 4.3 describes the interferometer with in-plane phase-stepping incorporated. Finally, preliminary results of work to extend the interferometer to three-dimensional sensitivity are described in Section 4.4.

4.1 INTRODUCTION

An example of vectorially combining the data from two in-plane phase maps was given in Figure 3.2. ESPI has also been used to measure three-dimensional steady-state vibrations¹²⁶ and static displacements⁷⁶: three separate interferograms with different sensitivity vectors were recorded and vectorially combined. In all three examples sequential recording of the displacement maps was adequate, because conditions during each recording were identical. Clearly this would not be the case for transient or non-repeatable events, which require simultaneous recording of displacements along the sensitivity vectors. This also applies to in-plane displacement field measurement with ESPI, which requires two in-plane interferograms to be recorded simultaneously so that identical strain conditions exist for both.

This chapter describes a technique that has been devised to record, simultaneously, two full-field in-plane interferograms. Observation of the displacement fields is truly simultaneous, unlike previous work where the displacement information from sequential measurements is combined¹²⁷. Because two interferograms are recorded, the full-field nature of ESPI measurements is maintained, unlike a three beam speckle pattern interferometer¹²⁸ used to measure in-plane strain. In this system, part of the test surface was illuminated by collimated laser beams I_A and I_B , Figure 4.1, whilst an adjacent region was simultaneously illuminated by beams I_A and I_C . (I_D was not used in this arrangement). Surface deformation produced two sets of fringe patterns corresponding to the two differently illuminated areas. The complete surface strain tensor could be calculated from the composite interferogram, but only along the line of intersection of the two fringe patterns. In addition to the loss of full-field resolution, the composite interferogram is difficult for the user to interpret.

Figure 4.1 shows schematically an illumination configuration for in-plane sensitive ESPI with two orthogonal sensitivity vectors. The axes of collimated beams I_A and I_B lie in the xz plane and are incident on the flat test surface at equal angles θ to the x axis. (This is the complimentary angle to that marked θ in Figure 2.4 and used throughout the thesis, but is used in Figures 4.1 and 4.2 only). The lens L forms a speckled image of the test surface along the z axis (the surface normal) in the plane of the camera faceplate CF , which is parallel to the xy plane. This image is processed electronically to form correlation fringes. If the illuminating beams are rotated to the positions I_C , I_D in the yz plane, the interferometer is sensitive to displacements parallel to the y axis only. An interferometer containing both beam pairs I_A, I_B and I_C, I_D would allow two interferograms to be recorded, from which the two-dimensional in-plane displacement field can be calculated. However, unless the speckle fields produced by the two beam pairs can be distinguished, the interferometer will be restricted to sequential recording of the two interferograms. (This is analogous to the system described by Jones¹²⁷). Also, to minimise the analysis required when combining the data obtained from each illumination direction, the corresponding interferograms should both relate, pixel

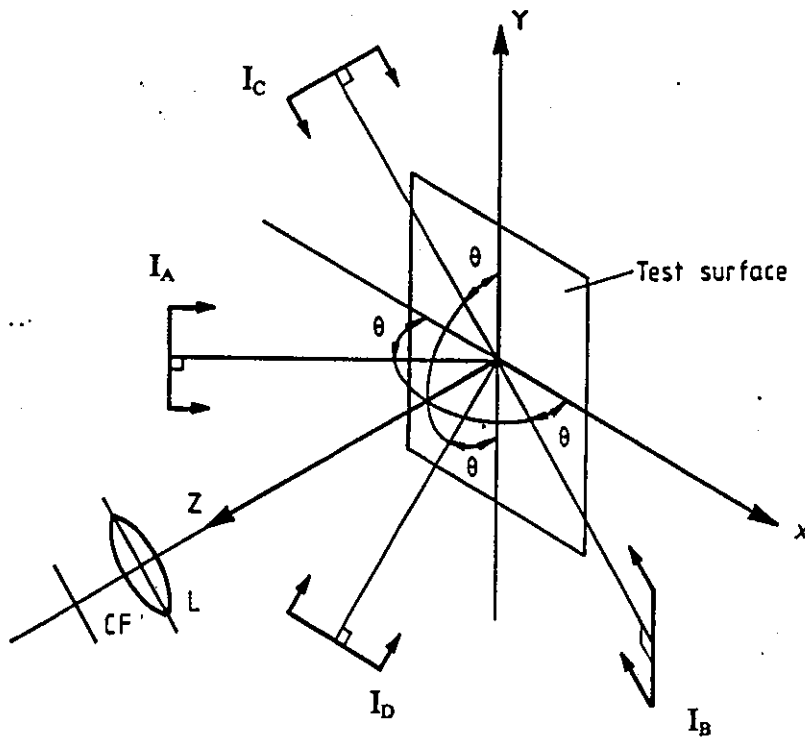


Figure 4.1 Arrangement for in-plane ESPI with orthogonal sensitivity vectors

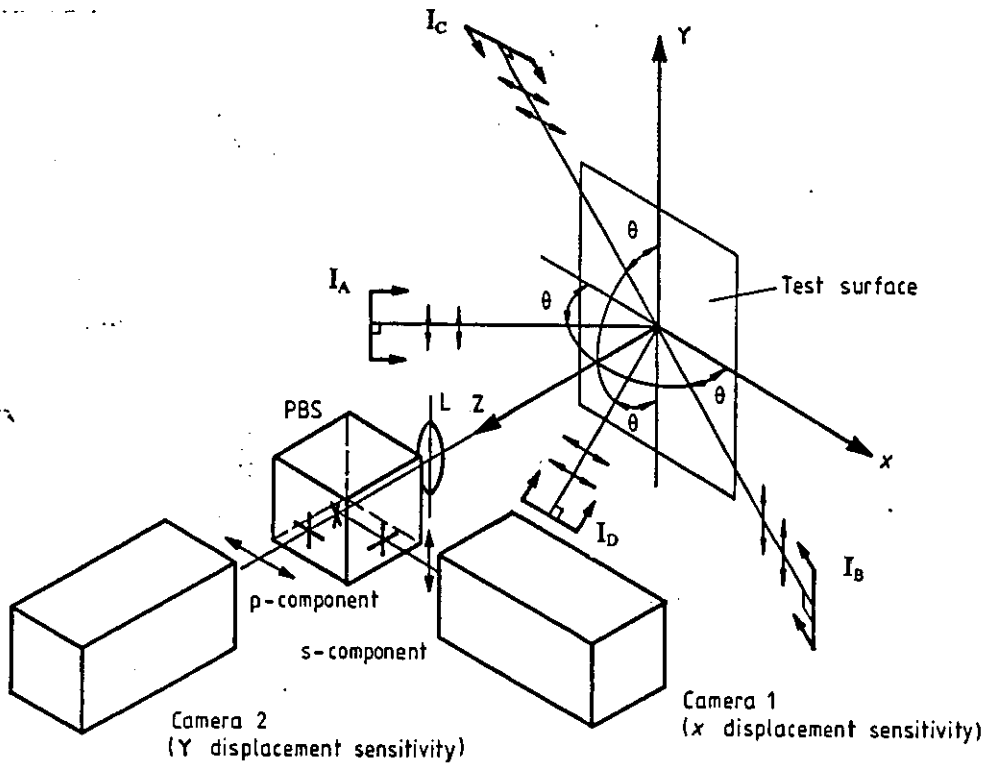


Figure 4.2 Arrangement for interferometer distinguishing horizontal and vertical in-plane interferograms by polarisation vector

by pixel, to the same points of the test object surface. Hence the interferometer must have a single viewing lens to eliminate perspective differences between the interferograms. Clearly then, the speckle fields associated with each beam pair must be independent from one another and optically distinguishable, to enable the interferograms to be separated beyond the imaging lens.

One solution would be to illuminate with wavelengths λ_1 for the I_A and I_B illumination directions and λ_2 for I_C and I_D . The speckle field associated with both sensitivity vectors is then characterised by a particular wavelength. Interference between the speckle fields is not possible and they may be separately imaged on to two TV cameras with a dichroic beamsplitting cube. An alternative arrangement using narrow-bandpass filters can be constructed, but the system would be somewhat optically inefficient. More importantly, the two interferograms could not be compared directly since the fringe pattern is a function of wavelength and therefore two different sensitivities would arise. For these reasons this solution was not pursued.

If a single wavelength illumination is to be used for both beam pairs, the two mutually coherent speckle fields scattered from the object surface will not interfere if they are linearly polarised with orthogonal polarisation states. A polarising beam splitting cube may then be used to separate the speckle fields to two separate TV cameras, provided that the eigenaxes of the beamsplitter correspond to the polarisation state of the speckle fields. Such a system is shown schematically in Figure 4.2. The collimated laser beams I_A to I_D are incident on the test surface with the same geometry as for Figure 4.1. I_A and I_B are both linearly polarised perpendicular to the plane of incidence, as suggested by the arrows in the figure. This azimuth corresponds to one eigenaxis of the polarising beamsplitter (PBS), and the image formed by the lens (L) is reflected to camera 1. I_C and I_D are linearly polarised with orthogonal azimuths to I_A and I_B and hence parallel with the other eigenaxis of the beamsplitter. An image of the test surface illuminated by I_C and I_D is formed at camera 2. The speckle fields associated with each illumination beam pair are therefore separated. The correlation fringes

produced from camera 1 correspond to displacements parallel to the x axis whilst camera 2 is sensitive to displacements parallel to the y axis.

Clearly the success of the technique is dependent on the polarisation state of the two speckle fields. The beamsplitter will reflect a linear polarisation state of azimuth 0° and transmit one of 90° . However, intermediate polarisation states are both partially transmitted and reflected, with a splitting ratio determined by the polarisation state. If, for example, the speckle field produced by I_A and I_B is depolarised, changes in the phase of speckles in both images will be produced by a displacement in the x direction (i.e. fringes corresponding to displacements parallel to the x axis will be produced by camera 2). The nature of the specimen surface contributes to the depolarisation of the scattered wavefront, and so it must be considered.

White matt paint is frequently used as a surface preparation for ESPI, to produce a uniformly scattering surface and good fringe contrast. Incident light is able to penetrate such a surface, and is multiply scattered. Consequently, the speckle pattern produced by illuminating the surface with a plane-polarised beam (I_A for example) will be depolarised. The interferogram produced by the combination of I_A and I_B is also depolarised¹²⁹. On the other hand, for a singly scattering surface such as lightly abraded metal¹²⁹ or silver spray-paint¹³⁰, the speckle pattern formed by I_A will be reflected with a retained polarised component. When I_A and I_B are polarised in the same plane, the interferogram produced by the coherent combination of the two speckle fields remains plane polarised. The suitability of abraded metal and silver spray-painted surfaces for this technique is investigated in the next section.

The technique described has analogies with laser-Doppler velocimetry (LDV), in which two laser beams are generally required to measure each velocity component. Wavelength¹³¹ and polarisation¹³² discrimination techniques have been established to separate the signals from a measurement volume illuminated simultaneously with two beam pairs, enabling simultaneous measurement of two

orthogonal velocity components.

4.2 DEMONSTRATION OF TECHNIQUE

At the end of the previous section, a distinction was drawn between single and multiply scattering surfaces and their effect on the polarisation state of scattered radiation. The results obtained in Section 4.2.1 show that the two singly scattering surfaces already mentioned (silver spray-paint and lightly abraded metal) do not completely depolarise the scattered wavefront, and may therefore be used with the interferometer. However, the degree of depolarisation of the scattered radiation from a single scattering surface is dependent on factors including the state of polarisation of the illumination beams, the illumination angle and the surface roughness. The resulting fringe visibility is also an important consideration. Thus the qualitative comparison of two surfaces for a certain illumination configuration is a simplification of the general problem, but is useful in demonstrating the successful operation of the interferometer. Initial results are presented in Section 4.2.2.

4.2.1 Investigation of Surface Preparation

In order to compare the performance of the silver spray-painted and abraded surfaces, the interferometer of Figure 4.2 was constructed. The x and y axes were taken to represent the horizontal and vertical directions respectively. Thus beams I_A and I_B gave horizontal in-plane sensitivity, and I_C and I_D gave vertical in-plane sensitivity. I_A was expanded from a 5mW HeNe laser directly on to the measurement region and also on to a plane mirror placed perpendicular to the specimen surface. I_B was formed from light of I_A reflected by the mirror on to the measurement region. I_A , and therefore I_B , were linearly polarised perpendicular to their plane of incidence. I_C was expanded from a second 5mW HeNe laser onto the measurement region. In a similar manner to I_B , I_D was derived as a portion

of I_C reflected from a second plane mirror placed adjacent to the specimen surface. I_C and I_D were orthogonally polarised to I_A and I_B (i.e. also polarised perpendicular to their plane of incidence). I_A and I_C were inclined at 45° to the surface normal (z axis). A narrow-bandwidth (633nm) polarising beamsplitter cube was used in the interferometer. Insertion losses for such a cube are minimal and deviation from 0° and 90° for the p- and s-components respectively is small. A CCD camera recorded horizontal in-plane displacements (camera 1 in Figure 4.2) and a vidicon tube camera recorded the vertical in-plane displacements. Due to the large physical dimensions of the vidicon camera, the CCD camera had to be turned on its side to position it sufficiently close to the beamsplitter to form an image. For this reason the reflected and rotated image from the CCD camera was not matched pixel-for-pixel with the digitised image from the vidicon camera. A single camera with polarising stripes laid across the faceplate could be used, with a corresponding loss in system resolution. However, a second camera is not a large part of component costs.

The object studied was an aluminium plate 18cm x 12cm x 0.6cm, placed 74 cm from the lens (L). Small regions of the plate were prepared with different surface finishes. Of the two surfaces of interest here, the first was a cross-hatched abraded surface. Abrasions were made with wire-wool. To ensure an even surface marking over a 50mm x 45mm area, the surface was divided with masking tape into adjacent strips, 15mm wide. Initially the surface was abraded heavily in the horizontal direction. The cross-hatch effect was produced by making twelve light scorings (for each 15mm strip) in the vertical direction. The number of vertical passes with the wire wool was based on fringe contrast obtained with the interferometer. The surface roughness varied with direction. For horizontal traverses of the surface $R_a=0.87\mu\text{m}$, and in the vertical direction $R_a=1.24\mu\text{m}$ (where R_a is the arithmetic mean of departures of the roughness profile from the mean line). The second test surface (50mm x 45mm) was sprayed with silver spray-paint, containing aluminium particles with sizes in the range 15-30 μm .

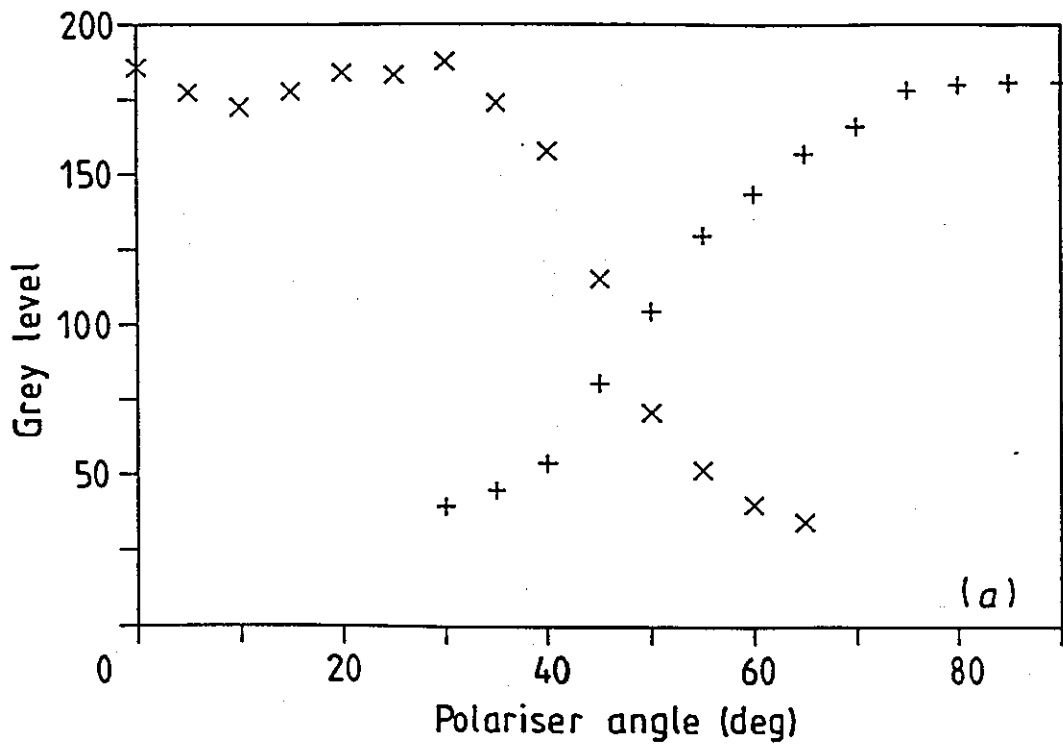
To study the depolarising effect of the two surfaces, a repeatable fringe pattern

was required, with a similar number of fringes in both the horizontal and vertical directions. This was achieved by clamping the plate rigidly to a stand along its right hand edge, and hanging a 200g weight from the bottom left-hand corner. The deflection of the stand rotated the plate anticlockwise by approximately 0.2 minutes of arc, giving uniform fringe patterns for both vertical in-plane illumination, Figure 4.4(a) and horizontal in-plane illumination, Figure 4.4(b), with similar fringe spacing.

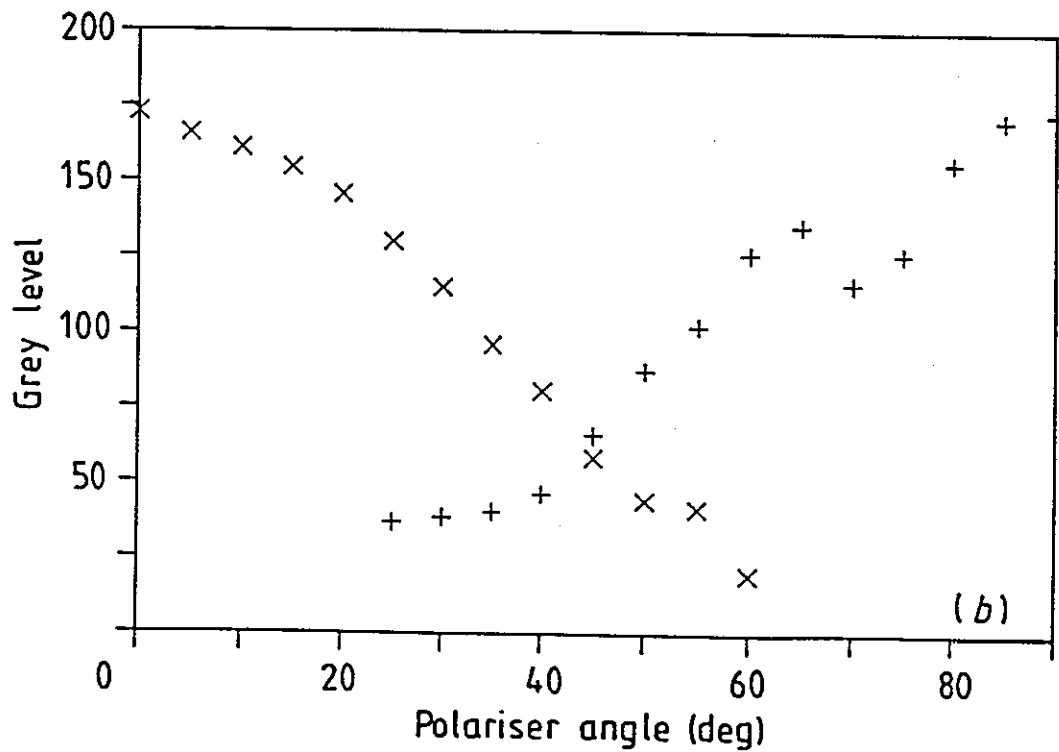
The abraded surface was illuminated with the horizontal in-plane illumination only (beams I_A and I_B). A polariser was placed in front of the imaging lens, and set to 0° (transmitting vertically polarised light). The horizontal fringe pattern produced on loading the plate was recorded. The polariser was rotated through 5° and when the plate had been reloaded to produce a second fringe pattern, a further recording was made. The process was repeated with the polariser eventually rotated through to 90° (transmitting horizontally polarised light) in 5° increments. Recording stopped when no fringes were visible. Each recorded fringe pattern was analysed down 256 vertical columns (i.e. perpendicular to the fringes) to find the maximum grey-level for each column. The average of these 256 values for each fringe field was plotted against polariser angle, Figure 4.3(a).

The test was repeated for the abraded surface with vertical in-plane illumination only. As the fringe field in this case contained vertical fringes, each recorded pattern was analysed along 256 horizontal rows, again to find the maximum grey-level in each row. The average of these values for each fringe pattern was plotted against polariser angle, (Figure 4.3(a)). However, due to the lower photometric sensitivity of the vidicon camera, each value has been multiplied by a scale factor needed to equalise the grey-level at 90° polariser angle to that obtained with the horizontal in-plane illumination at 0° polariser angle.

Repeating the test with the silver spray-painted surface produced the graph of Figure 4.3(b). As expected, neither surface completely depolarised the speckle field. (A completely depolarised wavefront would produce constant fringe



(a) Abraded surface



(b) Silver spray-painted surface

Figure 4.3 Variation in fringe brightness with polariser angle

brightness at any polariser angle). However, the abraded surface showed no reduction in fringe brightness for 30° of polariser rotation with the horizontal in-plane illumination only, and 15° with the vertical in-plane illumination. In contrast, the fringe brightness was reduced immediately (and symmetrically) for the silver spray-painted surface, suggesting that the wavefront scattered from the painted surface is less depolarised than that from the abraded surface. The greater depolarisation of the horizontal in-plane speckle field for the abraded surfaces was attributed to the difference in abrasion characteristics between the horizontal and vertical scratches that comprised the cross-hatched surface. Therefore the spray-painted surface would be preferred from depolarising considerations, though fringe brightness is reduced by 8% with respect to the abraded surface. In some tests, the fringe brightness for the abraded surface was reduced by as much as 30% with respect to a matt white surface. The silver spray-paint is also easier to apply and modifies the specimen surface properties less than the abraded surface.

The difficulties of using a depolarising surface with the technique have been discussed. However, with a slightly depolarising surface such as the abraded surface it can be concluded that the interferometer will work, but that there will be some cross-talk between the horizontal and vertical measurement channels. This is compounded by a reduction in the extinction ratio of the polarising beamsplitter when splitting a converging beam. The extinction ratio measured with a vertically polarised collimated beam of diameter 7mm was 300:1. Focusing this collimated beam through the beamsplitter resulted in an extinction ratio of 220:1. However, in the practical system, it was found that interference between the measurement channels was insufficient to produce spurious modulation of the fringe pattern. Cross-talk was therefore not quantified at this stage.

4.2.2 Experimental Demonstration

The interferometer described in the previous section was used to demonstrate the technique in practice, although obviously without the polariser in front of the lens.

The horizontal in-plane image must be reflected in the vertical axis to obtain the correct view. Figure 4.4 shows the effect of using a depolarising surface finish (white matt paint) with the system. The test specimen is again the clamped plate loaded at one corner. The fringes are obtained over a 57mm x 39mm area at the centre of the plate. Figures 4.4(a) and 4.4(b) show results from the interferometer for vertical in-plane illumination only and horizontal in-plane illumination only respectively. Due to depolarisation of the scattered wavefronts from the specimen surface, the polarisation selective beamsplitter was unable to separate the speckle patterns. Therefore both cameras produced the same fringe pattern, and results are shown for one camera only. With simultaneous horizontal and vertical in-plane illumination, the combined interferograms were seen by both cameras, Figure 4.4(c). However, with the cross-hatched abraded or silver spray-painted surfaces, it was possible to separate the interferograms to different cameras. Typical results for a 19mm x 21mm region of the cross-hatched abraded surface of Figure 4.3(a) are shown in Figure 4.5. Two columns are used to represent the simultaneous views from the vertical and horizontal in-plane cameras. With vertical in-plane illumination only and an aperture setting of $f/8$, Figure 4.5(a), good vertical sensitivity fringes were seen with the vertical in-plane camera. Due to the well polarised nature of the backscattered radiation, insufficient light was reflected by the cube to produce an image with the horizontal in-plane camera. When the aperture was opened to its widest setting ($f/3.5$), whilst maintaining the vertical in-plane illumination only, Figure 4.5(b), the increased amount of light entering the system caused the vertical in-plane camera to be saturated. However, it was then possible to obtain faint vertical in-plane sensitivity fringes with the horizontal in-plane camera. Hence some evidence of the cross-talk between channels is seen, but the intensity is too low to be recorded at the working aperture. Returning to the working aperture ($f/8$) and illuminating with horizontal in-plane illumination only, clear fringes were seen with the horizontal camera, but insufficient light was transmitted by the cube to produce an image with the vertical in-plane camera, Figure 4.5(c). Finally, when the specimen was illuminated with both beam pairs simultaneously, Figure 4.5(d), the interferograms were separately imaged to the two cameras. As seen from Figures 4.5(a) and 4.5(c) the components of vertical

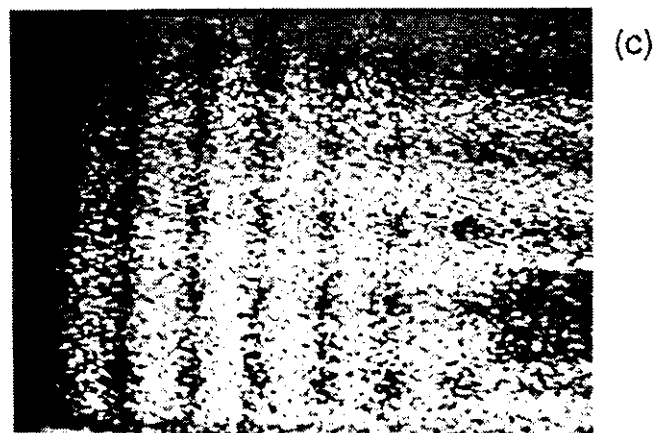
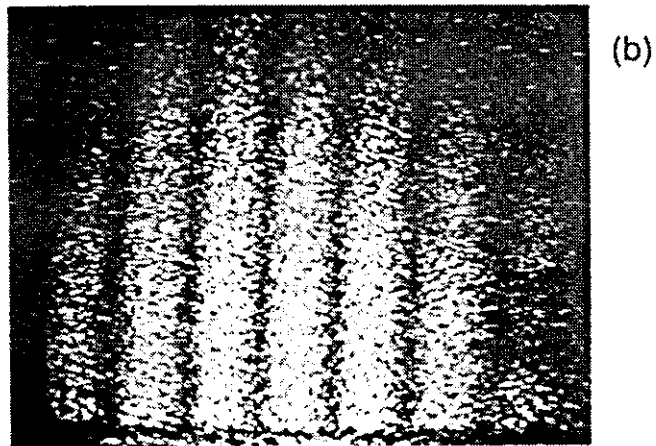
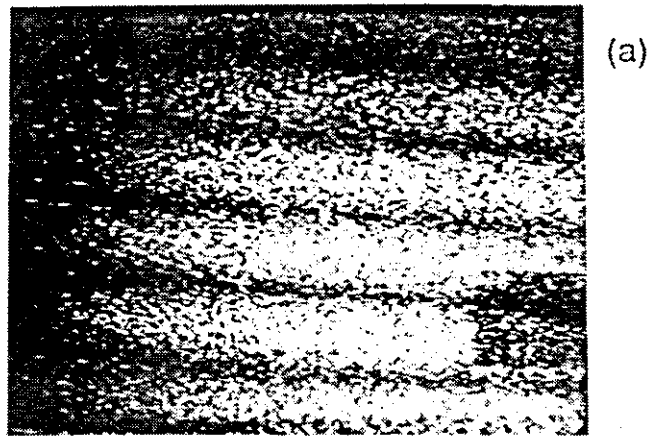
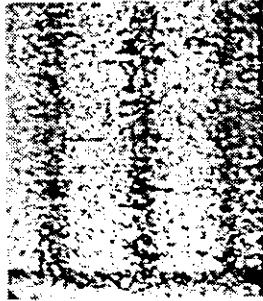


Figure 4.4 Interferometer results for a depolarising surface

Vertical in-plane camera

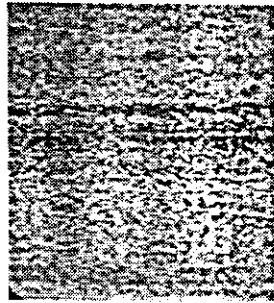


Horizontal in-plane camera

(a)

Light intensity too low to produce image

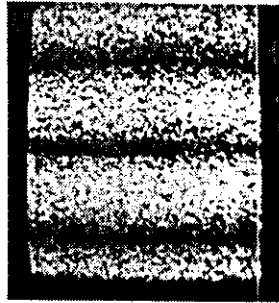
(b)



Camera saturated due to large aperture

(c)

Light intensity too low to produce image



(d)

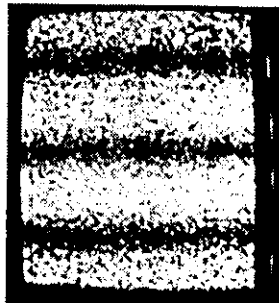
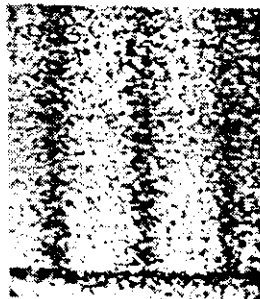


Figure 4.5 Interferometer results for a cross-hatch abraded surface

in-plane illumination radiation reaching the horizontal camera, and horizontal illumination reaching the vertical camera, do not contribute to the fringe patterns at the working aperture.

4.3 COMBINATION WITH PHASE-STEPPING

The phase-stepping technique was introduced to the dual sensitivity interferometer in a system used for all subsequent work presented in this thesis. The dedicated interferometer with matching CCD detectors is described in Section 4.3.1. Factors affecting the accuracy of automated displacement evaluation with the new system are investigated in Section 4.3.2. Results obtained from a simple test object are presented in Section 4.3.3.

4.3.1 Experimental System

The interferometer of Figure 4.6 was constructed to demonstrate the simultaneous recording of phase-shifted interferograms corresponding to orthogonal in-plane sensitivity vectors. Beams I_A and I_B were expanded directly from an argon-ion laser. I_C and I_D came from the same laser and were guided through York HB450 single mode highly birefringent optical fibre to the test surface. The output ends of the fibres were rotated to give polarisation vectors orthogonal to I_A and I_B . As before, all beams were linearly polarised perpendicular to their plane of incidence. I_B and I_D were not derived from I_A and I_C by mirrors placed adjacent to the specimen surface: these mirrors would have to be translated to introduce a phase-shift between the beam pairs I_A, I_B and I_C, I_D . Achieving linear phase-shifts over an expanded wavefront is difficult, and a translator for each mirror would be required. Therefore a single pzt-mounted mirror (PZT) in an unexpanded beam was used, and the beam divided to give I_B and I_C . The phase-stepped beams therefore correspond to the positive x and y axes. Two identical Phillips CCD cameras were used to view the test area through a narrow-bandwidth (514nm)

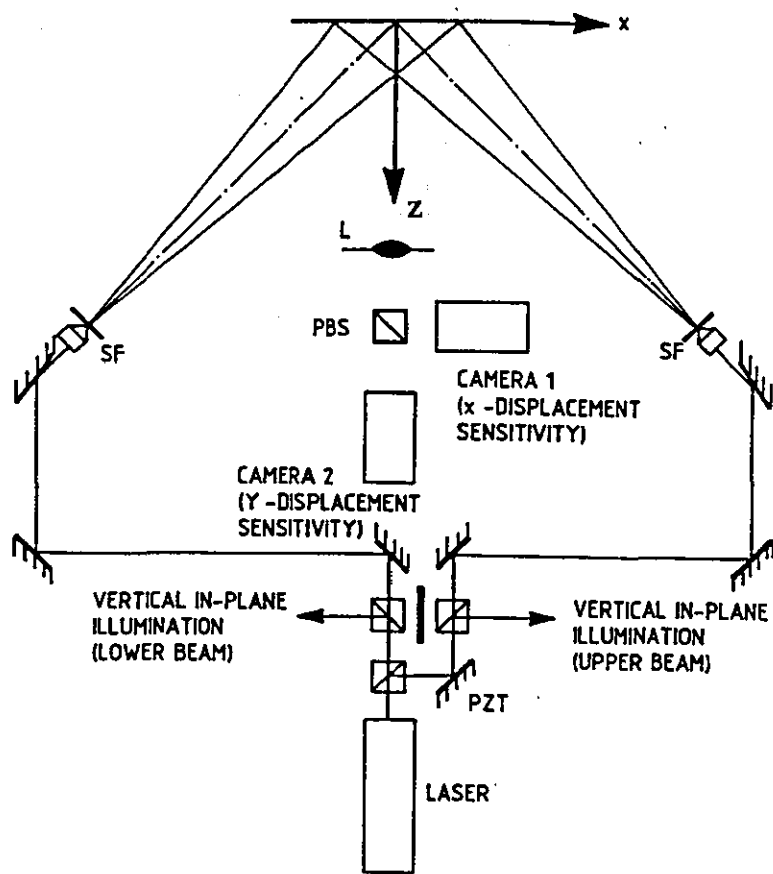
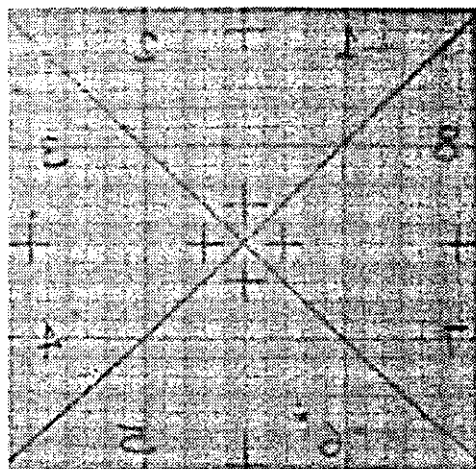
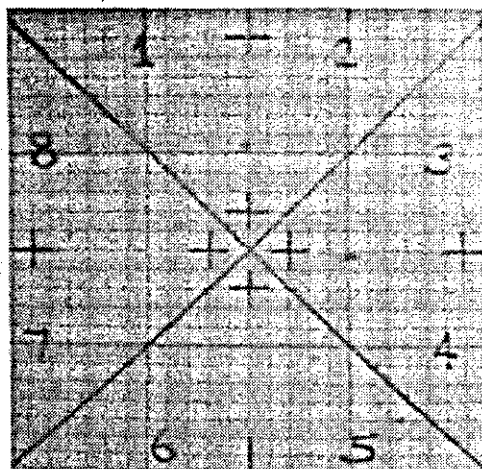


Figure 4.6 Dual sensitivity interferometer: phase-stepping arrangement

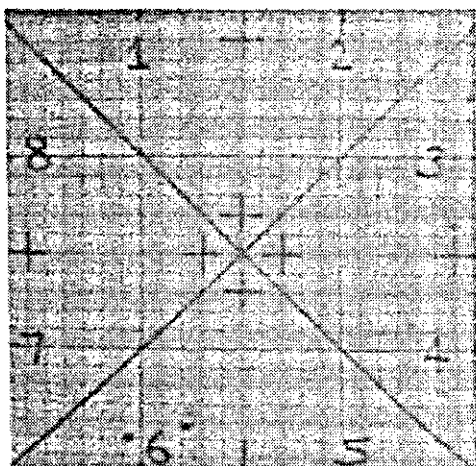
polarising beamsplitter cube. These components were housed in a dedicated interferometer. Manipulation of the cameras enabled two images of a test object viewed under white light to be matched virtually pixel for pixel. The procedure employed for camera alignment was to carefully align camera 2 with the z axis. A test image was digitised, Figure 4.7(b), and the centre point marked in the overlay of the image processor. The output from camera 1 was then digitised by the image processor, whilst keeping the central pixel marked in the overlay. Camera 1 was then adjusted until the centre of the test image appeared at the marked pixel, and there was no tilt to the image, Figure 4.7(a). Reflecting the image about the vertical axis, Figure 4.7(c), and subtracting, Figure 4.7(d), revealed a slight mismatch due to incorrect positioning of camera 1 and aberrations introduced by the cube. This error is smallest at the image centre i.e. the point used to align the images. The largest error of one pixel difference in both the x and y directions occurred in the bottom right hand corner. This corresponds to a positional inaccuracy of 0.5% of the object length viewed.



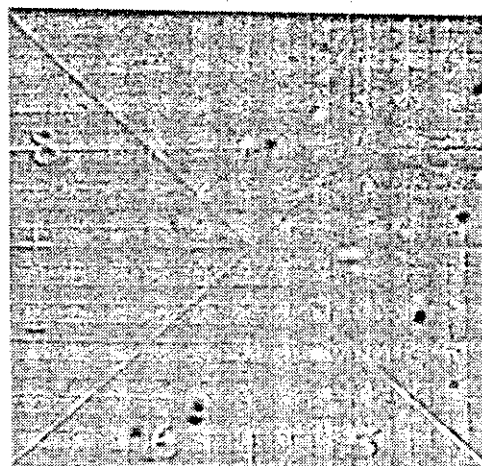
(a)



(b)



(c)



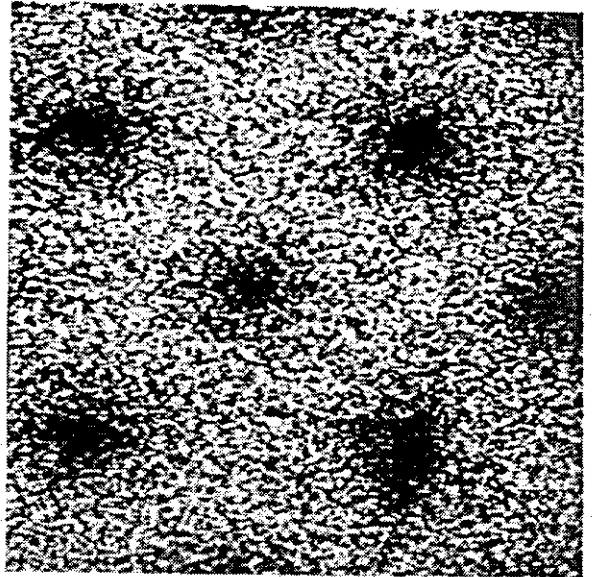
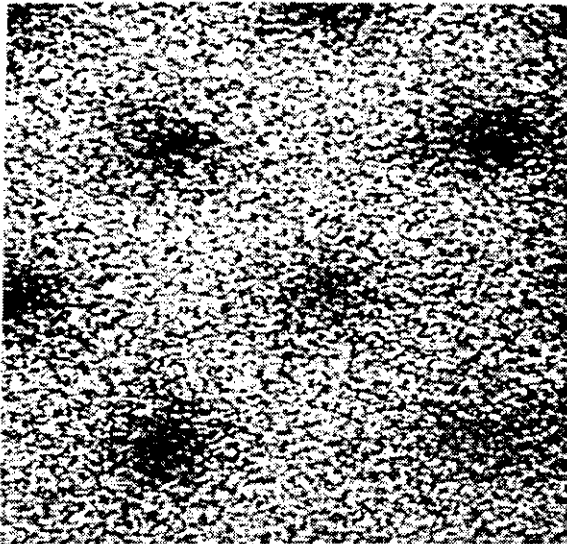
(d)

Figure 4.7 Alignment of cameras

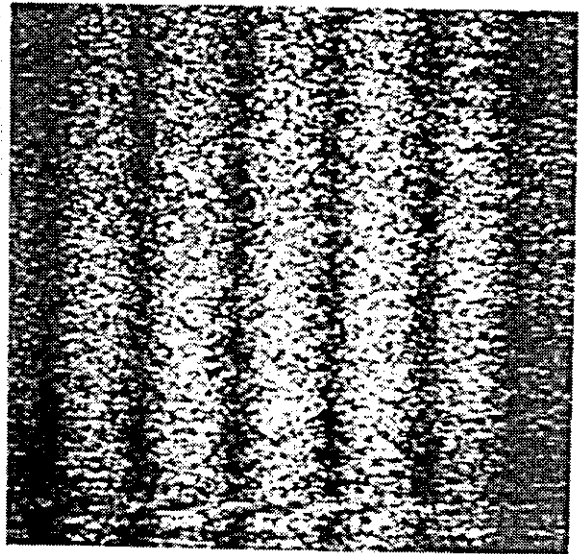
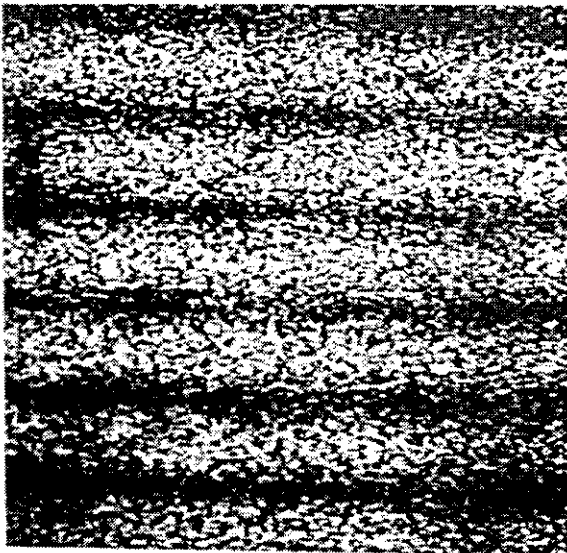
Initial results from the interferometer are shown in Figure 4.8 for aluminium plates mounted to a rotation stage. Figure 4.8(a) shows a white spray-painted surface illuminated by both beam pairs. As in Figure 4.4(c), the depolarised speckle pattern resulted in the same fringe pattern at both cameras. However, this time, beam pairs I_A, I_B and I_C, I_D were mutually coherent because they were derived from the same source, giving sensitivity vectors inclined at 45° to the x and y axes. The combined fringe pattern shows six sets of fringes: horizontal, vertical, two sets superimposed at 45° to the x axis and two sets superimposed at -45° to the x axis. Results are also shown for a cross-hatch abraded surface, Figure 4.8(b). Light scattered from the abraded surface maintained a sufficient degree of polarisation for the interferometer to work successfully. However, when a silver spray-painted surface was tested, the influence of 45° fringes was still apparent, indicating some depolarisation of the scattered radiation. This contrasts with the result for the HeNe rig, Figure 4.3, in which the silver spray-painted surface produced a speckle pattern with a higher degree of polarisation than the abraded surface. To investigate this effect the rotating polariser test of Section 4.2.1 was repeated. The polarisation selective beamsplitter was removed from the interferometer, and a polariser placed in front of the lens. Fringes were recorded from metal plates with various surface finishes mounted to a rotation stage. The results for horizontal in-plane illumination only are shown in Figure 4.9. Each data set has been scaled to the grey-level at 0° polariser angle obtained for the silver spray-painted surface. Results for a surface painted white are shown in Figure 4.9: the fringe brightness is independent of polariser angle. A bead-blasted surface was found to give results very similar to the spray-painted preparation. The theoretical curve, $I = I(0) \cos^2\theta$ for plane polarised light is also marked in the Figure. It can be seen that the cross-hatch abraded surface depolarised the speckle pattern the least in this configuration, verifying the qualitative observations from the fringe patterns. This result contrasts with Figure 4.3 obtained with the HeNe rig, in which the silver spray-painted surface gave the better performance. This has been attributed to the different wavelengths used in the two interferometers.

Camera 1

Camera 2



(a)



(b)

Figure 4.8 Interferometer results for white and cross-hatch abraded surfaces

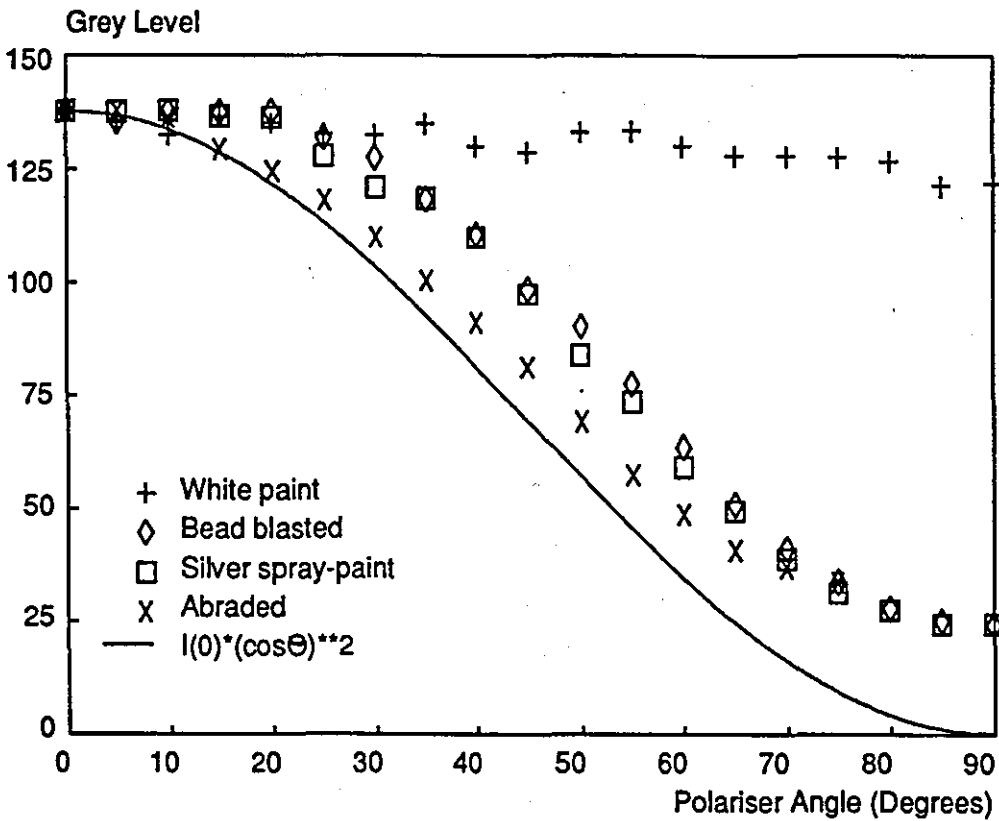


Figure 4.9 Variation of fringe brightness with polariser angle

4.3.2 Accuracy of Displacement and Strain Measurement

The accuracy of phase measurement was investigated experimentally for TPSSC in Section 3.2.5. However, several experimental conditions have changed between the system used in Section 3.2.5 and the dual-sensitivity interferometer described in the previous section. The effect on the error in measured phase should be determined. For example, diverging rather than collimated wavefronts were used. From Section 2.3.3, the wave function used for in-plane ESPI assumes that the angles of incidence of the two collimated wavefronts are equal and constant across the specimen surface. For a diverging wavefront, these angles will be unequal at all points across the surface (except at the axes origin) and will vary continuously. The wavefront is approximately plane if the distance from the expanding lens to the specimen is sufficiently large, thus reducing the error. However, the larger the length of object under test the greater the error. Taking typical values of object length 10cm and an expanding lens to specimen distance of 60cm, gives a

maximum 0.13% ($2\pi/770$) error at the image edges for $\theta=45^\circ$. From the considerations of Section 3.2.5, this may be ignored with respect to speckle noise. Another deviation from the earlier experimental investigation of accuracy is that a polarisation preserving surface was used. The likelihood of dark speckles increases, leading to an increased number of non-modulating pixels in the fringe pattern.

To determine if the measured error in phase and strain measurements made in Sections 3.2.5 and 3.3.2 respectively were still valid, a cross-hatch abraded metal plate was prepared and mounted to a rotation stage. The central 28mm x 28mm region was viewed with the dual sensitivity interferometer. Phase-stepped data sets were recorded for both the horizontal and vertical in-plane components of displacement, at three angles of plate rotation. Horizontal in-plane results were also recorded for a matt white surface for direct comparison. The data was filtered with a Fourier-domain circular mask filter of sufficient radius to cover the central diffraction spots, and the phase map evaluated for each data set. The standard deviation of the difference at each pixel between the measured phase and calculated value based on the angle of plate rotation was evaluated as in Section 3.2.5. Figure 4.10 shows the standard deviation of phase difference plotted against spatial frequency for both the abraded and white surfaces. For the abraded surface, two values exist at each spatial frequency, corresponding to the horizontal and vertical sensitivities. The Fourier filtered results and best fit line from Figure 3.12 have been included for direct comparison. No marked difference is apparent, and consequently the error in phase measurement determined previously is still valid.

Figure 4.11 shows the standard deviation in strain difference plotted against fringe spatial frequency. Again, the difference between the value determined experimentally from a 25 x 25 pixel least-squares plane fit to the unwrapped phase data and the value determined from the angle of rotation of the plate at each pixel was used. The Fourier filtered results, with a least-squares plane fit over a 25 x 25 pixel plane fit from Figure 3.14 have been included for comparison. The

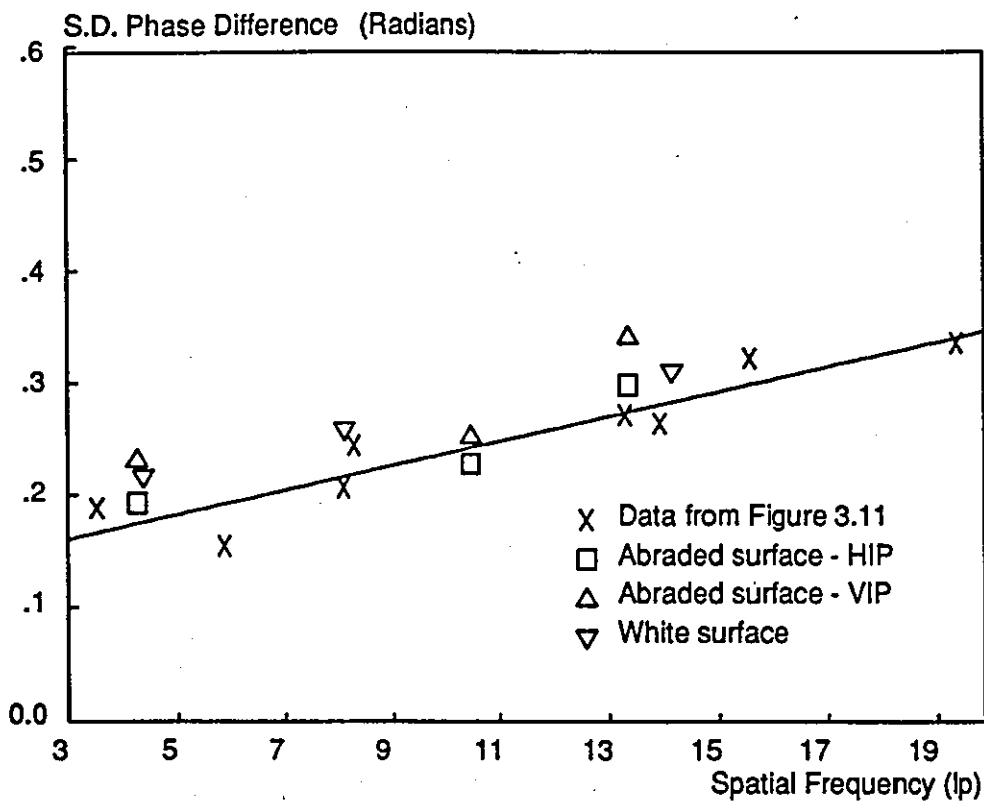


Figure 4.10 Standard deviation of phase difference against spatial frequency

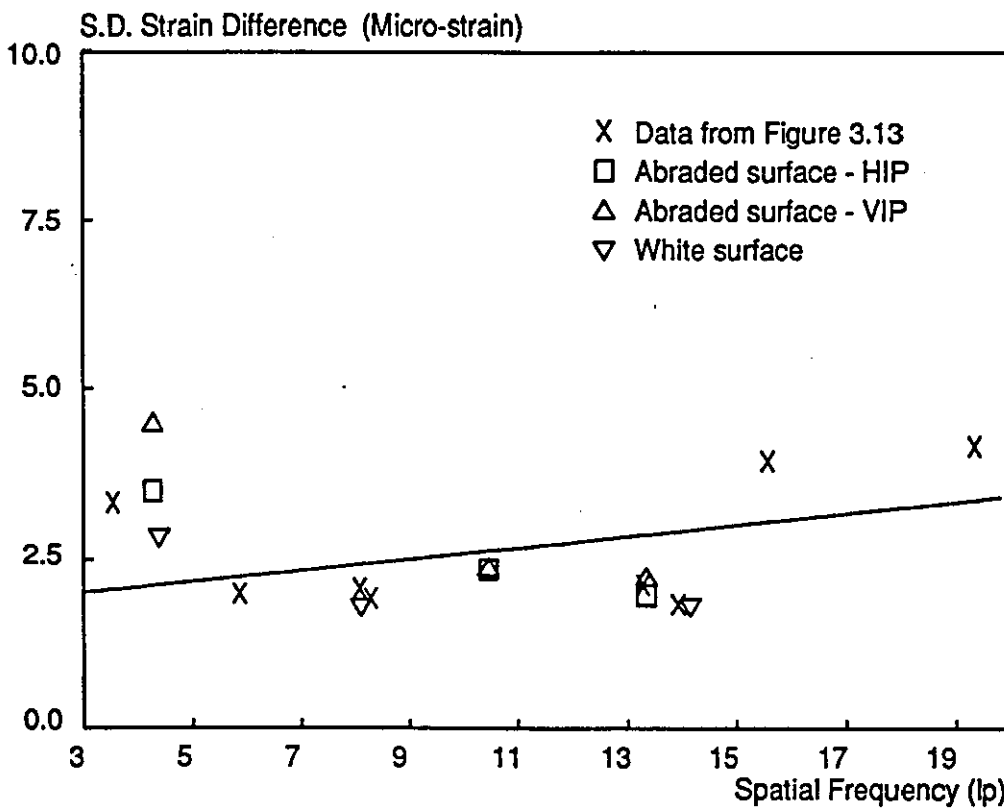


Figure 4.11 Standard deviation of strain difference against spatial frequency

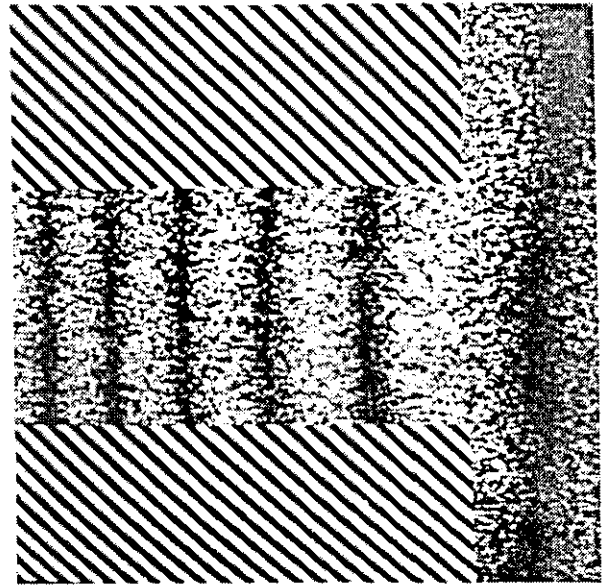
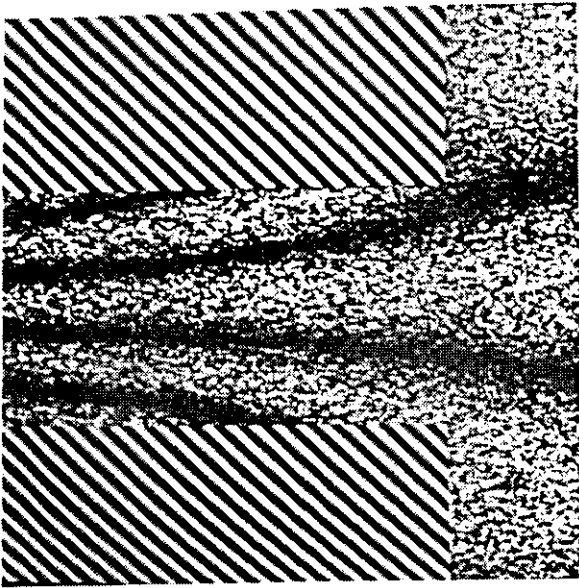
close agreement between the tests performed here and those of Chapter 3 indicate that the experimentally determined values for error in phase and strain measurement are valid for the dual-sensitivity interferometer. Furthermore, the tests performed in this section involved a magnification twice that used in Chapter 3. Thus, provided that the magnification is not so great as to cause the speckle pattern to decorrelate for relatively small rigid body motion, these accuracy figures appear to be applicable over a limited magnification range.

4.3.3 Experimental Demonstration

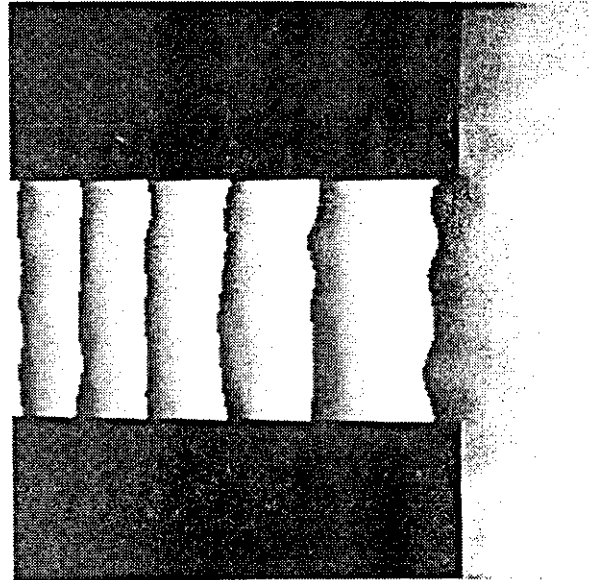
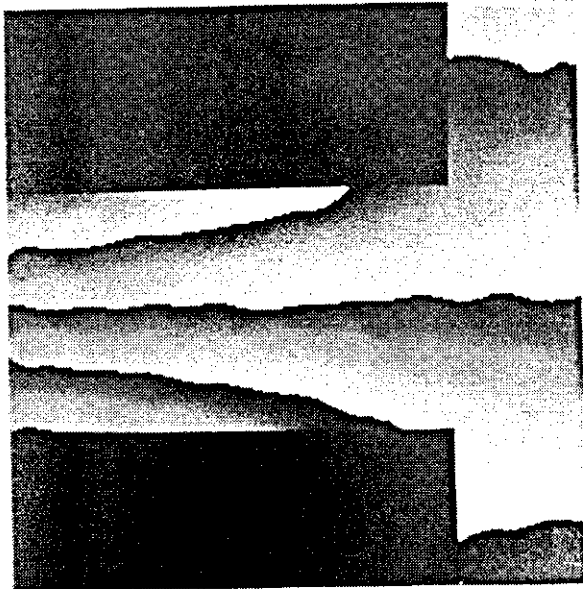
In order to demonstrate the techniques discussed so far, results were recorded for an HS3OTF aluminium alloy cantilever, machined integral with its support and loaded at its free end. The geometry of the cantilever is indicated in Figure 4.12. Load was applied by removing a 0.5kg mass from the cantilever tip causing the cantilever to deflect in the positive y direction. The load was removed since oscillations of the hanging weight influenced the stability of the fringe pattern for some seconds after its application. Interferograms corresponding to horizontal and vertical in-plane sensitivities were obtained at the two cameras simultaneously. Each camera was connected in turn to the image processor for the phase-stepping and image digitisation sequence. Sequential recording of the two sensitivity vectors was acceptable because the load was static. The advantage of using the dual-sensitivity interferometer in this instance was that the object did not need to be reloaded when switching between horizontal and vertical sensitivities, ensuring that identical strain conditions existed for both recordings. Figure 4.13(a) shows one of the three phase-stepped fringe patterns for the horizontal and vertical sensitivity directions. The left hand column of Figure 4.13 denotes horizontal in-plane sensitivity, and the right hand column vertical in-plane sensitivity. The large region of background around the cantilever arm was blanked with a computer generated sine function, so that low frequency noise present in this region had no influence when defining the Fourier filter mask. The peak-to-peak amplitude was made smaller than that of the ESPI fringes, and the wavelength sufficiently large

Horizontal in-plane

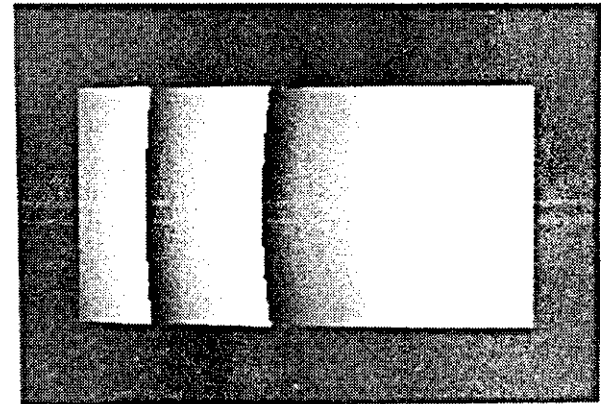
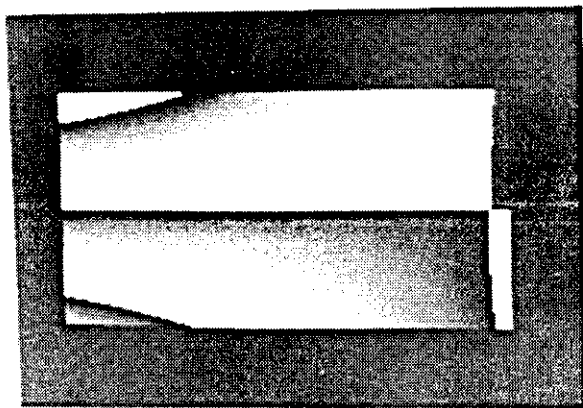
Vertical in-plane



(a)



(b)



(c)

Figure 4.13 Displacement of cantilever

literature. The shear modulus, $\mu = E/2(1+\nu)$. Displacements have been converted to wrapped phase for a visual comparison with Figure 4.13(b). Note that the solution does not apply to the cantilever support. A discrepancy between the measured displacement and the stress function solution is evident. The stress-function solution is only valid for the boundary conditions assumed in its derivation. These are discussed in Appendix A, and are not entirely satisfied in this instance. Furthermore, the stress function solution gives displacement due to bending only, but in practice the cantilever undergoes a further deflection due to the elasticity of the support. O'Donnel¹³³ estimated the additional deflection of the cantilever due to elasticity of the support, given by:

$$(v)_{y=0} = \frac{16.67}{\pi E} \left(\frac{Pl}{b}\right) \left(\frac{2}{c}\right)^2 x + \frac{(1-\nu)}{E} \left(\frac{P}{b}\right) \left(\frac{2}{c}\right) x \quad (4.2)$$

where b is the specimen thickness (6.35mm). To investigate these effects, the measured displacement v for the line $y=0$ is plotted in Figure 4.14. The solution due to bending only is given by equation (4.1) with $y=0$ i.e. the well known mechanics of solids solution:

$$(v)_{y=0} = \frac{Px^2}{6EI}(x+3l) \quad (4.3)$$

This bending theory solution, and the added deflection due to elasticity of the support, equation (4.2), are also plotted in Figure 4.14. Although the O'Donnel solution gives considerable improvement to the bending theory, a larger displacement was measured with ESPI. This is probably due to deformation of the support not present in the symmetrical system tested by O'Donnel. In order to model the ESPI results more accurately, the finite element mesh of Figure 4.12 was generated using the PAFEC Interactive Graphics System (PIGS). Loading and restraints are also shown in Figure 4.12. The mesh consisted of eight-noded isoparametric rectangular elements (element number 36210) for plane stress. Displacements calculated from the model for $y=0$ are shown in Figure 4.14 and are in better agreement with the ESPI measurements.

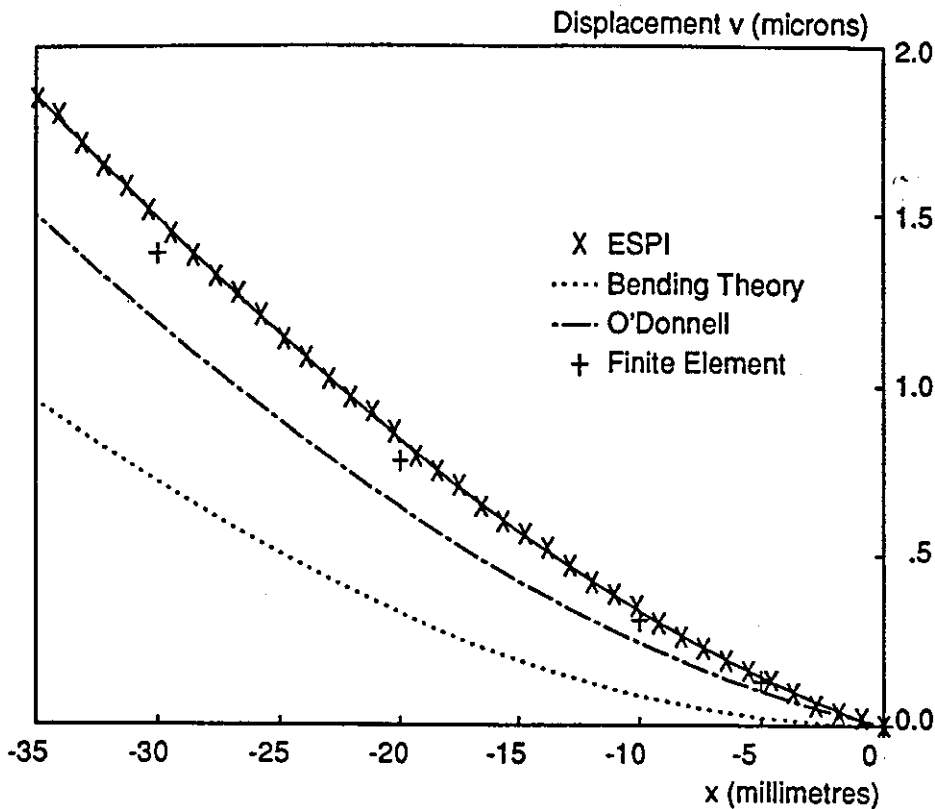


Figure 4.14 Vertical displacement, v , against position along cantilever

Expressions describing the strain distribution may be derived from equations (3.31) and (4.1):

$$\epsilon_{xx} = -\frac{P(x+l)y}{EI}$$

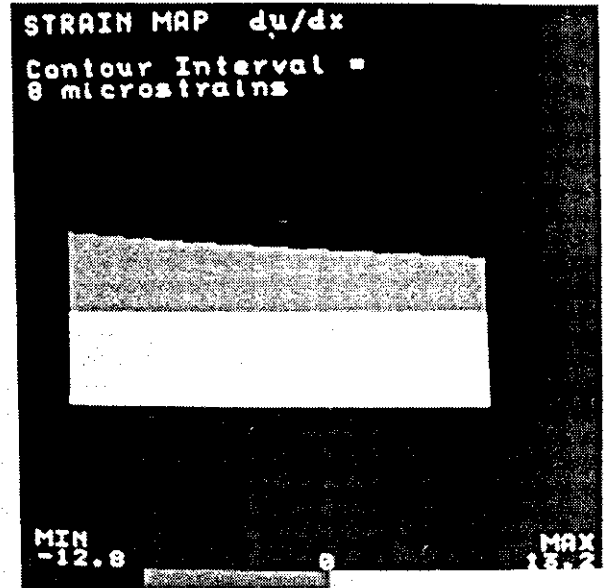
$$\epsilon_{yy} = \frac{vP(x+l)y}{EI} \tag{4.4}$$

$$\gamma_{xy} = \frac{P(y^2-c^2)}{2I\mu}$$

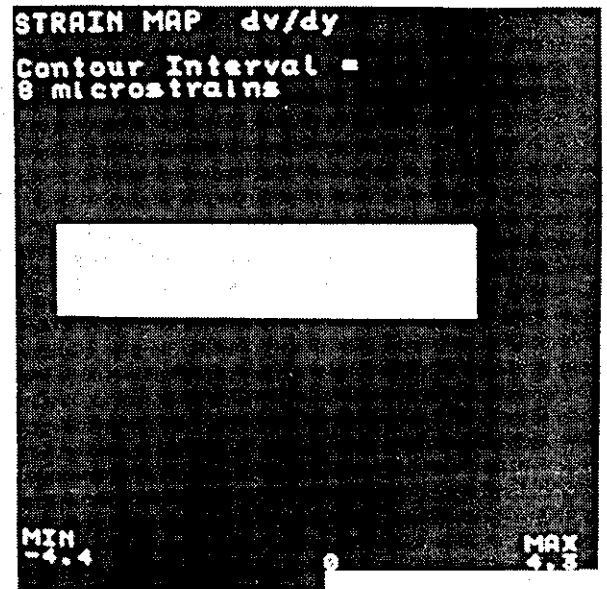
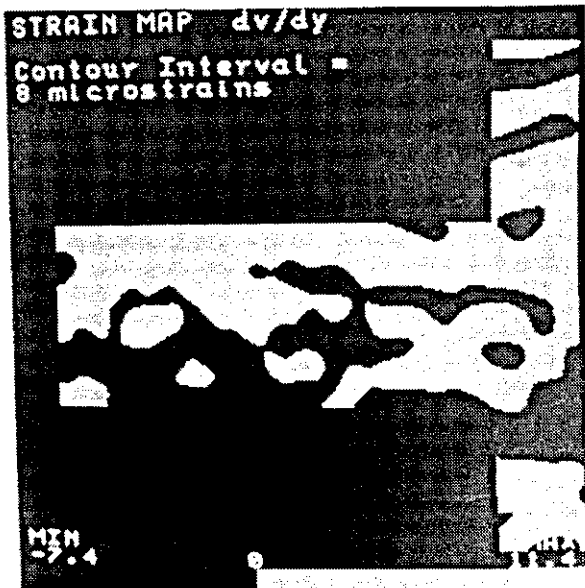
From the foregoing comparison of experimentally measured displacement with the stress function solution, it might be assumed that equation (4.4) would be valid as a first approximation only. However, the deflection of the support causes a rotation of the cantilever. This modifies the measured displacement field, but does not affect the measured strain (except for $\partial u/\partial y$ and $\partial v/\partial x$). The components of

Experimental

Theoretical



(a)



(b)

Figure 4.15 Strain distribution for cantilever (Continued overleaf)

Experimental

Theoretical



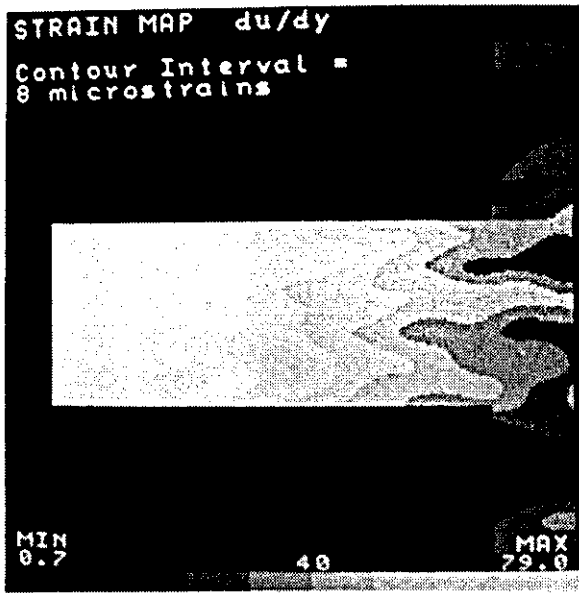
(c)



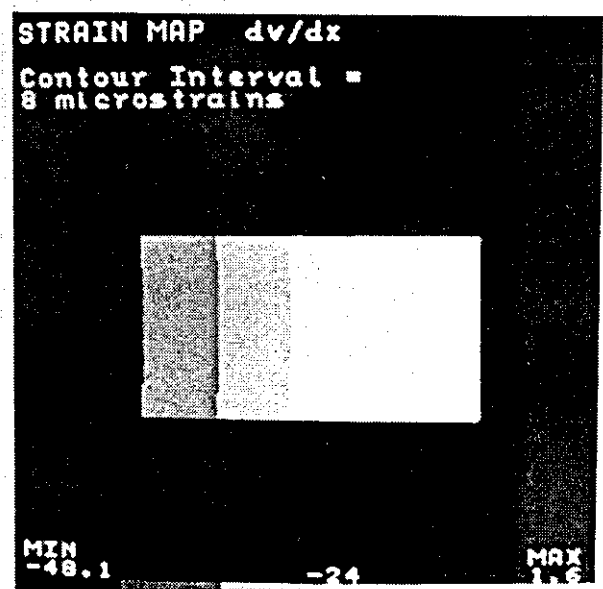
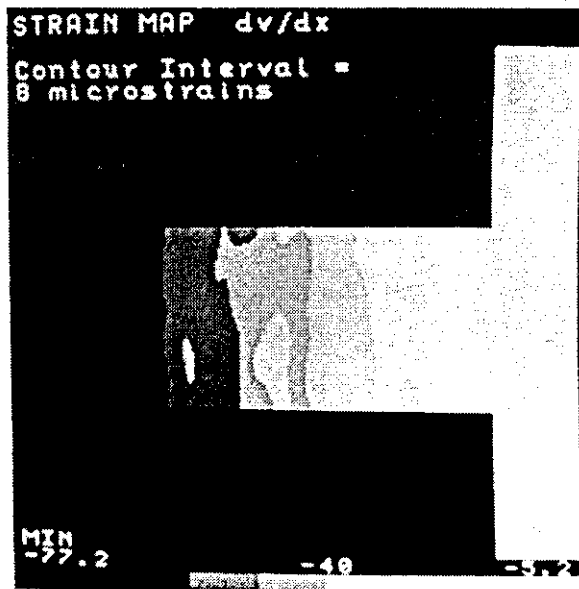
Figure 4.15 (continued) Strain distribution for cantilever (Continued overleaf)

Experimental

Theoretical



(d)



(e)

Figure 4.15 (continued) Strain distribution for cantilever

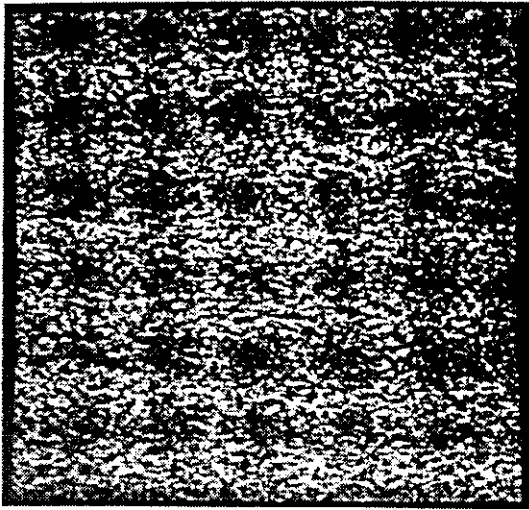
strain ϵ_{xx} and ϵ_{yy} are shown in Figure 4.15(a) and (b) respectively. Experimental values are shown in the left hand column, and theoretical plots in the right hand column. Values of strain are plotted in $8\mu\text{strain}$ bands, the width of which correspond to the error in any measurement. To calculate this width, the highest spatial frequency present in the fringe pattern was estimated from the Fourier transform calculated when applying the Fourier filter (~ 10 lp in this example). The uncertainty in strain measurement is therefore $5.7 + 10(3 \cdot 0.08) = 8.1\mu\text{strain}$. The value represented by each band is then scaled in the range 0 to 255 grey-levels for presentation. Note that the experimental plots include the cantilever support. Consequently the maximum and minimum values in the range for the experimental and theoretical plots differ and the same strain value occurring in both may be represented by a different grey-level. However, the position of the contours can be compared. The corresponding width of bands for the shear strain is $11.3\mu\text{strain}$, Figure 4.15(c). The theoretical plot can be represented by a single value, and hence appears blank. This is the clearest example of maximum and minimum values differing widely between experimental and theoretical plots due to the inclusion of the support in the former. Little information is available from this theoretical plot of shear strain, and so the components $\partial u/\partial y$ and $\partial v/\partial x$ have been included, Figure 4.15(d) and 4.15(e) respectively. These are again plotted in $8\mu\text{strain}$ contours. The large difference in values for these two plots is due to the contribution of rigid body rotation. In general, the reasonable agreement in profile and range of values is achieved for ϵ_{xx} , ϵ_{yy} and γ_{xy} . Noise in the data appears to be random, although some structure can be seen for $\partial u/\partial v$. "Lobes" of noise appear to follow the fringe line in the original data and are due to a small error in the size of the phase step.

4.4 CLOSURE

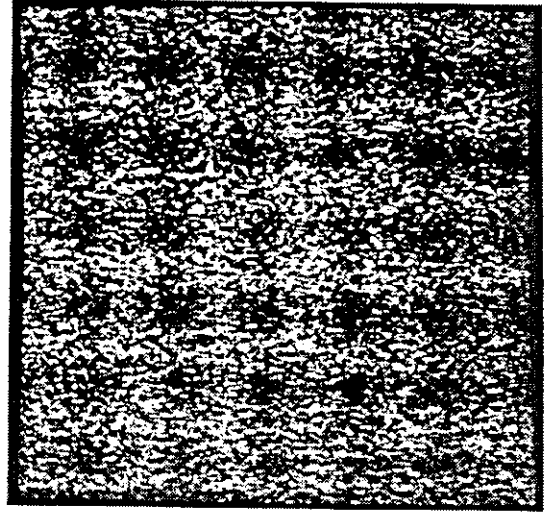
A technique has been established for the simultaneous measurement of two mutually orthogonal in-plane displacement fields. The interferograms are easily interpreted, and the information from both may be combined. Although the

technique is restricted to use with surfaces which retain a high degree of polarisation, initial results indicated that silver spray-paint could be used in the many situations where a matt white finish would normally be employed with ESPI. However, for the second system incorporating phase-stepping, the silver spray-paint was less successful, and a cross-hatch abraded surface gave better results. This was attributed to the different laser wavelengths used in the two systems. Preparing abraded surfaces for the objects tested in this thesis was not a problem, and polarisation discrimination was pursued throughout. This would not be the case for large objects with complex surface profiles. Thus a technique based on wavelength discrimination, as suggested in Section 4.1, would be more generally applicable. The resulting difference in fringe function between the two sensitivity directions would not be a problem now that automated fringe analysis has been introduced (via phase-stepping). Construction of an interferometer operating with wavelength discrimination was apparently started recently at MAN in Munich¹³⁴ although no details have appeared in the literature. It will use three laser diodes operating at well separated wavelengths in the red, green and blue, with a single imaging lens and three cameras. Two high-efficiency filters whose transition from reflection to transmission occurs at wavelengths between those of the laser diode separate the laser beams to the individual cameras. An out-of-plane and two in-plane configurations are proposed, each with their own piezo phase-stepper. However, if simultaneous measurements were to be made with a pulsed system, three sources would be an expensive solution. Thus polarisation discrimination has its advantages.

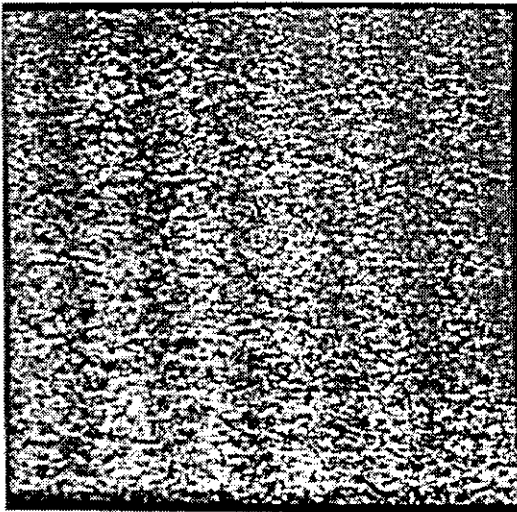
If it is necessary to measure only one in-plane component of displacement, the dual sensitivity interferometer can be extended easily to measure one in-plane and the out-of-plane components. Extension of the technique for simultaneous measurement of a third (out-of-plane) displacement component, in addition to the two in-plane components, using only two cameras is possible. If a second wavelength is used for the out-of-plane illumination configuration, out-of-plane sensitivity fringes will be superimposed on both the in-plane fringe patterns. Figure 4.16(a) shows results recorded with an out-of-plane interferometer



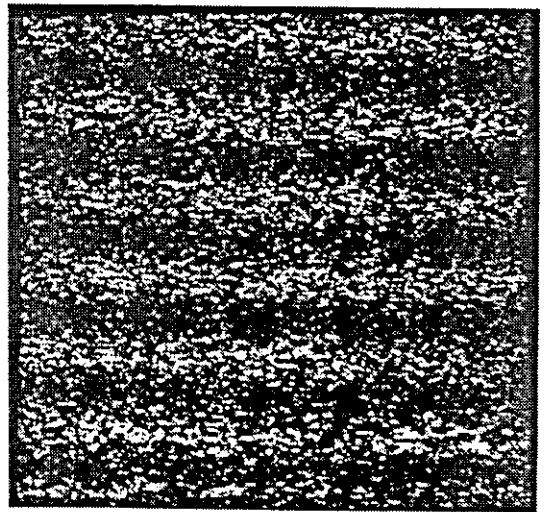
(a)



(b)



(c)



(d)

Figure 4.16 Separation of in-plane and out-of-plane displacement components

operating at 633nm. The test surface is also illuminated with an horizontal in-plane configuration at 514nm. The test object was once again a metal plate mounted on a rotation stage. The assembly was mounted to a second rotation stage to give a second degree of freedom. Horizontal fringes correspond to horizontal in-plane displacement for plate rotation in its own plane about the z axis; vertical fringes denote out-of-plane motion due to rotation about the y axis. The fringes have poor visibility and are initially confusing to the eye. The two fringe patterns of Figure 4.16(a) may be separated by applying a π radian phase-step to one beam of the in-plane interferometer, Figure 4.16(b). Adding the two patterns reinforces the stationary pattern i.e. the out-of-plane fringes Figure 4.16(c). The in-plane fringes are obtained by subtracting the two images, Figure 4.16(d). Alternatively, the symmetric patterns in this example could be separated in the Fourier plane. Although fringe analysis techniques allow the separation of data corresponding to each sensitivity vector, the most direct approach is probably to introduce a third camera.

Phase-stepping was introduced to the dual-sensitivity interferometer, and displacement and strain data obtained automatically for the cantilever loaded at its free end. Good agreement with theoretical models was demonstrated. By recording both views simultaneously, identical strain conditions existed for the horizontal- and vertical-sensitivity fringes: it was not necessary to reload the object when exchanging illumination directions. Simultaneous recording was not essential for this example, and alternative, sequential procedures not requiring the cantilever to be reloaded could be proposed. One such solution is proposed in Section 6.1.2. However, transient event studies using pulsed lasers will require both views to be recorded simultaneously.

5. FRACTURE MECHANICS APPLICATIONS

Having established procedures for automated in-plane displacement and strain evaluation, Chapter 3, and measurement along both in-plane sensitivity vectors simultaneously, Chapter 4, it remains to apply these techniques to fracture mechanics problems in a quantitative manner. From Chapter 2, the study of linear elastic problems for which established solutions exist is a necessary prelude to more advanced investigations involving, for example, fatigue loading and dynamic fracture. This chapter is concerned with two specimens loaded in the linear elastic regime. In Section 5.1 a centre-notched plate loaded in uniaxial tension is studied. The displacement and strain distribution are compared with a stress function solution and a finite element model. The opening-mode stress-intensity factor, crack-opening displacement and J-integral were highlighted as important fracture mechanics parameters in Section 2.2. These parameters are evaluated for three compact tension specimens of varying crack length in Section 5.2. Phase-stepped moire interferometry results are presented for the same compact tension specimens for direct comparison, to determine the relative merits of the technique with respect to ESPI.

5.1 CENTRE-NOTCHED PLATE

All ESPI results presented in this chapter were recorded with the argon-ion dual sensitivity interferometer of Section 4.3.1. The rigid hydraulic tensiometer used to load the specimens was also common to all tests. The tensiometer was clamped to the optics table, and hydraulic pressure applied remotely via a dead-weight tester. This loading method produced very little mechanical disturbance to the vibration isolated table. The tensiometer was built in-house, and incorporated an hydraulic ram with an upper load limit of 4.5kN. Frictional losses in the system required the tensiometer to be calibrated against an Instron 8032 tensile test

machine. The Instron load cell was certified to an accuracy of 0.5% indicated load. The excellent linearity of the calibration tests suggested a conservative estimate of the accuracy of the tensiometer to be 1% of the indicated load as determined after calibration.

The centre-notched HS30TF aluminium alloy specimen studied in this section is shown in Figure 5.1. This is not a standard specimen: the length of the specimen between the loading pins must be greater than two specimen widths to ensure uniform stress entering the crack plane²². Many expressions for the stress-intensity factor for the through-crack in a sheet of finite width loaded in uniform tension have been proposed, including the approximate solution due to Feddersen¹³⁵:

$$K_I = \frac{P}{BW} \sqrt{\pi a \sec\left(\frac{\pi a}{W}\right)} \quad (5.1)$$

This simple expression agrees to 0.3% for $a/W \leq 0.7$ with a 36 term power series expansion of the complex stress potential calculated by Isida¹³⁶ that gives the "exact" solution up to $a/W = 0.9$. With the distance between loading pins restricted by the compact design of the table-mounted tensiometer, it was decided to ignore width restrictions and to examine the displacement and strain distribution around a (non-standard) stress-concentrator. The region of interest ahead of the notch is marked in Figure 5.1 with a dashed line. The specimen surface was cross-hatched abraded as described in Section 4.2.1.

A load of 990N was applied to pre-stress the specimen mounts, and the horizontal and vertical in-plane reference images simultaneously digitised to the framestores. Figure 5.2 shows results for a 743N load increment. At this load, $K_I = 1.51 \text{ MN/m}^{3/2}$ from equation (5.1), approximately 3% higher than the infinite plate solution. The u and v displacement components measured by the interferometer are shown in Figure 5.2(a). The area viewed was approximately 24mm x 24mm. Three phase-stepped images were digitised to the image processor, firstly for the u and then the v components of displacement. Although both fringe patterns were visible at the same time, sequential recording was adequate for the static loading conditions

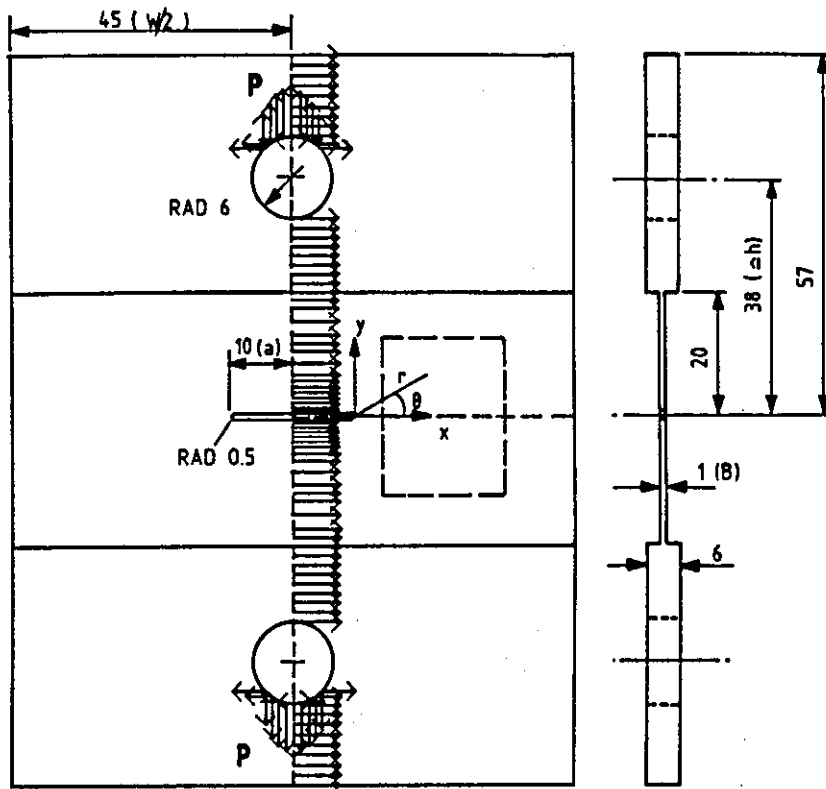


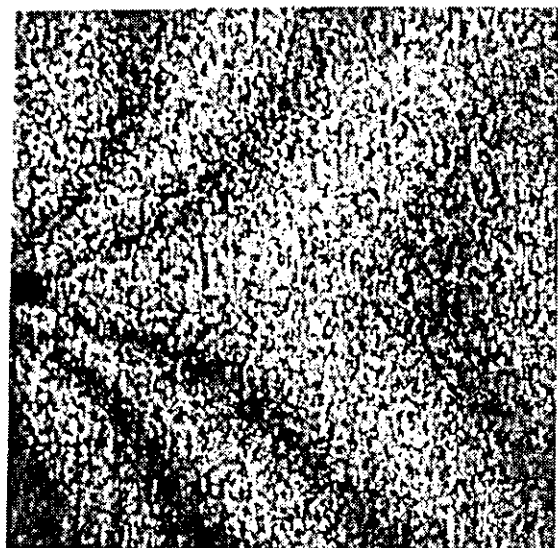
Figure 5.1 Centre-notched specimen (Dimensions in mm)

of this test. Simultaneous viewing ensured that the same load existed for both recordings and greatly simplified gathering the data compared to using a single camera. A Fourier filter was applied to both data sets before calculating the phase maps of Figure 5.2(b). The radius of the filter mask was defined by the vertical displacement component: a radius corresponding to ~ 13 lp cut-off frequency was used. Higher spatial frequency fringe information was lost at the notch tip during filtering even for substantially larger mask radii. Thus the mask radius chosen was a compromise between maximising the area of valid data ahead of the notch, and minimising the speckle noise in that area. From Figures 3.12 and 3.14, the expected error in displacement and strain measurements was $\pm 0.05 \mu\text{m}$ and $\pm 10 \mu\text{strain}$ respectively. Phase data was lost in the region $r \leq 3\text{mm}$ and was therefore excluded from the subsequent analysis. This restriction in the radius at which valid displacement information can be extracted is important for stress-intensity factor evaluation, and is discussed in Section 5.2.3.

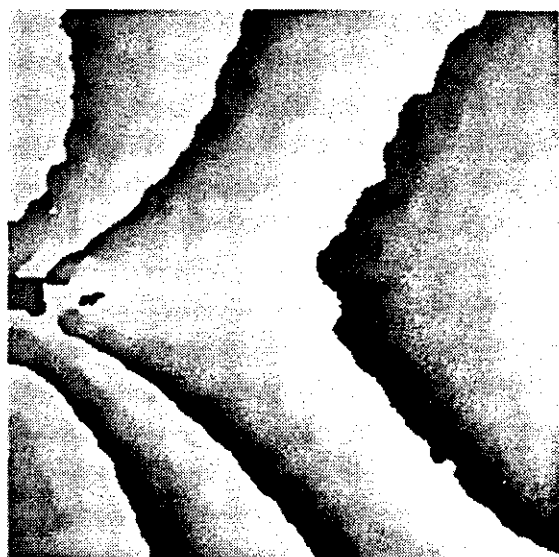
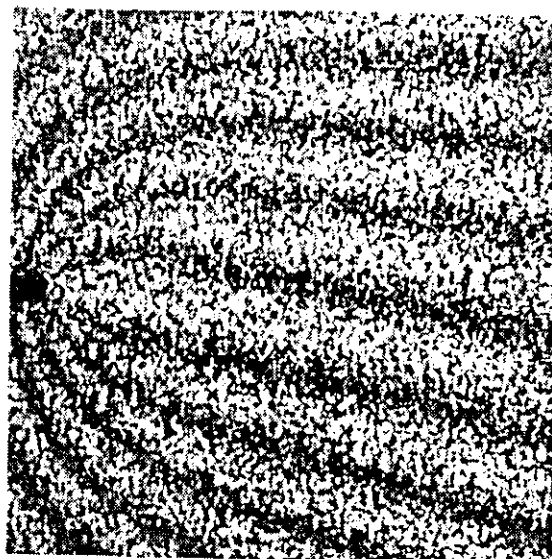
Theoretical plots of displacement, converted to wrapped phase for qualitative

Horizontal in-plane

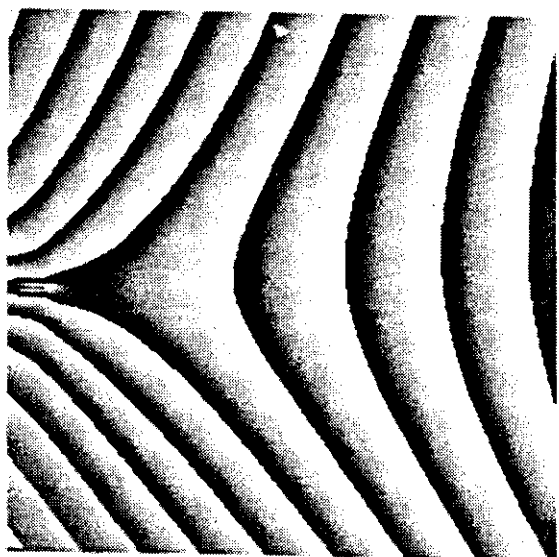
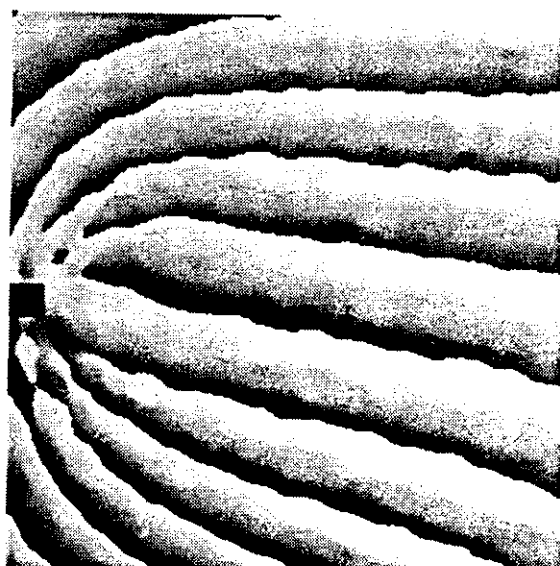
Vertical in-plane



(a)



(b)



(c)

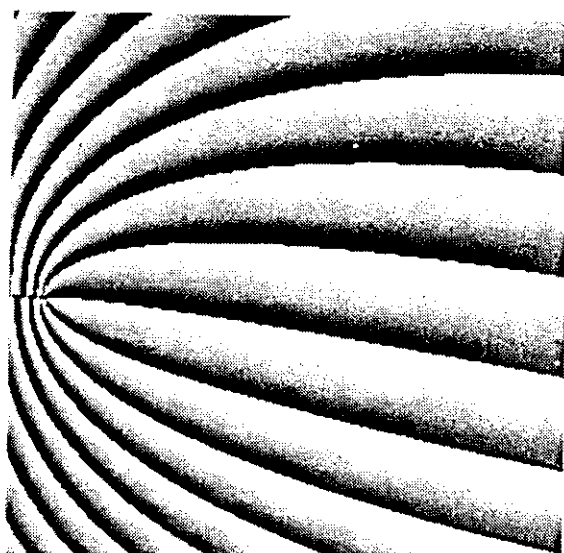


Figure 5.2 Displacements for centre-notched specimen

comparison, are included in Figure 5.2(c). These were calculated from the modified Westergaard solution¹³⁷, which for plane stress gives:

$$u = \frac{K_I}{\mu} \sqrt{\frac{r}{2\pi}} \cos\left(\frac{\theta}{2}\right) \left[\frac{1-\nu}{1+\nu} + \sin^2\left(\frac{\theta}{2}\right) \right] - \frac{\sigma}{E} r \cos\theta$$

$$\nu = \frac{K_I}{\mu} \sqrt{\frac{r}{2\pi}} \sin\left(\frac{\theta}{2}\right) \left[\frac{2}{1+\nu} - \cos^2\left(\frac{\theta}{2}\right) \right] + \frac{\nu\sigma}{E} r \sin\theta \quad (5.2)$$

This solution is discussed in Appendix A. K_I was evaluated from equation (5.1). $\sigma = P/(BW)$ and values of 69.5GN/m² and 0.33 were assumed for E and ν respectively. In addition to the displacement given by equations (5.2), a rigid body rotation about the crack tip of $\alpha = -11\mu$ radians (i.e. anticlockwise) has been added to both theoretical components of displacement, equation (3.38). This angle was estimated from the asymmetry of the measured ν displacement about the notch-line. The discrepancy between the experimental values and the model are immediately apparent, particularly for the u displacement component. There are several contributing factors, most notably the application of equations (5.2) at $r \gg a/50$. That $r < a/50$ is an approximate condition assumed in deriving equations (5.2), Appendix A. Secondly, the assumption of uniformly applied stress at the crack-line is doubtful due to the restricted length of the specimen. Finally, a blunted notch rather than a cracked specimen was used. Creager and Paris¹³⁸ have proposed elastic stress field equations for a blunt crack. The solution is similar in form to equation (5.2), and again is only valid for $r < a/50$ because second order terms are ignored.

In an attempt to construct a more accurate model, the finite element model of Figure 5.3 was generated using the PAFEC PIGS finite element system. Loading and restraints are shown in Figure 5.1. The mesh consisted of eight-noded isoparametric curvilinear quadrilateral elements (element number 36210) and associated six-noded triangular elements (36110) for plane stress. The mesh around the notch tip is based on the polar grid used by Oglesby and Lomacky¹³⁹ to calculate the stress-intensity factor for a range of specimens including a centre-

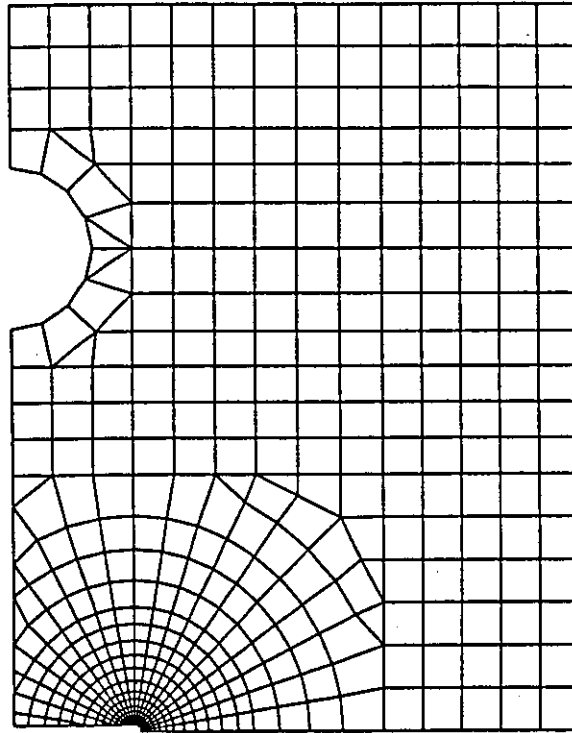
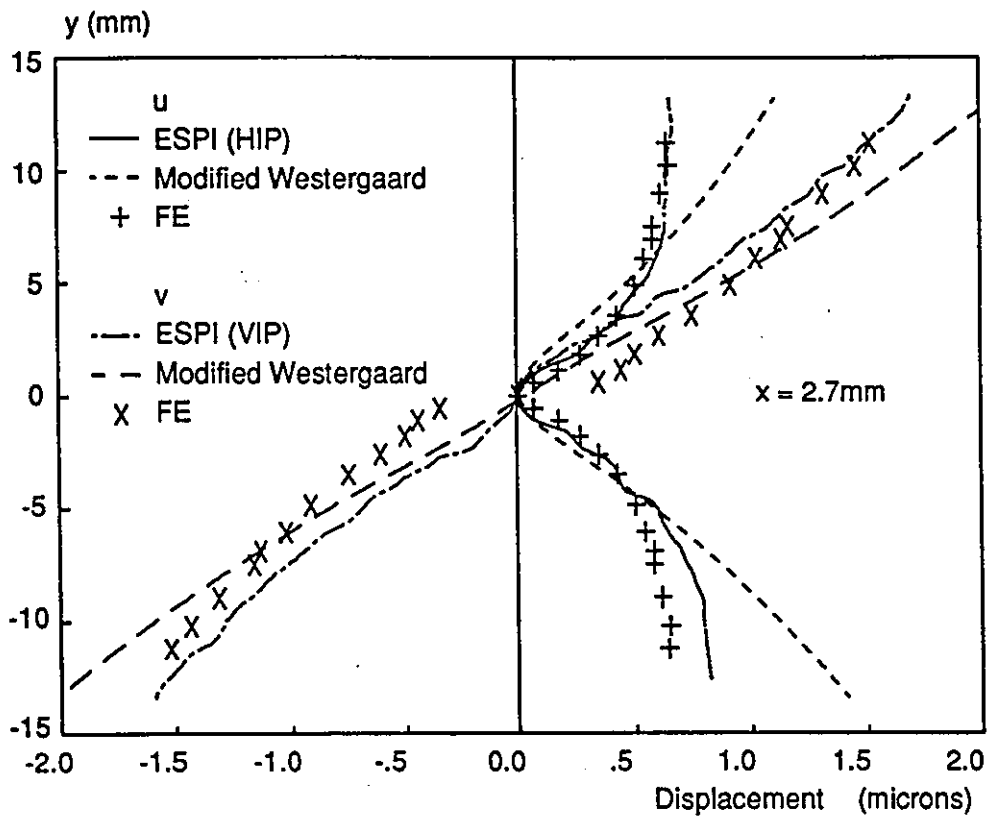


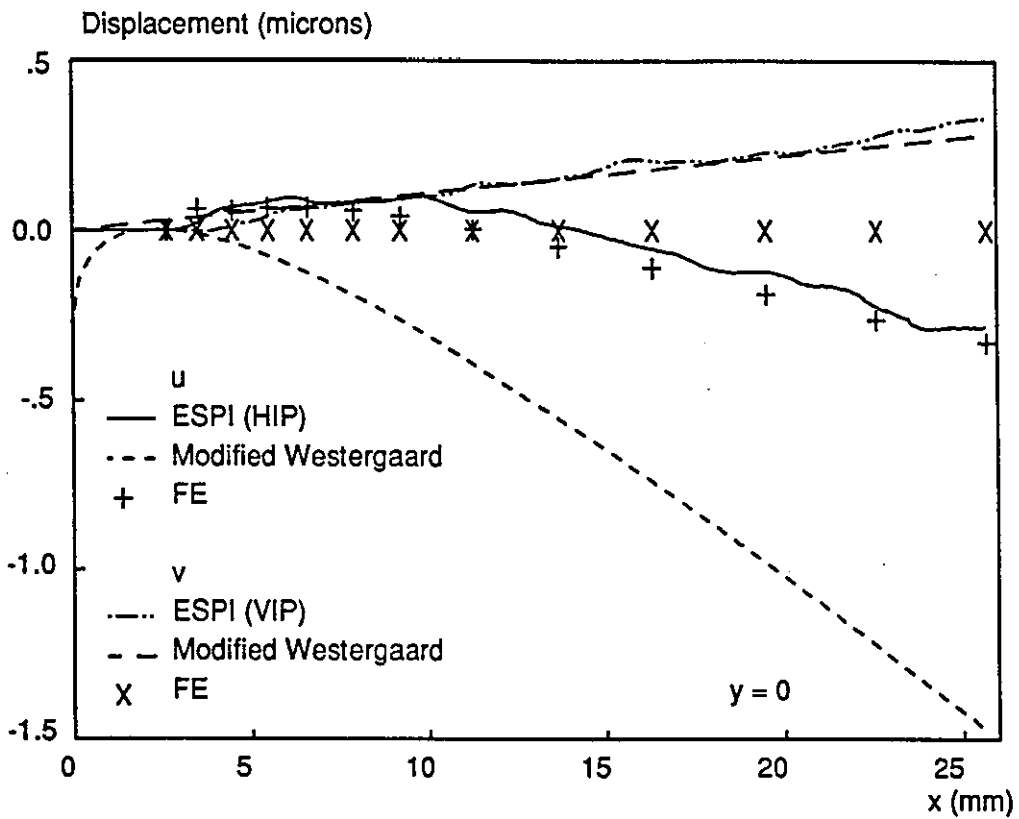
Figure 5.3 Quarter of FE mesh. See also Figure 5.1

cracked plate subjected to uniaxial tension ($a/W=0.15$). In the Oglesby study, a singular crack tip element (radius $a/50$) was surrounded by quadrilateral elements of linear dimension $a/200$ near the crack tip and $a/2$ far from the crack tip. Oglesby calculated the stress-intensity factor by the displacement method to within 5% of the value obtained by boundary collocation methods¹³⁶. The centre-notched specimen of Figure 5.1 was modelled with elements around the notch tip of linear dimension $a/127$. This was as close to the Oglesby ratio as could be achieved whilst maintaining the same mesh geometry. In the region of interest for strain calculation, Figure 5.1, the smallest elements are approximately $a/12$. Note that subsequently strain was calculated from the u and v displacements over a 25×25 pixel plane, corresponding to approximately $a/4$. Ideally, therefore, elements of linear size $a/4$ should be used in the region of interest so that the FE model does not predict strain variations which cannot be measured experimentally. However, the need for fine mesh at the notch tip made this requirement difficult to achieve.

Figure 5.4 shows u and v displacements calculated by the FE model. Figure 5.4(a)



(a)



(b)

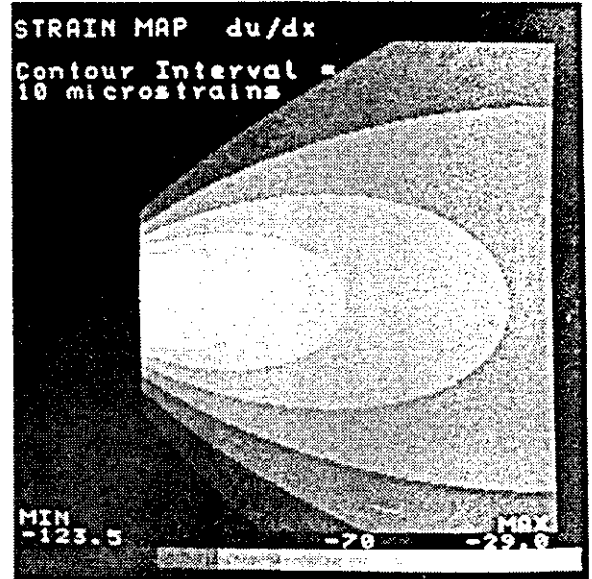
Figure 5.4 Displacement components along $x=2.7\text{mm}$ and $y=0$

considers the vertical line $x=2.7$ mm: this is the closest vertical line to the notch tip at which phase information from the vertical in-plane phase map is not corrupted by the Fourier filter. Displacements along the horizontal line $y=0$ are shown in Figure 5.4(b). Figure 5.4 also includes the u and v displacements recorded with ESPI, Figure 5.2(b), and from the modified Westergaard solution including rotation, Figure 5.2(c). The ESPI phase data was unwrapped with respect to the point $(2.7, 0)$ i.e. at the intersection of the two lines under consideration. In a similar fashion, the displacements calculated from the modified Westergaard solution and the FE model are also referenced to this point. No vertical line of nodes at $x=2.7$ mm exists in the FE model. Thus the displacement at nodes and midside nodes close to $x=2.7$ mm were recorded. This explains the uneven distribution of FE data points in Figure 5.4(a). Both graphs show reasonable agreement for v , and poor agreement for u , between the ESPI measurements and modified Westergaard solution, as indicated qualitatively by Figure 5.2. FE calculations for u show excellent agreement with the ESPI measurements. In Figure 5.4(a) the discrepancy is larger below the notch-line than above it, because no rotational component is included in the FE results. Agreement for v is less good, especially close to the notch tip, where a larger displacement is calculated than measured, Figure 5.4(a). The FE v values in Figure 5.4(b) require a rotational component to match the ESPI measurements and Westergaard solution. Overall, the FE model matched the ESPI measurements more successfully than the modified Westergaard solution. The model could be refined further to improve calculated v , especially at the notch tip, but this does not help validate the ESPI results.

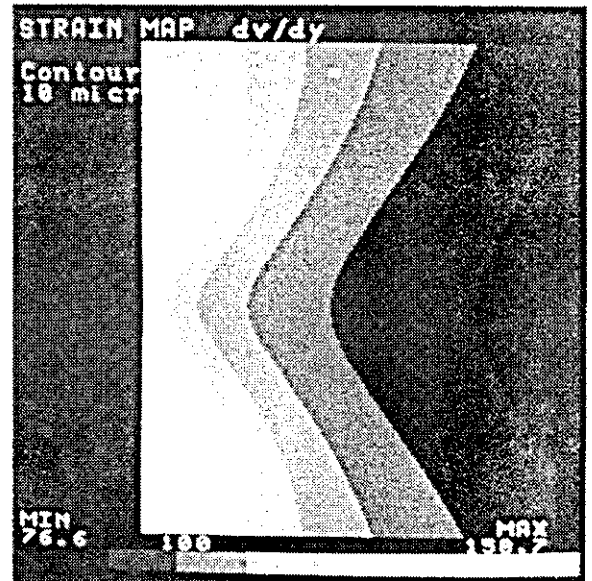
The components of strain calculated from the unwrapped phase data are shown in Figure 5.5. Experimental values are shown on the left. Theoretical strain distributions were calculated in Appendix A for the modified Westergaard solution, and are given by:

Experimental

Theoretical



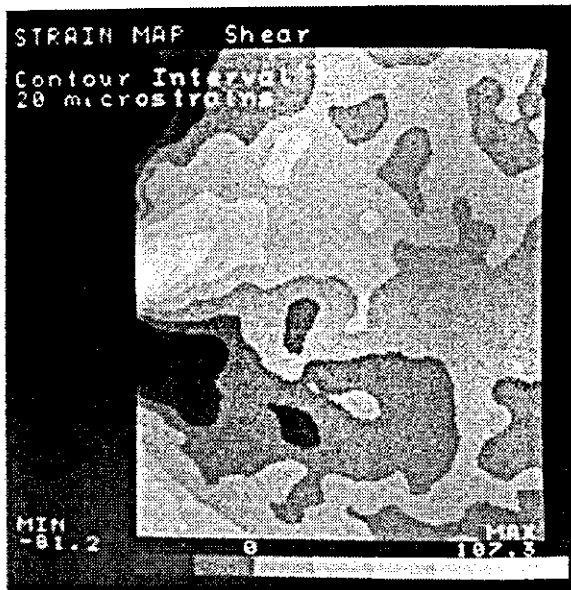
(a)



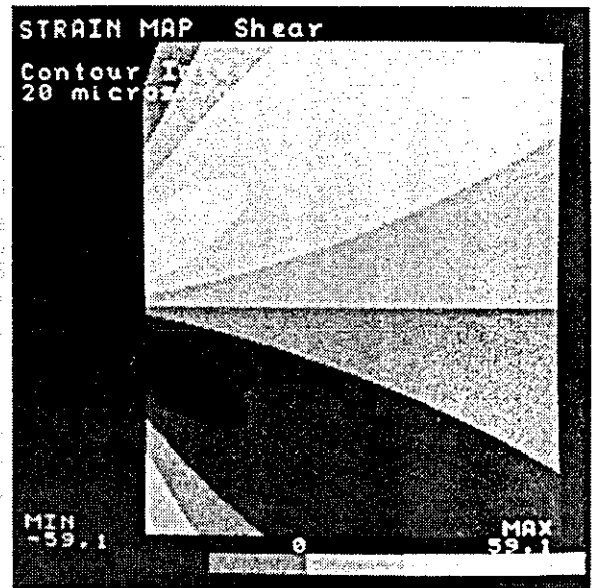
(b)

Figure 5.5 Strain distribution for centre-notched specimen
(Continued overleaf)

Experimental



Theoretical



(c)

Figure 5.5 (continued) Strain distribution for centre-notched specimen

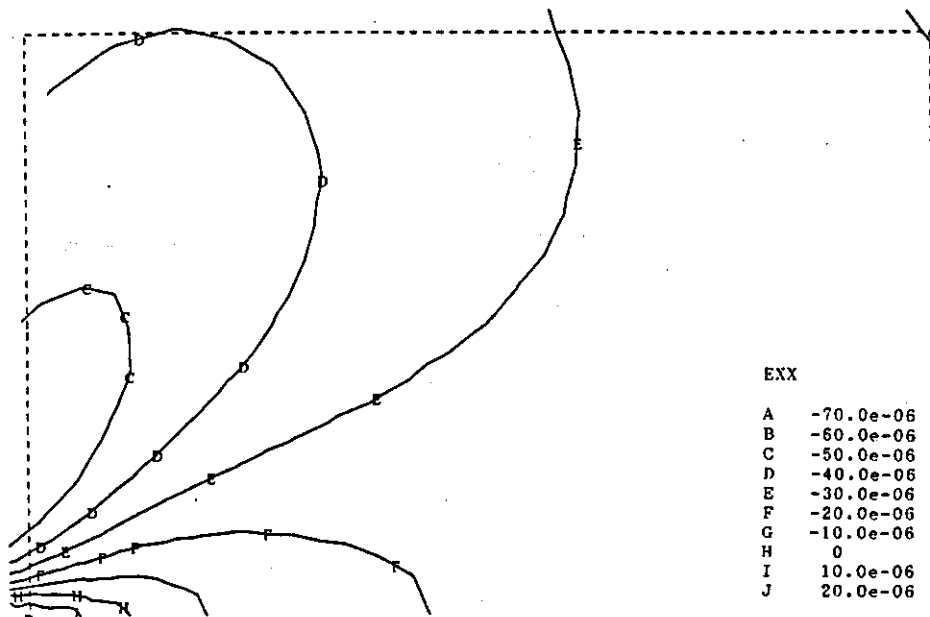
$$\epsilon_{xx} = \frac{K_I}{E\sqrt{2\pi r}} \cos\frac{\theta}{2} \left((1-\nu) - (1+\nu)\sin\left(\frac{\theta}{2}\right)\sin\left(\frac{3\theta}{2}\right) \right) - \frac{\sigma}{E}$$

$$\epsilon_{yy} = \frac{K_I}{E\sqrt{2\pi r}} \cos\frac{\theta}{2} \left(2 + (1+\nu) \left(\sin\left(\frac{\theta}{2}\right) \sin\left(\frac{3\theta}{2}\right) - 1 \right) \right) + \frac{\nu\sigma}{E} \quad (5.3)$$

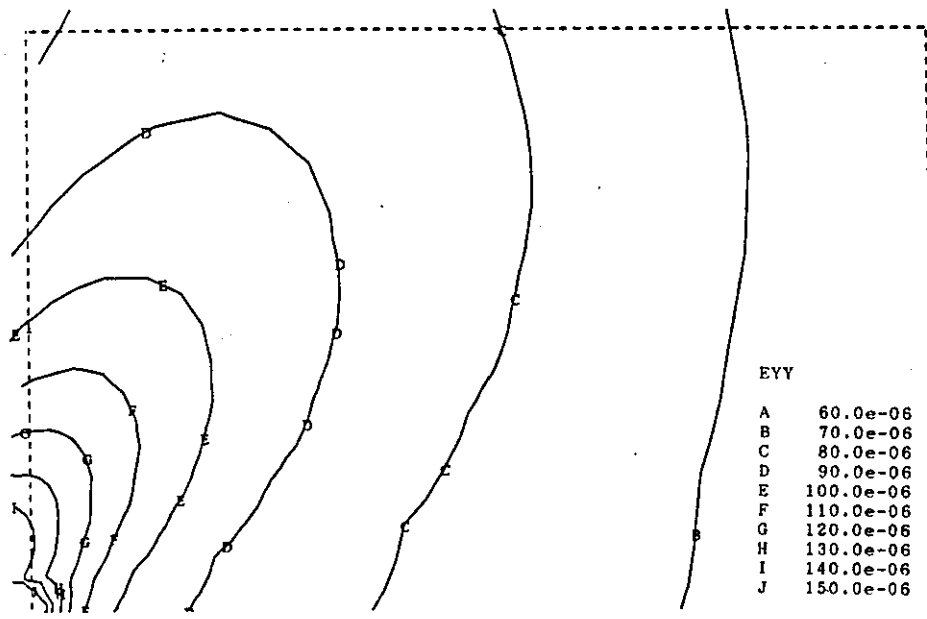
$$\gamma_{xy} = \frac{K_I}{E\sqrt{2\pi r}} 2(1+\nu) \sin\left(\frac{\theta}{2}\right) \cos\left(\frac{\theta}{2}\right) \cos\left(\frac{3\theta}{2}\right)$$

Equations (5.3) are plotted on the right hand side of Figure 5.5. Strain is plotted in $10\mu\text{strain}$ contours corresponding to the expected error in ϵ_{xx} and ϵ_{yy} , Figures 5.5(a) and 5.5(b) respectively. Due to the large range of values for shear strain, contours of width $20\mu\text{strain}$ were used, Figure 5.5(c). As previously, the contours have been scaled between 0 and 255 grey-levels. The experimental and theoretical strain distributions show reasonable agreement in shape, but not in range of values. The discrepancy is due to applying the modified Westergaard solution for $r \gg a/50$. The influence of the specimen boundary is clearly seen in the experimental ϵ_{xx} , Figure 5.5(a). This cannot be modelled by the two-parameter Westergaard solution: although K_I is modified for the finite plate width, the shape of the strain distribution is unaltered from that of the infinite plate distribution. Experimental ϵ_{yy} is noisier than ϵ_{xx} . The contours appear to have "lobes" extending in the direction of the original speckle fringes, suggesting that the applied phase step-size was in error. Noise was generally greater for the v (vertical in-plane) phase map; the fringes were not as stable as for the horizontal in-plane direction due to environmental disturbances to the optical fibres. The experimental shear strain distribution shows a considerably larger range of values than for the theoretical data, possibly due to the blunted notch and non-uniform applied stress.

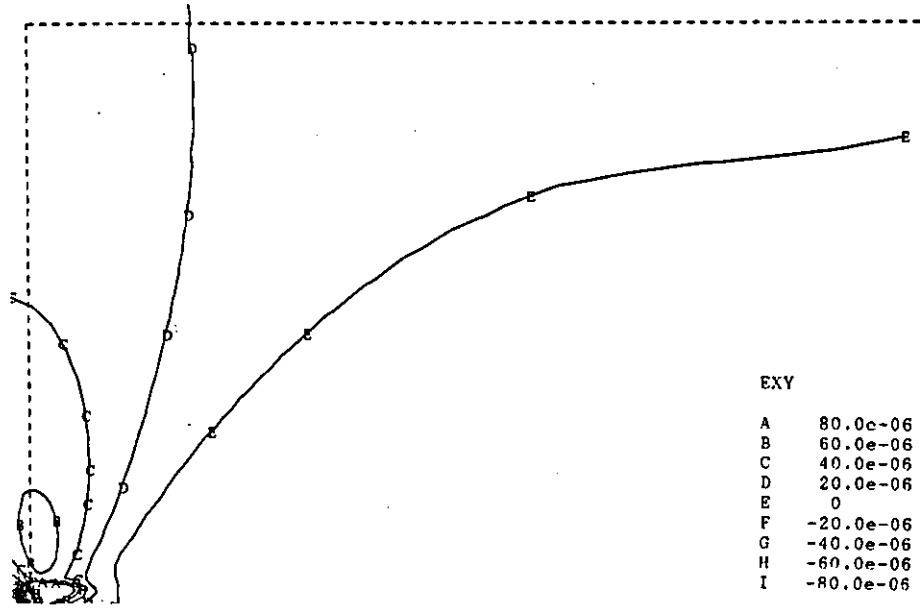
The strain distribution calculated from the FE model is shown in Figure 5.6. Good agreement with ESPI was obtained for ϵ_{xx} both in shape (e.g. effect of specimen



(a)



(b)



(c)

Figure 5.6 FE model of strain distribution for centre-notched specimen

boundary) and range of values. ϵ_{yy} gives a good approximation in the range of values. Some disturbance to the profile closest to the notch tip is seen, and the model close to the tip could be improved. The shear strain distribution shows values in the range 0 to $80\mu\text{strain}$ which is slightly misleading, in that higher strain values occur inside contour "A". A rapid rate of change of strain is calculated in this region that could not be measured by the 25×25 pixel plane fit. However, the model indicates the form of shear strain distribution ahead of the blunt notch that was measured in practice.

Studying the centre-notched plate highlighted several important points. Firstly, displacement (and therefore strain) could not be determined automatically close to the notch tip. The fringe pattern is barely discernible by the eye in this region, and is generally corrupted when lowpass filtering. Retaining high spatial frequency fringe information at the notch tip increases speckle noise in the remainder of the image. This leads to a compromise between measurement area and measurement noise. The shape of displacement and strain distributions was modelled reasonably well by the modified Westergaard solution, but the range of values was not good, e.g. horizontal in-plane displacement, Figure 5.2(c). Furthermore, the influence of boundaries cannot be accounted for, e.g. Figure 5.5(a). This demonstrates that the single-parameter (K) description of displacement, equation (5.2), cannot be used unless $r \ll a$, and yet ESPI cannot be used to make displacement measurements in this region. Thus a multi-parameter approach must be used to calculate K_I , Section 5.2.3. FE and ESPI results were in reasonable agreement, but notch tip conditions were not accurately modelled. This model could be "improved", but does not help to validate the ESPI results. The measurements of displacement and strain presented in this section may be used to calculate stress-intensity factor, K_I , crack-opening displacement, δ , and J-integral, J . This section has demonstrated the difficulty that would be experienced to validate these measurements for a non-standard specimen. Therefore a compact tension specimen was studied in the following section.

5.2 COMPACT TENSION SPECIMEN

Unlike the centre-notched plate of Section 5.1, the compact (CT) specimen is a standard for many fracture mechanics tests and consequently its characteristics are well documented. The specimen is described in Section 5.2.1. ESPI measurements made with the dual sensitivity interferometer are also presented in Section 5.2.1. Experimental work was also undertaken with another optical technique frequently used in fracture mechanics, namely moire interferometry. The aim was to verify measurements made using ESPI, and to provide a comparison between the techniques. Experimental details of the moire interferometry system and specimen preparation are described in Section 5.2.2. Phase-stepping enables the moire measurements to be processed similarly to the ESPI data. The methods used to determine K_I , δ and J from displacement fields are described in Section 5.2.3 to 5.2.5 respectively. Values for these parameters calculated from the ESPI and moire analysis are presented in Section 5.2.6.

5.2.1 ESPI Measurements

ESPI results were recorded using the dual sensitivity interferometer of Section 4.3.2. The HS30TF aluminium alloy compact tension (CT) specimens were loaded in the table-mounted tensiometer described in Section 5.1. One surface of each CT specimen was cross-hatch abraded as described previously.

The CT specimen geometry was originally fixed for fracture toughness (K_{Ic}) testing¹³, from the requirement that the plastic zone be small with respect to the region adequately described by a K-analysis. The plastic zone radius may be defined in terms of the ratio $(K_I/\sigma_y)^2$. Minimum values of a and W , required to ensure a suitably small plastic zone, were experimentally determined and defined in terms of this ratio¹². The overall dimensions of the CT specimens tested in this section, Figure 5.7, were derived from the loading pin separation of the hydraulic tensiometer, using the relationship $F=0.375W^{140}$. The loading pin diameter is 30%

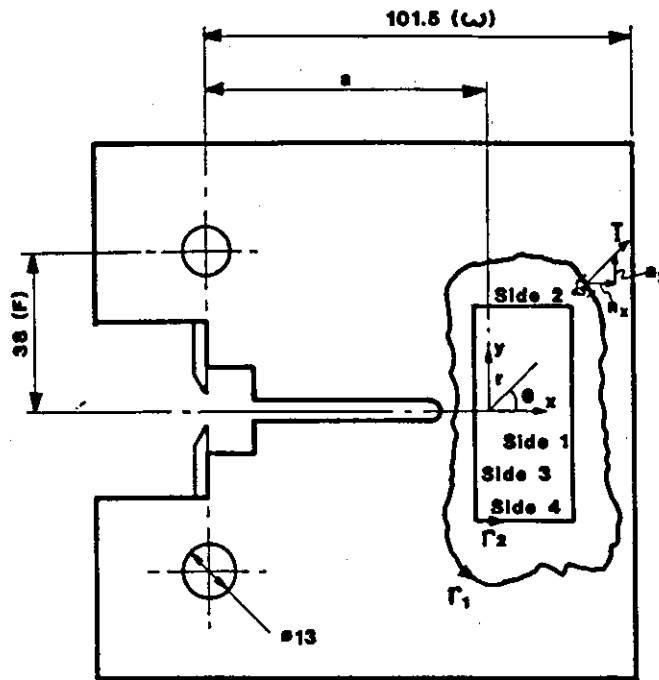


Figure 5.7 Compact tension specimen (Dimensions in mm)

smaller than specified. However, Newman¹⁴¹ found in a study of the effects of pin-loading on the CT specimen that the difference in K between a specimen with holes and one without was less than 1.5% for $a/W > 0.4$. Consequently the stress-intensity factor is reduced by less than 1.5% from the value given by²⁰:

$$K_I = \frac{P}{BW^{3/2}} Y \quad (5.4)$$

where:

$$Y = \frac{\left(2 + \frac{a}{W}\right)}{\left(1 - \frac{a}{W}\right)^{3/2}} \left(0.886 + 4.64\left(\frac{a}{W}\right) - 13.32\left(\frac{a}{W}\right)^2 + 14.72\left(\frac{a}{W}\right)^3 - 5.6\left(\frac{a}{W}\right)^4\right)$$

which is valid for $a/W \geq 0.35$. P and B are the applied load (kN) and specimen thickness (cm) respectively. W is also expressed in cm, to give K_I in $\text{MN/m}^{3/2}$ ($\text{MPa m}^{1/2}$). Another deviation from the standard geometry should be noted. In order to exclude all plasticity effects the specimen was not fatigued. Instead -4mm

Measurement	Specimen					
	CT1 (a/W)=0.56		CT2 (a/W)=0.66		CT3 (a/W)=0.75	
	Load (N)	LLD (μm)	Load (N)	LLD (μm)	Load (N)	LLD (μm)
1	99	10.9	74	16.3	25	11.7
2	198	22.1	149	32.6	50	21.4
3	297	36.1	223	47.0	74	33.0
4	396	48.1	297	61.3	99	43.5

Table 5.1 Applied load and load-line displacement (LLD) for ESPI tests

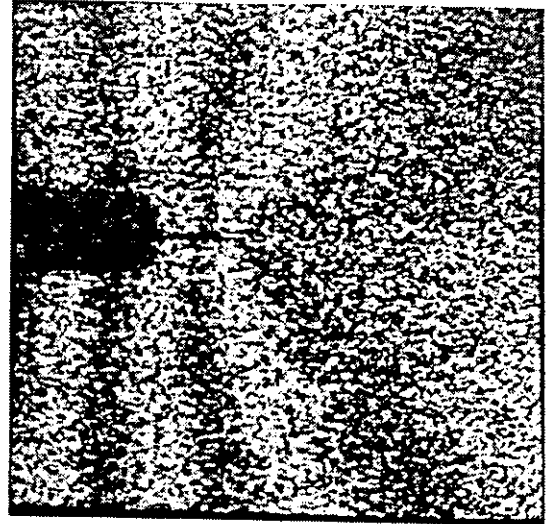
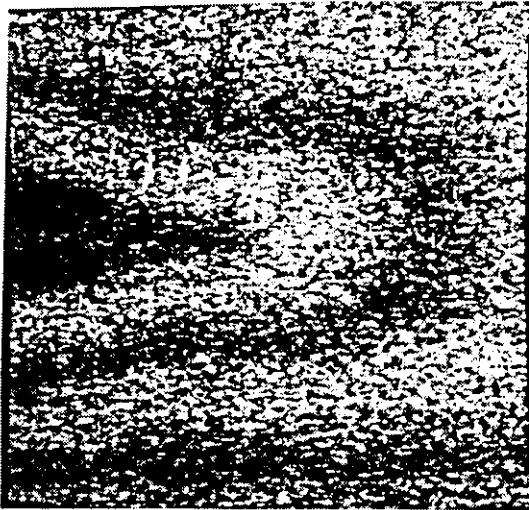
notches of width 0.2mm were introduced by electrodischarge machining. This is analogous to the use of a slitting saw in photoelasticity: although crack tip acuteness is important at the fracture event, notches of width 1.2mm are acceptable to accurately determine the geometrical shape factor, Y^{32} . The ratios a/W for the three specimens tested (including EDM notch) were 0.56, 0.66 and 0.75. These specimens were denoted CT1, CT2 and CT3 respectively. The corresponding Y values are 11.74, 17.83 and 30.04 from equation (5.4). A maximum specimen thickness $B=6.35$ mm could be accommodated by the tensiometer, insufficient to ensure plane strain conditions. This is acceptable because all testing remained in the linear elastic regime, and K_{Ic} was not to be determined.

For each specimen, 248N was applied to pre-stress the loading fixtures. Measurements of u and v displacements were made at four equal load increments above this initial load. Therefore eight phase-maps were recorded for each specimen: u and v at each of four loads. Between each load increment the

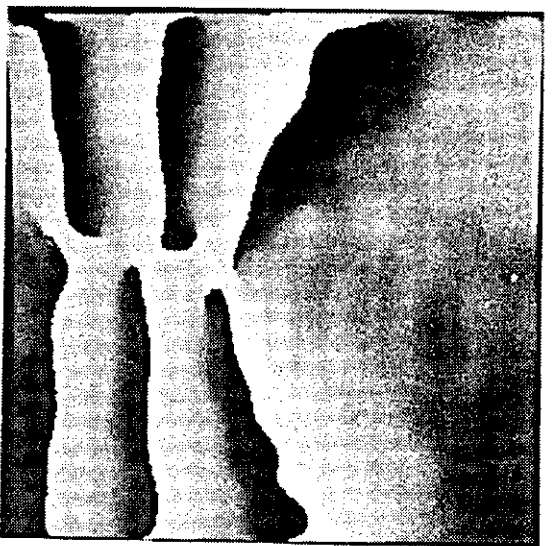
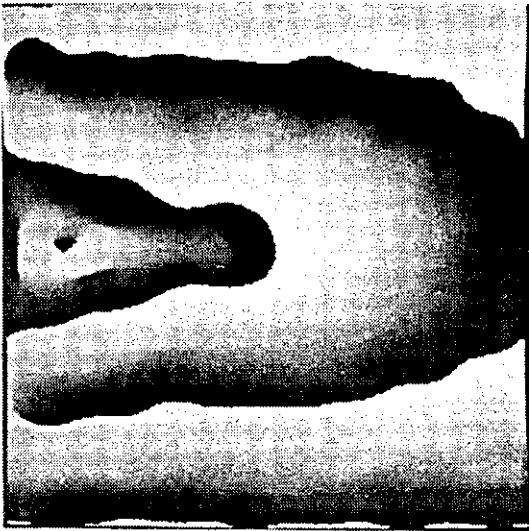
framestores were re-referenced. Consequently the phase-maps denote the incremental displacement between successive loads. The displacement at the load-line was monitored with a clip-gauge mounted between knife-edges, which were screwed to the CT specimen¹⁶. Calibration proved the clip-gauge to be linear over the range 0 to 0.7mm, with resolution of $0.4\mu\text{m}$ and an accuracy of approximately $\pm 2.3\%$. Table 5.1 shows the loads applied to each of the three specimens (in addition to the initial pre-stress value), and the recorded displacement at the load-line. Typical results are shown in Figure 5.8, for the specimen CT1 loaded at 99N. The measurement area is 25mm x 25mm. One of three phase-stepped fringe patterns for both the horizontal and vertical in-plane sensitivities are shown in Figure 5.8(a). Speckle noise was reduced with a Fourier filter (cut-off frequency $\sim 6\text{lp}$), and the phase-maps of Figure 5.8(b) calculated. From the previous calibration, the cut-off frequency of the Fourier filter corresponds to $\pm 0.03\mu\text{m}$ and $\pm 6.5\mu\text{strain}$ measurement error. A qualitative check of the measured u and v displacement data is given in Figure 5.8(c). Theoretical displacements have been calculated using a six-parameter expansion of the equations describing the displacement distribution around a crack. An expansion of this type was used to determine K_I from the u and v displacement fields, and its explanation is therefore deferred to Section 5.2.3. The relevant equation is (5.5), using $C_0 = K_I/\sqrt{(2\pi)} = 0.23\text{MN/m}^{3/2}$. The strain distribution can also be described by a similar series expansion. Explanation is again deferred to Section 5.2.3 where the relevant equation is (5.8). Equations (5.8) are plotted on the right-hand side of Figure 5.9. Strain values calculated from a 25x25 pixel plane fit to the unwrapped displacement data are shown on the left-hand side. The components of strain ϵ_{xx} , Figure 5.9(a), and ϵ_{yy} , Figure 5.9(b) are plotted in $6.5\mu\text{strain}$ contours, corresponding to the measurement error. Shear strain, Figure 5.9(c) is plotted in contours of $\sqrt{2}*(6.5)\mu\text{strains}$. Reasonable agreement in profile and range of values is achieved in all cases. Differences between experimental and theoretical plots are discussed in Section 5.2.3 when the model has been explained.

Horizontal in-plane

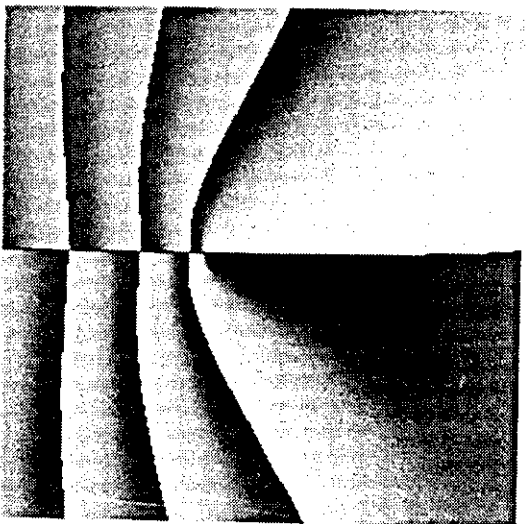
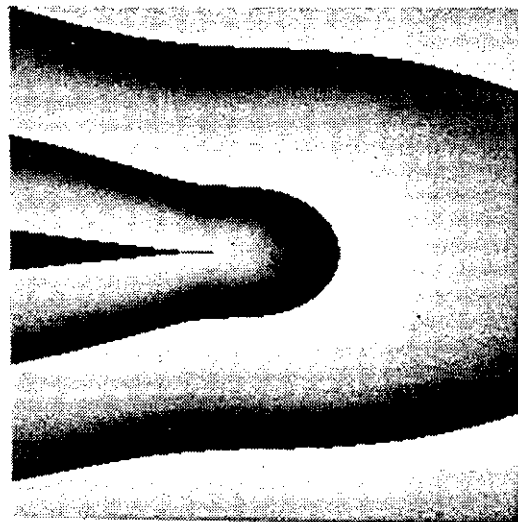
Vertical in-plane



(a)



(b)

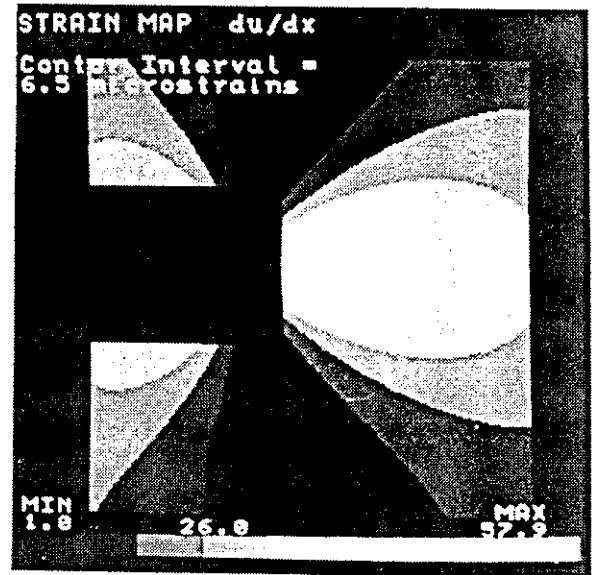
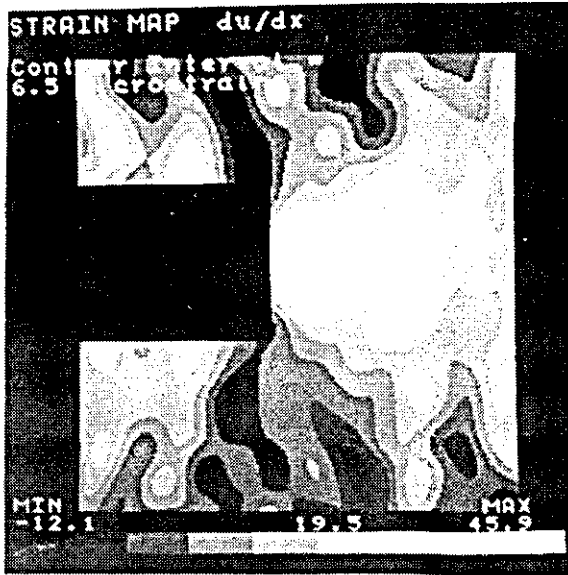


(c)

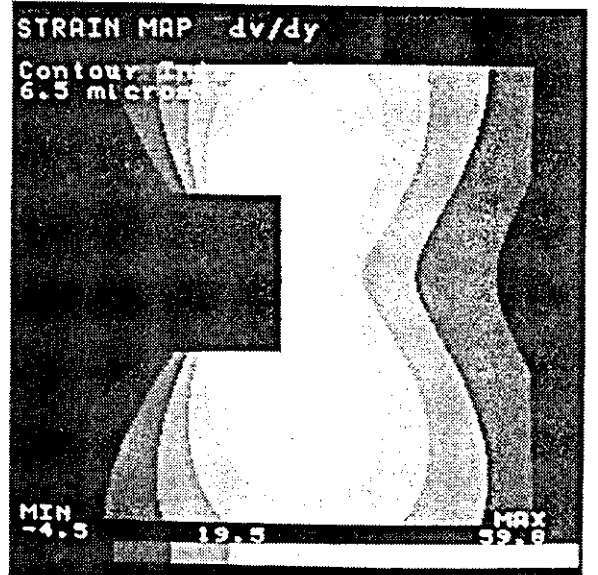
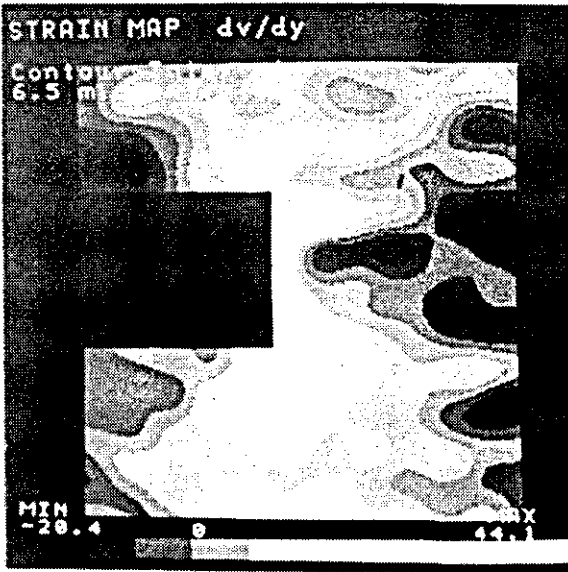
Figure 5.8 Typical ESPI results (CT1 at 99N)

Experimental

Theory



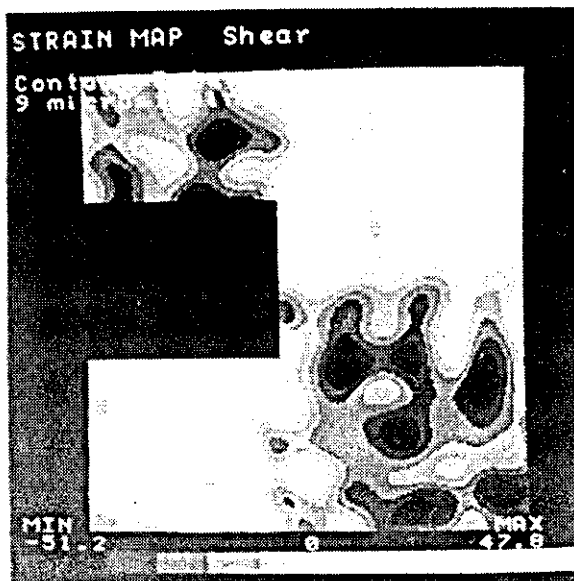
(a)



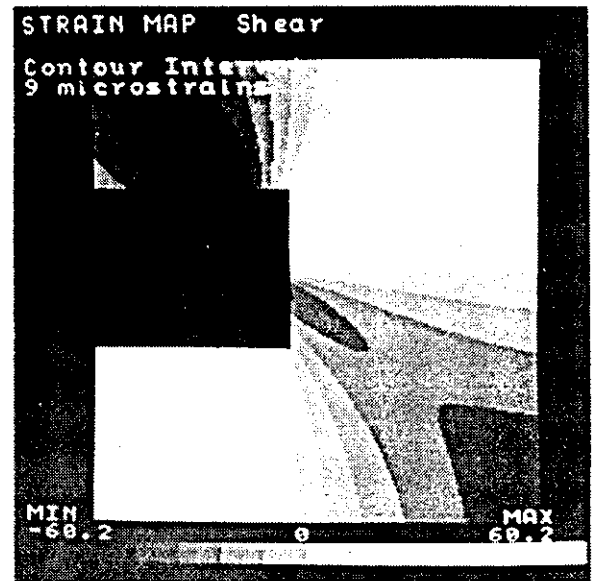
(b)

Figure 5.9 Strain distribution for CT1 at 99N (Continued overleaf)

Experimental



Theory



(c)

Figure 5.9 (continued) Strain distribution for CT1 at 99N

5.2.2 Moire Interferometry Measurements

Moire interferometric results were recorded for the CT specimens with the commercially available system Optecord, manufactured and sold by Strathclyde University¹⁴². The system consists of a single HeNe laser source which is divided into three 50mm diameter beams that illuminate the measurement region along the x, y and 45° directions. Interference between pairs of the beams can be considered to provide stable reference gratings at 0°, 45° and 90° to the x-axis. A suitable crossed diffraction grating is bonded to the object under test. When positioned correctly within the measurement region, moire fringes corresponding to in-plane displacements in the x, y and 45° directions are formed between the bonded grating and the selected reference grating. For these tests, the grating frequency was 950 lines/mm, yielding a moire sensitivity of 1.05 μm/fringe. Details of grating replication are given in the Optecord instruction manual¹⁴². The process involves casting a crossed diffraction grating in epoxy resin to the specimen surface; the mould is a silicone rubber replica made from a master grating. To enable reliable grating replication close to the notch tip, the notch was plugged with plasticine. Initial tests with the epoxy resin grating were found to be unrepeatable on unloading and reloading the specimens. This was attributed to the brittle epoxy pulling away from the specimen surface in the region of the notch. Thus silicone rubber gratings, including the dye normally used in the epoxy resin, were used for the experiments reported here. An extra replication process is required: master grating to silicone rubber replica; silicone replica to epoxy resin replica; epoxy replica to silicone rubber grating cast on the specimen surface. Consequently the final grating was generally not of such good quality as that cast in epoxy.

The Optecord system has been used to measure the J-integral for a CT specimen^{45,46}. Measurements with three different sensitivities (0, 45°, 90°) were required to resolve the direction-of-displacement ambiguity. Although fringe thinning was implemented⁴⁶ strain calculation was performed manually. If phase-stepping is used, only measurements with 0° and 90° sensitivities (i.e. horizontal

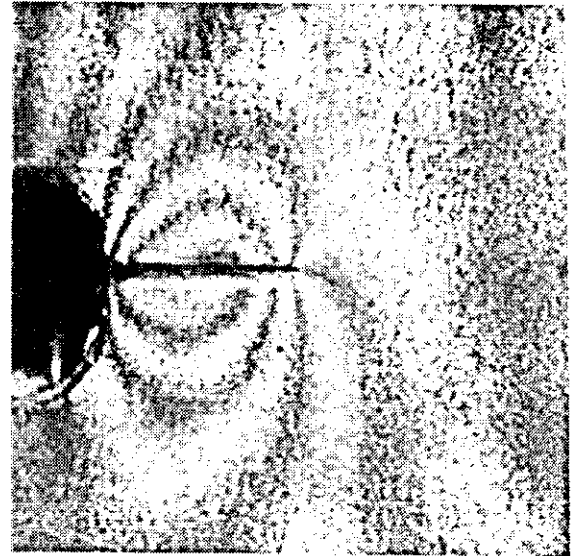
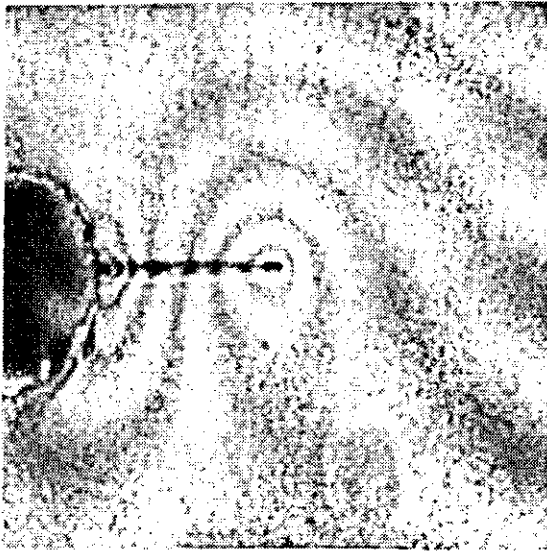
and vertical in-plane) are required to define the two-dimensional displacement field. Full-field strain data can then be automatically calculated from the unwrapped phase data as described in Chapter 3. Brownell has constructed such a system at Rolls Royce plc, Derby¹²⁵. The phase of one expanded beam of an Optecord interferometer can be stepped by rotating an optical flat positioned in the beam. Three phase-stepped images are digitised (256x256 pixels x 8-bit resolution) to an Imaging Technology VG100 board, and the phase calculated by equation (3.12). Switching between illumination geometries (i.e. reference gratings) enables phase maps corresponding to horizontal and vertical sensitivity vectors to be recorded. If desired, simultaneous recording along the two sensitivity vectors could be achieved using the system described in Chapter 4.

Figure 5.10 shows results recorded with the Rolls Royce interferometer for CT1, in an early test with an epoxy resin grating. Figure 5.10(a) shows one of three phase-stepped moire fringes recorded for the u (left-hand side) and v (right-hand side) displacement components. The displacements are due to a 248N load applied to pre-stress the specimen mounts. The corresponding phase maps are shown in Figure 5.10(b). These are termed the "reference" phase maps, and are used to remove errors due to non-linearities in the specimen grating. Pixels at which the intensity modulated with an amplitude of less than eight grey-levels were marked, and are displayed with zero grey-level in Figure 5.10(b). Since no pre-processing lowpass filter was applied to the moire fringes, many pixels in the background were marked automatically. In some instances this included data along the EDM notch, for example the v data of Figure 5.10(b). Often, however, the notch was not marked as background, and a hand drawn mask of invalid pixels was defined from the live image, for example, the u data of Figure 5.10(b). It was necessary to mask the EDM notch in order to avoid unwrapping errors, since displacement is not continuous across the notch.

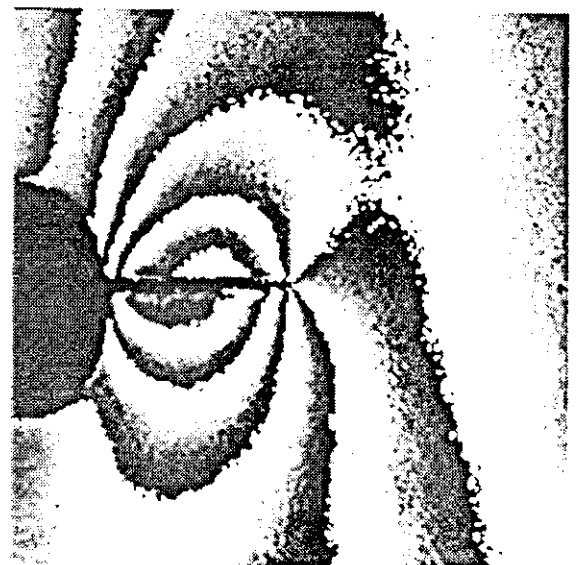
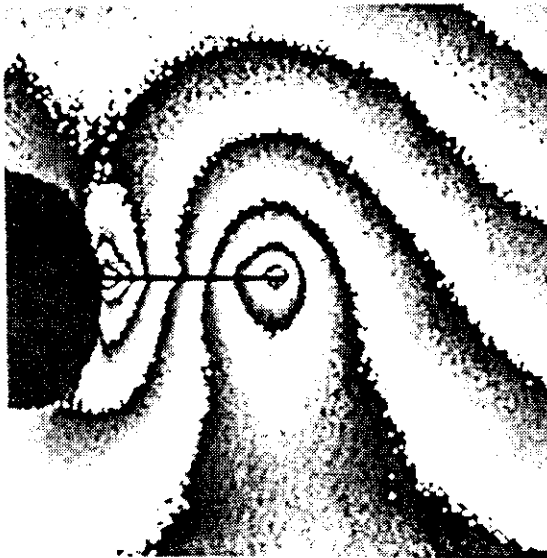
Figure 5.10(c) shows the u and v "measurement" phase maps recorded for an additional load of 941N. Non-linearities in the grating are removed if the unwrapped reference phase map, Figure 10(b), is subtracted from the appropriate

Horizontal in-plane

Vertical in-plane



(a)



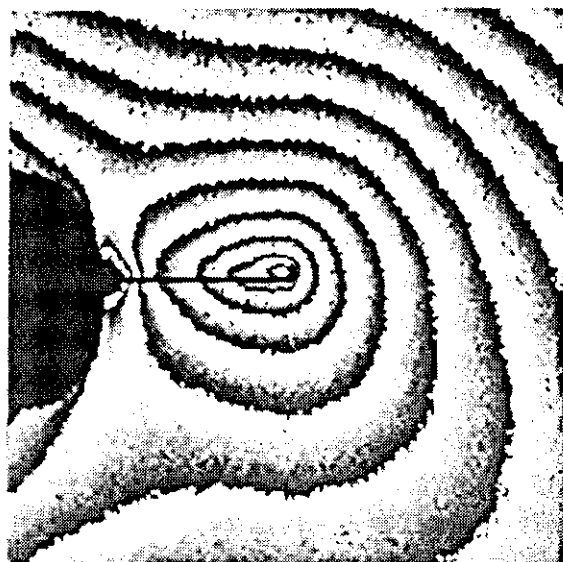
(b)

Figure 5.10 Moiré reference, measurement and corrected images

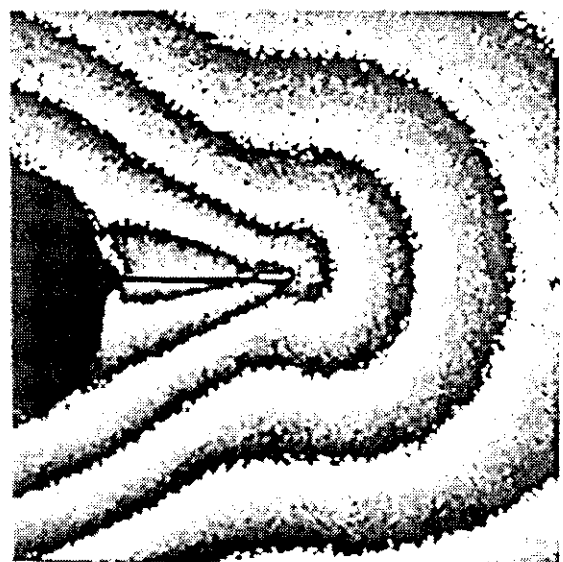
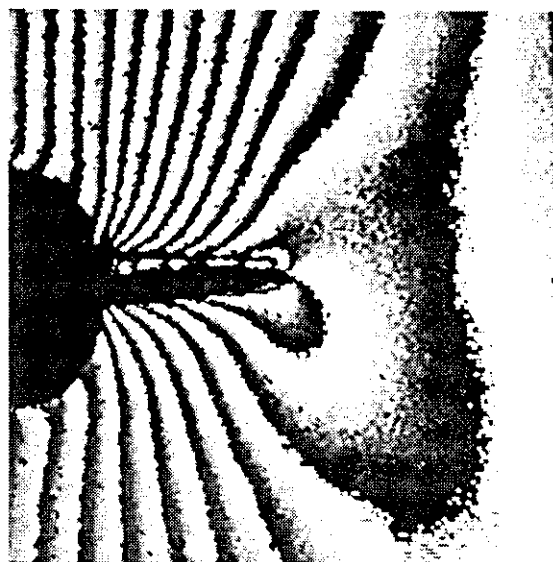
(Continued overleaf)

Horizontal in-plane

Vertical in-plane



(c)



(d)

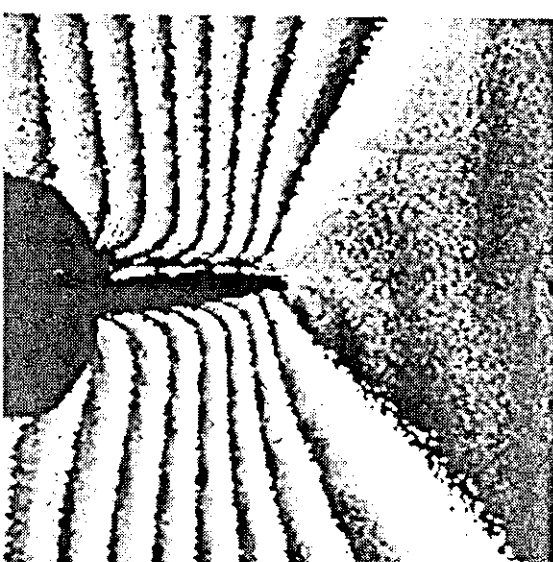
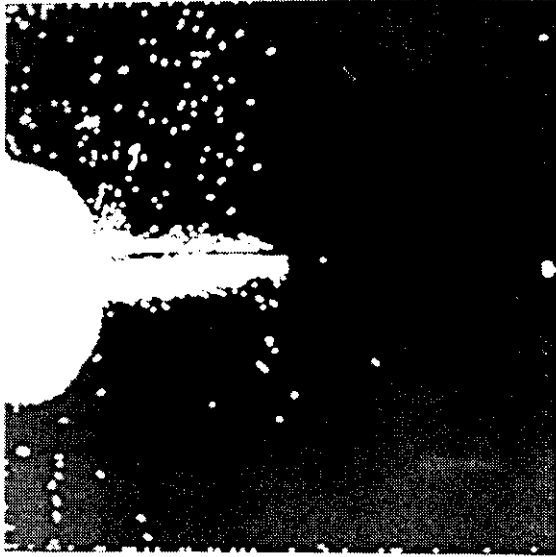


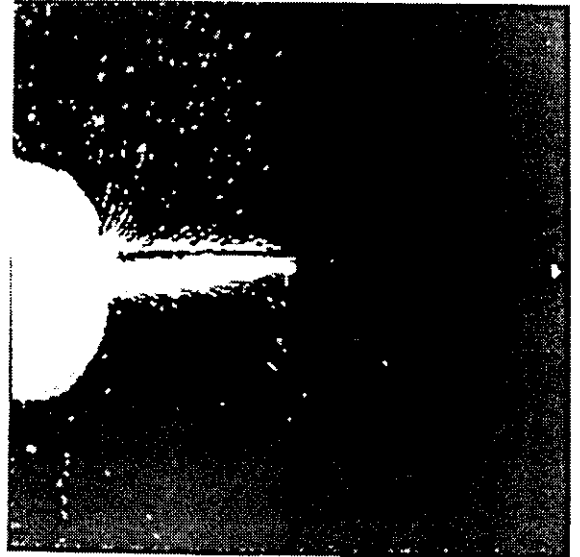
Figure 5.10 (continued) Moiré reference, measurement and corrected images

unwrapped measurement phase map, Figure 5.10(c). The result is the "corrected" phase maps of Figure 5.10(d), which have been re-wrapped for the figure. Pixels that are marked in either the reference or measurement phase map remain marked in the corrected phase map. These pixels retain a unique phase value, and are displayed in Figure 5.10(d) with a grey-level of zero. The corrected phase data for each measurement was stored to disk as 256 fixed length records; each record contained 512 bytes i.e. two bytes of unwrapped phase information per pixel. The formatted data file was transferred to the MicroVax for subsequent analysis. Figure 5.10 and subsequent moire results are recorded from the Kontron image processor. The image becomes elongated in the vertical direction: the measurement area of 15 mm (horizontal) x 10mm (vertical) is digitised to rectangular pixels by the VG100 board, whereas the Kontron uses square pixels.

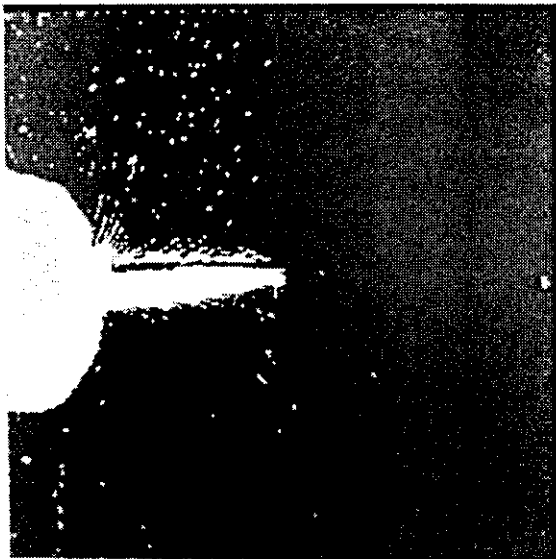
Figure 5.11(a) shows marked pixels from the vertical in-plane corrected phase map of Figure 5.10(d). Marked pixels include those marked manually along the notch-line and those at which the intensity modulation amplitude is insufficient in either or both of the reference and measurement phase maps. Marked pixels rarely occur in the measurement area for TPSSC, and so the strain calculation routines were not designed to accommodate them. Therefore it was necessary to remove marked pixels which were not part of the object background. To do this, the unique phase value that denoted a marked pixel was replaced by the average of valid (unmarked) pixels in the 3x3 pixel neighbourhood of each marked pixel. The pixel is no longer considered to be marked. If the marked pixel had no unmarked neighbours, the pixel remained marked. This process corresponds to an eight-connected erosion of the marked pixels¹⁴³. The process was repeated until no marked pixels remained in the phase data except those in the background. Figure 5.11(b) shows the result of three iterations of the marked pixel erosion. Marked pixels from Figure 5.11(a) that have been replaced by a valid unwrapped phase value are represented by a grey-level of 128. Finally, the same number of eight-connected dilations can be applied to restore the background, Figure 5.11(c). Three dilations have been used, once again marked pixels have the grey-level 255, and formerly marked pixels have the grey-level 128. Figure 5.11(d) shows the



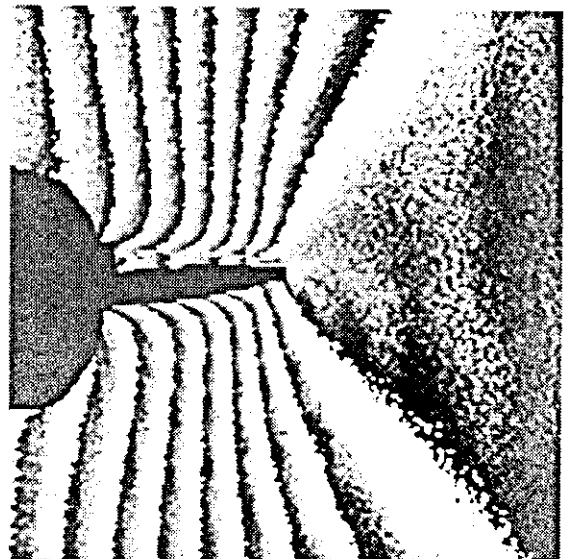
(a)



(b)



(c)



(d)

Figure 5.11 Removal of marked non-background pixels

Measurement	Specimen					
	CT1 (a/W)=0.56		CT2 (a/W)=0.66		CT3 (a/W)=0.75	
	Load (N)	LLD (μm)	Load (N)	LLD (μm)	Load (N)	LLD (μm)
1	495	60.6	495	103.7	248	116.9
2	990	124.2	743	161.5	446	219.3
3	1486	186.0	990	214.3	664	320.7
4	1981	254.7	1238	279.5	842	418.9

Table 5.2 Applied load and load-line displacement (LLD) for moire tests

unwrapped phase data after removal of non-background marked pixels, re-wrapped for display. This corresponds to the corrected phase data of Figure 5.10(d), to which the strain evaluation routines of Chapter 3 may now be applied.

Results were recorded with the silicone rubber gratings for the same three CT specimens already described in Section 5.2.1. For each specimen, an upper load limit was determined at which the unwrapping routine repeatedly failed for the v data due to the high fringe density. A reference phase map was recorded with a pre-load of 248N for each specimen. Measurement phase maps were then recorded at four loads evenly distributed between the pre-load and the unwrapping-determined load limit. The load increments in addition to the pre-stress load are shown in Table 5.2, along with the recorded displacement at the load-line. Corrected phase maps were created and written to formatted data files. Thus eight data files were transferred to the MicroVax for each specimen: corrected u and v phase maps at each of four loads. Non-background marked pixels were removed by the process already described. The data was then in a

compatible format to the ESPI measurements of Section 5.2.1 for subsequent analysis.

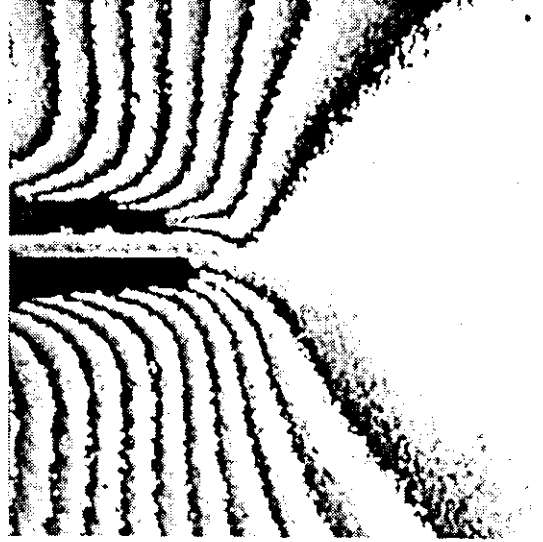
In Section 3.3.1 it was noted that the ordinate intercept of the 25x25 pixel plane, fitted to the unwrapped displacement data to calculate strain, could be used to smooth the data. In general this has not been done, because it does not represent the fundamental accuracy of the technique. However, the u-measurements made from specimen CT1 were found to be very noisy. Figure 5.12(a) and 5.12(b) show the corrected u- and v-displacement measurements respectively for CT1 at a load of 1486N. Non-background marked pixels have been removed. The results have been converted to wrapped phase in order to highlight the poor quality of the u data. The silicone rubber used to cast this grating was already starting to cure at the time of its application to the CT1 specimen surface, possibly due to a slight excess of curing agent. This may be responsible for the "ripple" effect that is visible in Figure 5.12(a). A 25x25 pixel window has been used to smooth the unwrapped displacement data, by equation (3.36). The result is shown in Figure 5.12(c), again converted to wrapped phase. It should be re-emphasised that smoothing was only applied to the u data for CT1. All other corrected phase maps were of similar quality to Figure 5.12(b), and were used without smoothing. Close to the notch-line, the phase discontinuities in the v data run parallel to the notch, Figure 5.12(b). This was occurred for all v-measurements for the three specimens, possibly because the grating was not cut along the notch-line. The regions above and below the notch at which the vertical phase discontinuities began to curve parallel to the notch were excluded from the subsequent analysis.

5.2.3 K_I -Evaluation from Displacement Measurements

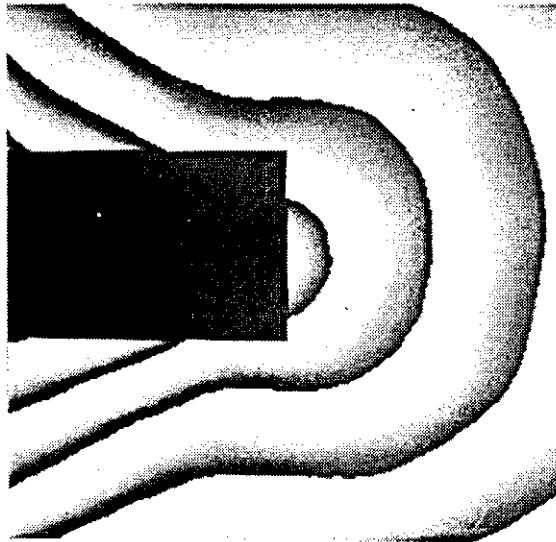
Equations (5.2) adequately describe the displacement distribution in the singularity-dominated zone ($r < a/50$). Displacements may be defined in terms of a single parameter, namely the stress-intensity factor, K . Therefore, displacement measurements made within the singularity zone can be used to determine K ; some



(a)



(b)



(c)

Figure 5.12 Moire results for CT1

examples were given in Section 2.2. Preliminary experimental work showed that it is difficult to make displacement measurements with ESPI in the singularity zone. Firstly the rigid body motion required to decorrelate the reference and object speckle patterns decreases with increased magnification, equation (3.37). Herbert et al⁷⁵ obtained fringes of poor quality when measuring the out-of-plane deformation with ESPI in a 1mm² region around crack tips. Secondly, high spatial frequency fringe information at the crack tip is removed by the lowpass filter required by the TPSSC method, Section 5.1. Thus the single-parameter crack tip displacement field characterisation cannot easily be used to determine K with ESPI. The same is true for many other experimental mechanics techniques, and a method of determining the stress-intensity factor from data gathered outside the singularity zone must be used.

One solution is to use a multi-parameter description of the displacement field surrounding the crack-tip. Sanford¹⁴⁴ addressed this problem, having noticed that isochromatic fringes formed ahead of the crack in photoelastic studies involving cracks approaching the boundary in CT specimens. This implied that the maximum shear stress, i.e. the principal stress difference, varied along the crack-line. The Westergaard and modified Westergaard solutions assume this value to be zero and constant respectively, Appendix A. Sanford proposed a generalised solution incorporating the original Westergaard solution plus a polynomial function. The Westergaard solution itself can be expressed in terms of an infinite series, giving a solution as the sum of polynomials. Details of this solution are given in Appendix A, from which the generalised Sanford solution for the displacement field around the crack is given by:

$$\begin{aligned}
Eu &= \sum_{j=0}^J C_{2j+1/2} \frac{r^{j+1/2}}{j+1/2} [(1-\nu)\cos(j+1/2)\theta - (1+\nu)(j+1/2)\sin\theta\sin(j-1/2)\theta] \\
&\quad + \sum_{j=0}^J C_{2j+1} \frac{r^{j+1}}{j+1} [2\cos(j+1)\theta - (1+\nu)(j+1)\sin\theta\sin j\theta] \\
Ev &= \sum_{j=0}^J C_{2j+1/2} \frac{r^{j+1/2}}{j+1/2} [2\sin(j+1/2)\theta - (1+\nu)(j+1/2)\sin\theta\cos(j-1/2)\theta] \\
&\quad + \sum_{j=0}^J C_{2j+1} \frac{r^{j+1}}{j+1} [(1-\nu)\sin(j+1)\theta - (1+\nu)(j+1)\sin\theta\cos j\theta]
\end{aligned} \tag{5.5}$$

The number of terms required to adequately describe the displacement field increases with distance from the crack tip and the proximity of any boundaries. For example, with $j=0$, the two-parameter description of displacement is identical to equation (5.2) and is therefore valid only in the singularity zone. A comparison of equations (5.2) and (5.5) shows that:

$$C_0 = \frac{K_I}{\sqrt{2\pi}} \tag{5.6}$$

The number of terms required, and the coefficient for each term, may be estimated by a comparison of the experimentally measured displacement field with a plot of equation (5.5). For example, Chona et al¹⁴⁵ performed a photoelastic study of wedge loaded CT specimens with various a/W ratios. Data was gathered in a region of radius 12.75 mm around the crack tip, and a six-parameter stress-field representation modelled the experimental pattern well. Taking $a/W=0.56$, the non-dimensionalised parameters C_0' to C_5' may be estimated from Figure 6 of reference 145, and used to calculate the first six parameters. This gives:

$$\begin{aligned}
C_1 &= C_1' C_0 / W^{1/2} = 0.53 C_0 / W^{1/2} \\
C_2 &= C_2' C_0 / W = -4.0 C_0 / W \\
C_3 &= C_3' C_0 / W^{3/2} = 1.25 C_0 / W^{3/2} \\
C_4 &= C_4' C_0 / W^2 = -3.3 C_0 / W^2 \\
C_5 &= C_5' C_0 / W^{5/2} = -6.7 C_0 / W^{5/2}
\end{aligned} \tag{5.7}$$

The parameters of equation (5.7) may be substituted into equation (5.5). If $K_1=0.58\text{MNm}^{-3/2}$ and $W=101.5\text{mm}$, an approximation to the u and v displacement components for specimen CT1 at a load of 99N is obtained, Figure 5.8(c). These displacements have been converted to wrapped phase for a qualitative comparison with the experimentally determined phase maps, Figure 5.8(b). Differences between the experimental and theoretical plot exist due to the crudity of the model: no terms describing rigid body motion of the specimen have been included, and the coefficients were calculated for wedge loading. However, the suitability of this type of analysis with ESPI displacement measurements is confirmed. The strain distribution described by Sanford's polynomial expansion is derived in Appendix A, and is given by:

$$\begin{aligned}
 E\varepsilon_{xx} &= \sum_{j=0}^J C_{2j} r^{j-1/2} [(1-\nu)\cos(j-1/2)\theta - (1+\nu)(j-1/2)\sin\theta\sin(j-3/2)\theta] \\
 &\quad + \sum_{j=0}^J C_{2j+1} r^j [2\cos j\theta - (1+\nu)j\sin\theta\sin(j-1)\theta] \\
 E\varepsilon_{yy} &= \sum_{j=0}^J C_{2j} r^{j-1/2} [(1-\nu)\cos(j-1/2)\theta - (1+\nu)(j-1/2)\sin\theta\sin(j-3/2)\theta] \\
 &\quad + \sum_{j=0}^J C_{2j+1} r^j [(1+\nu)j\sin(j-1)\theta - 2\nu\cos j\theta] \\
 \mu\gamma_{xy} &= - \sum_{j=0}^J C_{2j} r^{j-1/2} (j-1/2)\sin\theta\cos(j-3/2)\theta \\
 &\quad - \sum_{j=0}^J C_{2j+1} r^j [j\sin\theta\cos(j-1)\theta + \sin j\theta]
 \end{aligned} \tag{5.8}$$

These equations were plotted in Figure 5.9 with the coefficients of equation (5.7). Reasonable agreement between theory and experimental values is obtained. Notice that strain data is not calculated immediately adjacent to the crack-line, because the window is reduced by $(p-1)/2$ pixels at all edges, Section 3.3.1.

In order to calculate the actual coefficients from the ESPI and moire displacement data for the specimens CT1-CT3, a least-squares method originally proposed by Barker et al⁴³ was used. The method is outlined briefly here: details specific to this implementation are given in the next paragraph. Referring to equation (5.5), assume that n coefficients (i.e. $j=0$ to $n/2$) are required to accurately describe the displacement profile over the data acquisition region. Both u and v are linear functions with respect to the unknown coefficients C_n . At any point (r_i, θ_i) the displacement may be written in the form:

$$\begin{aligned} Eu_i &= S_{inu}(r_i, \theta_i)C_n \\ Ev_i &= S_{inv}(r_i, \theta_i)C_n \end{aligned} \quad (5.9)$$

where $S_{inu}(r_i, \theta_i)$ and $S_{inv}(r_i, \theta_i)$ represent the n positional constants determined by equation (5.5) for the u and v components respectively. If displacement measurements are made at m points ($m > n$) a set of over-determined linear equations is obtained, that may be expressed in matrix form by:

$$\begin{aligned} [Eu] &= [S_u][C] \\ [Ev] &= [S_v][C] \end{aligned} \quad (5.10)$$

$[S_u]$ and $[S_v]$ are m (rows) and n (columns) matrices containing the positional constants, and $[Eu]$ and $[Ev]$ are $m \times 1$ matrices of displacement at the points (r_i, θ_i) . The $n \times 1$ elements of the coefficient matrix $[C]$ must be determined. Provided that $m > n$, the unknown coefficients can be determined in a least-squares sense i.e. the problem reduces to determining the coefficients of the series that produce the best match to the displacement measurements at the selected points. This least-squares method was originally proposed by Sanford and Dally³⁵ to calculate K_I and K_{II} for photoelastic specimens. K_I and K_{II} are, however, non-linear functions of the isochromatic fringe order, and an iterative procedure was used to solve the

equations in addition to the minimisation process associated with the least squares method. Data sets of 20 points gave more accurate results than traditional two- and three-data-point methods, and made use of the full-field nature of photoelastic measurements. Sanford¹⁴⁶ proposed the non-linear least-squares method to determine K_I in photoelastic studies when the crack tip position was obscured by a caustic shadow: the isochromatic fringe order is also non-linear with respect to r and θ . Huntley and Field⁶⁶ used this non-linear least-squares method with displacement data obtained by speckle photography and noted that a reasonable initial estimate of the coefficients was required to ensure convergence to the global minimum. They performed a preliminary linear analysis followed by a non-linear analysis including the parameters r and θ to allow for uncertainty in the measured crack tip position. Locating the EDM notch tip was not difficult, and consequently a linear analysis was implemented for the ESPI and moire measurements.

Programs were written on the MicroVax to collect (r_i, θ_i, u_i) , and (r_i, θ_i, v_i) data sets from the unwrapped phase map from a grid of points. This is substantially easier than defining points on the fringe maxima and manually entering the fringe order^{35,43,145,146}. The u_i and v_i measurements include a contribution due to rigid body motion of the specimen. Barker et al^{5,23} proposed a method of dealing with rigid body motion, but the interpretation is slightly different with phase-stepped ESPI and moire interferometry. Rigid body translations cause a constant fringe shift over the entire field, but make no contribution to the unwrapped phase data. Provided that the starting pixel for phase-unwrapping (the reference point) is defined at the notch tip, rigid body translation can be ignored. It was rarely possible, however, to unwrap phase to the notch tip. Therefore a constant term that modelled the actual displacement at the reference point with respect to the displacement at the notch tip was required. Rigid body rotations introduce a constant gradient fringe field dependent on the angle of rotation, and a fractional shift that depends on the centre of rotation. A constant fractional fringe shift may be ignored by the preceding discussion, and so the constant gradient field is assumed to lie at the notch tip. The added displacement at the point (r_i, θ_i) is

given by equation (3.38). Combining the two "rigid body motion" terms in the form of equation (5.7) gives:

$$\begin{aligned} Eu_i &= Pr\sin\theta + R \\ Ev_i &= Qr\cos\theta + S \end{aligned} \quad (5.11)$$

The experimental displacements u_i and v_i are obtained by adding the rigid body displacement, equation (5.11) to the crack tip displacement, equation (5.5). The result for u is linear in the unknowns C_0 to C_n , P , R , and for v is linear in C_0 to C_n , Q and S . A solution of the form of equation (5.10) is therefore still applicable.

The linear least-squares evaluation was performed by the NAG Fortran library subroutine FO4AMF. This routine selects the matrix $[C]$ in order to minimise the sum of the squares of the residuals, S , e.g.

$$\sum_{i=1}^m S^2 = ([Eu] - [S_u][C])^T ([Eu] - [S_u][C]) \quad (5.12)$$

Iterative refinement of the solution is repeated until full machine accuracy has been obtained. An eight-parameter solution was chosen i.e. $j=0$ to 4 in equation (5.5). To determine if eight parameters was sufficient for the measurement area of the ESPI and moire tests, the masks of Figure 5.13(a) and Figure 5.13(b) were generated for the u and v data respectively. The horizontal line denotes the notch position. The marks show those regions in which the displacement calculated by equation (5.5) with the coefficients C_0 to C_4 of equation (5.7) differed by more than 3% from the corresponding six-parameter (i.e. C_0 to C_5) solution. Displacement values at these pixels were excluded from the (r_i, θ_i, u_i) and (r_i, θ_i, v_i) data sets. It was assumed that eight parameters would be sufficient in the remaining region. Figure 5.13 also shows a circle of radius $B/2$ centred at the notch tip. Points falling within this circle were also excluded from the K analysis: displacements made less than one-half of the plate thickness from the crack tip should not be used, to ensure that the surface displacements are representative of displacements through the specimen thickness¹⁴⁷. Barker et al¹⁴³ investigated the number of points required to minimise the effect of random errors. These were

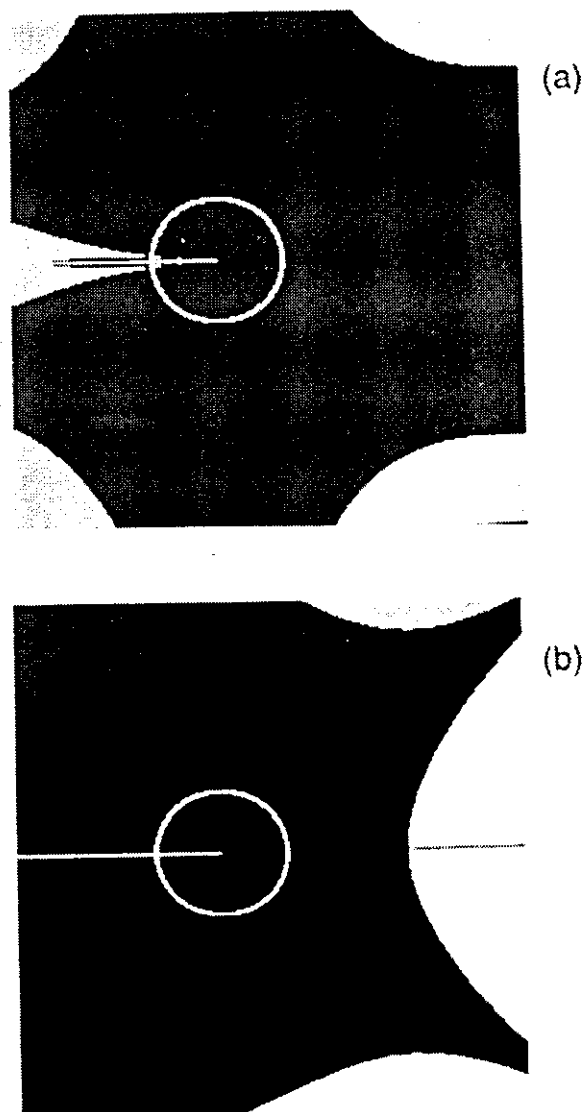


Figure 5.13 Regions of invalid data for (r, θ, u) and (r, θ, v) data sets

assumed to arise from positional uncertainty in the coordinates of fringe maxima located for each data point. They concluded that the number of data points should be ten times the number of coefficients for the average error to tend to zero. Thus at least 100 data points were gathered for each data set, so that random phase errors present in both phase-stepped ESPI and moire data sets were reduced. Typically between 300 and 400 points were used. Two data sets were gathered for each phase map. Results are presented in Section 5.2.6.

5.2.4 Crack-Opening Displacement Evaluation

With sufficient magnification and accurate phase data adjacent to the notch tip, the crack-opening displacement could be measured as the difference in v either side of the crack-line immediately behind the crack tip. This is the simplest solution, although the exact position of these two points with respect to the crack tip may be open to interpretation. However, valid phase data was not generally available at the notch tip with either ESPI or moire, and so another method was required. With all the testing performed in the linear elastic regime it can be assumed that the crack faces remote from the tip remain linear throughout the test. Therefore a straight line may be least-squares fitted to the v -displacement values that occur along two horizontal lines either side of the notch-line and equidistant from it. Combining the values for the ordinate at the origin of these fitted lines gives the crack-tip opening displacement, δ , as shown in Figure 5.14. The data points were recorded with ESPI for CT1. A cyclic variation due to a small phase-step error is noticeable, particularly for data above the notch-line. The load-line displacement can be determined by extrapolation, also indicated in the figure. Ideally, the v -displacement data from horizontal lines immediately adjacent to the notch should be used. However, this was not possible for either the ESPI or moire measurements. This was due to distortion of the fringe pattern approaching the notch-line for the moire data, Figure 5.12(b); with ESPI the Fourier filter renders phase measurements close to areas of background unreliable. Thus judgement was needed to select the first horizontal lines of valid

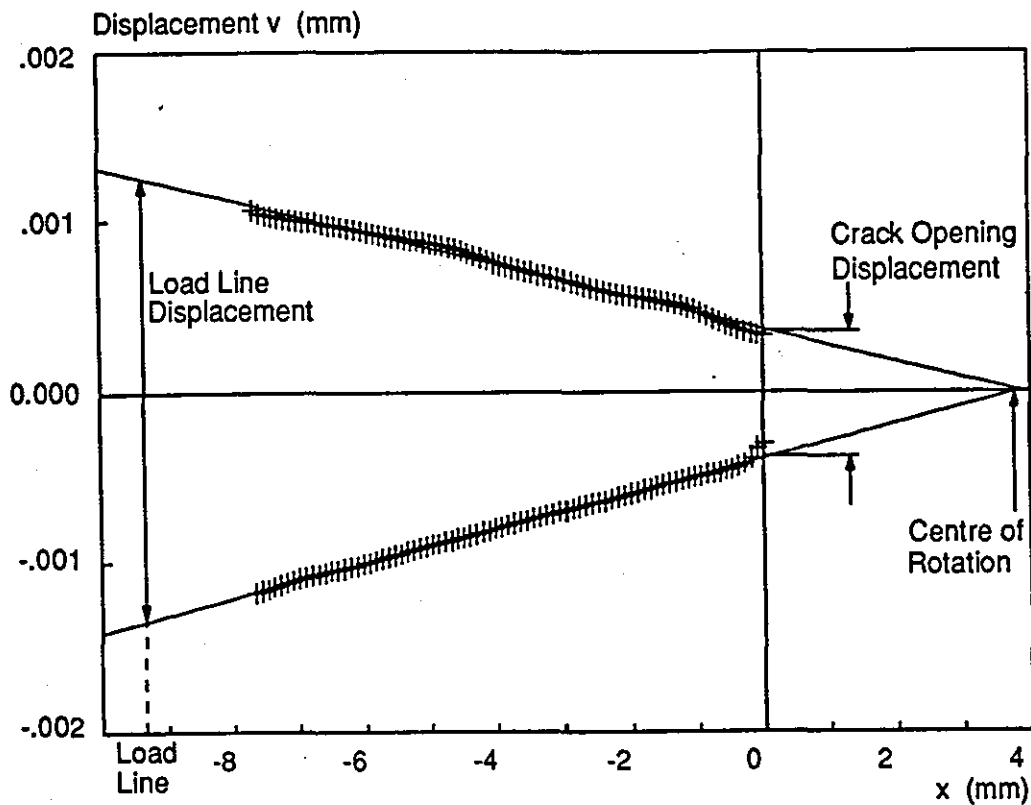


Figure 5.14 Measurement of crack-opening displacement

phase data lying as close to the notch as possible. For the 12 δ measurements made with ESPI, the average distance of the horizontal data line from the notch-line was 2.9 mm; for moire the corresponding figure was 1.7 mm.

The position of the centre of rotation does not change with increasing load in the linear elastic regime. Furthermore the load-line displacement is proportional to the load. It is apparent from Figure 5.14 that δ is proportional to K_I when δ is determined by this method, rather than the squared relationship given by equation (2.7). Therefore the values of LLD determined from the v data are used in Section 5.2.6 to estimate the compliance of each specimen, and are also compared directly with the clip-gauge readings. Compliance measurements were then used as an independent measure of J .

5.2.5 J-Integral Evaluation

The contour-independent line integral, J , was discussed in Section 2.1.3, and is defined by equation (2.9). In this equation, W is the strain energy density¹²⁴, defined under plane stress conditions by:

$$W = \frac{E}{2(1-\nu^2)} (\epsilon_{xx}^2 + \epsilon_{yy}^2 + 2\nu\epsilon_{xx}\epsilon_{yy}) + \frac{\mu}{2}\gamma_{xy}^2 \quad (5.13)$$

$T = \sigma_{ij}n_j$ is the traction vector on Γ according to an outward unit vector \mathbf{n} (with direction cosines n_j) normal to the curve. In matrix form:

$$T = \begin{pmatrix} \sigma_{xx} & \tau_{xy} \\ \tau_{xy} & \sigma_{yy} \end{pmatrix} \begin{pmatrix} n_x \\ n_y \end{pmatrix} \quad (5.14)$$

The partial differential of the displacement vector, \mathbf{u} , can also be expressed in matrix form:

$$\frac{\partial \mathbf{u}}{\partial \mathbf{x}} = \begin{pmatrix} \epsilon_{xx} \\ \partial v / \partial x \end{pmatrix} \quad (5.15)$$

Combining equations (5.14) and (5.15) yields:

$$T \frac{\partial \mathbf{u}}{\partial \mathbf{x}} = \left(\sigma_{xx}\epsilon_{xx} + \tau_{xy} \frac{\partial v}{\partial x} \right) n_x + \left(\sigma_{yy} \frac{\partial v}{\partial x} + \tau_{xy}\epsilon_{xx} \right) n_y \quad (5.16)$$

The direct strain ϵ_{xx} and rotational term $\partial v / \partial x$ are available from the strain evaluation routines. The components of stress, under plane stress, are given by rearranging equations (A.1) i.e:

$$\begin{aligned} \sigma_{xx} &= \frac{E}{(1-\nu^2)} (\epsilon_{xx} + \nu\epsilon_{yy}) \\ \sigma_{yy} &= \frac{E}{(1-\nu^2)} (\epsilon_{yy} + \nu\epsilon_{xx}) \\ \tau_{xy} &= \mu\gamma_{xy} \end{aligned} \quad (5.17)$$

For each pair of phase maps, the quantities, W , σ_{ij} , ϵ_{xx} and $\partial v/\partial x$ were written to a data file to avoid time consuming recalculation. The evaluation of equation (5.16) is greatly simplified for a rectangular contour, Γ_2 in Figure 5.7, because n_j take the values 0, -1 and 1. On defining two opposite corners of a rectangular contour, equation (2.9) was automatically evaluated from values read from the data file. It was not necessary to interpolate between separated measurement points on the contour, since full-field data is available (unlike reference 66) without prohibitively slow manual calculations (unlike reference 46). Typical strain distributions were shown in Figure 5.9, and it was noted that strain was not calculated immediately adjacent to the crack-line. Thus for any contour enclosing the crack tip, Side 3 will include a length for which no valid data is available. W and $T\partial u/\partial x$ are smaller close to the free surface than at other points on the contour, and therefore the omission of a few data points makes very little difference to the overall contour integral. However, for moire data sets in which the region of horizontal discontinuities adjacent to the notch-line was excluded, no W and $T\partial u/\partial x$ values existed for a considerable proportion of side 3. Thus the contour evaluation for side 3 included a straight-line fit to valid W and $T\partial u/\partial x$ values above and below the notch-line. These lines were extrapolated to the notch-line in order to evaluate equation (2.9) at points adjacent to the notch-line. Unwrapping failures occurred in the moire data above the notch-line for specimens CT2 and CT3, which restricted the number of contours that could be defined in this region. Thus J was calculated over "half" a contour defined below the notch-line, and the result doubled for the moire results for these two specimens.

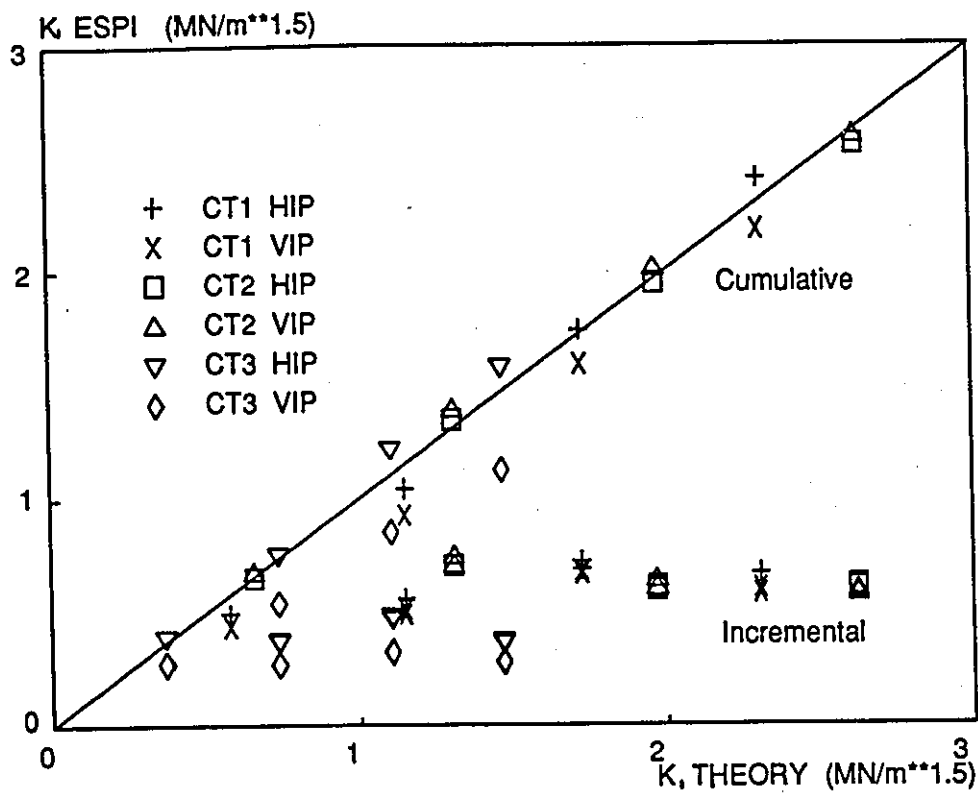
5.2.6 ESPI and Moire Interferometry Results

K_I measurements for the three CT specimens are shown in Figure 5.15. The graphs for ESPI, Figure 5.15(a), and moire interferometry, Figure 5.15(b), both contain 48 measurement points: two (r_i, θ_i, u_i) and two (r_i, θ_i, v_i) data sets gathered at each of the four loads for three specimens. The experimentally determined K_I values (ordinate) were calculated from the leading coefficient, C_0 , of the least-

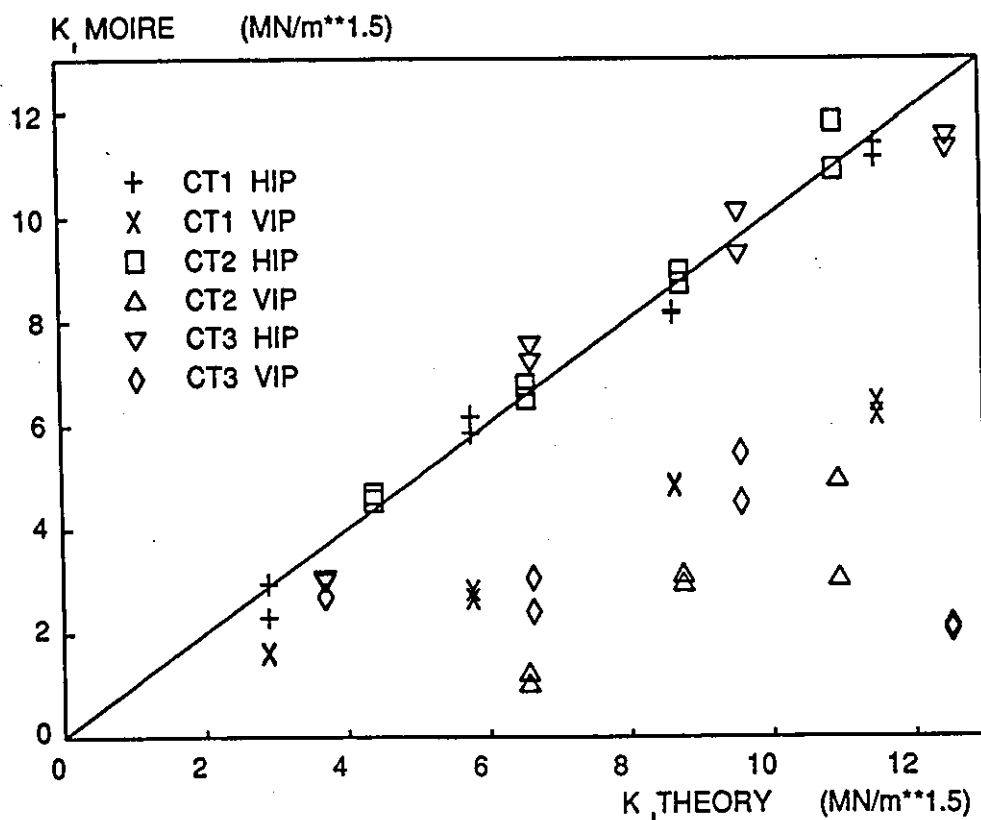
squares fit using equation (5.6). The theoretical K_I values (abscissa) were calculated from equation (5.4) using the loads given in Tables 5.1 and 5.2.

The framestores were re-referenced between each load increment for the ESPI measurements. Each phase map therefore measures the incremental displacement between successive loads; hence the increase in K_I between successive loads is calculated from each phase-map. The pair of "incremental" K_I measurements for each phase map is seen at the bottom of Figure 5.15(a). K_I is linearly related to displacement. Consequently, the mean of each pair of incremental measurements has been added to give a "cumulative" horizontal in-plane (HIP) and vertical in-plane (VIP) total for each specimen, Figure 5.15(a). An alternative solution would be to sum successive displacement measurements before collecting the (r_i, θ_i, u_i) and (r_i, θ_i, v_i) data sets. Moire interferometry measures this total (cumulative) displacement giving K_I at each load directly, Figure 5.15(b). It is evident from both graphs that in some cases the solution calculated from vertical in-plane displacement data converges to a least-squares best-fit set of coefficients that is not correct for the fringe pattern analysed. (CT3 VIP in Figure 5.15(a), CT1, CT2, CT3 VIP in Figure 5.15(b)). In fact a negative K_I value was obtained at load 1 from the vertical in-plane moire data for CT2. Chona et al¹⁴⁵ encountered this problem in photoelastic studies and proposed a sampled least-squares method for analysis of the data, to be used "whenever necessary". These erroneous solutions are generally consistent for both the data sets taken from each vertical in-plane phase map, and in some instances increase linearly with load (CT3 VIP in Figure 5.15(a), CT1, CT2 VIP in Figure 5.15(b)). Consequently it is not apparent from the vertical in-plane K_I values alone when recourse to the sampled least-squares solution is necessary, unless the result is wildly in error e.g. negative. Rather than using a sampled least-squares solution, therefore, only experimental K_I values calculated from horizontal in-plane phase maps were used in the subsequent analysis.

Deviations between theoretical and experimental K_I values arise due to residual speckle noise in the phase data: no systematic error is apparent for the horizontal



(a)



(b)

Figure 5.15 K_I measurements for CT1, CT2 and CT3

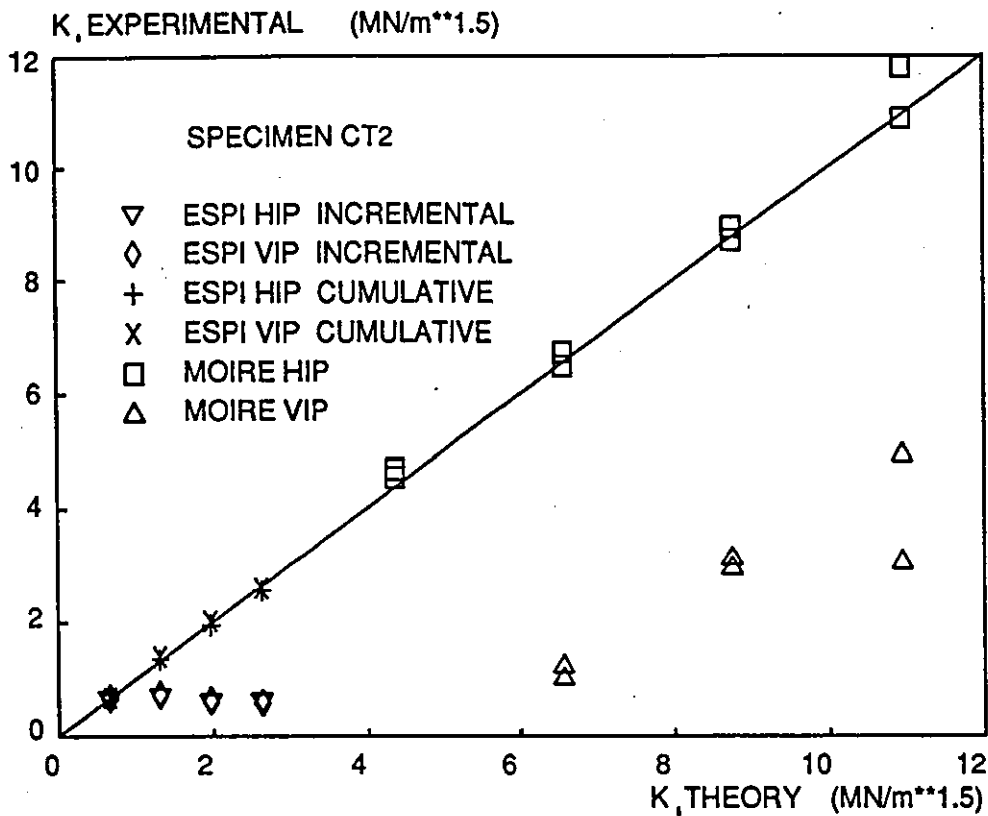


Figure 5.16 Comparison of ESPI and moire K_I measurements for CT2

in-plane values. The mean difference between two measurements taken from the same horizontal in-plane phase map is $0.01\text{MN/m}^{3/2}$ and $0.35\text{MN/m}^{3/2}$ for the ESPI and moire tests respectively. This corresponds to a signal-to-noise ratio of 36dB and 30dB over the respective measurement ranges of $-0.7\text{MN/m}^{3/2}$ for ESPI and $-11.7\text{MN/m}^{3/2}$ for moire. All cumulative ESPI and moire results fall within $\pm 9.8\%$ and $\pm 11.3\%$ respectively of the theoretical values. Thus the accuracy of both techniques is comparable. Figures 5.15(a) and 5.15(b) are combined for specimen CT2 in Figure 5.16. This emphasises the sensitivity of ESPI, although the measurement range is significantly less than for moire interferometry. However, it is possible to calculate cumulative values with ESPI as demonstrated.

As discussed in Section 5.2.4, the method to determine crack-opening displacement from v measurements will not enable the relationship with K_I^2 to be investigated. Instead, values of load-line displacement (LLD) determined by the same method are presented in Figure 5.17. Results from the ESPI tests have been plotted against the recorded clip gauge value. The ESPI measurement at each

load increment has been summed to give a cumulative LLD. Good agreement is obtained between the two techniques. More interestingly, these LLD values may then be used to determine the compliance, C , of each specimen. The values in Tables 5.1 and 5.2 were plotted on a graph of load against load point displacement. The compliance of each specimen is defined as (1/gradient) of the load-displacement graph. Compliance was calculated separately for the ESPI and moire tests, and are plotted in Figure 5.18 against crack length, a . A cubic spline interpolation is shown, from which a rather crude estimate of $(\partial C/\partial a)$ was calculated manually. These values are shown in the figure. Compliance testing was an early fracture mechanics technique by which the strain energy release rate, G , was calculated via⁹:

$$G = \frac{P^2}{2B} \left(\frac{\partial C}{\partial a} \right) \quad (5.18)$$

For linear elastic conditions, $J \equiv G$, Section 2.2.1. This gives an independent approximation to J .

The J integral should be constant for any contour that encloses the notch tip, and zero otherwise. Speckle noise in the measured strain data will cause J to vary with the contour chosen. In order to study the noise present in J measurements, the following test was performed. Referring to Figure 5.7 showing the rectangular contour, sides 1, 2 and 4 were defined at the edge of available data. Side 3 was then traversed from the left hand edge of the image to the right, one pixel at a time. J was calculated for each contour thus defined. The process was then repeated, but with sides 1, 2 and 3 at the image edges and side 4 traversed down the image. This test can be performed very quickly, since the required data is available at nearly all points in the image (i.e. full-field measurement, and J is evaluated automatically). Figure 5.19 shows the result of continuous variation in the position of side 3 for specimen CT1. ESPI measures the J increment between successive loads, Figure 5.19(a), while moire interferometry, Figure 5.19(b), measures the cumulative J value. The x -position of the notch tip is indicated by a vertical line in both graphs. When side 3 is positioned to the left of this line, the

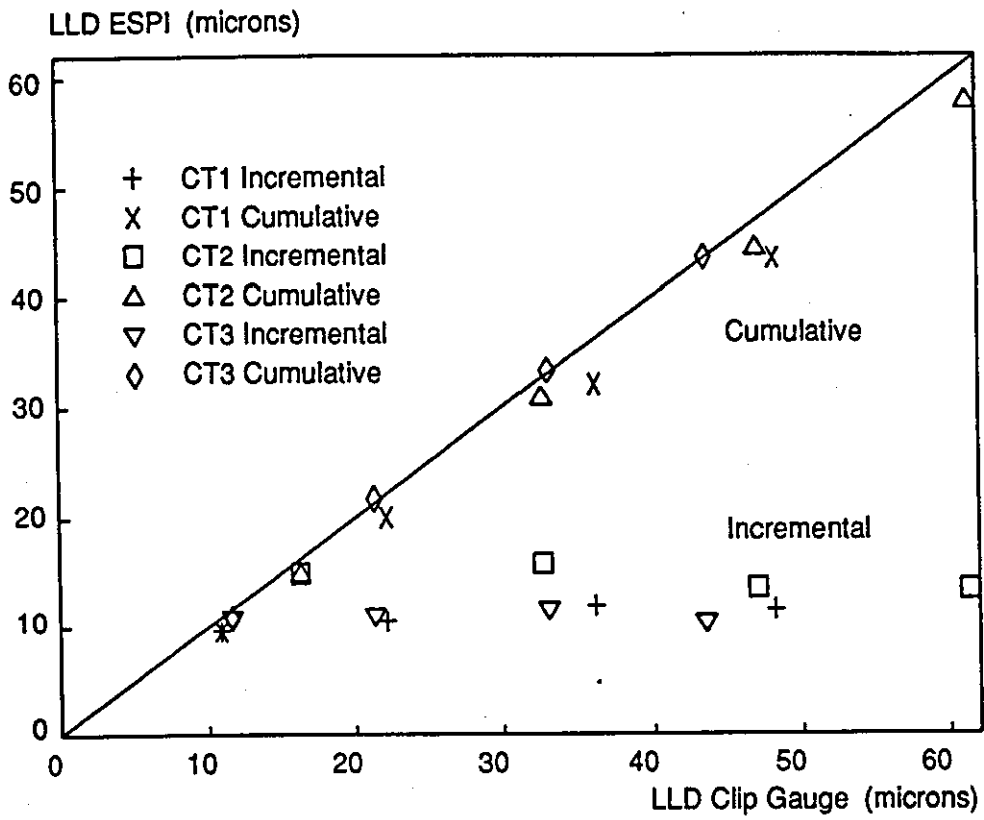


Figure 5.17 Load-line displacement measurements from ESPI data

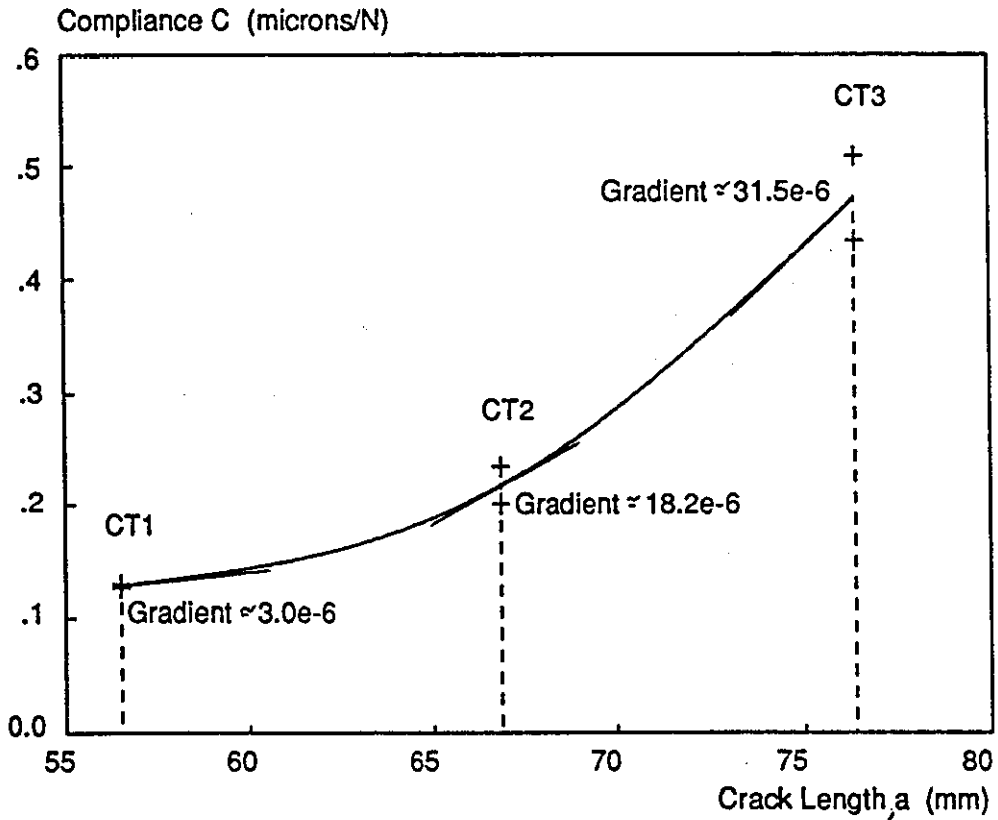


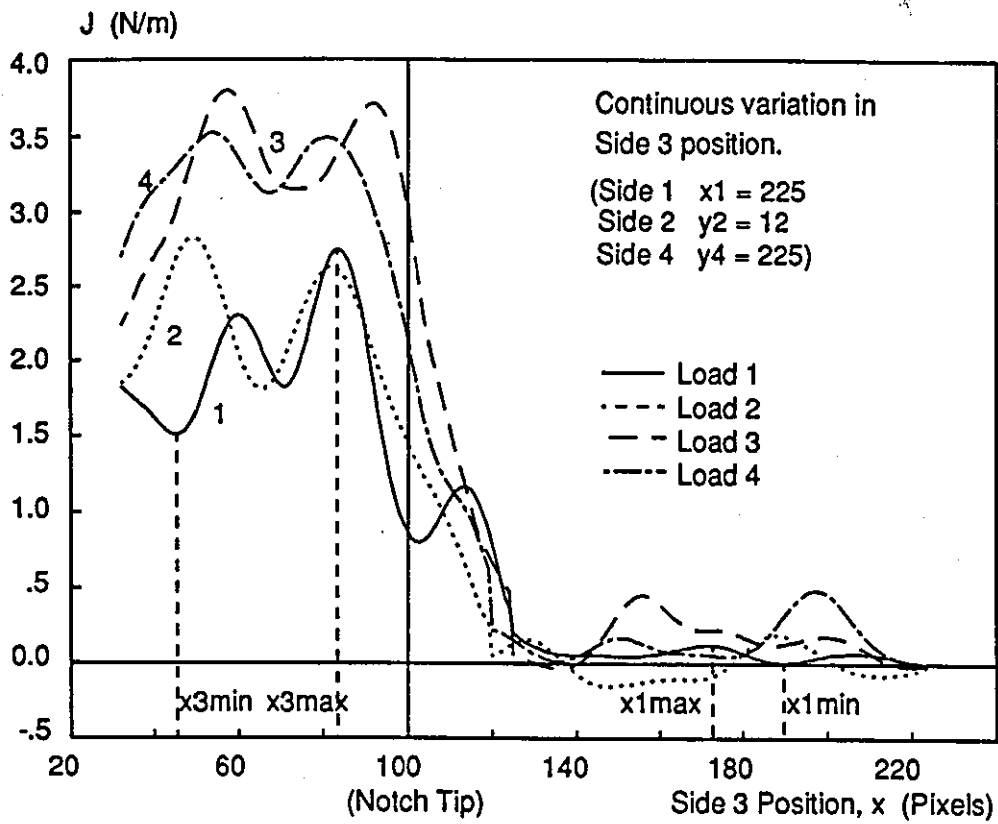
Figure 5.18 Compliance of specimens CT1, CT2 and CT3

contour encloses the notch tip and J takes a positive, theoretically constant, value. The notch tip is not enclosed to the right of the line, and J falls theoretically to zero. Values in the transition region immediately adjacent to the notch-line were excluded from the analysis. Consider the J measurement for load 1 in Figure 5.19(a). The x values at which local maxima and minima occur to the left of the notch tip have been denoted $x_{3,max}$ and $x_{3,min}$ respectively. Similarly, to the right of the notch tip, the maxima and minima are marked at $x_{1,max}$ and $x_{1,min}$. With the y -positions of sides 2 and 4 given in the figure, maximum J occurs for side 3 at $x_{3,max}$ and side 1 at $x_{1,min}$. The minimum value will be given with sides 3 and 1 at $x_{3,min}$ and $x_{1,max}$ respectively. It is possible to determine the corresponding values $y_{2,max}$, $y_{2,min}$, $y_{4,max}$ and $y_{4,min}$ from the plot of J with continuous variation in side 4. From these x and y values, two final contours were constructed: $x_{1,min}$, $y_{2,min}$, $x_{3,max}$, $y_{4,max}$ for sides 1 through 4 respectively giving "maximum" J , whilst $x_{1,max}$, $y_{2,max}$, $x_{3,min}$, $y_{4,min}$ gave a "minimum". Clearly not every possible J value has been calculated by this procedure, but the two contours give a reasonable approximation to the global maximum and minimum J values.

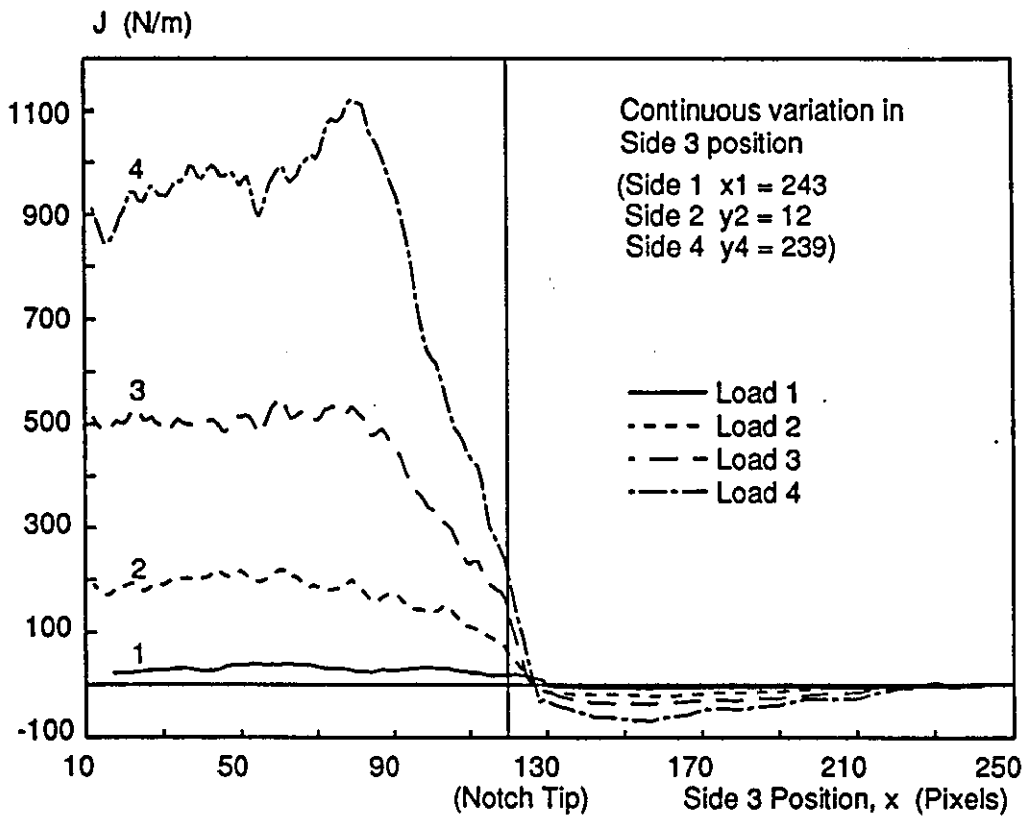
The range of J values calculated for each specimen at each load is shown by the error bars in Figure 5.20. Incremental ESPI measurements are shown at the bottom of Figure 5.20(a). To determine the cumulative J value, $J_{2,cum}$, from successive incremental measurements K_1 , J_1 and K_2 , J_2 , a relationship of the form $J=cK^2$ was assumed ($c = \text{constant}$), equation (2.10). Then:

$$\begin{aligned} J_{2,cum} &= c(K_1 + K_2)^2 \\ &= J_1 + 2\sqrt{J_1 J_2} + J_2 \end{aligned} \quad (5.19)$$

The mean value for each measurement has been marked. An uncertainty in any single J measurement of 33% is indicated. Due to the cyclic variation in J with contour position, Figure 5.19(a), this can be reduced by averaging several measurements. This cyclic variation is possibly due to small errors in the size of the applied phase-step caused by environmental disturbances. The moire results for specimen CT1 are shown in Figure 5.20(b). Results for CT2 and CT3 have also been included, despite the fact that measurements were doubled from half

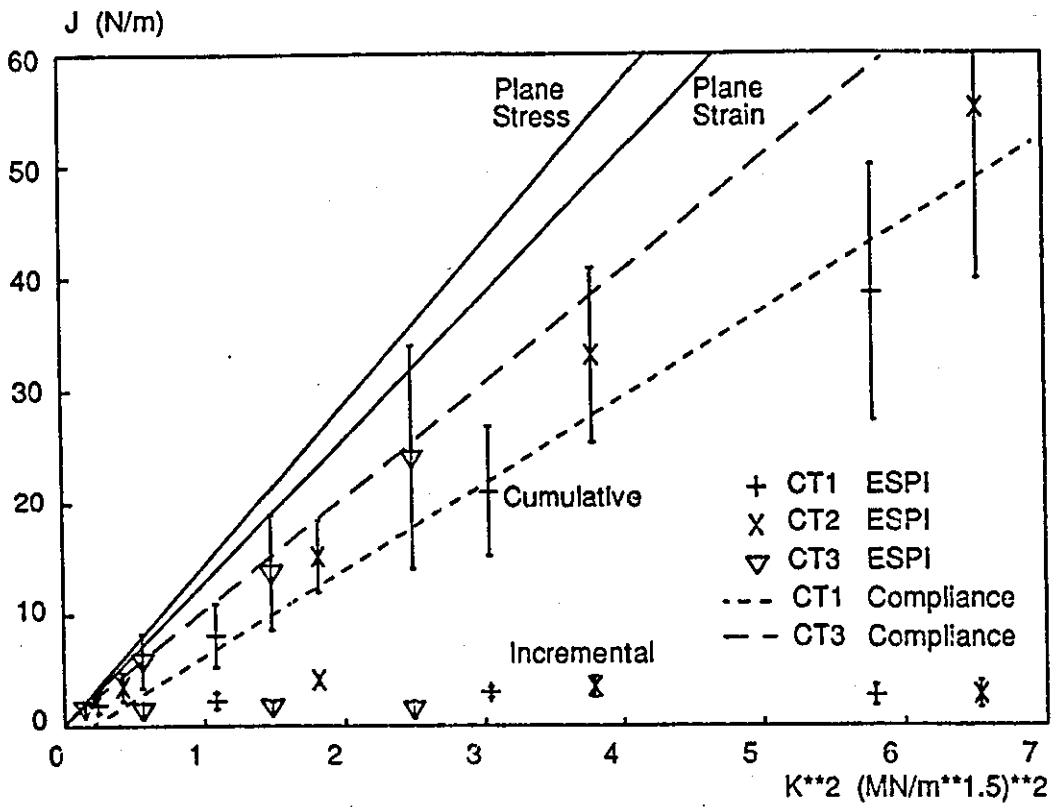


(a)

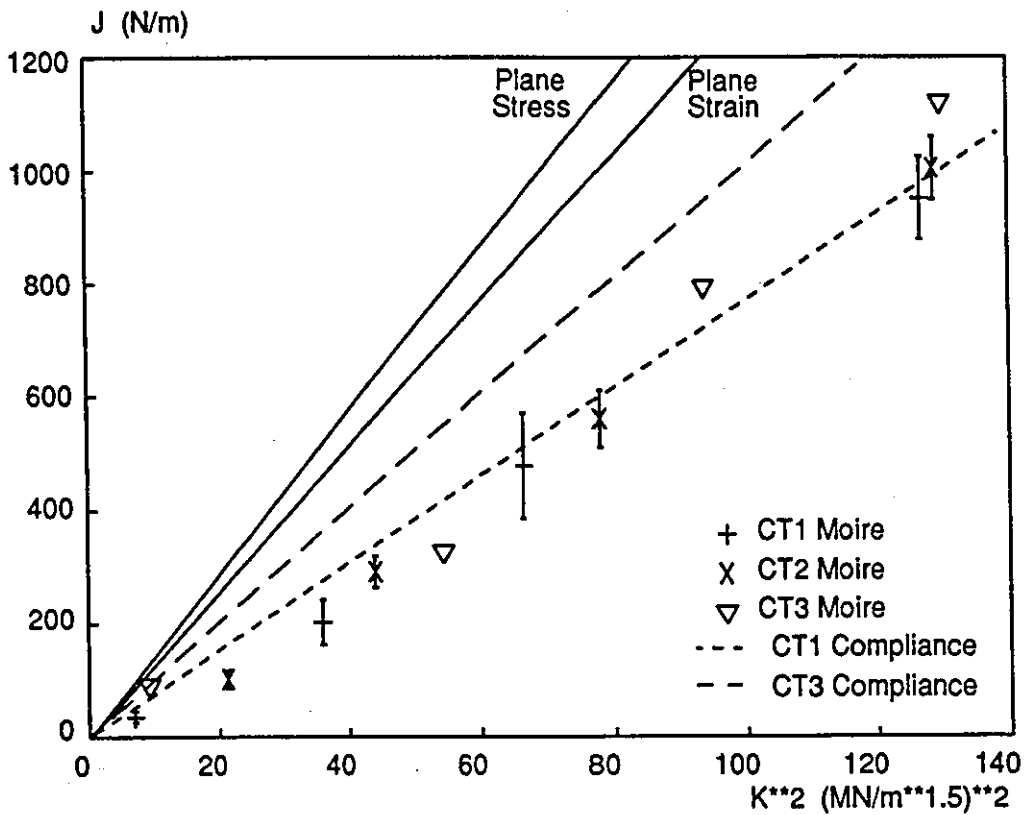


(b)

Figure 5.19 J variation with contour position for CT1



(a)



(b)

Figure 5.20 J-measurement for CT1, CT2 and CT3

a contour below the notch-line. Furthermore, no range of values could be calculated for CT3, because the transition region about the notch tip, Figure 5.19, extended to the image edge, and no plateau value was available. The uncertainty in a single J measurement for CT1 is 18%. The noise in the moire J measurements appears random, Figure 5.19(b). Consequently the uncertainty in J may also be reduced by averaging several measurements.

The expected relationships between J and K^2 under plane stress, equation (2.10), and plane strain conditions are plotted in both graphs. A variation is seen between these theoretical values and the experimental results. A possible explanation is the presence of the EDM notch rather than a true stress singularity. The J-evaluation routines were not in error, because tests on theoretical data sets, such as Figure 5.9, gave the result predicted by equation (2.10). Secondly the moire measurements confirm the ESPI results. As an independent check, the strain energy release rate, G, was evaluated at each K_1^2 using equation (5.19). Figure 5.20 shows the best fit line to G values for CT1 and CT3, which bound the ESPI measurements. The mean ESPI measurements typically fall within 10% of the value calculated from the specimen compliance. This is surprising, considering the crudeness of $(\partial C/\partial a)$ measurements. Moire results for CT1 also agree well with the compliance values. Agreement is less good for CT2 and CT3, probably due to the difficulties in making the measurements for these specimens discussed earlier. Finally cumulative ESPI and moire results are plotted on the same axes in Figure 5.21. Again this highlights the sensitivity of ESPI and the substantially larger dynamic range of moire measurements.

5.3 CLOSURE

Results were presented in this chapter for two different specimens, recorded with the dual in-plane interferometer. Displacement and strain were automatically determined by the phase-stepping method. The first specimen studied was the centre-notched plate loaded in uniaxial tension. Testing revealed the difficulty in

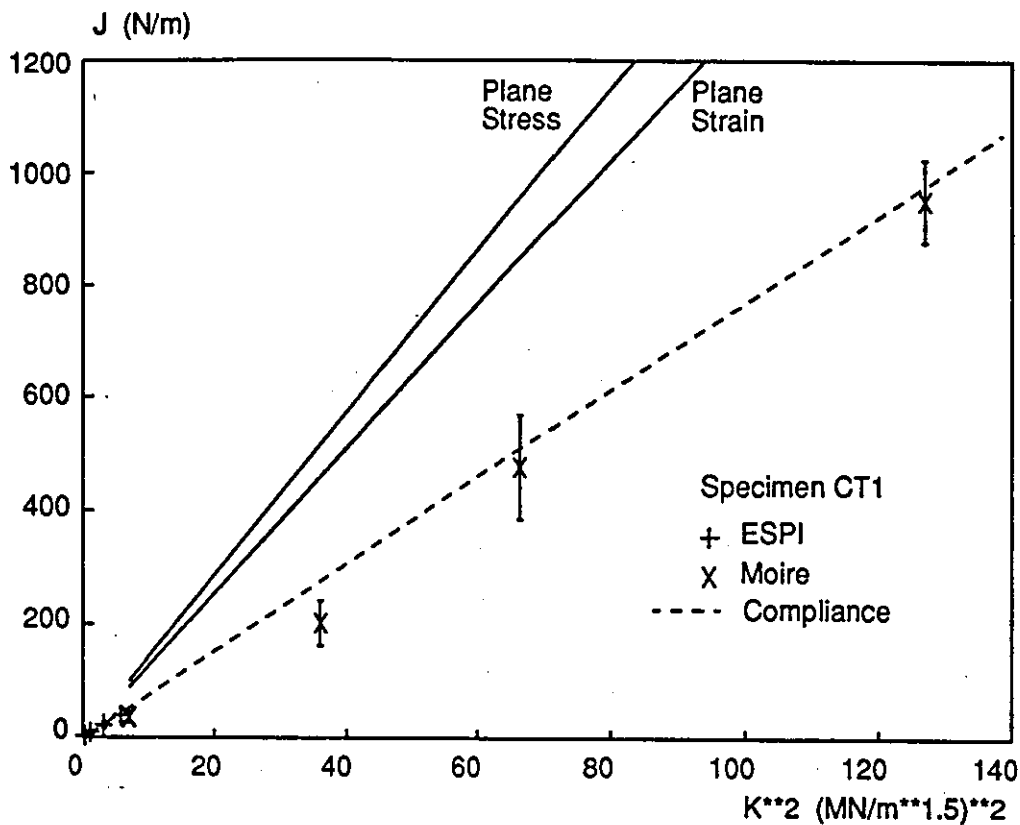


Figure 5.21 Comparison of ESPI and moire J-measurements for CT2

making measurements close to the notch tip, because the ESPI fringes must be filtered prior to phase-stepping. Thus each measurement was a compromise between maximising the measurement area and reducing speckle noise in that area to a minimum. Displacement and strain measurements were compared with a two term stress function solution. The plots gave good agreement in profile, but poor overall agreement in values particularly for u , Figure 5.8. These differences were primarily due to applying the solution when $r \gg a/50$. The presence of rigid body rotation was noted from the asymmetry of the patterns about the notch-line. The FE model also gave good qualitative agreement with the experimental measurements of displacement and strain. Quantitative agreement was better than for the stress function solution, but still in error close to the notch tip. This highlights the advantage of making experimental measurements in situations where constructing a suitable model is difficult. However, to verify that K , δ and J could be measured from ESPI displacement and strain data required a standard specimen to be tested.

Measurements of K , δ and J were made from three compact tension specimens. Automated displacement and strain evaluation made these parameters relatively straightforward to measure with ESPI. Results were compared with well-established theory for the standard CT specimen. Results were also verified by phase-stepped moire interferometry. This is the first time truly automated moire analysis has been used for fracture mechanics applications, to the best of the author's knowledge. The procedure to calculate crack-opening displacement, δ , required a line-fit to the measured v parallel to the notch-line, because accurate phase data was not available at the notch tip. This gave K proportional to δ , which could not be compared to equation (2.7). Therefore load-line displacement was measured by the same method, and good agreement with independent clip gauge readings was obtained, Figure 5.17. Details of measured K and J are summarised in Table 5.3. K measurements in Table 5.3 consider horizontal in-plane data only. K_I values from vertical in-plane measurements were often found to deviate from theory. In some instances the solution was clearly in error: for example, negative K_I value and/or non-linear increase in K_I with load. The exact cause of this error was not determined. Chona et al⁴⁵ encountered a similar difficulty in photoelastic studies, and suggested a selected least-squares solution to be applied "whenever necessary". As discussed previously, it would not always be apparent in general testing when this solution should be used. Consequently horizontal in-plane measurements were relied on for subsequent analysis. The uncertainty in a single J measurement was easily determined; full-field measurements and automated evaluation enabled many contours to be processed quickly. The uncertainty in J measured from a single contour was unexpectedly large. However, the average of several contours may be taken due to the cyclic nature of these errors. This has generally been the procedure adopted by workers^{45,66} using other optical methods. The cyclic variation in J with contour position was probably due to small phase-step errors introduced by environmental disturbances. These appear as "lobes" in the strain data, Figure 5.9. Strain, and therefore stress, will contain cyclic errors causing a similar error in J . Phase-step errors were most common in the v data: a better means of isolating the fibres was required. J values were found to be proportional to K^2 , Figure 5.20, but did not

		ESPI	Moire
K _I	Dynamic Range	0.7MN/m ^{3/2}	11.7MN/m ^{3/2}
	SNR	36dB	30dB
	Accuracy	±9.8%	±11.3%
J	Dynamic range	5N/m	1200N/m
	Accuracy	±33%	±18%

Table 5.3 K and J measurement with ESPI and moire interferometry

have the 1/E slope predicted by equation (2.10). This must be specimen related, possibly because an EDM notch was used rather than a stress singularity (fatigue crack). The EDM notch was used to exclude all plasticity effects from the tests. Another contributing factor may be that conditions through the specimen thickness were neither plane stress nor plane strain. However, we can have confidence in the measured J values: agreement between moire and ESPI was good. Also a separate estimation of J was made from the compliance of each specimen. This test was extremely crude, and yet reasonable agreement between the compliance values and experimental measurements was found.

These tests highlighted the sensitivity of ESPI with respect to moire interferometry. Both techniques have their niche. Moire interferometry is useful for relatively large scale deformation (e.g. plasticity) when coherent interferometric conditions would be lost for ESPI. However, moire requires a reference phase grating to be bonded to the specimen surface, which must be relatively flat. ESPI can be used for objects of arbitrary surface profile without the need to apply a surface grating. Also, dynamic studies involving pulsed ESPI would be well suited to this sensitivity range: the pulse separation can be adjusted to vary the sensitivity further.

6. DISCUSSION

This chapter draws the thesis to a close by discussing the work presented in the preceding five chapters. Section 6.1 considers the experimental results obtained in Chapters 3 to 5 and attempts to put the work into a more general context. This includes a comparison of ESPI for fracture mechanics analysis with respect to the other optical methods reviewed in Chapter 2. Although the broad aims of the project outlined in Chapter 1 have been met (namely automated in-plane analysis and its application in quantitative fracture mechanics studies) there is obviously scope for further work. Possible areas are discussed in Section 6.2.

6.1 EXPERIMENTAL RESULTS

Chapters 3, 4 and 5 contained an individual discussion (closure) of the results presented. It is the aim of this section to put the results in a more general context: the scope of information that has been obtained, the practical limitations and problems which have been encountered, and the suitability of ESPI to perform strain analysis in general and fracture mechanics analysis in particular. Each chapter is considered in turn in the following three sections.

6.1.1 Chapter 3

The aim of Chapter 3 was to automate in-plane ESPI fringe analysis. A brief review of available techniques highlighted phase-stepping as a suitable method. The temporal phase-stepped speckle correlation (TPSSC) technique was applied to in-plane ESPI with an external framestore for the first time. This complimented the phase-stepped out-of-plane ESPI study undertaken by Kerr¹⁰⁹ at Loughborough University during the same period. The calculation of surface

strain, and estimation of measurement errors are specific to in-plane ESPI and represent the first study of its kind. Only one other research group is routinely extracting strain information from ESPI fringe data. This work is due to Vrooman and Maas⁷⁸ at Delft Technical University. There, the DiPSSI method is used with an out-of-plane interferometer with three different illumination directions. The in-plane components of displacement are then extracted in much the same way as for holographic interferometry. The TPSSC and DiPSSI methods are compared later in this section.

Fourier filtering ESPI fringes was found to reduce speckle noise most effectively, Section 3.2.5. With a fringe spatial frequency of three line pairs, the phase can be determined with an uncertainty of $\pm 2\pi/14$ radians. This experimental figure includes error sources such as incorrect phase-step size reduced to their practical limits, and was therefore deemed to be the practical error in any measurement from the system. The error increases with increasing fringe spatial frequency, Figure 3.12, due to the increasing overlap between fringe and speckle spatial frequencies and the reduction in fringe visibility. Strain was initially calculated by performing a 25 pixel line fit to the unwrapped phase data, and subsequently a 25x25 pixel plane fit. A small difference in noise rejection was found, Figure 3.14, but at the cost of a significant increase in computation time: for a 256x256 pixel image, a plane fit required approximately seven minutes of processing time, whereas the line fit required approximately two minutes. In some applications this difference may be important, but post-processing time required to calculate strain was not crucial for the results presented in this thesis. The number of pixels chosen for the line and plane fits (25) was somewhat arbitrary, but a standard was selected for consistency throughout the thesis. The gauge length chosen corresponds to approximately one fringe if ten line pairs is the maximum fringe spatial frequency present (i.e. midway between zero fringes and the unwrapping defined limit of approximately 20 fringes). Furthermore, the noise rejection at this spatial frequency ($\pm 7.5\mu\text{strains}$) seemed an acceptable compromise with gauge length, Figure 3.13. Strain measurements will also include systematic errors associated with fitting a plane surface to an arbitrary phase profile, which can only

be estimated in any particular application. For the compact tension specimen, Section 5.2, the theoretically predicted strain values calculated from equations (5.8) were compared with those obtained by applying the strain calculation routine to the theoretically predicted displacement given by equation (5.5). The greatest difference occurred close to the crack tip, where the rate of change of strain is highest. For both the ESPI and moire data sets, this error was not greater than 4%.

An experimental assessment of the error in measured phase and strain was made. This study is largely dependent on the experimental system, although even a theoretical study would be largely system dependent. For example, Nakadate and Saito¹¹⁰ demonstrated TPSSC for an out-of-plane interferometer with a speckle reference beam. Negative values produced on subtracting speckle patterns were removed by squaring the result. Equation (3.12) cannot be applied to I^2 fringes. Nakadate and Saito used a three-step algorithm instead. Other workers have ignored the negative values from subtraction (half-wave rectification), in which case it is not apparent which phase-stepping algorithm is applicable, or taking the modulus of the values from subtraction (full-wave rectification, used in the FORA framestore, Appendix C) for which any algorithm is applicable. Furthermore, analogue band-pass filters centred on the speckle frequency in the TV signal and amplification (sometimes non-linear) of the TV signal are applied on an *ad hoc* basis between research groups. Thus, any thorough theoretical assessment will almost certainly apply only to one experimental system. Having understood this, it is then a question of whether the accuracy^{of} results obtained in Sections 3.2.5 and 3.3.2 are applicable throughout the thesis. Generally, results were recorded with an optical magnification, $M=0.4$, whereas the calibration experiments used $M=0.2$. Later experiments suggested that over this limited magnification range the accuracy is independent of the magnification, Figures 4.10 and 4.11. A physical argument can be proposed to support these findings. Two physical effects must be considered when increasing the magnification, and both would need to be incorporated into a model of the theoretical accuracy of a given measurement in order to account for widely varying magnifications. Firstly, an increase in

magnification increases the speckle diameter. This will reduce speckle averaging over a pixel and consequently increase the intensity modulation, and hence the accuracy of calculated phase at that pixel, equation (3.26). However, in most ESPI systems without a pinhole aperture, some speckle averaging occurs. These effects are difficult to quantify, and have not been fully understood even for DiPSSI implementations where its interpretation is more critical. These problems are exacerbated by two D-A and two A-D conversions in the camera-framestore-image processor chain, at three different resolutions, Appendix C. The fringe pattern is also filtered prior to phase calculation to reduce speckle noise. With these considerations, it is understandable that small changes in speckle diameter will not affect the accuracy obtained. The second physical effect of increasing magnification is that less rigid body motion is required to decorrelate the speckle pattern, equation (3.37). Therefore fewer fringes can be observed. Provided that a reduction in measurement range is accepted, the fringe pattern will still have good fringe visibility. There is then no reason to suppose that the accuracy will then be different from that obtained in Figures 3.12 and 3.14. A theoretical calculation of accuracy may be worthwhile for an ideal image processing system in which one pixel of the camera corresponds to one pixel of the image processor. Many cameras and image processors have the capability of digital output and input respectively, but then "real-time" (video frame-rate) operations such as subtraction for fringe generation are not generally available.

The TPSSC and DiPSSI methods were described in Sections 3.2.1 and 3.2.2 respectively. The DiPSSI technique is generally considered to be more accurate than TPSSC, because each pixel is treated individually. However, a smooth phase ramp is not obtained: the data is speckled with points at which the intensity does not modulate. In general, a more "robust" unwrapping routine is required for DiPSSI than for TPSSC, to accommodate these non-modulating pixels. The example of DiPSSI given in Figure 3.3, is of poorer quality than generally published by workers who use the DiPSSI method. This is probably due to the speckle averaging and digitisation effects discussed in the preceding paragraph. Further noise occurs in the measured phase due to speckle decorrelation, which

must be subsequently filtered out. For example, Vrooman and Mass have used 30x30 pixel plane fit to smooth the phase data, analogous to the smoothing method applied for Figure 5.12. This reduces noise in the measured phase, but at the expense of increasing systematic errors. The greater accuracy achieved in DiPSSI arises because a lowpass filter is not used to reduce speckle noise, and in practice may be double that achieved with TPSSC (i.e. $2\pi/30$ radians). Eliminating the lowpass filter gives DiPSSI two further advantages over TPSSC: the technique has greater dynamic range (limited only by the detector resolution) and phase may be calculated to the object edges. It is possible, therefore, that phase could be calculated closer to the notch tip with DiPSSI than achieved with TPSSC. The advantages of TPSSC with respect to DiPSSI include less image memory and data acquisition time, and the ability to work directly with correlation fringes. TPSSC is also generally faster to implement than DiPSSI and therefore offers a practical and reasonably accurate solution without some of the problems associated with DiPSSI.

Two new phase-stepping algorithms for ESPI were proposed in Section 3.2.3. The analytical removal of speckle noise from subtraction and addition correlation fringes enables some of the advantages of TPSSC and DiPSSI to be combined. For subtraction fringes, this includes fewer images and the ability to use correlation fringes directly (TPSSC) whilst treating each pixel as an individual interferometer (DiPSSI). This would suggest that an accuracy of $\pm 2\pi/30$ radians is achievable with the new algorithm, although this has yet to be confirmed experimentally. The second algorithm enabled phase-stepping with addition fringes to be achieved for the first time. There is further work to be done on both algorithms. Both require a correct solution to be chosen from the values calculated at each pixel: for subtraction this is one of four values and for addition one of two values. Generating a comparison phase map to select the correct value was acceptable to demonstrate the technique, but cannot be calculated for addition fringes generated in twin-pulse mode. Thus an algorithm is required to select the correct solution at each pixel without calculating a reference phase map. The effects of pulse stability and speckle decorrelation (rigid body motion) could

then be investigated. It should be recognised that the advantages of twin-pulsed ESPI lie in transient and temporally unstable applications. Thus phase-stepped addition ESPI (and the subtraction of consecutive addition fringe patterns to improve fringe visibility⁸¹) are only partial solutions to the real problem. Phase-extraction from a single interferogram is required, and is discussed in Section 6.2.1.

6.1.2 Chapter 4

Chapter 4 considered a new interferometer for the simultaneous measurement of two in-plane components of displacement. Proof of principle was demonstrated with the helium-neon laser system; an argon-ion system was used for the remainder of the experimental work. In general, the need for an abraded surface is a drawback: the measurement area is restricted and a general three-dimensional surface may not be amenable to abrading. In particular, surface abrasions may cause errors in some fracture studies, although apparently not for the work presented in this thesis. A solution would be to determine a suitable painted surface for the argon-ion illumination as found in the silver-spray paint with the helium-neon illumination. The paint could then be applied in the many situations where a white painted surface is used, although the intensity of backscattered radiation reaching the camera may be reduced by 30%, Section 4.2.1.

For small-scale, static applications different wavelengths in the two illumination directions may prove an attractive solution. This solution was proposed, but not pursued due to the resulting difference in fringe function, Section 4.1. Simultaneous measurement implies the study of transient phenomena, which in turn suggests the use of more expensive pulsed lasers. Two, and perhaps ultimately three, laser systems is then not a viable solution and polarisation discrimination once again becomes more attractive. An alternative solution may be to use a single pulsed laser, with one illumination direction frequency shifted with respect to the other.

The interferometer head designed to house the two CCD cameras performed well. The image distortion introduced by the cube was certainly no worse than that introduced by, for example, the wedge used to combine the object and reference beams in the Ealing Vidispec ESPI system, and internal reflections were eliminated with careful alignment. In practice, some difficulty was experienced in aligning the two cameras. A procedure was established working with the live images from the two cameras, Section 4.3.1. Camera height and tilt was adjusted by sticking tape to the rails on which each camera was mounted, and proved to be a laborious process. Furthermore, aligning the cameras from the live image presents an added difficulty when subtraction begins: subtraction adds a delay to the TV signal, and the vertical in-plane view translates approximately five pixels to the left. However, the horizontal in-plane view is reflected, and is effectively translated five pixels to the right. It was not difficult to shift the horizontal in-plane image when it is reflected in the image processor, but it should be remembered that the images in subtraction are horizontally displaced. Alignment of the live images that was maintained with a change in magnification was not achieved. Based on these observations, some recommendations can be made for improvements to the system. A minimum requirement is three translational degrees of freedom about the cartesian axes of Figure 4.2, and one rotational degree of freedom about the z-axis for the horizontal in-plane camera i.e. the reflected image. The alignment procedure of Section 4.3.1, where the horizontal in-plane image is adjusted to match the vertical in-plane (assumed to be a satisfactory reference), would then be considerably easier. If the translation and rotation stages were automatically controlled, a semi-automatic process could be used to align the cameras. This process might be based on minimising the intensity during real-time subtraction of the image from each camera, using a carefully designed test pattern. The process would be simplified if the horizontal in-plane image was reflected before subtraction, possibly optically (with a mirror between the polarising cube and the horizontal in-plane camera) or electronically (reverse the direction in which each horizontal line is scanned). Another alternative may be to accurately bond the CCD camera faceplates to the surface of the polarisation selective beamsplitter. The cube and cameras could then be moved

as one unit.

Phase-stepping was introduced to the dual-sensitivity interferometer and displacement and strain data obtained automatically for a cantilever loaded at its free end. Good agreement with theoretical models was demonstrated. By recording both views simultaneously, identical strain conditions existed for the horizontal and vertical sensitivity fringes: it was not necessary to reload the object when exchanging illumination directions. Simultaneous recording was not essential for this example, because the loading was static. Indeed, the facilities did not exist to simultaneously digitise two images, although image processors which accept two and three camera inputs are now available. The application of such systems offers an attractive avenue for further research in simultaneous two and three sensitivity vector ESPI, possibly using the techniques discussed in Section 4.4. In this work, the dual-sensitivity system provided a convenient solution to recording both in-plane views without the need to reload the specimen. The alternative, to record horizontal and vertical in-plane views sequentially with a single camera and without reloading the specimen would have been tedious. For example:

- i) with horizontal in-plane illumination only, store reference speckle pattern to first framestore;
- ii) with vertical in-plane illumination only, switch camera output to second framestore and store reference speckle pattern;
- iii) deform object and digitise vertical in-plane fringes;
- iv) reverse camera output to first framestore, connect image processor to this framestore, select horizontal in-plane illumination only and digitise horizontal in-plane fringes.

Whatever level of automation is achieved in this process, the horizontal in-plane fringe pattern could not be observed whilst loading the object. This explains the advantage of the dual-sensitivity system for static loading. Future transient event studies using pulsed lasers will require both views to be recorded simultaneously.

6.1.3 Chapter 5

This chapter was concerned with the application of the dual sensitivity system with automated displacement and strain evaluation to some fracture mechanics problems. Results were presented for two specimens. The first study used the centre-notched specimen, and an area of approximately 25mm x 25mm ahead of the notch was viewed. Displacement and strain measurements at a given load increment were compared with a two-term stress-function solution. The plots gave good agreement in profile but poor overall agreement in values, particularly for u , Figure 5.8. These differences were primarily due to applying the stress function solution for $r \gg a/50$. To satisfy the condition $r < a/50$ would have required measurements of $r \approx 0.2$ mm. The specimen would need to be viewed through a microscope objective, as performed by Herbert et al⁷⁵ for out-of-plane ESPI. However, as the magnification increases, the fringe pattern has increasingly poor visibility due to speckle decorrelation. This reduces measurement accuracy, equation (3.26) and ultimately prevents automated evaluation entirely. In future experiments, in-plane ESPI with high magnification could be used, possibly with camera translation to minimise the effects of rigid body motion (as sometimes used in speckle photography). Also, a local reference beam could be used to eliminate rigid body motion. By this method, the reference beam path includes a mirror bonded to the test surface and provides a common path length change for both interferometer beams in the presence of rigid body motion. The use of a local reference beam is common for out-of-plane interferometry. Camera translation and local reference beam have not previously been attempted with in-plane ESPI, and may be an interesting avenue of research. However, the simplest solution to obtain good quality in-plane fringes for automatic processing was to accept a larger measurement area i.e. reduce the magnification. The results obtained at this magnification demonstrated the difficulty in making displacement measurements close to the notch tip with the TPSSC method, due to the lowpass filtering required to reduce speckle noise. The phase-stepping algorithm proposed for subtraction fringes without the need for a lowpass filter, Section 3.1.4, may be one solution to this problem.

A finite element model of the centre-notched specimen was made, and gave good qualitative agreement with the experimental measurements of displacement and strain. Quantitative agreement was better than for the stress function solution, but was in error close to the notch tip. This highlights the need to validate analytical and calculated solutions: an FE model has the advantage of being predictive, but is at best an approximation and is inherently reliant on the accuracy of the model. The solution was used to investigate the large difference between experimentally measured u and the stress function solution. The model was not further refined to model notch tip conditions: crack tip mesh design can (and has) formed doctoral theses in its own right. From this study it was concluded that measurement of fracture parameters with ESPI would require a standard specimen. It may also be concluded that FE and ESPI are suitable as complimentary techniques, the former for prediction and interpretation, and the latter for confirmation and correction.

Measurements of K , δ and J were made for three compact tension specimens. Automated displacement and strain evaluation made measurement of the three chosen parameters simple for the operator: routines were written so that only the region of data to be used need be selected. The procedure then implemented for the measurement of each parameter was detailed in Section 5.2. Testing revealed the lack of reliable phase data at the notch tip prevented the measurement of crack-opening displacement. However, an estimate was made by fitting a straight line to the measured v displacement parallel to the notch line. The same procedure was used to measure load-line displacement, and results were in good agreement with independent clip gauge readings, Figure 5.17. ESPI was successfully used for K_I measurement for the three specimens. Results from horizontal in-plane displacement data agreed to within 10% of theoretical predictions. However, when applied to vertical in-plane data, convergence to an incorrect solution was often obtained. The exact reason for this was not established. A selected least-squares solution may be the answer to this problem; this was not pursued for the reasons given in Section 5.2.4. An alternative method to obtain reliable measurements for the vertical in-plane data may be to use the

combined displacement $\sqrt{(u^2+v^2)}$ in the least-squares solution for K_I . In the presence of reliable K_I values from u -measurements, this was not attempted. J measurements from a single contour were found to have an uncertainty of approximately $\pm 33\%$. This figure was determined by calculating J for successive contours, a process performed quickly with automated routines. A cyclic variation in J with contour position was revealed, and was attributed to small errors in the phase-step size due to environmental disturbances. This leads to a cyclic variation in measured phase which is amplified when calculating strain. (Differentiation acts as a filter whose gain is proportional to frequency). Due to the cyclic variation in J , errors may be reduced by averaging over several contours. The J value measured in this way was proportional to K_I^2 , although the $1/E$ gradient predicted by equation (2.10) was not found. Confidence in the measured K_I and J values was high: repeat tests from the same specimens was performed by moiré interferometry and found to be in good agreement with ESPI. Furthermore, crude compliance tests were found to give reasonable agreement with the measured J values. The difference between the measured gradient and $1/E$ predicted by theory was attributed to notch tip conditions and was discussed in Section 5.3.

With the experience gained in using ESPI for measuring fracture parameters, the technique may now be compared with other optical methods previously used for this purpose. The techniques are discussed in the order they were considered in Chapter 2. This discussion considers fracture mechanics applications only, the more general aspects for each technique were given in Chapter 2. It should be remembered that no one technique is superior for every application.

Photoelasticity remains one of the few techniques capable of measuring stress in the interior of bodies, and is therefore amenable to general three-dimensional analysis. Measurements may be made close to the crack tip i.e. $r/a < 0.03$, for which Etheridge and Dally³⁴ estimated errors of $\pm 5\%$ in measured K_I . The technique is amenable to dynamic studies. The primary difficulty of photoelastic analysis is the laborious task of model slicing and fringe analysis. Thus the trend in experimental mechanics is for surface measurement techniques to validate

three-dimensional finite element predictions, from which the strain at interior points may be determined. To model yielding requires photo-plasticity theory i.e. a non-linear relationship between strain and induced birefringence. The evaluation of rotation terms $\partial v/\partial x$ is not possible without added computation, and therefore the evaluation of J is difficult.

Moire and moire interferometry are attractive techniques for fracture study and have been used extensively in the literature. Large rigid body motions can be tolerated by manipulating the reference grid, and fringes of good visibility may be obtained⁴⁶. The sensitivity of the interferometer may be varied with the appropriate choice of gratings. The technique is therefore well suited to the linear elastic and elastic-plastic regimes; in the case of moire interferometry it may be assumed that the surface reference grating follows surface deformation faithfully. For ESPI, speckle decorrelation generally makes the study of plasticity difficult in tough materials, due to the large associated rigid body motions. During the course of this study, gross yielding prior to fracture was observed with out-of-plane ESPI. The specimen was identical to that used in Section 5.1, with the notch symmetrically extended by 2mm fatigue cracks. The recording required manual re-referencing of the framestore at approximately two second intervals when the fringes became too densely packed together. Four such intervals were recorded prior to fracture. This demonstrates that plastic yielding may be observed with ESPI provided that it is large compared to the rigid body motion of the specimen. This contrasts with moire and moire interferometry, where the long correlation length and lower sensitivity enable the plastic initiation and growth to be observed with respect to the undeformed state. These are the reasons why moire interferometry is well suited to measuring, for example, the differential displacement between adjacent layers in composite materials and ESPI is not. However for measurements in the linear elastic regime, it was demonstrated that similar accuracy may be achieved with ESPI and moire interferometry. In this case ESPI generally overcomes some of the disadvantages of moire interferometry, such as the need for a surface grating and the restrictions this puts on the measurement area and test surface flatness. The preceding arguments for ESPI

are also true for holographic interferometry due to the similarity between techniques. Holographic interferometry gives greater measurement accuracy ($2\pi/100$ radians and 1μ strain for heterodyne detection¹⁰³) than ESPI due to the superior fringe quality. ESPI offers an easier measurement process, and allows the in-plane displacement components to be isolated from the out-of-plane displacement. Thus the measurement of parameters such as K_I , K_{II} and J , which give rise to predominantly in-plane displacements, is simplified.

Speckle photography was the last optical technique discussed in Chapter 2. Speckle photography is less sensitive than ESPI which can be an advantage for measurements in the elastic-plastic regime. Typically displacements of several hundred microns can be measured. The technique is well suited to dynamic studies. Rigid body motion (in static applications) may be compensated by suitable translation of the photographic plate containing the reference speckle pattern. Displacements may also be made extremely close to the crack tip ($<0.2\text{mm}$)⁶⁴. Although the technique is full-field, making visual inspections is slower than with ESPI.

Evaluation of contour parameters, such as J , therefore requires interpolation between separated measurement points if the processing time is not to be excessive.

With these comparisons in mind and the techniques used in this thesis to measure fracture mechanics parameters with ESPI, some practical fracture mechanics applications may be proposed. These are discussed in the following section.

6.2 FURTHER WORK

Areas for further study may be divided into two sections: potential applications, Section 6.2.1, and the ESPI technique, Section 6.2.2. Potential applications are discussed first, because it follows logically from the comparison of optical techniques discussed in the preceding section. From these applications, some requirements for further study of the ESPI technique are recognised. Suggestions

for further work involving multi sensitivity ESPI were already made in Section 6.1.2 and are not repeated here.

6.2.1 Potential Applications

ESPI is well suited for detecting the position of defects in a structure: the data obtained is full-field and the measurement process is simple and fast. Thus large objects may be inspected rapidly for surface or near-surface defects. Traditionally defects are identified by the operator as regions of densely packed or discontinuous fringes although automated algorithms to recognise the position of defects have been proposed⁸². Phase-stepping and the automated J-evaluation procedure of Figure 5.19 offer an alternative solution. Scanning the J-contour across the image would enable defects to be located by a sudden change in the J value. Also, the likely severity of such a defect could be determined from the magnitude of the J. Difficulties are apparent with automating this procedure, primarily due to errors in phase-unwrapping; discontinuities in unwrapped phase would yield a non-zero value of J. Unlike the study of Section 5.2, the crack position would not be previously known. The unwrapping procedure should therefore be sufficiently robust to handle discontinuities in the phase data. This would increase the processing time for unwrapping.

ESPI provides a simple method of measuring the opening-mode stress-intensity factor, K_I . By adjusting the parameters used in the least-squares fit of equation (5.10) to the measure data, the method may be modified to measure both K_I and K_{II} (i.e. mixed-mode loading) for example Hyde and Warrior¹⁴⁹ with photoelasticity. A similar modification may be made for displacement data, and so it would be a simple extension of the techniques used in this thesis to measure K_I and K_{II} with ESPI. Hyde has also determined the ratio K_I/K_{II} as the direction of crack propagation varies under mixed-mode fatigue loading. The specific application was steel specimens fatigue loaded at elevated temperature¹⁵⁰. Some general advantages of using ESPI can be seen by considering its application to this

specific example. Firstly the specimens, rather than photoelastic models, could be tested at certain points in the fatigue cycle. For a static load, the ratio K_I/K_{II} could be evaluated from the actual specimen by the techniques of Section 5.2. Alternatively, the tests could be performed *in situ*. Again a small static load could be applied, but the specimen would not need to be removed from the heated environment. The suitability of holographic interferometry at elevated temperatures was illustrated in Section 2.2.3. However, ESPI enables the in-plane components to be measured directly. Also no surface reference grating, possibly deposited by photo-engraving or vacuum deposition to withstand high temperatures, would be needed as for moire interferometry. More ambitiously, the analysis could be attempted with a pulsed laser without stopping the fatigue cycle. The use of a Nd:YAG in twin-pulsed operation has been used to obtain ESPI fringes in an industrial environment⁸¹. The fatigue-load frequency would be synchronised with the camera frame rate to give the drive signal for twin laser pulses. Twin-pulse separation would be adjusted to give the desired sensitivity as the load increased within the loading cycle. Phase-extraction from a single interferogram would then be required before the techniques of Section 5.2 could be applied.

Electronic processing of the speckle patterns at the TV frame rate will restrict ESPI to slow, stable crack growth or fatigue crack growth applications. This is because a typical brittle (rapid) fracture may advance at 400m/s. High-speed cameras may record of the order of 30,000 frames per second. The crack advances approximately 13mm between frames. Several frames may therefore be recorded, depending on the optical magnification and the specimen size used. The ability of the system to freeze motion depends on the duration of the pulsed illumination; for white light sources used with photoelasticity this may be of the order of 400ns, corresponding to 0.2mm crack advance during exposure. The TV frame rate of 25Hz exposes a frame every 16m of crack advance in this example i.e. the specimen will generally have failed. Certainly no more than a single frame could be recorded for each test. Synchronising the camera frame and laser pulses to the crack front position could possibly be achieved: an approximation to the transient

crack tip conditions could be made by combining the data from many tests. This solution seems unpractical and prone to error. The study of transient events may require either a high speed photographic camera or a high speed video. The study is then limited by the maximum frequency of twin-pulses given by the Nd:YAG laser ($\approx 100\text{Hz}$) An alternative might be to study the interaction of a mechanical shock wave with a stationary crack, to simulate dynamic stress conditions at the crack tip. Testing is performed with a single specimen and the delay between laser pulses and loading can be accurately adjusted. A pseudo-dynamic study may then be performed¹⁵¹.

6.2.2 ESPI Technique

The TPSSC method was suitable for the statically loaded specimens considered. As noted throughout the discussion, temporal phase-stepping methods cannot be used for transient events. Thus the algorithm for phase-stepping addition fringes, Section 3.2.3, is a first and partial solution to the problem. Similarly the subtraction of π radian phase-stepped addition fringes to obtain fringes of sufficient visibility⁸¹ for the application of TPSSC is also a partial solution, although no results have been published for this method yet. The TPSSC method may be used if spatially separated phase-stepped ESPI fringes are recorded simultaneously¹⁰⁴. An alternative solution is to use an algorithm that requires only one fringe pattern, although these generally require parallel carrier fringes in each interferogram. Transient event studies would require the carrier fringes to be generated between twin laser pulses. An alternative form of the Fourier transform method which does not require carrier fringes has been proposed¹⁵². Care is needed in its implementation, but its application to ESPI could be usefully investigated.

Knowledge of the object shape is required to convert the measured displacement to local out-of-plane and in-plane components. Shape may be measured by ESPI contouring. ESPI systems combining displacement and shape measurement have

been reported in the literature^{76,78}. The combination of ESPI contouring with techniques presented in this thesis would make a powerful tool for measuring fracture parameters from a general three-dimensional body. In general, fibre-optic illumination is ideal for ESPI contouring as it enables the wavefronts to be translated (to generate contour fringes) simply by moving the fibre output ends. If the fibre outputs are mounted on piezoelectric translators controlled by the computer, it could be possible to automate the contouring process as well as three-dimensional displacement measurement, all with the same apparatus.

This thesis was concerned with the automated analysis of displacement fringes for evaluation of fracture parameters. J measurement requires the components of surface strain. Speckle shearing interferometry may be used to measure the spatial derivative of deformation (i.e. strain) directly⁷¹. In a speckle shearing camera, diffusely scattered light from the object (with a single illumination beam) is split into two wavefronts, and the two sheared images of the object are formed on the target of the TV camera. A fixed amount of shear may be introduced by a glass wedge partially covering the imaging lens, or a Twyman-Green interferometer may be used to vary the amount of shear. The gauge length for strain measurement is related to the amount of shear. Sheared speckle patterns before and after deformation are correlated to yield fringes of constant displacement gradient. Speckle shearing interferometry is less sensitive to environmental disturbances than ESPI because the interfering wavefronts are separated only in the camera. These techniques deserve investigation for the measurement of fracture mechanics parameters: displacement measurement used in this thesis is one solution to the problem. The eight-parameter expression for K_I could be re-written in terms of surface strain. J evaluation would require three shearing directions to obtain ϵ_{xx} , ϵ_{yy} and $\partial v/\partial x$.

7. CONCLUSIONS

1. A detailed study of in-plane displacement measurement with ESPI has been undertaken. As a result of this work, it was demonstrated that ESPI may be used for semi-automated, quantitative stress analysis. Two areas of study were required to reach this objective: (i) automatic extraction of displacement and strain data from ESPI fringe patterns; (ii) refinements to the ESPI technique. This enabled a quantitative fracture mechanics study to be undertaken.
2. In order to extract displacement data automatically from ESPI fringe patterns, the TPSSC technique was applied to in-plane ESPI with an external framestore for the first time. Computer routines were devised to calculate surface strain by least-squares fitting a 25x25 pixel plane to the displacement data. Although devised for static in-plane studies, it was demonstrated that the routines are applicable to harmonic in-plane vibration analysis with a pulsed laser. An experimental study of the achievable accuracy of measurement of displacement and strain was undertaken, particularly with respect to the pre-processing filter required to suppress random speckle noise. Fourier filtering was found to be the most successful filter: threshold errors of approximately $\pm 2\pi/14$ radians ($\approx 0.03\mu\text{m}$ for the in-plane system used) and $\pm 6\mu\text{strains}$ were obtained. Experimental graphs of error against increasing correlation fringe spatial frequency were obtained.

From considerations of the phase-stepping technique, two new algorithms were proposed for phase extraction from subtraction and addition ESPI fringes. Both algorithms enabled the random speckle phase to be eliminated analytically, thus avoiding the need for a pre-processing lowpass filter. It was demonstrated that such an algorithm can improve the

accuracy of phase measurement for subtraction fringes. The algorithm for addition fringes enabled the first demonstration of phase evaluation for ESPI addition fringes. This latter algorithm will no doubt be the subject of further study.

3. A new ESPI interferometer was devised to simultaneously measure displacement along two orthogonal sensitivity vectors, using polarisation discrimination. Phase-stepping was incorporated into the interferometer for subsequent analysis. Whilst not essential for the static loads used in this thesis, it greatly simplified the data acquisition and ensured that strain conditions were identical for the two recordings. Methods for extending the technique to one in-plane and out-of-plane sensitivity, as well as two in-plane and out-of-plane sensitivity, were discussed. Methods based on wavelength discrimination were also discussed. However, it was not necessary to pursue these avenues of research for the work undertaken in this thesis.
4. The automated fringe analysis and dual-sensitivity techniques were combined to enable quantitative strain analysis. The work presented in this thesis, and that published concurrently by Vrooman and Maas using the DiPSSI method of phase-stepping, are the first extensive strain analyses undertaken with ESPI. The quantitative fracture mechanics study of the CT specimen is the first of its kind with ESPI. Techniques to evaluate the mode 1 stress-intensity factor, K_I , crack-opening displacement, δ , and J-integral from ESPI displacement measurements were devised and/or adapted from the literature (as detailed in the text). It was demonstrated that ESPI may be successfully used to measure K_I with a signal-to-noise ratio of 36dB over the measurement range of $0.65\text{MN/m}^{3/2}$. All cumulative ESPI results fell within 10% of the theoretical values. An uncertainty in any single J measurement of $\pm 33\%$ was found. J values averaged over several contours typically agree to within 10% with compliance measurements. All results were verified with phase-stepped moire

interferometry measurements made from the same specimens: K_I values from moire showed a signal-to-noise ratio of 30dB over the measurement range of $11.6\text{MN/m}^{3/2}$; systematic errors in J of $\pm 18\%$ were recorded for $J < 1200\text{ N/m}$. This is believed to be the first automated evaluation of fracture mechanics parameters with phase-stepped moire interferometry. Moire and ESPI results were in excellent agreement. The comparison highlighted the sensitivity of ESPI, although the measurement range is significantly less than for moire interferometry. However, it was demonstrated that cumulative values could be calculated with ESPI. The procedure for determining the range of J values could form the basis of an automatic fault detection system. Measured crack-opening displacement could not be compared directly with theory; however, measured load line displacement agreed with clip gauge measurements. The quantitative fracture mechanics study means that the principal objective of this research was achieved.

APPENDICES

A. STRESS FUNCTION THEORY

The purpose of this Appendix is to briefly review the main concepts of stress function theory, and to obtain approximate expressions of displacement and strain for the cantilever loaded at its free end and the centre-notched plate loaded in uniaxial tension. In both examples, we are concerned with in-plane displacements and strains. Consequently two-dimensional stress functions are considered, Section A.1. The stress components σ_{zz} , τ_{xz} and τ_{yz} have been assumed zero on both faces of the plate i.e. plane stress conditions. Plane stress expressions for displacement and strain are obtained for the cantilever, Section A.2 and the centre-notched plate, Section A.3. Plane strain expressions may be derived from the plane stress equations by substituting E and ν in the latter by $E/(1-\nu^2)$ and $\nu/(1-\nu)$ respectively, where E is Young's modulus and ν is Poisson's ratio. This substitution leaves the shear modulus, $\mu = E/2(1+\nu)$, unchanged. The notation of Timoshenko and Goodier¹²⁴ has been used throughout.

A.1 TWO-DIMENSIONAL STRESS FUNCTION

The purpose of any theory of elasticity is to determine the stress state in a body due to an applied load. For two-dimensional problems, the components of normal stress σ_{xx} , σ_{yy} and the shear stress τ_{xy} must be determined at each point in the plane. This stress distribution is the same for plane stress or plane strain. However, the strains and consequently the displacements, are different in the two conditions. Using Hooke's law for the case of plane stress, the components of strain are given by:

$$\epsilon_{xx} = \frac{1}{E}(\sigma_{xx} - \nu\sigma_{yy}); \quad \epsilon_{yy} = \frac{1}{E}(\sigma_{yy} - \nu\sigma_{xx}); \quad \gamma_{xy} = \frac{1}{\mu}\tau_{xy} \quad (\text{A.1})$$

The displacements u and v can then be obtained from the equations:

*For displacement boundary conditions, this condition may not hold.

$$\epsilon_{xx} = \frac{\partial u}{\partial x}; \quad \epsilon_{yy} = \frac{\partial v}{\partial y}; \quad \gamma_{xy} = \frac{\partial u}{\partial y} + \frac{\partial v}{\partial x} \quad (\text{A.2})$$

The components of strain remain unchanged if the following linear functions are added to u and v respectively:

$$u_{RB} = a - by; \quad v_{RB} = c + bx \quad (\text{A.3})$$

where a , b and c are constants. This represents the addition of rigid body motion to the displacements due to the internal strains. The constants a and c represent a translation of the body, whilst b denotes a rotation of the body about the z -axis. In-plane ESPI displacement measurements are unaffected by a rigid body translation, provided it is sufficiently small to avoid decorrelation. However, rigid body rotations will affect the fringe pattern, introducing a constant gradient fringe field. This will be accompanied by a linear translation (not visible in the fringe pattern) if the centre of rotation is not in the field of view. These effects were discussed in Section 3.3.1.

In order to determine the stress components, the differential equations of equilibrium:

$$\begin{aligned} \frac{\partial}{\partial x} (\sigma_{xx} - V) + \frac{\partial \tau_{xy}}{\partial y} &= 0 \\ \frac{\partial}{\partial y} (\sigma_{yy} - V) + \frac{\partial \tau_{xy}}{\partial x} &= 0 \end{aligned} \quad (\text{A.4})$$

together with the compatibility equation in terms of stress for plane stress:

$$\left(\frac{\partial^2}{\partial x^2} + \frac{\partial^2}{\partial y^2} \right) (\sigma_{xx} + \sigma_{yy}) = (1+\nu) \left(\frac{\partial^2 V}{\partial x^2} + \frac{\partial^2 V}{\partial y^2} \right) \quad (\text{A.5})$$

are integrated. The equilibrium equations (A.4) are derived by considering the equilibrium of an element of the body influenced by forces arising from stress variations throughout the body and the body forces per unit volume. The body forces are assumed to have potential, V , giving components:

$$X = -\frac{\partial V}{\partial x}; \quad Y = -\frac{\partial V}{\partial y} \quad (\text{A.6})$$

The compatibility equation (A.5) is derived from the condition that the displacements u and v must be continuous functions in the plane. Equations (A.4) and (A.5) may be solved by introducing a new function, $\phi(x,y)$, called the stress function. Equation (A.4) is satisfied if:

$$\sigma_{xx} - V = \frac{\partial^2 \phi}{\partial y^2}; \quad \sigma_{yy} - V = \frac{\partial^2 \phi}{\partial x^2}; \quad \tau_{xy} = -\frac{\partial^2 \phi}{\partial x \partial y} \quad (\text{A.7})$$

Several functions will give solutions to equations (A.7), but the correct solution is that which also satisfies the compatibility equation (A.5). Substituting equation (A.7) in equation (A.5) gives:

$$\frac{\partial^4 \phi}{\partial x^4} + \frac{2\partial^4 \phi}{\partial x^2 \partial y^2} + \frac{\partial^4 \phi}{\partial y^4} = -(1+\nu) \left(\frac{\partial^2 V}{\partial x^2} + \frac{\partial^2 V}{\partial y^2} \right) \quad (\text{A.8})$$

The solution of a two-dimensional problem reduces to finding a stress function that satisfies equation (A.8) and that also satisfies the boundary conditions.

A.2 CANTILEVER LOADED AT FREE END

Timoshenko and Goodier¹²⁴ consider the case of the cantilever of Figure 4.12, in which the upper and lower edges are not loaded, and shearing forces having a resultant P are distributed at $x=-l$. The full working of a solution using a fourth degree polynomial stress function is given, i.e:

$$\phi = \frac{a_4}{4(3)}x^4 + \frac{b_4}{3(2)}x^3y + \frac{c_4}{2}x^2y^2 + \frac{d_4}{3(2)}xy^3 + \frac{e_4}{4(3)}y^4 \quad (\text{A.9})$$

is given. The coefficients derived depend on the boundary conditions that are assumed. Timoshenko and Goodier assume that:

- i) the shearing force at the loaded end is distributed parabolically;
- ii) the intensity of normal force at the built in end is proportional to y .

If these conditions are not met, which is indeed the case for Figure 4.12, the coefficients will take different values. In general, however, the resulting change in stress distribution is only significant near the ends of the beam, and the simple solution is accurate at points away from the ends. A further boundary condition assumed is that the beam cannot rotate in the xy plane about the z axis. This constraint is realised by assuming that an element of the axis of the beam is fixed at the origin i.e. $(\partial v/\partial x)_{x=0,y=0} = 0$ giving displacements due to bending only. This again is not valid: in practice the cantilever will deflect an added amount due to the effect of shearing force and elasticity of the support. This explains the comparison of the experimental displacement data with the investigation by O'Donnell¹³³ into the elasticity of the support in Section 4.3.3. Bearing in mind these approximations, the displacements due to bending only are given by¹²⁴:

$$\begin{aligned}
 u &= -\frac{P(x+l)^2y}{2EI} - \frac{vPy^3}{6EI} + \frac{Py^3}{6I\mu} + \left(\frac{Pl^2}{2EI} - \frac{Pc^2}{2I\mu} \right) y \\
 v &= \frac{vP(x+l)y^2}{2EI} + \frac{P(x+l)^3}{6EI} - \frac{Pl^2(x+l)}{2EI} + \frac{Pl^3}{3EI}
 \end{aligned}
 \tag{A.10}$$

The xy coordinate system has been shifted to the cantilever base from the free end, and y is rotated through 180° from the Timoshenko and Goodier solution. The components of strain may then be calculated from equations (A.2) and are given in equations (4.4).

A.3 CENTRE-NOTCHED PLATE IN UNIAXIAL TENSION

Rectangular coordinates are adequate to define a stress function for the cantilever. For more complex objects, for example cracks in plates, the boundary is more simply defined using complex variables. Timoshenko and Goodier¹²⁴ demonstrate that the stress function can always be defined in terms of two analytic potential functions $\psi(z)$ and $\chi(z)$, where $z=x+iy$. The stress function may be

expressed in the form:

$$\phi = \operatorname{Re}[\bar{z}\psi(z) + \chi(z)] \quad (\text{A.11})$$

where \bar{z} denotes the complex conjugate of z , and $\operatorname{Re}[\]$ is the real part of the term in brackets. The choice of $\psi(z)$ and $\chi(z)$ depends on the boundary conditions. Substituting equation (A.11) into (A.7) and ignoring body forces gives:

$$\begin{aligned} \sigma_{xx} &= \operatorname{Re}[-\bar{z}\psi''(z) + 2\psi'(z) - \chi''(z)] \\ \sigma_{yy} &= \operatorname{Re}[\bar{z}\psi''(z) + 2\psi'(z) + \chi''(z)] \\ \tau_{xy} &= \operatorname{Im}[\bar{z}\psi''(z) + \chi''(z)] \end{aligned} \quad (\text{A.12})$$

where $\operatorname{Im}[\]$ is the imaginary part of the term in brackets and $\psi'(z)$, $\psi''(z)$ are the first and second differentials of $\psi(z)$ with respect to z respectively. The displacements for plane stress may be evaluated from:

$$2\mu(u+iv) = \frac{3-\nu}{1+\nu}\psi(z) - z\bar{\psi}''(\bar{z}) - \bar{\chi}'(\bar{z}) \quad (\text{A.13})$$

MacGregor¹⁵³ considered the special case of normal loading on the semi-plane i.e. $\tau_{xy}=0$ for $y=0$, which from equation (A.12) gives:

$$0 = \operatorname{Im}[\bar{z}\psi''(z) + \chi''(z)]$$

which is satisfied by:

$$0 = z\psi''(z) + \chi''(z) + A \quad (\text{A.14})$$

where A is a real constant. Equation (A.14) can be substituted into (A.12) to eliminate $\chi''(z)$ and obtain the stress distribution expressed in terms of a single potential function:

$$\begin{aligned} \sigma_{xx} &= \operatorname{Re}[\psi'(z)] - 2y \operatorname{Im}[\psi''(z)] + A \\ \sigma_{yy} &= \operatorname{Re}[\psi'(z)] + 2y \operatorname{Im}[\psi''(z)] - A \\ \tau_{xy} &= -2y \operatorname{Re}[\psi''(z)] \end{aligned} \quad (\text{A.15})$$

The corresponding plane stress displacement distribution, equation (A.13) becomes:

$$\begin{aligned} 2\mu u &= \frac{2(1-\nu)}{(1+\nu)} \operatorname{Re}[\psi(z)] - 2y \operatorname{Im}[\psi'(z)] + Ax \\ 2\mu v &= \frac{4}{(1+\nu)} \operatorname{Im}[\psi(z)] - 2y \operatorname{Re}[\psi'(z)] - Ay \end{aligned} \quad (\text{A.16})$$

Westergaard¹⁵⁴ used equation (A.15) to define a stress function for an infinite medium with a central crack of length $2a$ along the x axis. The boundary conditions are:

$$\begin{aligned} \sigma_{yy} = \tau_{xy} &= 0 && \text{for } y=0 \text{ and } -a < x < a \\ \sigma_{xx} = \epsilon\sigma; \sigma_{yy} = \sigma; \tau_{xy} &= 0 && \text{for } \sqrt{(x^2+y^2)} \rightarrow \infty \end{aligned}$$

where $\epsilon = \sigma_{yy}/\sigma_{xx}$. Westergaard used MacGregor's original formulation of equation (A.15) in which A had been omitted. Thus the original Westergaard solution was restricted to the case of uniform biaxial tension i.e. $\epsilon=1$ and $A=0$. Sih¹³⁷ recognised this omission and proposed a modified solution:

$$\begin{aligned} 2\psi(z) &= Z(z) - A \\ &= \frac{\sigma z}{(z^2 - a^2)^{1/2}} - (1-\epsilon)\frac{\sigma}{2} \end{aligned} \quad (\text{A.17})$$

where the first term on the right hand side, $Z(z)$, is Westergaard's original solution. Irwin¹⁰ calculated the displacement distribution due to $Z(z)$ in terms of polar coordinates with origin at the crack tip, by making the substitution $z=a+re^{i\theta}$. This gives:

$$\begin{aligned} Z(z) &= \frac{\sigma(a+re^{i\theta})}{\sqrt{2are^{i\theta}}} \left(1 + \frac{re^{i\theta}}{2a}\right)^{-1/2} \\ &\approx \sigma \sqrt{\frac{a}{2r}} e^{-i\theta/2} \end{aligned} \quad (\text{A.18})$$

At the same time Irwin introduced the quantity $K_I = \sigma\sqrt{(\pi a)}$, which he called the stress-intensity factor. Equation (A.18) represents the first term in a series due to the expansion of $(1+re^{i\theta}/2a)^{-1/2}$. Higher order terms are ignored by making the

assumption $r \ll a$, and consequently the solution is only valid close to the crack tip. These higher order terms are included for evaluation of K_I from displacement data measured away from the crack tip. Irwin's result gives the first two terms on the right hand side of equation (A.16); making the substitution for A from equation (A.17) gives the modified Westergaard displacement distribution for plane stress¹³⁷:

$$\begin{aligned} u &= \frac{K_I}{\mu} \sqrt{\frac{r}{2\pi}} \cos\left(\frac{\theta}{2}\right) \left[\frac{1-\nu}{1+\nu} + \sin^2\left(\frac{\theta}{2}\right) \right] - \frac{\sigma}{E} (1-\epsilon) r \cos\theta \\ v &= \frac{K_I}{\mu} \sqrt{\frac{r}{2\pi}} \sin\left(\frac{\theta}{2}\right) \left[\frac{2}{1+\nu} - \cos^2\left(\frac{\theta}{2}\right) \right] + \frac{\nu\sigma}{E} (1-\epsilon) r \sin\theta \end{aligned} \quad (\text{A.19})$$

For uniaxial tension $\epsilon=0$, equations (5.2). The components of strain may be evaluated using equation (A.2), again for $\epsilon=0$:

$$\begin{aligned} \epsilon_{xx} &= \frac{\partial u}{\partial x} = \cos\theta \frac{\partial u}{\partial r} - \frac{\sin\theta}{r} \frac{\partial u}{\partial \theta} \\ &= \frac{K_I}{E\sqrt{2\pi r}} \cos\frac{\theta}{2} \left((1-\nu) - (1+\nu) \sin\left(\frac{\theta}{2}\right) \sin\left(\frac{3\theta}{2}\right) \right) - \frac{\sigma}{E} \end{aligned}$$

$$\begin{aligned} \frac{\partial u}{\partial y} &= \sin\theta \frac{\partial u}{\partial r} + \frac{\cos\theta}{r} \frac{\partial u}{\partial \theta} \\ &= \frac{K_I}{E\sqrt{2\pi r}} \sin\frac{\theta}{2} \left((1-\nu) + (1+\nu) \left(1 + \cos\left(\frac{\theta}{2}\right) \sin\left(\frac{3\theta}{2}\right) \right) \right) \end{aligned}$$

$$\epsilon_{yy} = \frac{\partial v}{\partial y} = \sin\theta \frac{\partial v}{\partial r} + \frac{\cos\theta}{r} \frac{\partial v}{\partial \theta} \quad (\text{A.20 Continued over})$$

$$= \frac{K_I}{E\sqrt{2\pi r}} \cos\frac{\theta}{2} \left(2 + (1+\nu) \left(\sin\left(\frac{\theta}{2}\right) \sin\left(\frac{3\theta}{2}\right) - 1 \right) \right) + \frac{\nu\sigma}{E}$$

$$\frac{\partial v}{\partial x} = \cos\theta \frac{\partial v}{\partial r} - \frac{\sin\theta}{r} \frac{\partial v}{\partial \theta}$$

$$= \frac{K_I}{E\sqrt{2\pi r}} \sin\frac{\theta}{2} \left(-2 + (1+\nu)\cos\left(\frac{\theta}{2}\right)\cos\left(\frac{3\theta}{2}\right) \right)$$

$$\gamma_{xy} = \frac{\partial u}{\partial y} + \frac{\partial v}{\partial x} \quad (\text{A.20 continued})$$

$$= \frac{K_I}{E\sqrt{2\pi r}} 2(1+\nu) \sin\left(\frac{\theta}{2}\right) \cos\left(\frac{\theta}{2}\right) \cos\left(\frac{3\theta}{2}\right)$$

The maximum in-plane shear stress, τ_m , is related to the cartesian components of stress by:

$$(\tau_m)^2 = \left(\frac{\sigma_{xx} - \sigma_{yy}}{2} \right)^2 + (\tau_{xy})^2 \quad (\text{A.21})$$

Considering the special case of zero shear stress on the semi-plane ($y=0$), and introducing equations (A.15), equation (A.21) becomes:

$$\tau_m = |A| \quad (\text{A.22})$$

Thus for any stress function $\psi'(z)$, τ_m will be constant along the line $y=0$. Isochromatic fringes in photoelasticity represent contours of constant principal stress difference (i.e. locus of constant τ_m). Sanford¹⁴⁴ noticed that for cracks approaching the boundary of a compact tension specimen, isochromatic fringes form ahead of the crack i.e. τ_m is not constant as implied by equation (A.22). Consequently he proposed a further generalisation of the Westergaard solution, in which the real constant A is replaced by the complex function, $Y(z)$. Equation (A.17) then becomes:

$$2\psi'(z) = Z(z) - Y(z)$$

Equations (A.15) can be expressed in terms of Westergaard's original stress function, $Z(z)$, and the new function, $Y(z)$:

$$\begin{aligned}\sigma_{xx} &= \operatorname{Re} Z - y \operatorname{Im} Z' - y \operatorname{Im} Y' + 2 \operatorname{Re} Y \\ \sigma_{yy} &= \operatorname{Re} Z + y \operatorname{Im} Z' + y \operatorname{Im} Y' \\ \tau_{xy} &= -y \operatorname{Re} Z' - y \operatorname{Re} Y' - \operatorname{Im} Y\end{aligned}\tag{A.23}$$

Sanford noted a Westergaard stress function for use with the boundary collocation method to solve opening mode crack problems with finite boundaries:

$$\begin{aligned}Z(z) &= \frac{K_I}{\sqrt{2\pi z}} + \sum_{n=1}^N A_n z^{n-1/2} \\ &\equiv \sum_{j=0}^J C_j z^{j-1/2}\end{aligned}\tag{A.24}$$

where C is a real constant. This is analogous to including the terms truncated in the Irwin derivation of equation (A.18). With this in mind, Sanford proposed:

$$Y(z) = \sum_{j=0}^J C_{j+1} z^j\tag{A.25}$$

i.e. the extra term is a sum of polynomials, the required order of which is determined by the fit of the predicted displacement field to that measured. More terms are required as the distance from the crack tip increases, or the distance to a boundary decreases. Barker et al⁴³ derived the displacement components from this stress function in the usual manner, including the substitution from cartesian to polar coordinates. They obtained:

$$\begin{aligned}
 Eu &= \sum_{j=0}^J C_{2^{j+1/2}} \frac{r^{j+1/2}}{2^{j+1/2}} [(1-\nu)\cos(j+1/2)\theta - (1+\nu)(j+1/2)\sin\theta\sin(j-1/2)\theta] \\
 &\quad + \sum_{j=0}^J C_{2^{j+1}} \frac{r^{j+1}}{2^{j+1}} [2\cos(j+1)\theta - (1+\nu)(j+1)\sin\theta\sin(j\theta)]
 \end{aligned} \tag{A.26}$$

$$\begin{aligned}
 Ev &= \sum_{j=0}^J C_{2^{j+1/2}} \frac{r^{j+1/2}}{2^{j+1/2}} [2\sin(j+1/2)\theta - (1+\nu)(j+1/2)\sin\theta\cos(j-1/2)\theta] \\
 &\quad + \sum_{j=0}^J C_{2^{j+1}} \frac{r^{j+1}}{2^{j+1}} [(1-\nu)\sin(j+1)\theta - (1+\nu)(j+1)\sin\theta\cos(j\theta)]
 \end{aligned}$$

For the case $j=0$, both u and v are the sum of two terms. This is equivalent to equation (A.19) with $\epsilon=0$, where $C_0=K_1/\sqrt{(2\pi)}$ and $C_1=-\sigma/2$. Equations (A.26) are used to calculate K_1 in Section 5.2.3.

B. ESPI FRINGE INTERPRETATION

ESPI provides measurement information as the temporal voltage variation of a video signal or as the spatial intensity distribution of the displayed image. Considering the latter, it is necessary to know how the spatial intensity variation (i.e. fringes) is related to the measured quantity (e.g. surface displacement) in order to make quantitative measurements. This is called the fringe function. This appendix presents the basic equations needed to interpret ESPI fringe patterns. The theory presented has been derived individually by previous researchers. It is the purpose here to cast the theory into a consistent form with that used throughout the thesis and to provide sufficient information to keep the thesis self-contained. The fringe function is derived in general form in terms of optical phase change, and can then be applied to the interferometer configurations described in Section 2.3.

B.1 SPECKLE PATTERN INTERFEROMETRY

When an optically rough surface is illuminated by a coherent light source (e.g. a laser) the light scattered from the surface gives the appearance of a random distribution of "speckles" of varying brightness. Speckles arise because the light arriving at any point in the image plane comprises a number of components scattered diffusely from an area of the object, the area being determined by the optical resolution of the imaging system. The phase of the component is assumed to be random due to the roughness of the surface, although the amplitudes are similar. Thus the intensity at each point in the image plane varies randomly, giving rise to the speckled appearance.

The principle behind ESPI requires that for small surface displacements or deformations, the intensity of individual scattered components from the resolution

area remains constant, and that the phase change for each component is approximately equal. This implies that the position of each speckle remains substantially the same. Therefore, the phase of each speckle in the image plane contains information due to the surface motion. If a second, mutually coherent wavefront is added to the speckle pattern, it acts as a phase reference. The intensity of each speckle is then a function of the phase relationship between the two wavefronts, which in turn is related to the surface deformation. Surface deformation can then be seen as a difference in speckle intensities i.e. the difference between two phase-referenced speckle patterns, one recorded before deformation and the second recorded after deformation. In regions where the surface has not moved, the speckles maintain their original intensity; elsewhere the speckle intensity varies accordingly. The two speckle patterns are normally compared (or correlated) by the addition of intensities on the camera faceplate or by electronic subtraction using a video store. Differences between the speckle patterns are revealed by alternating bright and dark fringes corresponding to loci of equal phase difference between the two wavefronts. This phase difference is related to the optical path difference introduced by the motion of the surface.

B.2 GENERALISED FRINGE FUNCTION

Consider a general, two-beam interferometer, where the two interfering beams are mutually coherent. The general coordinate system with Cartesian axes x , y and z is defined such that the imaging system views the object along the z -axis, Figure 2.2. Point (x,y,z) in object space is imaged to (m,n) in the image plane, where it is assumed that a focused-image viewing system is used with sufficient depth of field to view the whole object. The instantaneous amplitudes U of two wavefronts plane-polarised in the same direction may be represented by:

$$\begin{aligned} U_A &= u_A e^{i(\omega t + \psi_A)} \\ U_B &= u_B e^{i(\omega t + \psi_B)} \end{aligned} \tag{B.1}$$

where subscripts A and B denote the two beams, u is the real amplitude, ω is the

angular frequency, ψ the phase and t is time. Both u and ψ are functions of m, n and t . The amplitude of the combined wavefront is:

$$\begin{aligned} U_T &= U_A + U_B \\ &= u_A e^{i(\omega_A t + \psi_A)} + u_B e^{i(\omega_B t + \psi_B)} \end{aligned} \quad (\text{B.2})$$

The total intensity at $P(m,n)$ is given by:

$$\begin{aligned} I &= U_T U_T^* \\ &= u_A^2 + u_B^2 + 2u_A u_B \cos(\omega t + \psi) \end{aligned} \quad (\text{B.3})$$

where U_T^* is the complex conjugate of U_T , ω is the frequency difference ($\omega_A - \omega_B$) and ψ is the phase difference ($\psi_A - \psi_B$). Thus for mutually coherent beams with a frequency difference of ω , the interference pattern is time dependent and beats with the difference frequency, ω . This effect is used in heterodyne interferometry, Section 3.2.1. For the case $\Delta\omega=0$ used in this thesis, equation (B.3) may be written:

$$I = I_A + I_B + 2\sqrt{I_A I_B} \cos\psi \quad (\text{B.4})$$

Any relative phase-shift between the two wavefronts at P will cause the intensity to change to:

$$I = I_A + I_B + 2\sqrt{I_A I_B} \cos(\psi + \phi) \quad (\text{B.5})$$

The phase difference ϕ may be introduced by deformation or displacement of the object surface. It is assumed here that ψ and ϕ do not vary with time i.e. that the object is static and undergoes static displacement. For classical interferometry I_A , I_B and ψ generally vary continuously with position (m,n). For speckle interferometry, I and ψ for one or both beams vary randomly with position. Thus measurements must be made by observing the *change* in speckle intensity. The formation of speckle correlation fringes by intensity subtraction and addition is discussed in Sections 3.2.1 and 3.2.3 respectively.

An interferometer is sensitive to one spatial component of displacement at any

point in the object space. The direction of sensitivity can be defined by a unit vector \mathbf{n} called the sensitivity vector. If the displacement vector of each object point is $\mathbf{d}(x,y,z)$, then the interferometer will be sensitive to the component of \mathbf{d} resolved along the sensitivity vector:

$$d_n = \mathbf{n} \cdot \mathbf{d} \quad (\text{B.6})$$

The optical phase change per unit displacement is determined by the wave number $k=2\pi/\lambda$ (where λ is the wavelength of the illuminating light). The phase change at the image plane due to a unit phase change in the object space can be defined as a fringe sensitivity factor, Γ , that determines how many fringes correspond to a given surface displacement. Then:

$$\phi' = k \Gamma d_n \quad (\text{B.7})$$

Γ and \mathbf{n} are determined by the optical geometry of the interferometer, and are functions of (x,y,z) . Three-dimensional deformation analysis requires the object displacement function $\mathbf{d}(x,y,z)$ to be determined. The interferogram represented by equation (B.5) is processed to determine ϕ , from which d_n may be calculated using equation (B.7) with known values of k and Γ . d_n is only one resolved component of \mathbf{d} , and therefore at least three different d_n measurements must be obtained to completely define \mathbf{d} in three dimensions. A different sensitivity vector, \mathbf{n} is required for each measurement. Ideally three mutually perpendicular sensitivity vectors should be used because this obviates the need to solve simultaneous equations. ESPI configurations which satisfy this condition are described in Section 2.3.

C. IMAGE PROCESSING HARDWARE AND SOFTWARE

This appendix describes the image processing hardware and software used throughout the thesis. Relevant details of other equipment used are given the first time that piece of equipment is encountered in the thesis. Hardware is described in Section C.1 and software in Section C.2. A complete software listing is of doubtful use: therefore the most important steps are shown in flow diagrams. These steps can then be implemented on any image processor in the particular programming language being used.

C.1 HARDWARE

All phase-stepped work was performed with Phillips CCD cameras with an active picture element cell size of $10\mu\text{m}$ (horizontal) x $7.8\mu\text{m}$ (vertical). The CCIR output of the camera was passed directly to a FOR-A framestore. These framestores were modified in-house to provide filtering and contrast stretching prior to digital subtraction. Filtering and stretching may be switched off if desired. If selected, the signal is high-pass filtered (centred on 1.1MHz) to pass speckle data and to suppress low frequency structure such as Gaussian beam profile; the signal is then linearly amplified between the video signal limits of 300mV and 1V. Real-time subtraction of a reference image from the current TV image is performed through exclusive-or logic. The CCIR signal is therefore digitised over 416×512 pixels with 6 bit resolution. Digitisation is nominally to 512×512 elements, but digitisation begins over the front porch of the TV signal and thus misses $(12/64) \times 512 = 96$ pixels in the horizontal direction. Following subtraction, the framestore outputs the result in CCIR format to a TV monitor and the image processor.

A Kontron pipeline image processor was used, and the output from the

framestore digitised with 256x256 x 8 bit resolution. The Kontron provided standard image processing routines such as filtering and edge detection. The Kontron is hosted by a DEC MicroVax computer that runs the system and allows programming in Fortran. Fortran programs may call Kontron image processing subroutines to work directly on images in memory (e.g. filtering), or transfer image data to MicroVax memory for user specific applications (e.g. calculation of phase). The architecture of the system has been described by Kerr and Tyrer¹⁰⁹ as an example of the requirements of an image processing system for phase-stepped ESPI. The transfer of data between the Kontron and MicroVax takes place through a tri-directional interface which limits the speed of the system: approximately 30 seconds are required for 256x256 x 8 bit image transfer. Thus although phase calculation may take approximately eight seconds including neighbourhood average filtering, processing takes at least two minutes (3x30 seconds to transfer data from Kontron image memory to MicroVax, and 30 seconds to display the calculated wrapped phase). This time is increased four-fold and sixteen-fold for 512x512 and 1024x1024 resolutions respectively, and consequently the full resolution capability of the Kontron was not exploited for the work presented in the thesis. The image processor was state-of-the-art in 1986, but with the rapid development of personal computer image processors, the system has begun to show its age. However, the advantage of the system is the large image memory of the Kontron (2.5MBytes) coupled with large programming memory area and hardware floating point capability of the MicroVax. This makes the system ideal for program development. Image data need only be transferred to the Vax once, so that all subsequent processing is not delayed by the tri-directional interface. D-A conversion on one MicroVax communication port enables a voltage step to be applied to a piezo translator for phase-stepping controlled by the computer.

C.2 SOFTWARE

This section describes the steps used to obtain phase (displacement) and strain

data from ESPI fringe patterns. A flow diagram is given for each process (i.e. displacement and strain calculation) although in actuality these were subdivided into more than two programs to keep the software suite simple and flexible. The approximate time required for each stage is indicated at the left-hand side of the charts, based on 256x256 images. Data required by the program is shown on the right-hand side. The flow charts assume that horizontal in-plane measurements are made. The programs for vertical in-plane sensitivity and simultaneous horizontal and vertical in-plane measurements can then be derived from the flow charts quite simply.

Figure C.1 shows the steps used to record and display full-field displacement data. Two-step phase evaluation, equation (3.12), has been assumed. The first stage is to digitise three phase-stepped fringe patterns from the optimised interferometer to the Kontron image memory. Three calls to the Kontron image-digitisation subroutine were made from the MicroVax with a 1/25 second delay (i.e. one frame) between each call. The delay between grabbing images was used to move the piezo-mounted mirror. Three frames were therefore grabbed in five frame periods, making certain that the piezo was not translating or undergoing transient vibrations about the required position whilst the subsequent image was digitised. The piezo must be previously calibrated to determine the required voltage for a given size of phase-step. The user must also specify at this stage whether the left or right hand illumination beam is to be stepped, and whether mirror motion increases or decreases the relative path length between the two beams. As stated in Section 4.3.1, the default used throughout the thesis was stepping the right-hand beam for horizontal in-plane and the upper beam for vertical in-plane, with the path difference decreasing (mirror moving toward object) in both cases. Should the other beam be stepped or the mirror direction be reversed, then the phase ramp in the calculated phase map is reversed. Without modification, the unwrapping routine will give the correct amplitude of displacement, but in the wrong direction. Two solutions were included in the software to avoid modifying the unwrapping routine. The first used a multiplication factor, *signh*, every time the displacement was calculated from the unwrapped phase data. In the default

Time (Seconds)	Step	Variables Required
0.2	Digitise three phase-stepped fringe patterns from optimised interferometer to Kontron image memory	Piezo-calibration
4 LP1 60 Fourier	Lowpass filter in Kontron image memory	
90	Transfer three images to MicroVax [Data type: 256x256 x 2 byte integer]	
2	Load look-up-table (LUT) [Data type: 512x1024 x 4 byte floating point]	Pre-calculation of LUT
4	Select phase value from LUT address $m = I_3 - I_2$; $n = 2I_1 - I_2 - I_3$ [Data type: 256x256x 4 byte floating point]	
1	Store phase data to disk	
30	Transfer wrapped phase data to Kontron [Data type: 256x256x 2 byte integer]	
2	Unwrap phase data [Data type: 256x256 x 4 byte floating point]	Discontinuity parameter Reference point
30	Transfer display to Kontron: i) Grey-scale unwrapped phase data (One of three modes, see Table C.1) [Data type: 256x256 x 2 byte integer]	
120	ii) Overlay arrow at grid plus print-out of displacement	Grid spacing λ, θ

Figure C.1 Flow chart for displacement calculation and display

setting $signh=1$ (step right hand beam, path length decreases). Should the other beam be stepped or the mirror direction be reversed, $signh=-1$. If both are changed (i.e. the other beam is stepped and the mirror direction is reversed) $signh=1$. The second solution eliminated the need to include the factor $signh$ every time displacement was calculated. Instead, if $signh=-1$ the wrapped phase map was inverted i.e. the phase, ϕ , at each point (m,n) in the phase map is set to the absolute value of $(\phi-2\pi)$.

The digital images must be lowpass filtered. All the filters used in the thesis (neighbourhood average, median, Fourier) were available on the Kontron. Following filtering, the three images were transferred to the MicroVax as 256×256 integer arrays. Phase was calculated through a look-up-table, following closely an implementation due to Kerr at Loughborough University. The look-up-table is stored as a 512×1024 element data file on the MicroVax hard disk. Element (m,n) contains the value $\arctangent(\sqrt{3}m/n)$, and therefore includes all possible values for $m=I_3-I_2$, $n=2I_1-I_2-I_3$. The four-byte floating-point result is scaled to give the angle in the range 0 to 2π radians. Four-byte representation ensures seven digits of precision in the mantissa, well within the measurement accuracy of $\pm 2\pi/14$ radians due to speckle noise, Section 3.2.5. This wrapped phase-map is stored to disk, and serves as the source for subsequent analysis. The wrapped phase values are scaled in the range 0 to 255, converted to an integer array, and returned to the Kontron for display.

The unwrapping procedure used was described in Section 3.2.1. The operator must select the absolute phase difference between adjacent pixels (the discontinuity search parameter) above which a phase discontinuity is identified. A value of π radians was assumed for the thesis. The coordinates of a reference point (zero displacement) can also be entered, and all unwrapped phase values are referenced to the phase value at this point. The rectangular area to be unwrapped is selected by the user. Thus to unwrap around a crack tip (e.g. Figure 5.8) three overlapping rectangular areas are selected. Two methods were used to display displacement. For the first, unwrapped phase values were linearly scaled

between 0 and 255, and transferred to the Kontron for display. Black therefore denotes the most negative phase displacement. This is a particularly useful way to spot unwrapping inconsistencies. No examples of this form of output are shown in the thesis, but the result is similar to the grey-scaled plots of surface strain, for example, Figure 4.15. Continuous grey-scale or contours of phase may be selected, and are discussed further under the representation of strain values later in this section. The second method to display displacement was to calculate the displacement at a user-defined grid of points. From equation (2.21), this requires values for the illumination wavelength, λ , and the illumination angle, θ , to be defined. Displacement at each point was printed in microns. The phase values at these points were scaled in the range zero to the grid spacing minus one. The absolute value of this result defines an arrow length to be plotted in the overlay plane of the Kontron, whilst the sign gives the direction (i.e. to the left or right). Examples for horizontal and vertical phase data are given in Figures 3.2(a) and 3.2(b) respectively. To combine two orthogonally-sensitive phase maps, displacement values are calculated by the vector addition of the values at the grid of points. Thus only positive values are output to the printer. Direction is given by an associated angle in the printed output and again by scaled arrows in the image overlay plane, Figure 3.2(c). Arrows were found to be the clearest method of displaying in-plane displacement.

The flow diagram for strain calculation is displayed in Figure C.2. The starting point is a wrapped phase map stored on disk. This may be unwrapped as described above, although the specification of a reference point is not necessary. The operator then selects the window size in pixels of the plane to be fitted to the unwrapped phase data. The results presented in this thesis use 25x25 pixels. Strain is calculated at the central pixel of each 25x25 pixel plane in a rectangular area defined by the user. As with unwrapping, strain calculation around the crack tip is achieved by defining three overlapping rectangular areas. For each 25x25 pixel plane, the rate of change of phase per pixel is calculated in the horizontal and vertical directions i.e. a_1 and a_2 in equation (3.36). The calculation of a_0 in equation (3.36) for smoothing the phase data, e.g. Figure 5.12(c), is performed

Time (Seconds)	Step	Variables Required
1	Retrieve phase data from disk [Data type: 256x256x 4 byte floating point]	
2	Unwrap phase data [Data type: 256x256x 4 byte floating point]	Discontinuity parameter
460	Calculate equation (3.36) at central pixel of each plane in defined rectangular area [Data type: Two 256x256x 4 byte floating point]	Plane side length
60	Transfer display to Kontron: i) Grey-scale strain data. One of three modes (see Table C.1) [Data type: Two 256x256x 2 byte integer] ii) Printer output	λ, θ Scale factor

Figure C.2 Flow chart for strain calculation and display

Mode	Output		User Input
	Kontron	Printer	
1	Continuous grey-scale	Maximum and minimum strain values	None
2	Specified number of strain contours	Strain value at each contour (μS)	Number of contours
3	Specified width of strain contours	Strain value at each contour (μS)	Width of contours (μS) plus starting strain value (μS)

Table C.1 Modes for strain (and unwrapped phase) display

separately. Four-byte floating-point arithmetic is used throughout. For seven decimal figures of accuracy in the phase data, digital noise will limit the accuracy of calculated rate of change of phase per pixel to approximately four decimal figures for a 25×25 pixel plane fit. With a strain noise threshold of $6\mu\text{S}$ due to speckle and an approximate maximum measurement range of $150\mu\text{S}$, four-byte representation is again adequate.

To display the calculated strain, values were scaled between 0 and 255 (black representing most negative) and transferred to the Kontron as an integer array. Three modes of display were found useful. These modes are outlined in Table C.1, and were also available for displaying unwrapped phase data. Mode 3 was used for all results presented in the thesis, because this enabled experimental and theoretical results to be compared most conveniently. Printer output and the specification of contour width in $\mu\text{strains}$ requires a conversion from rate of change of phase per pixel to rate of change of displacement per unit distance. Hence λ and θ are again required to convert from phase to displacement, and a calibration of metres/pixel is required from the live image. This was calculated from a live image of graph paper placed on the object surface.

D. LIST OF SYMBOLS

This appendix lists the symbols most commonly used in the thesis. Those not included are defined in the text. It is noted that combining two fields of study (optics and fracture mechanics) leads to an overlap in notation: e.g. I for light intensity and second moment of area. However, the correct meaning should be self-evident from the context.

2a	Crack length (m)
B	Specimen thickness (m)
d	General displacement (m)
E	Young's modulus (N/m ²)
G	Energy release rate (N/m)
I	Light intensity (W/m ²) or Second moment of area (m ⁴)
J	J-integral (N/m)
k	Wave number (radians/m)
K _I	Opening-mode (Mode 1) stress-intensity factor (N/m ^{3/2})
r,θ	Polar coordinates
m,n	Image plane coordinates
M	Speckle correlation cells per pixel or Plastic constraint factor
NA	Numerical aperture
P	Load (N)
u,v,w	Displacement components relative to Cartesian coordinates (m)
x,y,z	Cartesian coordinates
Z(z)	Stress function
α	Rigid body rotation (radians)
Γ	Fringe sensitivity factor or Contour enclosing crack tip

$\gamma_{xy}, \gamma_{yz}, \gamma_{xz}$	Shear strain
δ	Crack-opening displacement (m)
$\epsilon_{xx}, \epsilon_{yy}, \epsilon_{zz}$	Strain components relative to Cartesian components
ϵ_{ys}	Elastic strain to yield point
ϵ_1, ϵ_2	Principal strains
θ	Angle between illumination beam and surface normal (radians) or Polar coordinate
λ	Wavelength (m)
μ	Shear modulus (N/m ²)
$\sigma_{xx}, \sigma_{yy}, \sigma_{zz}$	Stress components relative to Cartesian coordinates (N/m ²)
σ_{ys}	Yield stress (N/m ²)
σ_1, σ_2	Principal stresses (N/m ²)
$\tau_{xy}, \tau_{yz}, \tau_{xz}$	Shear stress (N/m ²)
ν	Poisson's ratio
ϕ	Optical phase due to displacement (radians)
ψ	Random speckle phase (radians)
$\chi'(z), \psi'(z)$	Stress functions
ω	Frequency (Hz)

E. PUBLICATIONS

The following list of publications arose from the work presented in the thesis. A discussion of twin-pulsed ESPI not included in the thesis can be found in papers 7 and 9.

1. Moore A.J. and Tyrer J.R.
"An electronic speckle pattern interferometer for complete in-plane displacement measurement"
Measurement and Science Technology (formerly J Phys E) 1 1024-1030 (1991)
2. Selected for republication in Engineering Optics 4(1) 33-39 (1991)
3. Moore A.J. and Tyrer J.R.
"Phase-shifting speckle interferometry for complete in-plane displacement measurement"
in *Applied Optics Digest*, Dainty J.C. (ed), Institute of Physics 267-268 (1990)
4. Moore A.J. and Tyrer J.R.
"Surface strain measurement with ESPI applied to fracture mechanics"
in *Hologram Interferometry and Speckle Metrology*, Society for Experimental Mechanics 192-198 (1990)
5. Moore A.J. and Tyrer J.R.
"Evaluation of fracture mechanics parameters from ESPI fringe patterns"
in *Fringe Analysis '92*, Halliwell N.A. et al (eds), FASIG, 155-163 (1992)

6. Selected for republication in Optics and Lasers in Engineering (in press 1993)

7. Mendoza Santoyo F. and Moore A.J.
"Subtraction of twin-pulse addition fringe patterns from ESPI"
Proc SPIE 1756: Interferometry (Applications) (in press 1993)

8. Tyrer J.R. and Moore A.J.
"Extraction of strain data from ESPI fringe patterns"
Proc SPIE 1821: Industrial Applications of Optical Inspection and Metrology (in press 1993)

9. Moore A.J., Tyrer J.R. and Mendoza Santoyo F.
"Phase extraction from ESPI addition fringes"
Submitted to Applied Optics

REFERENCES

1. Knott J.F. "Fundamentals of fracture mechanics" Halsted Press (1973)
2. Rolfe S.T. and Barsom J.M. "Fracture and fatigue control in structures. Applications of fracture mechanics" Prentice-Hall (1977)
3. Broek D. "Elementary engineering fracture mechanics" Martinus Nijhoff (1986)
4. Griffith A.A. "The phenomena of rupture and flow in solids" Phil Trans Royal Soc A221 163-198 (1920)
5. Griffith A.A. "The theory of rupture" Proc 1st Int Congr Applied Mechanics, Delft 55-63 (1924)
6. Orowan E. "Fracture and strength of solids" Rep Prog in Phys 12 185-232 (1949)
7. Felbeck D.K. and Orowan E. "Experiments on brittle fracture of steel plates" Welding Journal Research Supplement 34 570s-575s (1955)
8. Irwin G.R. and Kies J.A. "Fracturing and fracture dynamics" Welding Journal Research Supplement 31 95s-100s (1952)
9. Irwin G.R. and Kies J.A. "Critical energy rate analysis of fracture strength" Welding Journal Research Supplement 33 193s-198s (1954)
10. Irwin G.R. "Analysis of stresses and strains near the end of a crack traversing a plate" J Appl Mech 24 361-364 (1957)
11. Irwin G.R. "Relation of stresses near a crack to the crack extension force" Proc 9th Int Conf Appl Mech, Brussels 245-251 (1957)
12. Brown W.F. and Srawley J.E. "Plane strain crack toughness testing of high strength metallic materials" ASTM STP 410 (1967)
13. British Standard 5447 "Methods of test for plane strain fracture toughness (K_{Ic}) of metallic materials" (1977)
14. Wells A.A. "Unstable crack propagation in metals: cleavage and fast fracture" Proc Crack Propagation Symposium, Cranfield 210-230 (1960)
15. Burdekin F.M and Stone D.E.W. "The crack-opening displacement approach to fracture mechanics in yielding materials" J Strain Analysis 1(2) 145-153 (1966)

16. British Standard 5762 "British standard methods for crack-opening displacement(COD) testing"
17. Rice J.R. and Rosengren G.F. "Plane strain deformation near a crack tip in a power-law hardening material" *J Mech Phys Solids* 16 1-12 (1968)
18. Hutchinson J.W. "Singular behaviour at the end of a tensile crack in a hardening material" *J Mech Phys Solids* 16 13-31 (1968)
19. Begley J.A. and Landes J.D. "The J-integral as a fracture criterion" *ASTM STP 514* 1-20 (1972)
20. American Society for Testing and Materials (ASTM) Standard E813 "Standard test method for J_{Ic} , a measure of fracture toughness" (1989)
21. Kraft J.M., Sullivan A.M. and Boyle R.W. "Effects of specimen dimensions on fracture instability of notched sheets" *Proc Crack Propagation Symposium, Cranfield* 8-26 (1961)
22. ASTM Standard E561 "Standard practice for R-curve determination" (1986)
23. Paris P.C. and Erdogan F. "A critical analysis of crack propagation laws" *Trans ASME J Basic Eng D* 85-93 (1963)
24. Hellen T.K. "The virtual crack extension method of creep fracture" *Proc. Practical Applications of Fracture Mechanics, Institute of Physics* (1990)
25. Landes J.D. And Begley J.A. "A fracture mechanics approach to creep crack growth" *ASTM STP 590* 128-148 (1976)
26. Blackburn W.S. "Path independent integrals to predict onset of crack instability in an elastic-plastic material" *Int J Fract Mech* 8 343-346 (1972)
27. Rooke D.P. and Cartwright D.J. "Compendium of stress intensity factors" *HM Stationary Office* (1976)
28. Cartwright D.J. and Rooke D.J. "Evaluation of stress intensity factors" *J Strain Analysis* 10(4) 217-224 (1975)
29. Post D. "Photoelasticity" in *Manual on Experimental Stress Analysis*, Kobayashi A.S. (ed), SESA, Chapter 4 (1978)
30. Sanford R.J. "Visualising stress fields with photoelastic holography" *Opt Eng* 21(3) 489-495 (1982)
31. Patterson E.A. and Wang Z.F. "Towards full-field automated photoelastic analysis of complex components" *Strain* 49-56 (May, 1991)

32. Kobayashi A.S. "Photoelasticity techniques" in *Manual on Experimental Stress Analysis*, Kobayashi A.S. (ed), SESA, Chapter 6 (1978)
33. Wells A.A. and Post D. "The dynamic stress distribution surrounding a running crack - a photoelastic analysis" *Proc SESA* 16(1) 69-92 (1958)
34. Etheridge J.M. and Dally J.W. "A critical review of methods for determining stress-intensity factors from isochromatic fringes" *Exp Mech* 17 248-254 (1977)
35. Sanford R.J. and Dally J.W. "A general method for determining mixed-mode stress-intensity factors from isochromatic fringe patterns" *Eng Fract Mech* 11 621-633 (1979)
36. Smith C.W. "Use of three-dimensional photoelasticity in fracture mechanics" *Exp Mech* 13(12) 539-544 (1973)
37. Gerberich W.W. "Plastic strains and energy density in cracked plates" *Exp Mech* 4 335-334 (1964)
38. Muller T. and Gross D. "Experimental investigations of the path independence of the J-integral for large plastic zones" in *Fracture and Fatigue*, Pergamon Press, 177-184 (1980)
39. Oppel G.U. and Hill P.W. "Strain measurements at the root of cracks and notches" *Exp Mech* 4(7) 206-211 (1964)
40. Underwood J.H. and Kendall D.P. "Measurement of microscopic plastic strain distributions in the region of a crack tip" *Exp Mech* 9 296-304 (1969)
41. Sciammarella C.A. "The moire method - a review" *Exp Mech* 22 418-433 (1982)
42. Post D. "Developments in moire interferometry" *Opt Eng* 21(3) 458-467 (1982)
43. Barker D.B., Sanford R.J. and Chona R. "Determining K and related stress field parameters from displacement fields" *Exp Mech* 25(12) 399-407 (1985)
44. Epstein J.S., Jung H.Y. and Reuter W.G. "Stress-intensity factor extraction using moire interferometry based on a two-parameter displacement eigenfunction" *Opt and Las in Eng* 13 167-180 (1990)
45. Gray T.G.F., McKelvie J., MacKenzie P. and Walker C.A. "Interferometric measurement of J for arbitrary geometry and loading" *Int J of Fracture* 24 R109-R114 (1984)

46. Marshall S.J., Rixon R.C., Caulfield M.M. and MacKenzie P.M. "The application of automatic fringe analysis in fracture mechanics" *Opt and Las in Eng* 7 175-193 (1987)
47. Asundi A. "Moire interferometry for displacement measurement" *Opt and Las in Eng* 11 281-292 (1989)
48. Vest C.M. "Holographic interferometry" Wiley (1979)
49. Ennos A.E. "Measurement of in-plane surface strain by hologram interferometry" *J Phys E* 2(1) 731-734 (1968)
50. Boone P.M. "Holographic determination of in-plane deformation" *Opt Tech* 94-98 (1970)
51. Schluter M. and Nowatzky A. "In-plane deformation measurement by video-electronic hologram interferometry" *Opt Act* 27(6) 799-808 (1980)
52. Adams F.D. and Maddux G.E. "Synthesis of holography and speckle photography to measure 3-D displacements" *Appl Opt* 13(2) 219 (1974)
53. Boone P.M. "Use of reflection holograms in holographic interferometry and speckle correlation for measurement of surface displacement" *Opt Act* 22(7) 579-589 (1975)
54. Dudderar T.D. "Application of holography to fracture mechanics" *Exp Mech* 9 281-285 (1969)
55. Dudderar T.D. and Gorman H.J. "The determination of mode-one stress-intensity factors by holographic interferometry" *Exp Mech* 13(3) 145-149 (1973)
56. Juptner W. "Holographic interferometry as a means for non-destructive testing and flaw quantisation" *Proc SPIE* 699 88-93 (1986)
57. Hsu T.R., Lewak R. and Wilkins B.J.S. "Measurements of crack growth in a solid at elevated temperature by holographic interferometry" *Exp Mech* 18 297-302 (1978)
58. Fan H.T. and Shen C.H. "Experimental evaluation of J-integral for a centre-cracked plate subject to quasi-static thermal load" *Proc SPIE* 814 390-397 (1987)
59. Burch J.M. and Tokarski J.M. "Production of multiple beam fringes from photographic scatterers" *Opt Act* 15 101-111 (1968)
60. Archbold E. and Ennos A.E. "Displacement measurement from double-exposure laser photographs" *Opt Act* 19(4) 253-271 (1972)

61. Duffy D.E. "Moire gauging of in-plane displacement using double exposure aperture imaging" *Appl Opt* 11 1778-1781 (1972)
62. Leendertz J.A. "Interferometric displacement measurement on scattering surfaces utilising speckle effect" *J Phys E* 3 214-218 (1970)
63. Archbold E., Burch J.M. and Ennos A.E. "Recording in-plane surface displacement by double-exposure speckle photography" *Opt Act* 17(12) 883-898 (1970)
64. Evans W.T. and Luxmoore A. "Measurement of in-plane displacements around crack tips by a laser speckle method" *Eng Fract Mech* 6 735-743 (1974)
65. Huntley J.M. "An image processing system for the analysis of speckle photographs" *J Phys E* 19 43-48 (1986)
66. Huntley J.M. and Field J.E. "Measurement of crack displacement field using laser speckle photography" *Eng Fract Mech* 30(6) 779-790 (1988)
67. Chiang F.P., Adachi J., Anastasi R. and Beatty J. "Subjective laser speckle method and its application to solid mechanics problems" *Opt Eng* 21(3) 379-390 (1982)
68. Asundi A. and Chiang F.P. "Theory and application of the white light speckle method for strain analysis" *Opt Eng* 21(4) 570-580 (1982)
69. Boone P.M. "Use of close range objective speckles for displacement measurement" *Opt Eng* 21(3) 407-410 (1982)
70. Chiang F.P. and Hareesh T.V. "Three-dimensional crack tip deformation: an experimental study and comparison to the HRR field" *Int J of Fract* 36 243-257 (1988)
71. Jones R. and Wykes C. "Holographic and speckle interferometry" Cambridge University Press (1983)
72. Shellabear M.C. "Application of ESPI to the study of three-dimensional mechanical vibrations" PhD Thesis, Loughborough University (1991)
73. Holscher C., Gulker G., Hinsch K., Kramer A. and Neunaber H. "The investigation of natural stones under test conditions by ESPI" *Proc SPIE* 863 162-166 (1987)
74. Barker D.B. and Fourney M.E. "Three-dimensional speckle interferometric investigation of the stress-intensity factor along a crack front" *Exp Mech* 17(6) 241-247 (1977)

75. Herbert D.P., Al-Hassani A.H.M. and Richardson M.O.W. "The use of ESPI in the crack propagation analysis of epoxy resins" *Opt and Las in Eng* 5 1-14 (1984)
76. Winther S. "3-D strain measurements using ESPI" *Opt and Las in Eng* 8 75-57 (1988)
77. Button B.L., Dobbins B.N., He S.P., Kapasi S. and Wang L.S. "3-D deformation measurement using DSPI" in *Applied Optics Digest*, Dainty J.C. (ed), Institute of Physics 283-284 (1990)
78. Vrooman H.A. and Maas A.A.M. "Image processing in digital speckle interferometry" *Proc 4th Int Conf of FASIG, Loughborough*, (April 1989)
79. Spectradata GmbH, Uferstrasse 74, D-2900 Oldenburg, Germany. Technical sales literature
80. Cookson T.J., Butters J.N. and Pollard H.C. "Pulsed lasers in electronic speckle pattern interferometry" *Opt Las Tech* 10 119-124 (1978)
81. Shellabear M.C., Mendoza Santoyo F. and Tyrer J. "Processing of addition and subtraction fringes from pulsed ESPI for the study of vibration" in *Hologram Interferometry and Speckle Metrology*, SEM 238-244 (1990)
82. Reid G.T. "Automatic fringe analysis: a review" *Opt and Las in Eng* 7 37-68 (1986)
83. Funnel W.R.J. "Image processing applied to the interactive analysis of interferometric fringes" *Appl Opt* 20(18) 3245-3250 (1981)
84. Yatagai T., Ideswara M., Yamaashi Y. and Suzuki M. "Interactive fringe analysis system: applications to moire contourogram and interferogram" *Opt Eng* 21(5) 901-906 (1982)
85. Button B.L., Cutts J., Dobbins B.N., Moxon C.J. and Wykes C. "The identification of fringe positions in speckle patterns" *Opt and Las Tech* 17 189-192 (1985)
86. Nakadate S., Yatagai T. and Saito H. "Computer-aided speckle pattern interferometry" *Appl Opt* 22(2) 237-243 (1983)
87. Cline H.E., Holik A.S. and Lorensen W.E. "Computer-aided surface reconstruction of interference contours" *Appl Opt* 21(24) 4481-4488 (1982)
88. Schemm J.B. and Vest C.M. "Fringe pattern recognition and interpretation using non-linear regression analysis" *Appl Opt* 22(18) 2850-2853 (1983)

89. Hurden A.P.M. "vibration mode analysis using electronic speckle pattern interferometry" *Opt Las Tech* 21-25 (Feb, 1982)
90. Crane R. "Interference phase measurement" *Appl Opt* 8(3) 538-542 (1969)
91. Dentino M.J. and Barnes C.W. "Measurement of complex amplitude in a coherent optical image" *J Opt Soc Am* 60 420-421 (1970)
92. Dandliker R., Ineichen B. and Mottier F.M. "High resolution hologram interferometry by electronic phase measurement" *Opt Comm* 9(4) 412-416 (1973)
93. Dandliker R. and Thalman R. "Heterodyne and quasi-heterodyne holographic interferometry" *Opt Eng* 24(5) 824-831 (1985)
94. Macovski A., Ramsey S.D. and Schaefer L.F. "Time-lapse interferometry and contouring using television systems" *Appl Opt* 10(12) 2722-2727 (1971)
95. Wyant J.C. "Use of an ac heterodyne lateral shear interferometer with real-time wavefront correction systems" *Appl Opt* 14(11) 2622-2626 (1975)
96. Stumpf K.D. "Real-time interferometer" *Opt Eng* 18(6) 648-653 (1979)
97. Creath K. "Phase-shifting speckle interferometry" *Appl Opt* 24(18) 3053-3058 (1985)
98. Ichioka Y. and Inuiya M. "Direct phase detecting system" *Appl Opt* 11(7) 1507-1514 (1972)
99. Bruning J.H., Herriot D.R., Gallagher J.E., Rosenfield D.P., White A.D. and Brangaccio D.J. "Digital wavefront measuring interferometer for testing optical surfaces and lenses" *Appl Opt* 13(11) 2693-2703 (1974)
100. Carre P. "Installation et utilisation du comparateur photoelectrique et interferentiel de Bureau International des Poids et Mesures" *Metrologia* 2(1) 13-23 (1966)
101. Frantz L.M., Sawchuk A.A. and von der Ohe W. "Optical phase measurement in real time" *Appl Opt* 18(19) 3301-3306 (1978)
102. Hariharan P., Oreb B.F. and Brown N. "A digital phase-measurement system for real-time holographic interferometry" *Opt Comm* 41(6) 393-396 (1982)
103. Dandliker R., Thalman R. and Willemin J-F. "Fringe interpolation by two-reference-beam holographic interferometry: reducing sensitivity to hologram misalignment" *Opt Comm* 42(5) 301-306 (1982)

104. Kujawinska M., Spik A. and Robinson D.W. "Analysis of ESPI interferograms by phase-stepping techniques" Proc 4th Int Conf of FASIG, Loughborough University (April 1989)
105. Takeda M., Hideki I. and Kobayashi S. "Fourier-transform method of fringe-pattern analysis for computer based topography and interferometry" J Opt Soc Am 72(1) 156-160 (1982)
106. Mertz L. "Real-time fringe pattern analysis" Appl Opt 22(10) 1535-1539 (1983)
107. Womack K.H. "Interferometric phase measurement using spatial synchronous detection" Opt Eng 23(4) 391-395 (1984)
108. Kerr D., Mendoza Santoyo F. and Tyrer J.R. "Extraction of phase data from ESPI fringes using a single-phase-step method: a novel approach" J Opt Soc Am 7(5) 820-826 (1990)
109. Kerr D. and Tyrer J.R. "The application of phase-stepping to the analysis of ESPI fringe patterns" Proc SPIE 814 379-389 (1987)
110. Nakadate S. and Saito H. "Fringe scanning speckle pattern interferometry" Appl Opt 24(14) 2172-2180 (1985)
111. Not used
112. Osten W. and Hofling R. "The inverse modulo process in automatic fringe analysis - problems and approaches" in *Hologram Interferometry and Speckle Metrology*, SEM 301-309 (1990)
113. Mendoza Santoyo F., Shellabear M.C. and Tyrer J.R. "Whole-field in-plane analysis using phase-stepped ESPI" Appl Opt 30(7) 717-721 (1991)
114. Robinson D.W. and Williams D.C. "Digital phase-stepping speckle interferometry" Opt Comm 57 26-30 (1986)
115. Scwider J., Burrow R., Elsner K-E., Grzanna J., Spolaczyk R. and Merkel K. "Digital wavefront measuring interferometry" Appl Opt 22(21) 3421-3432 (1983)
116. Cheng Y-Y. and Wyant J.C. "Phase-shifter calibration in phase-shifting interferometry" Appl Opt 24(18) 3049-3052 (1985)
117. Creath K. "Comparison of phase-measurement algorithms" Proc SPIE 680 19-28 (1986)

118. Slettemoen G.A. and Wyant J.C. "Maximal fraction of acceptable measurements in phase-shifting speckle interferometry: a theoretical study" *J Opt Soc Am A* 3(2) 210-214 (1986)
119. Jones R. and Wykes C. "Decorrelation effects in speckle pattern interferometry. Displacement dependent decorrelation and applications to the observation of machine induced stress" *Opt Act* 24(5) 533-550 (1977)
120. Goodman J.W. "Statistical properties of laser speckle patterns" in *Laser Speckle and Related Phenomena*, Dainty J.C. (ed), Springer-Verlag 9-75 (1984)
121. Slettemoen G.A. "First-order statistics of displayed speckle patterns in electronic speckle pattern interferometry" *J Opt Soc Am* 71(4) 474-482 (1981)
122. Varman P. and Wykes C. "Smoothing speckle and moire patterns by computer processing" *Opt and Las in Eng* 3(2) 87-100 (1982)
123. Kerr D., Mendoza Santoyo F. and Tyrer J.R. "Manipulation of the Fourier components of speckle fringe patterns as part of an interferometric analysis process" *J Mod Opt* 36(2) 195-203 (1989)
124. Timoshenko S.P. and Goodier J.N. "Theory of Elasticity" Third Edition, McGraw-Hill (1970)
125. Brownell J.B. and Parker R.J. "Optical techniques for in-plane strain measurement in an industrial environment" *Proc SPIE* 1084 2-18 (1989)
126. Shellabear M.C. and Tyrer J.R. "Three-dimensional vibration analysis using electronic speckle pattern interferometry (ESPI)" *Proc SPIE* 952 (1988)
127. Jones R. "The design and application of a speckle pattern interferometer for total plane strain field measurement" *Opt and Las Tech* 8 215-219 (1976)
128. Jones R. and Leendertz J.A. "Elastic constant and strain measurements using a three beam speckle pattern interferometer" *J Phys E* 7 653-657 (1974)
129. Ennos A.E. "Speckle interferometry" in *Laser Speckle and Related Phenomena*, Dainty J.C. (ed), Springer-Verlag (1975)
130. Tyrer J.R. "Experimental investigations into fringe contrast of time averaged ESPI" MSc Thesis, Cranfield Institute of Technology (1981)
131. Grant G.R. and Orloff K.L. "Two-colour dual-beam, backscatter laser Doppler velocimeter" *Appl Opt* 12 2913-2916 (1973)

132. Blake K.A. "Simple two-dimensional laser velocimetry optics" J Phys E 5 623-624 (1972)
133. O'Donnell W.J. "The additional deflection of a cantilever due to the elasticity of the support" J Appl Mech 27 461-464 (1960)
134. Shellabear M.C. Private communication
135. Feddersen C.E. Discussion to Reference 12
136. Isida M. "Analysis of stress-intensity factors for the tension of centrally cracked strip with stiffened edges" Eng Fract Mech 5 647-655 (1973)
137. Sih G.C. "On the Westergaard method of crack analysis" Int J of Fract Mech 2 628-631 (1966)
138. Creager M. and Paris P.C. "Elastic field equations for blunt cracks with reference to stress corrosion cracking" Int J of Fract Mech 3 247-252 (1967)
139. Oglesby J. and Lomacky O. "An evaluation of finite element methods for the computation of elastic stress-intensity factors" Naval Ship Research and Development Centre Report 3751 (1971)
140. ASTM Standard E1290 "Standard test method for crack tip opening (CTOD) fracture toughness measurement" (1989)
141. Newman J.C. "Stress analysis of the compact tension specimen including the effects of pin-loading" ASTM STP 560 105-121 (1974)
142. Anon "Optecord live fringe interferometer: instruction manual" Strathclyde University
143. Maas A.A.M. "Phase-shifting speckle interferometry" PhD Thesis, Delft University (1991)
144. Sanford R.J. "A critical re-examination of the Westergaard method for solving opening-mode crack problems" Mechanics Research Communications 6(5) 289-294 (1979)
145. Chona R., Irwin G.R. and Sanford R.J. "Influence of specimen size and shape on the singularity-dominated zone" ASTM STP 791 I23-I23 (1983)
146. Sanford R.J. "Application of the least-squares method to photoelastic analysis" Exp Mech 20(6) 192-197 (1980)
147. Yang W. and Freund L.B. "Transverse shear effects for through-cracks in an elastic plate" Int J Solids Struct 21 977-994 (1985)

148. Not used
149. Hyde T.H. and Warrior N.A. "Photoelastic determination of mixed-mode stress-intensity factors for inclined semi-circular cracks in thin tubes" *J Strain Analysis* 24(2) 83-94 (1989)
150. Hyde T.H. Private communication
151. Huntley J. and Benckert L "Measurement of dynamic crack tip displacement field by speckle photography and interferometry" in *Fringe Analysis '92* Halliwell N.A. et al (eds), FASIG (1992)
152. Kries T. "Digital holographic interference phase measurement using the Fourier transform method" *J Opt Soc Am* 3(6) 847-855 (1986)
153. MacGregor C.W. "The potential function method for the solution of two-dimensional stress problems" *Trans American Mathematical Soc* 38(1) 177-186 (1935)
154. Westergaard H.M. "Bearing pressures and cracks" *J Appl Mech* A49-A53 (1939)

